Chem Soc Rev

ROYAL SOCIETY OF CHEMISTRY

REVIEW ARTICLE

View Article Online
View Journal

Check for updates

Cite this: DOI: 10.1039/d3cs00795b

The design and development of glucose probes for sensing and imaging within biological systems

Hao Wang, †[af] Chunfang Li, †[a] Fangyuan Zhang, †[a] Benjamin Kersch-Hunt, [b] Jordan E. Gardiner, [bij] Lijuan Ren, [a] Ying Li, [a] Simon E. Lewis, [b] Yanling Mu, [a] Qingqiang Yao, [a] Luling Wu, [be] Robin R. Groleau, *[bc] Wenhao Zhai, †*[ag] Zhen Liu, *[e] Tony D. James, *[bh] Eric V. Anslyn *[d] and Kai Wang *[ab]

Received 21st January 2026

DOI: 10.1039/d3cs00795b

rsc.li/chem-soc-rev

Glucose and glucose homeostasis are central to the regulation of biological processes, and the development of probes for glucose sensing and imaging in biological systems has long been of significant interest to the biological and chemical sciences community. The resulting body of literature is therefore vast, and this review aims to outline major contributions and approaches to provide insight into these probes' working mechanisms with the aim of fostering the development of new glucose-sensing systems. This review summarizes advances in the design of glucose probes for biological sensing, and discusses the design principles behind seminal and more recent glucose probes, covering glucose analogue-based tracers, enzyme-based probes, fluorescent protein-based probes, lectin-based probes, and boronic acid-based glucose probes. Throughout, design principles will be emphasized and limitations and challenges of the existing landscape will be discussed, highlighting future opportunities and potential research directions.

1. Introduction

The development of glucose probes for sensing and imaging in biological systems is of great scientific importance,[1] as glucose plays a key role throughout nature, acting as the primary source of energy for many living systems. It is typically metabolized by oxidation and catabolism to release energy to maintain physiological functions in organisms. These metabolic processes can differ in spatial and temporal distribution, and the functional roles of glucose can vary under different physiological and pathological conditions (Fig. 1), hence the requirement for better sensing, tracking, and imaging tools. Improved understanding of glucose-based processes requires high resolution dynamic monitoring in complex biological environments, whilst also needing to differentiate glucose from numerous other saccharides, all in the presence of active interfering biomolecules.[2]

Glucose homeostasis is a key aspect of managing glucose's role and importantly, its dysregulation, is a focus of life sciences.[3] Glucose homeostatic balance is essential for organisms to be able to withstand internal and external environmental changes. Glucose absorption in humans occurs mainly *via* the small intestine (Fig. 2a), and once in the bloodstream glucose is circulated throughout the body, contributing to intracellular glucose metabolic cycles through cellular uptake *via* glucose transporter proteins (GLUTs). Energy and carbon are then provided through a combination of anaerobic metabolism (glycolysis), aerobic catabolism, and the pentose phosphate pathway to maintain normal cell growth and reproduction. Imbalance in glucose homeostasis and abnormal metabolism play a crucial role in pathological processes such as malignancy,[4] diabetes,[5] and neurodegenerative disorders.[6] Oxidative metabolism of glucose within the mitochondrial matrix is a driver for insulin release,[7] secreted by pancreatic β-cells as a response to increased blood sugar glucose, acting to reduce these levels and maintain blood

---

[a] *State Key Laboratory of Advanced Drug Delivery and Release Systems, School of Pharmaceutical Sciences & Institute of Materia Medica, Shandong First Medical University & Shandong Academy of Medical Sciences, Jinan 250117, Shandong, People's Republic of China. E-mail: wk-sandy@mail.nankai.edu.cn*

[b] *Department of Chemistry, University of Bath, Bath, BA2 7AY, UK. E-mail: t.d.james@bath.ac.uk*

[c] *Department of Life Sciences, University of Bath, Bath, BA2 7AY, UK. E-mail: rg598@bath.ac.uk*

[d] *Department of Chemistry, University of Texas at Austin, Austin, Texas 78712, USA. E-mail: anslyn@austin.utexas.edu*

[e] *State Key Laboratory of Analytical Chemistry for Life Science, School of Chemistry, Nanjing University, 163 Xianlin Avenue, Nanjing 210023, People's Republic of China. E-mail: zhenliu@nju.edu.cn*

[f] *College of Medical Engineering, Jining Medical University, Jining 272067, Shandong, People's Republic of China*

[g] *College of Pharmacy, Ningxia Medical University, Yinchuan 750004, Ningxia, People's Republic of China. E-mail: 20220104@nxmu.edu.cn*

[h] *School of Chemistry and Chemical Engineering, Henan Normal University, Xinxiang 453007, People's Republic of China*

[i] *Lifecare Chemistry, Bath, BA2 4BL, UK*

[j] *Lifecare Chemistry Laboratory, Science Creates, Bristol, BS2 0XJ, UK*

† These authors contributed equally to this work.

glucose homeostasis. Specifically, the oxidation of glucose in β-cells increases the ATP (adenosine triphosphate) : ADP (adenosine diphosphate) ratio in the cytoplasm, leading to the closure of ATP-sensitive K^+ channels (K_{ATP}), which in turn induces the influx of extracellular Ca^{2+}, ultimately triggering insulin secretion (Fig. 2b).

Dysregulation of these processes is key to disease states, for instance in 2019 the group of Chen showed that high glucose concentration can activate mitochondrial activity in T-cells, leading to reactive oxygen species (ROS) overproduction which in turn activates transforming growth factor β (TGF-β) to ultimately upregulate the expression of the receptor RORγt

From left to right: Fangyuan Zhang, Lijuan Ren, Benjamin Kersch-Hunt, Robin R. Groleau, Tony D. James, Luling Wu, Kai Wang, Ying Li and Chunfang Li

Fangyuan Zhang BS Degree from Shandong First Medical University (2018-2022). She is currently a postgraduate student in Pharmacy at School of Pharmaceutical Sciences of the university.

Lijuan Ren BS Degree in Pharmacy from Shandong First Medical University in 2022, and her MSc degree in Pharmacy from Shandong First Medical University in 2025.

Benjamin Kersch-Hunt MChem from the University of Birmingham in 2022. He is currently a PhD student at the University of Bath in collaboration with Lifecare.

Robin R. Groleau is a Lecturer in Medicinal Chemistry at the University of Bath. He is a graduate of the Universities of Bristol (MSci), Cardiff (MRes), and completed his PhD in organic chemistry at the University of Bath under the supervision of Prof. Steve Bull.

Tony D. James is Professor at the University of Bath Fellow of the Royal Society of Chemistry and Fellow of the European Academy of Science.

Luling Wu is a tenure-track Assistant Professor and "Tang Scholar" at Nanjing University. He obtained a PhD in 2021, supported by the China Scholarship Council (CSC) and the University of Bath. He was an EPSRC postdoctoral research fellow at the University of Bath and postdoctoral research fellow at Westlake University.

Kai Wang received his BSc degree in Pharmacy from Binzhou Medical University in 2014, MS degree in Pharmaceutical Chemistry from University of Jinan in 2017, and PhD degree in Pharmaceutical Analysis from Nankai University in 2021 (China). He joined in Shandong First Medical University in 2022, and in 2025 as a visiting professor joined in the Department of Chemistry at University of Bath (2025-2026).

Ying Li BSc degree in Pharmacy from Shandong University of Traditional Chinese Medicine in 2013, her MSc degree in Pharmacy from Jinan University in 2016, and her PhD degree in Internal Medicine from Shandong First Medical University in 2025. She joined Shandong First Medical University in 2025.

Chunfang Li BS Degree from the School of Medicine and Nursing, Dezhou University (2019–2023). She is pursuing an MS degree in Pharmacy at Shandong First Medical University.

Wenhao Zhai

Wenhao Zhai received his BSc from Qilu University of Technology in 2016. He subsequently completed his PhD in Medicinal Chemistry from the College of Pharmacy at Nankai University in 2021. In 2022, he began his academic career at Ningxia Medical University, and in 2025 as a visiting researcher joined in the School of Pharmaceutical Sciences at Shandong First Medical University. His research focuses on the design of nanotheranostic peptides and their applications in antitumor therapy.

Zhen Liu

Zhen Liu is a Zhicheng Distinguished Professor at Nanjing University. His main research interests encompass biomimetic molecular recognition and its empowered biomedical applications. He was awarded the National Science Fund for Distinguished Young Scholars in 2014. He has received a few prestigious awards, including the Science & Technology Award (First Class) by China Association for Instrumental Analysis (2011, 2017), the Humanity in Science Award (Silver Recognition) by Phenomenex & Analytical Scientist (2016) and the Advances in Measurement Science Lectureship by the American Chemical Society (2020).

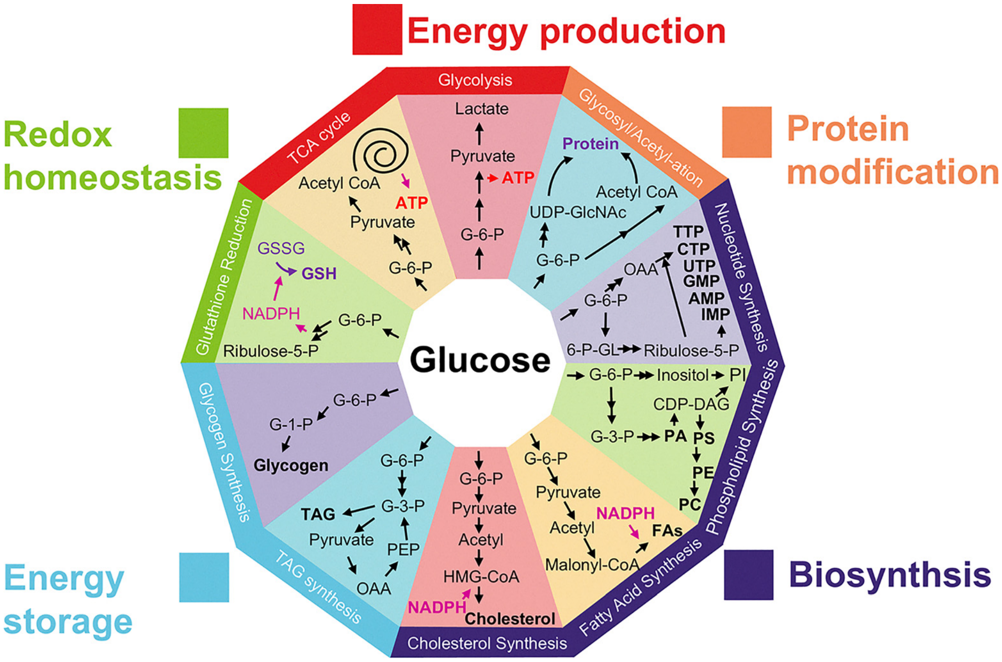

Fig. 1 Schematic representation of the main biological functions of glucose: energy source, protein modification, biosynthesis, energy storage, and redox homeostasis.

(retinoic acid-related orphan receptor gamma t), promoting Th17 differentiation.[8] This ultimately shifts immune regulation in a pro-inflammatory direction and exacerbates autoimmune diseases (Fig. 2c). As a source of energy, glucose contributes to disease development such as in tumor growth, where malignant tumor cells depend on glycolysis and convert glucose to lactic acid (Fig. 2d, under sufficient oxygenation), taking up large amounts of glucose to maintain rapid tumor cell growth and proliferation (Warburg effect).[9]

Alongside its core role as a source of energy and carbon, glucose is increasingly being viewed as a key "messenger" molecule to modulate metabolism-related proteins through its involvement in signal transduction.[10,11] At present, these regulatory mechanisms and their biological impact are still unclear, slowing pathological research into related diseases and treatment, illustrating the need for the development of robust sensing probes to monitor even small glucose changes. Glucose probe development is a long-standing and active field, replete with excellent and comprehensive reviews of select areas in the field such as James and Sun's extensive review of supramolecular glucose sensing in 2015, focusing on artificially synthesized supramolecular systems (*e.g.*, cyclodextrins, calixarenes, metal–organic frameworks).[12] In 2020 and 2023, the groups of Pemble[13] and Guo[14] covered electrochemical glucose biosensors and minimally invasive electrochemical continuous glucose monitoring (CGM) sensors, respectively. The current review is comprehensive in nature and outlines general and unique design principles employed in developing all types of glucose probes (up until 2025), and outlines chemical, biological, and fluorescence mechanisms (Fig. 3). These aspects are illustrated using seminal and recent research involving glucose analogue-based tracers, enzyme-based probes, fluorescent protein-based probes, lectin-based probes, boronic acid glucose probes, *etc.*

2. Glucose analogue tracers for biological imaging

Glucose tracer probes are typically composed of three parts: (i) a glucose moiety that determines cellular uptake patterns of the glucose analogue; (ii) a signaling group, for bioimaging by either Positron Emission Tomography (PET), Single Photon Emission Computed Tomography (SPECT), fluorescence, or Magnetic Resonance Imaging (MRI); (iii) and a linker connecting both functional components. The most notable example is the PET imaging tracer 2-[^{18}F]-fluoro-deoxy-glucose, 2-[^{18}F]-FDG (**1**), known as the 'molecule of the 20th century',[15,16] which is now a common glucose imaging probe in oncology, cardiology and neurology. This and other examples will be outlined here, although it must be noted these are glucose-derived sensing

Eric V. Anslyn

Eric V. Anslyn is the Welch Regents Chair of Chemistry at the University of Texas at Austin. His research interests encompass sensor development, functional materials, and mechanistic organic chemistry. He has received several prestigious awards in the areas of supramolecular chemistry and physical organic chemistry, as well as many teaching awards from Univ. Texas at Austin.

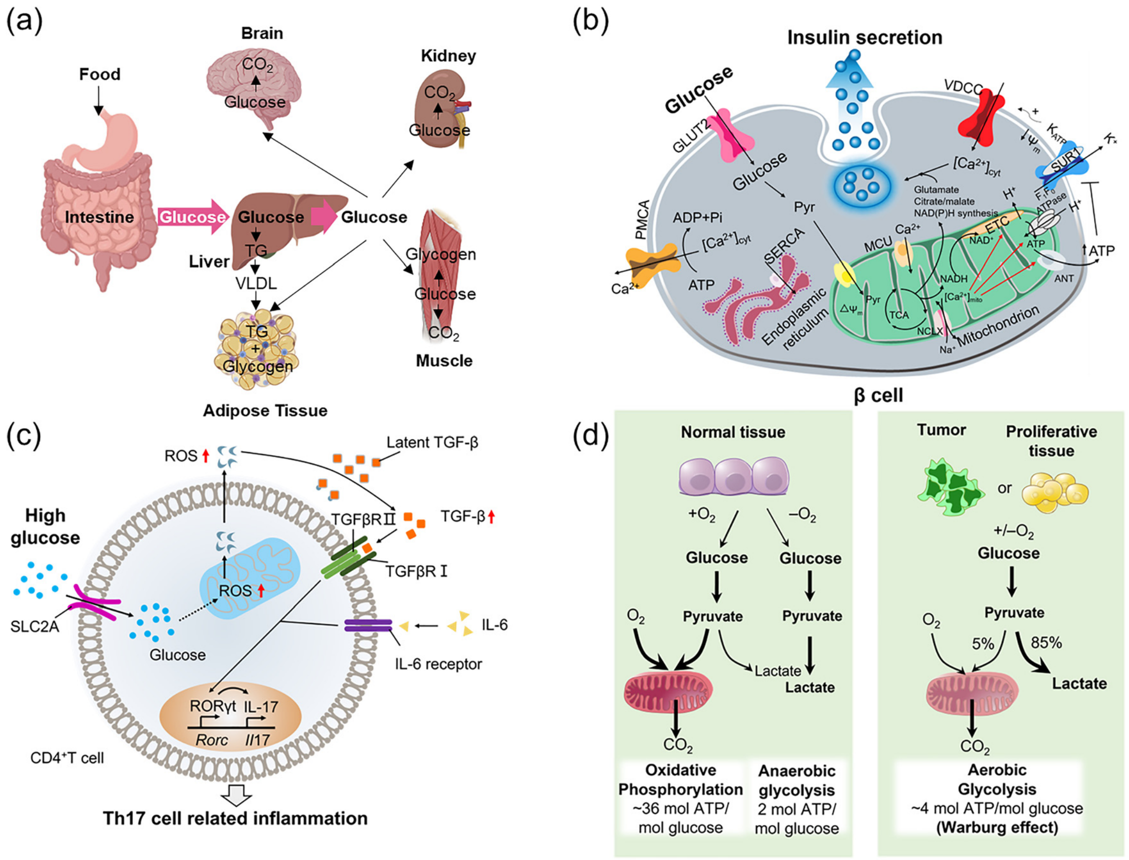

Fig. 2 (a) The process of glucose absorption and distribution. (b) Spatiotemporal correlation of glucose with Ca^{2+} and insulin release: Schematic diagram of glucose metabolism in normal islet β cells. (c) Temporal and spatial correlation of glucose and ROS: Schematic diagram of heightened autoimmunity through ROS-mediated TGF-β cytokine activation. (d) Variation in glucose metabolism between normal and tumor tissues. Panel b: Adapted with permission from ref. 7, published by Springer Nature. Panel c: Adapted with permission from ref. 8. Copyright (2019) Elsevier Inc. Panel d: Adapted with permission from ref. 9. Copyright (2009) The American Association for the Advancement of Science.

motifs, rather than glucose sensors, and so they enable the evaluation of processes which use glucose rather than detection or quantification of glucose itself.

2.1. Radiolabeled glucose derivatives

Although most of this review will look at optical imaging, we should first outline some examples of nuclear imaging, as it is a common application of glucose-derived tracers such as PET and SPECT[17] (*e.g.*, FDG, *vide supra*, Fig. 4). In nuclear imaging, radiolabeled probes are introduced into a patient and allowed to distribute, and radioactive emissions arising from nuclear decay are subsequently detected externally (X-ray CT (computed tomography), PET, SPECT...), enabling visualization of glucose distribution. These techniques have been widely applied in clinical medical diagnostics and other research fields.[18]

A key feature of glucose that enables these approaches is the ease by which it can be functionalized to produce a range of glucose-analogous probes, including incorporation of radioactive nuclei. As previously discussed, tumor cells are often characterized by abnormal glucose metabolism (Warburg effect, *vide supra*), and so radiolabeled glucose analogues have found application in tumor evaluation and diagnosis. Particularly noteworthy is the non-invasive nature of these probes which require only administration and imaging, leading to their widespread clinical use for *in vivo* imaging using glucose derivatives to which radioisotopes such as carbon-11 (^{11}C),[19] fluorine-18 (^{18}F),[20] and technetium-99m (^{99m}Tc),[21] have been introduced.

Due to the ubiquity of carbon, ^{11}C isotopomers are common.[22] This substitution produces only minor change (*cf.* stable ^{13}C), and so these analogues retain the same chemical and physiological properties and are nearly indistinguishable from the normal unlabeled species. ^{11}C glucose is therefore commonly employed as a radiotracer for imaging metabolic activity across various organs, allowing not only the study of glucose distribution, but also its metabolism by quantifying and characterizing the ^{11}C-labeled metabolites produced.[23,24] The only major limitation of ^{11}C radiolabeled analogues is the short half-life of ^{11}C, with $t_{1/2}$ = 20 min, requiring rapid labelling and immediate administration and imaging, which limits the types of measurements and research possible, and decreasing some of its clinical applicability.

Far more common is ^{18}F (*cf.* stable ^{19}F) which has a much more suitable half-life (*ca.* 110 min).[25–29] ^{18}F has the added benefit of facile generation from proton bombardment of ^{18}O, which is readily done on-site before incorporation of the newly formed ^{18}F into the desired compound. These features explain in part the incredible success of ^{18}F-labelled FDG **1**, which

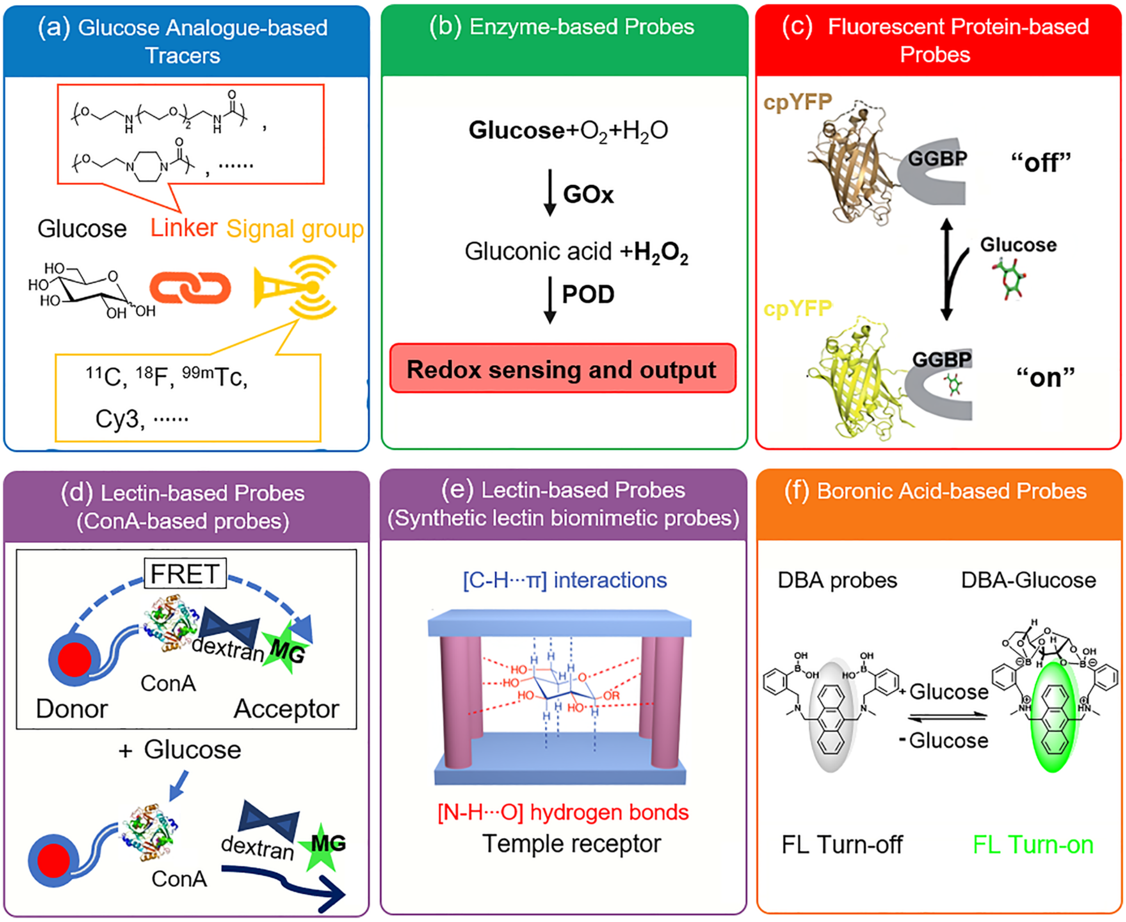

Fig. 3 Design principles and detection mechanisms of representative glucose probes. (a) Glucose analogue-based tracers consist of a glucose moiety, a linker, and a signaling group (*e.g.*, radionuclide, fluorophore, or contrast agent). Detection relies on metabolic trapping or specific glucose transporter-mediated uptake. (b) Enzyme-based probes. Typically utilizing glucose oxidase (GOx) to catalyze glucose oxidation, producing hydrogen peroxide to trigger signal production. (c) Fluorescent protein-based probes: Composed of a fluorescent protein (*e.g.*, circularly permuted yellow fluorescent protein, cpYFP) combined with glucose/galactose-binding protein (GGBP). Glucose binding induces a hinge-twist conformational change in GGBP, thereby altering the fluorescence properties of the fluorescent protein to generate a ratiometric signal proportional to glucose concentration. (d) Lectin-based (ConA) probes: Glucose competitively displaces concanavalin A (ConA)-conjugated malachite green (MG)-dextran, triggering Förster resonance energy transfer (FRET)-mediated fluorescence signal recovery. (e) Lectin-based (synthetic biomimetic) probes: Employ glucose-binding synthetic receptors to mimic lectin function. Glucose binding induces conformational changes, directly switching the fluorescence or colorimetric signal. (f) Boronic acid-based probes: employ boronic acid recognition units that form reversible esters with the *cis*-diol groups of glucose, resulting in switching (*e.g.*, "turn-on" or "turn-off") of the fluorescence or electrochemical signals.

accounts for over 90% of PET radiotracer use in oncology.[30,31] It is simply glucose in which the 2-hydroxyl group has been replaced by ^{18}F, producing an isoelectronic compound of near-identical mass to glucose. It enters cells as normal *via* GLUTs and is subsequently phosphorylated by hexokinase to 2-[^{18}F]-FDG-6P (Fig. 4a). This fluorinated intermediate is not a competent substrate of glucose-6-phosphate dehydrogenase, preventing further metabolism, a process known as metabolic trapping. Phosphorylated **1** being neglected, this metabolite remains sequestered, causing accumulation which can be imaged (Fig. 4b).[32] Furthermore, the ^{18}F isotope in **1** ultimately decays to ^{18}O over a short period of time, resulting in the production of natural (if isotopically-enriched) D-glucose, thus allowing the continuation of the regular glycolytic pathway and minimal toxicity.

The excellent localization of ^{18}FDG and its high sensitivity for tumor detection has made **1** indispensable in addressing various clinical challenges. This is exemplified in Fig. 5 where ^{18}F-FDG PET/CT imaging has been used to visualize lung carcinoma.[18]

Driven by the clinical success of **1**, a series of fluorinated carbohydrate tracers (**2–7**) have been developed for nuclear imaging applications (Fig. 6).[33–38] To produce these ^{18}F-labelled glucose analogues using proton bombardment an accelerator (and some additional synthetic steps) is required, limiting to an extent availability and impacting the cost of these radiolabeled imaging techniques, hindering true widespread adoption. In contrast, the global number of SPECT devices significantly exceeds that of PET scanners, endowing SPECT imaging with broader clinical applicability and potential.[39] ^{99m}Tc is used for this thanks to its long half-life of 6.02 hours, emission of 140 keV gamma rays, availability *via* ^{99}Mo-^{99m}Tc generators, and its wide range of oxidation states from −1 to +7 allowing a rich catalogue of coordination chemistries. These characteristics facilitate the

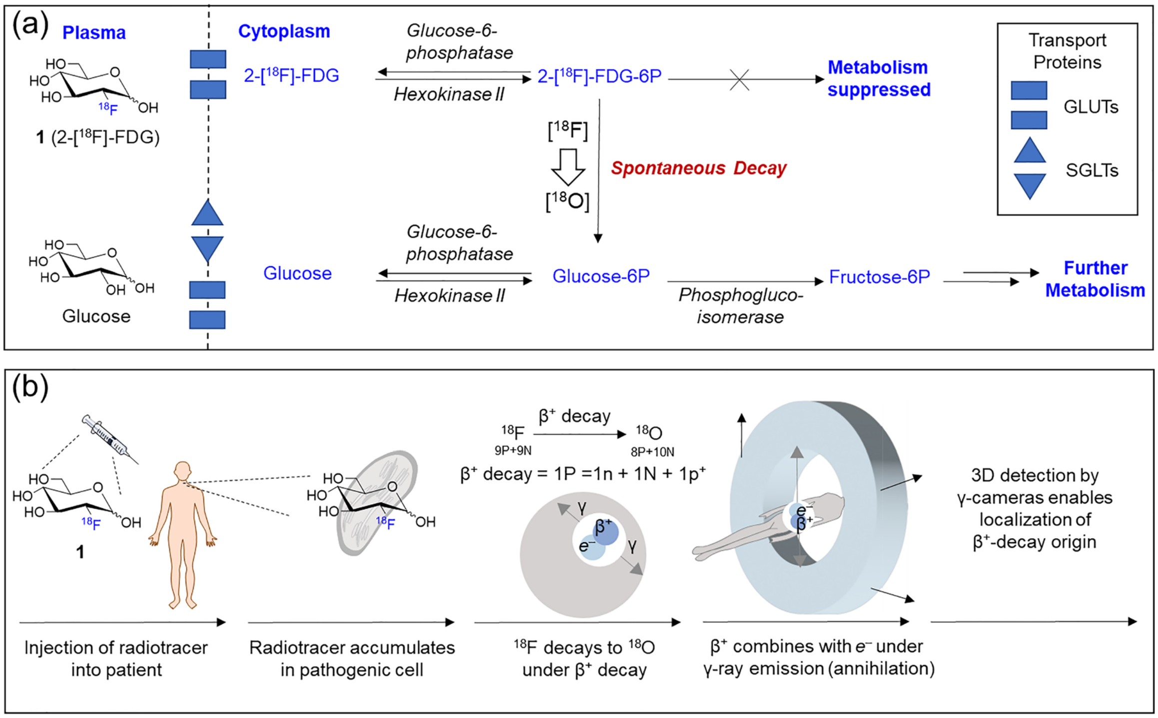

Fig. 4 (a) Metabolism of D-glucose and **1** (2-[^{18}F]-FDG). (b) PET imaging process: Following intravenous injection of **1** into the patient, **1** accumulates in cells. Subsequently, β$^+$ radiative decay occurs (producing ^{18}O) to release a positron (p$^+$). Collision with electrons produces γ-radiation emitted at an 180° angle. These γ-rays are then detected by the circular 3D PET scanner which reconstructs an image. Adapted with permission from ref. 20, published by Royal Society of Chemistry.

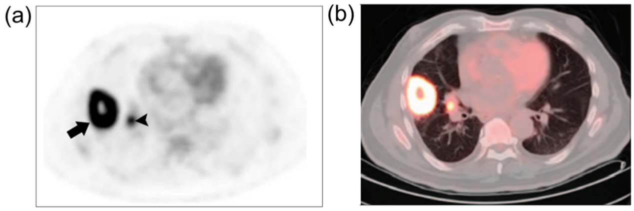

Fig. 5 FDG PET/CT fusion image of lung carcinoma. (a) and (b) Axial images from FDG-PET and fused PET/CT scans of a lung cancer patient reveal heightened FDG uptake in a 4 × 5 cm tumor located in the right lung (indicated by arrow), with evidence of central necrosis. Adapted with permission from ref. 18. Copyright (2007) American Chemical Society.

design and synthesis of various ^{99m}Tc-labeled radiopharmaceuticals with excellent performance. Given these ideal properties, the development of ^{99m}Tc-labeled glucose derivatives (**8–11**) for tumor imaging has become a major focus in the field of ^{99m}Tc-based tumor radiopharmaceuticals.[40–45]

2.2. Fluorescent-labeled glucose derivatives

A similar approach has been employed to develop fluorescent glucose analogues, though of course functional modifications/additions are far more extensive, as they require the addition of an entire fluorescent motif. In 1985, Kutchai and Speizer *et al.* synthesized the fluorescent glucose analogue **12** (6-deoxy-*N*-(7-nitrobenz-2-oxa-1,3-diazol-4-yl)-aminoglucose, 6-NBDG, Fig. 7), bearing a fluorescent aminonitrobenzoxadiazole at the 6-hydroxymethyl position.[46] This probe was used to explore the hexose transport system within human red blood cells, enabled by excitation and emission signals at 470 nm and 538 nm, respectively, and a promising detection limit in an aqueous environment of 50 nM. Cell-based experiments revealed that at concentrations of D-glucose near hexose's K_m (*ca.* 2 mM), the uptake of **12** is inhibited, with a stereospecific inhibitory effect observed (no inhibition with L-glucose). This suggests that despite the significant structural modification, **12** behaves akin to D-glucose, entering red blood cells through the usual mechanisms, indicating that these systems are likely a reliable means by which to study glucose metabolism.

Following this work, in 1996 Matsuoka and Yoshioka *et al.* developed **13** (2-NBDG, Fig. 7), a fluorescent glucose derivative with a nitrobenzoxadiazole at the C-2 position instead, and used it for monitoring intracellular metabolic activity.[47] This compound was readily synthesized by reaction of D-glucosamine (GlcN) and 4-chloro-7-nitrobenz-2-oxa-1,3-diazole (NBD-Cl), as is the case with many of the systems shown in Fig. 7, often only requiring the coupling of glucose with an appropriate fluorescent motif to allow rapid synthesis and wide accessibility. Uptake inhibition assays revealed that D-glucose competitively inhibited uptake of **13** with a K_i of 0.5 μM, whereas L-glucose showed no significant inhibitory effect. Subcellular localization analysis using fluorescence microscopy demonstrated that **13** was predominantly localized in the cytoplasm of *E. coli* (*Escherichia coli*) cells, illustrating the value in these probes for quantitative assessment of glucose uptake activity and studying transport mechanisms.

Two-photon microscopy (TPM) offers several advantages over classical single photon fluorescence, including increased penetration depth, localized excitation, and extended observation times. These characteristics make it suitable for the development of two-

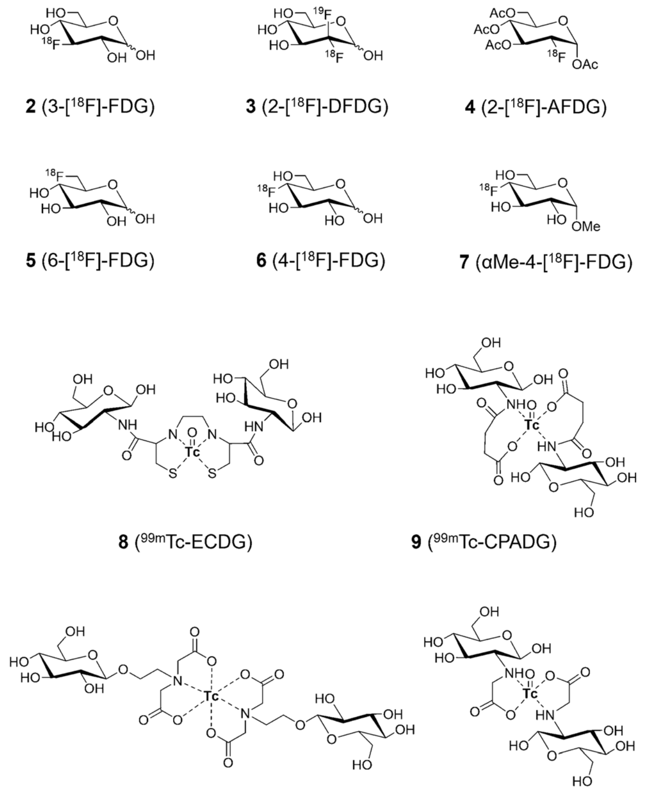

Fig. 6 Representative examples of ^{18}F glucose tracers (**2**–**7**) and ^{99m}Tc glucose tracers (**8**–**11**).

photon tracers designed to visualize glucose uptake. In 2009, Cho and colleagues introduced the two-photon probes **14a** (AG1) and **14b** (AG2) bearing C-1-linked naphthalene derivatives (Fig. 7), for monitoring glucose metabolism in living cells and tissues.[48] Cells treated with **14b** exhibited a higher uptake rate and generated brighter TPM images compared to those treated with **14a**. Cell uptake experiments confirmed that **14b** was more efficiently internalized by cancer cells (*e.g.*, A549 and HeLa cells) compared to normal cells (*e.g.*, HEK293 and NIH/3T3 cells). Additionally, the uptake rate of **14b** in colon cancer tissues was faster than in normal tissues, and pretreatment with taxol significantly reduced uptake (Fig. 8), as expected for a potent anticancer therapeutic. In tissue imaging studies, **14b** could be monitored for over 3000 s at depths of 75–150 μm. Moreover, **14b** exhibited high photostability and low toxicity, making it a promising candidate for colon cancer diagnosis.

Near-infrared (NIR) dyes have garnered significant interest for their potential in cancer detection and photodynamic therapy (PDT). A key feature of tumors is their enhanced glycolytic activity, which contributes to their malignant behavior. Motivated by this, researchers proposed that the glucose transport system could be leveraged to deliver diagnostic and therapeutic agents directly to tumor cells. In 2003, Zheng and Zhang *et al.* developed the novel photosensitizer **15** (Pyro-2DG, Fig. 7), which serves as both a tumor-targeted NIR-glucose fluorescence probe and PDT agent.[49] After intravenous administration **15** selectively accumulates in tumor tissues, leading to enhanced fluorescence in tumor margins (Fig. 9, top row) when compared to the surrounding normal tissue, such as muscle (middle row). Upon PDT treatment, mitochondrial damage is specifically induced in the irradiated tumor region. This work provides a strong foundation for the development of glucose-analogue mixed diagnostic/therapeutic agents which can both differentiate between tumor and normal tissue through the difference in metabolism and deliver treatment in a targeted manner.

Looking to create multi-functional systems that exploit complementary interactions, in 2004 Achilefu and Ye *et al.* employed a carbocyanine dye containing a dicarboxylic acid moiety as the central core, and reacted it with unprotected D-(+)-glucosamine to generate a series of glucosamine dendritic arrays based on the scaffold **16** (GlcN-Cypate, Fig. 7).[50] Preliminary *in vivo* studies demonstrated enhanced uptake of these probes in proliferating tumor cells, possibly mediated by GLUTs.

In 2006, Gambhir and Cheng *et al.* conjugated NIR fluorophore Cy5.5 (cyanine 5.5) with D-glucosamine to afford Cy5.5-D-glucosamine conjugate **17** (Cy5.5-2DG, Fig. 7), suitable for NIR fluorescence imaging of tumors in preclinical tumor xenograft models.[51] *In vivo* experiments indicated that both **17** and Cy5.5-NHS (Fig. 10a) rapidly accumulated in tumors within U87MG tumor models, peaking 30 min post-injection followed by a time-dependent gradual decline. In the U87MG glioma model, Cy5.5-NHS showed significantly higher tumor-to-normal tissue (T/N) fluorescence intensity ratios than **17** at both 4 h and 24 h post-injection, with the latter ratios reaching 3.34 (± 0.23) and 2.81 (± 0.10), respectively (Fig. 10b and c). The authors did not directly provide a clear mechanistic explanation for the phenomenon that Cy5.5-NHS has a higher T/N ratio than **17**, which may be related to differences in molecular structure, uptake/retention mechanisms, and clearance kinetics in normal tissues. In addition, this study highlighted that the size of near-infrared dyes is critical, as overly large fluorophores (such as Cy5.5 in **17**) may disrupt interactions with GLUTs and hexokinase, highlighting the need to select appropriately sized NIR dyes to retain specific targeting capabilities.

In 2007, the Park group designed and synthesized both anomers (α and β) of fluorescent-labeled D-glucose analogues: **18a** (Cy3 (cyanine 3)-labeled α-D-glucose, Fig. 7) and **18b** (Cy3-labeled β-D-glucose, Fig. 7).[52] This diastereomeric pair of probes was then employed in cell assays, exhibiting significant differences in uptake in A549 cells based on C-1 stereochemistry, the α-anomer **18a** exhibiting a 40% higher uptake than its β isomer (**18b**). Notably, **18a** also exhibited significantly higher glucose-uptake tracing efficiency than the previously reported 2-NBDG, generating comparable fluorescence intensities at only one tenth of the concentration. Using this highly effective probe **18a**, Park *et al.* developed a high throughput screening system for evaluating anticancer agents by quantitatively monitoring metabolic activity and changes *via* glucose uptake measurements in cancer cells (Fig. 11).

In 2009, Olive and Kovar *et al.* developed a NIR glucose tracer **19** (IRDye 800CW 2-DG, Fig. 7) for tumor imaging in mice by labeling 2-DG with the near-infrared (NIR) dye IRDye 800CW

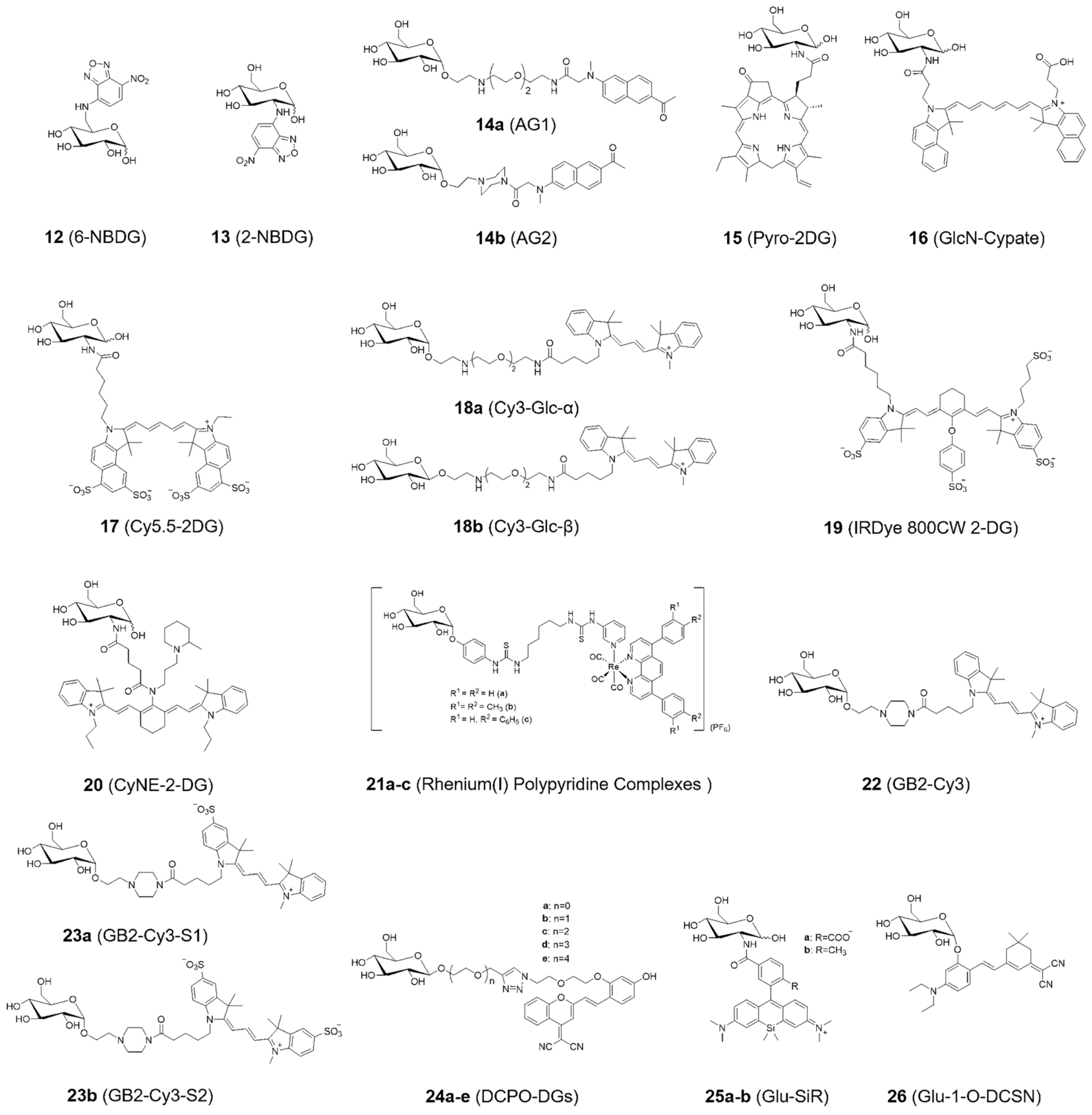

12 (6-NBDG) **13** (2-NBDG) **14a** (AG1) **14b** (AG2) **15** (Pyro-2DG) **16** (GlcN-Cypate)

17 (Cy5.5-2DG) **18a** (Cy3-Glc-α) **18b** (Cy3-Glc-β) **19** (IRDye 800CW 2-DG)

20 (CyNE-2-DG) **21a-c** (Rhenium(I) Polypyridine Complexes) **22** (GB2-Cy3)

23a (GB2-Cy3-S1) **23b** (GB2-Cy3-S2) **24a-e** (DCPO-DGs) **25a-b** (Glu-SiR) **26** (Glu-1-O-DCSN)

Fig. 7 Selected examples of fluorescence-labelled glucose tracers.

(emission maximum: 794 nm).[53] The accumulation of **19** was systematically evaluated both *in vitro* using multiple tumor cell lines and *in vivo* in murine models. *In vivo* experiments showed that **19** exhibited over four-fold higher sensitivity for detecting and monitoring multiple tumor types compared to the unlabeled fluorophore, and it preferentially localized in viable yet relatively hypovascular regions of the tumors (Fig. 12a and b). The specific accumulation of **19**, observed both microscopically *in vitro* and in tumor-bearing mice *in vivo*, underscores its translational potential for preclinical cancer research and early-stage clinical investigations. IRDye 800CW 2-DG has since been developed into a commercial glucose tracer.[54,55] IRDye 800CW boasts clear advantages such as high water solubility, high salt tolerance, low non-specific binding, and a high signal-to-noise ratio, a variety of commercial products have been derived from it, which are widely applied in fields such as protein labeling, antibody labeling, nucleic acid applications, and *in vivo* imaging.[56–58]

In 2010, Chang *et al.* developed an amine-acetylated tricarbocyanine dye (CyNA) scaffold,[59] which exhibited robust photophysical properties, minimal aggregation in aqueous solution, and NIR fluorescence. Later, in 2011, the Chang group leveraged this scaffold to synthesize a novel NIR fluorescent glucose derivative, **20** (CyNE 2-DG, Fig. 7).[54] When compared to commercially-available **19**, probe **20** exhibited significantly improved cancer cell staining and exhibited enhanced cell permeability, making it a promising candidate for NIR-based cancer cell imaging. Cross-cell line experiments revealed that **20** was preferentially taken up by cancer cells and effectively competed with unlabeled D-glucose. Additionally, cell imaging assays confirmed that **20** exhibited superior cell permeability compared to the commercially available NIR tracer **19**, further validating its suitability for NIR cancer cell imaging (Fig. 13).

Alternatives to organic polyaromatic fluorophores can also be used as the reporter, for instance luminescent rhenium(I)

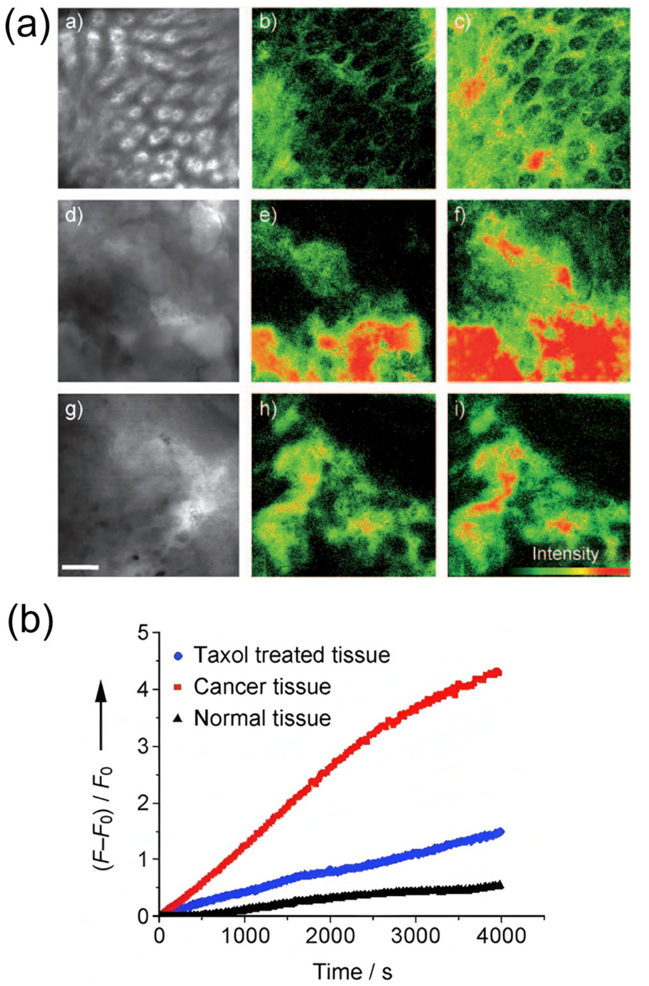

Fig. 8 (a) TPM images of **14b** in normal tissue (a)–(c), cancer tissue (d)–(f), and cancer tissue treated with taxol (g)–(i). (b) Two-photon-excited fluorescence changes plotted as a function of time following the administration of taxol. Adapted with permission from ref. 48. Copyright (2009) Wiley-VCH Verlag GmbH & Co. KGaA, Weinheim.

polypyridine complexes, as exploited by Lo and Louie *et al.* by incorporation of an α-D-glucose moiety in 2011.[60] They synthesized three rhenium(I) polypyridine glucose complexes, $Re(N^{\wedge}N)(CO)_3(py\text{-}3\text{-}glu)$ (complexes **21a–c**, Fig. 7). The results indicated that cellular uptake of these luminescent rhenium(I) polypyridine glucose complexes was *via* GLUTs (glucose transporter enzymes). Fluorescence microscopy indicated that **21c** was predominantly localized in the cytoplasm of HeLa cells, with significant accumulation in the mitochondrial compartment (Fig. 14). Furthermore, complex **21c** exhibited notably superior photostability compared to the 2-NBDG benchmark, highlighting its potential for long-term imaging applications.

In 2011, Park and Lee *et al.* synthesized a range of fluorescent glucose analogues by conjugating Cy3 fluorophores to the α-anomeric position of D-glucose using diverse linkers.[61] Through systematic quantitative evaluation using flow cytometry, and confocal imaging, **22** (GB2-Cy3, Fig. 7) was identified as the optimal probe, exhibiting a tenfold increase in sensitivity over the standard fluorescent glucose tracer 2-NBDG. Using wortmannin, a specific PI3K (phosphoinositide 3-kinase) inhibitor, to pretreat C2C12 myocytes, **22** enabled the monitoring of changes in cellular glucose uptake using fluorescence confocal microscopy. This study established **22** as a highly robust fluorescent glucose bioprobe for real-time quantitative monitoring of glucose uptake in living cells.

In 2014, Park *et al.* sought to investigate the impact of charge on GLUT-mediated cellular uptake of glucose tracers. Two additional **22**-derived probes were synthesized: **23a**, overall zwitterionic neutral; and **23b** overall mono-anionic (Fig. 7).[62] In cellular imaging experiments, cellular uptake of **22** was found to be superior to that of both **23a** and **23b**, similarly zebrafish larvae treatment with glucose uptake enhancers also exhibited enhanced uptake of **22** (Fig. 15a–c). This study indicates that the molecular charge of glucose tracers plays a crucial role in determining their cellular uptake behavior. Positively charged **22** exhibited GLUT-specific cellular uptake, providing valuable insights for the design of novel tracers. Furthermore, the use of **22** as an *in vivo* glucose tracer in zebrafish was successfully validated, showing superior performance compared to 2-NBDG, thus offering another promising tool for metabolic disease research and the development of anti-diabetic drugs.

Most currently available NIR dyes contain charged moieties in their molecular structures, which as we have just seen can adversely affect their uptake and membrane permeability. In 2016, Lu and Chen *et al.* employed the charge-neutral NIR dye DCPO based on the dicyanomethylene-4*H*-pyran (DCM) core structure, to design and synthesize a new class of fluorescent-labeled glucose analogues **24a–e** (DCPO-DGs, Fig. 7).[63] These compounds exhibited clear GLUT-1-mediated uptake, and their uptake was effectively inhibited by both phloretin (a specific GLUT-1 inhibitor) and free D-glucose through competitive inhibition. This study demonstrated that **24c**, which contains a diethylene glycol spacer as the linker between the dye and glucose moieties, exhibited an optimal linker length (corresponding to two ethylene glycol units) resulting in the highest cellular uptake among the **24a–e** series (Fig. 16a–c). These findings complement Park's research on charged systems, highlight the excellent optical properties and neutral charge characteristic of DCPO, and suggest its further integration into other such systems for *in vivo* and *in vitro* bioimaging.

In 2018, Park and Jo *et al.* introduced a pair of novel NIR glucose tracers, **25a** (Glc-SiR-COOH, Fig. 7) and **25b** (Glc-SiR-Me, Fig. 7),[64] which incorporated a silicon rhodamine (SiR) fluorophore. To further investigate the role of charge on cellular uptake, different net charges (0, +1) were introduced through modification of the SiR substituents. Photophysical analyses revealed that **25a** and **25b** both exhibited comparable near-infrared excitation/emission wavelengths, with $\lambda_{ex}/\lambda_{em}$ values of 648/676 nm for **25a** and 650/676 nm for **25b.** Cellular uptake assays demonstrated that **25a** (overall neutral) produced a distinct cytoplasmic fluorescence signal in HeLa cells, whereas **25b** (monocation) did not. These results suggest that a positive net charge hinders cellular uptake, an observation with serious ramifications given the common structural features of NIR fluorophores. Furthermore, inhibition of cellular uptake of **25a** by D-glucose was more efficient

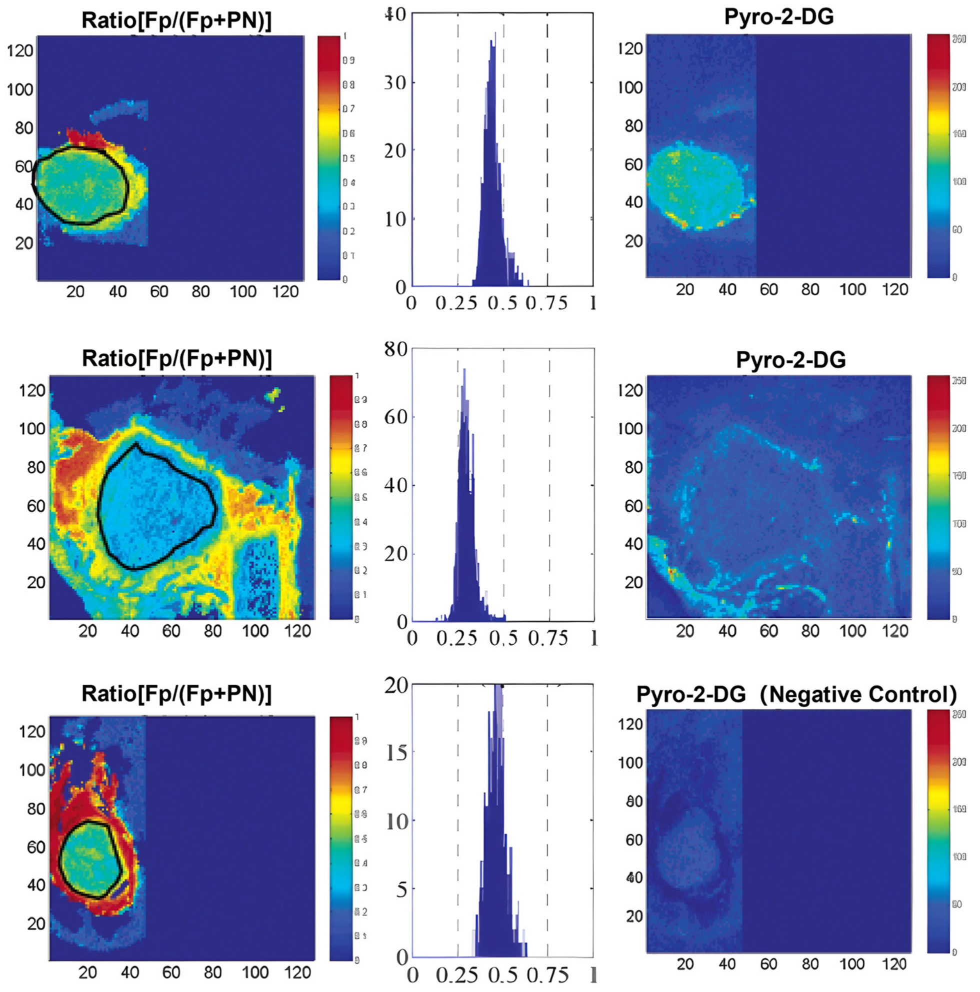

Fig. 9 Fluorescence images of three test groups of 9L glioma-bearing animals: drug control (top row: tumor + **15** Pyro-2DG), normal tissue control (middle row: normal tissue from the same animal), and tumor control (bottom row: tumor alone). Adapted with permission from ref. 49. Copyright (2003) American Chemical Society.

than that observed with the standard fluorescent tracer 2-NBDG (Fig. 17a). Cell imaging studies revealed that **25a** could efficiently distinguish cancer cells from normal cells. The uptake of **25a** by breast cancer cells (MDA-MB-231 and MCF7) was 7.8-fold higher than that by normal breast cells (MCF12A), which correlated with the upregulated expression of GLUT-1 and GLUT-4 in the former (Fig. 17b). Furthermore, treatment of cancer cells with combretastatin A4 (tubulin polymerization inhibitor) significantly reduced the cellular uptake of **25a** (Fig. 17c), suggesting that the tracer can be used to monitor the impact of anticancer drugs on cellular metabolism. This tracer is capable of visualizing GLUT-mediated glucose uptake in live cells and holds significant potential for imaging-based assessments of anticancer drug efficacy.

Dicyanoisophorone (DCI)-based fluorophores are attractive candidates due to their structural simplicity and synthetic accessibility. In 2020, Li and Cheng *et al.* introduced a novel deep-red emitting glucose tracer **26** (Glu-1-O-DCSN, Fig. 7),[65] by appending a DCI at the C-1 position of D-glucose. This molecule features a donor–π–acceptor (D–π–A) configuration, inducing good photophysical characteristics with an excitation maximum of 530 nm in ethanol, a large Stokes shift of up to 140 nm and a moderate fluorescence quantum yield. Fluorescence imaging revealed that **26** could be successfully applied for the real-time imaging of intracellular glucose uptake (Fig. 18a and b). In xenograft mouse models, intratumoral administration of **26** resulted in efficient tumor labeling. Following intravenous injection, the probe gradually accumulated at tumor sites, with notable signal enhancement from 6 h and a maximum around 23 h post-injection (Fig. 18c and d). This probe enables real-time monitoring of glucose uptake *in vitro*, as well as *in vivo* visualization of glucose metabolism dynamics. Owing to its pronounced tumor accumulation, **26** exhibits promise for anticancer drug screening, efficacy evaluation, and clinical translation for image-guided surgery through intraoperative tumor visualization.

2.3. Other types of glucose derivatives

Though radio- and fluorescence-labelled systems are by far most common and dominate clinical applications, other types of reporters and imaging techniques can be employed in conjunction with labelled glucose-derived probes. Nuclear Magnetic Resonance

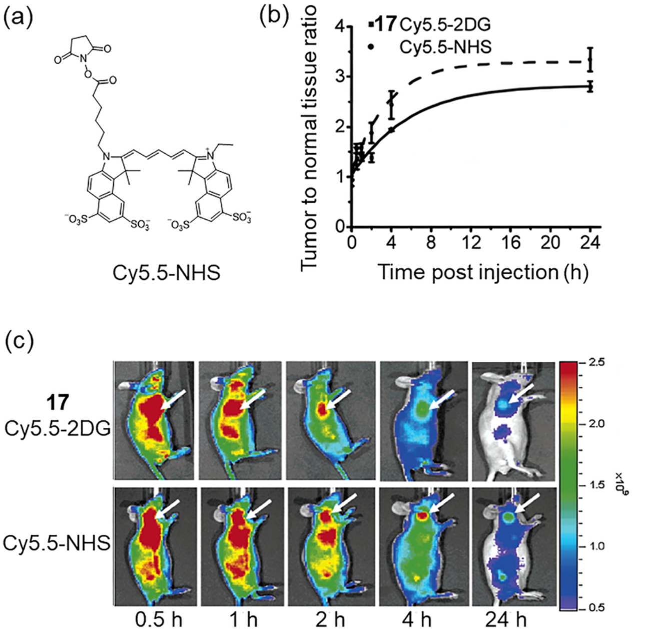

Fig. 10 (a) Cy5.5-NHS. (b) Tumor contrast (tumor/normal tissue ratio) is plotted as a function of time following the administration of **17** (■, solid line) and Cy5.5-NHS (⧫, dashed line). (c) *In vivo* fluorescence detection of subcutaneous U87MG glioblastoma in tumor-bearing nude mice was performed after intravenous injection of either **17** (top) or Cy5.5-NHS (bottom). Adapted with permission from ref. 51. Copyright (2006) American Chemical Society.

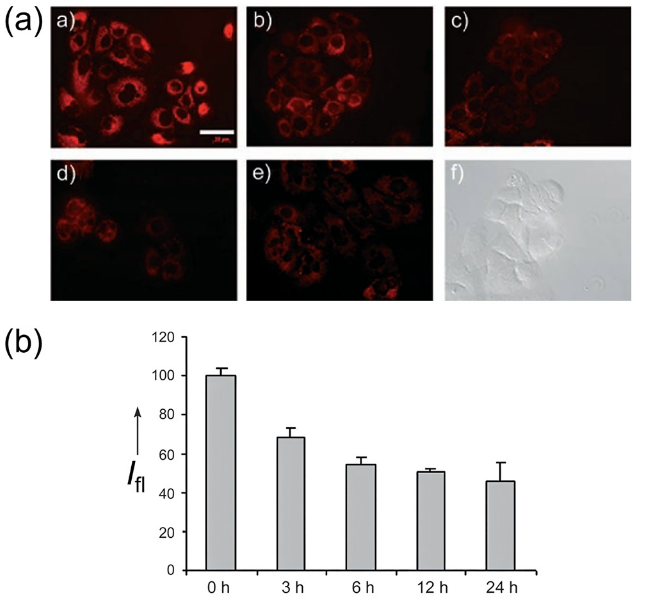

Fig. 11 (a) Confocal fluorescence images showing **18a** uptake by A549 cells following treatment with taxol for: (a) 0 h, (b) 3 h, (c) 6 h, (d) 12 h, (e) 24 h, and (f) Phase contrast image after 6 h incubation. (b) Fluorescence intensities of A549 cells following uptake of **18a** at 0 h, 3 h, 6 h, 12 h, and 24 h after treatment with taxol. Adapted with permission from ref. 52. Copyright (2007) Wiley-VCH Verlag GmbH & Co. KGaA, Weinheim.

(NMR), for instance, as demonstrated by Shulman and Cline *et al.* in 1998. They developed a novel approach for measuring intracellular glucose levels in the skeletal muscle of rats *in vivo*, using the

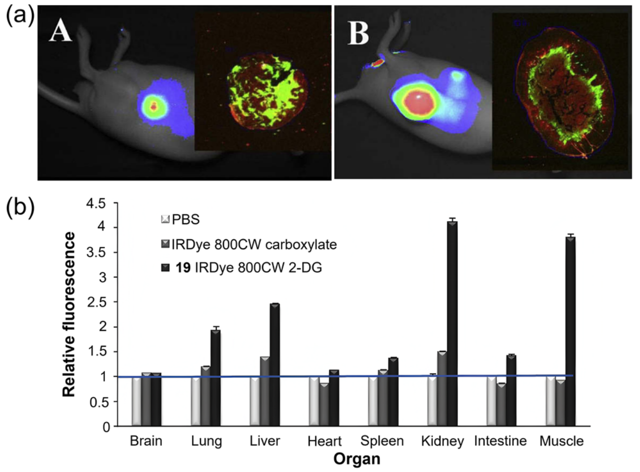

Fig. 12 (a) Images of athymic nude mice bearing 22Rv1 (A) or A431 (B) tumors 24 h after tail vein injection of **19**. Additional fluorescence imaging of the excised tumors on the Odyssey Imaging System after being fixed, excised, embedded, and sectioned. (b) The specific distribution of phosphate-buffered saline (PBS), IRDye 800CW carboxylate, or **19** in different tissues and organs during *in vivo* imaging. Adapted with permission from ref. 53. Copyright (2009) Elsevier Inc.

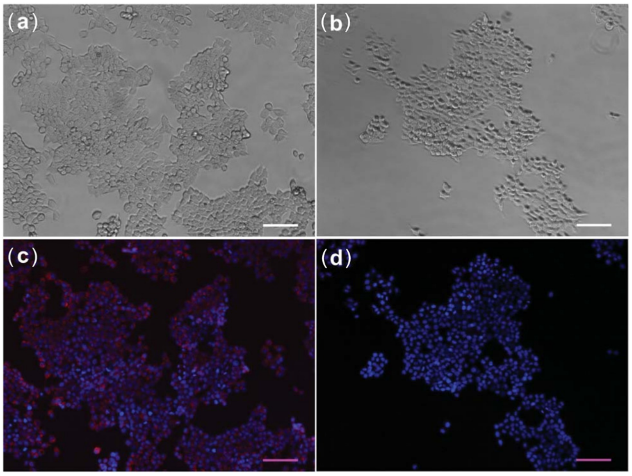

Fig. 13 Fluorescence imaging of MCF7 cells stained with **20** (a) and (c) and **19** (b) and (d). Adapted with permission from ref. 54. Copyright (2011) Royal Society of Chemistry.

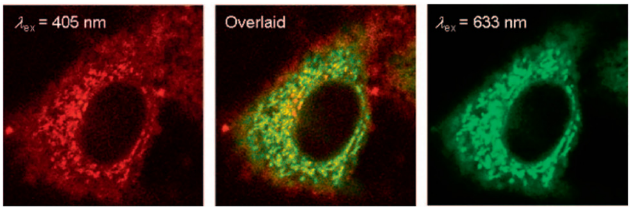

Fig. 14 Confocal fluorescence imaging of a HeLa cell upon staining with MitoTracker Deep Red FM and complex **21b** (λ_{ex} = 633 nm and 405 nm, respectively) in a glucose-free medium. Adapted with permission from ref. 60. Copyright (2011) Wiley-VCH Verlag GmbH & Co. KGaA, Weinheim.

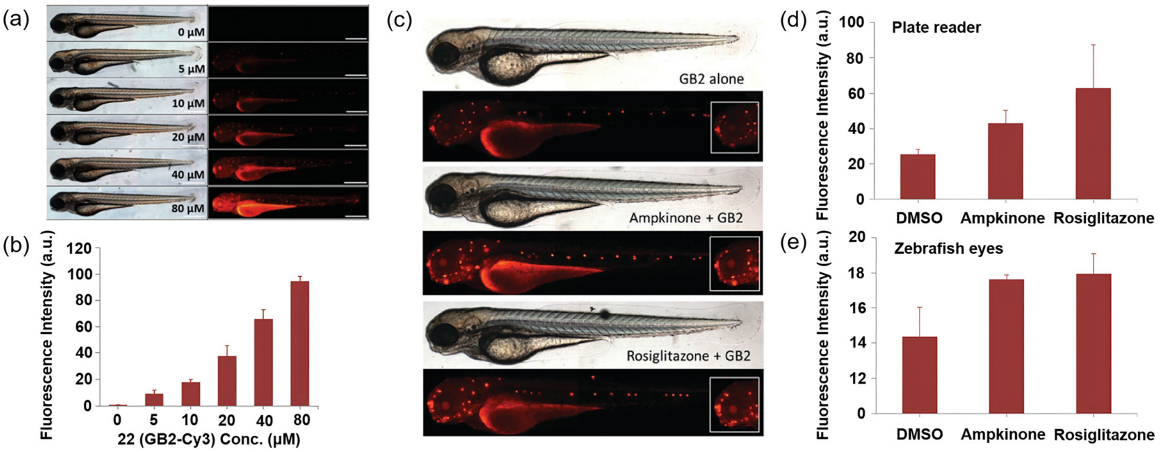

Fig. 15 (a) and (b) Dose-dependent uptake of **22** (GB2-Cy3) in zebrafish (a) and its fluorescence quantification data (b). (c) Fluorescence imaging of zebrafish stained with **22** after treatment with glucose uptake enhancers (ampakine and rosiglitazone). (d) Comparison of fluorescence intensity for **22** uptake in lysed larva using a plate reader after treatment with ampakine and rosiglitazone. (e) Comparison of fluorescence intensity for **22** uptake in zebrafish larval eye after treatment with ampakine and rosiglitazone. Adapted with permission from ref. 62. Copyright (2014) Royal Society of Chemistry.

tracer probe **27** [1-^{13}C]-glucose.[66] Unlike previous radiolabeled probes discussed in Section 2.1, this glucose isotopomer is NMR spin-active, rather than radioactive, and so it can be detected using ^{13}C NMR spectroscopy. This study demonstrated the feasibility of employing non-invasive ^{13}C NMR techniques to quantify intracellular glucose concentrations in live organisms. When compared to traditional methods such as biopsy-based biochemical assays and glucose uptake kinetics, NMR technology offers several advantages, including the ability to perform *in vivo* measurements and the capability for repeated measurements over time.

The related technique, Magnetic Resonance Spectroscopy (MRS, similar to MRI) can also make use of ^{13}C isotopes and can identify metabolites, though the limited sensitivity remains a significant limitation. Dynamic nuclear polarization (DNP) technology can improve the sensitivity of the ^{13}C signals, facilitating real-time imaging of hyperpolarized ^{13}C tracers. In a 2014 study, Brindle and Rodrigues *et al.* used hyperpolarized [U-^{2}H, U-^{13}C]glucose **28** to track glycolytic activity and assess therapeutic responses in mouse tumor models using both ^{13}C MRS and spectroscopic imaging (Fig. 19).[67] This research illustrates that the use of **28** facilitates real-time imaging of glycolytic flux within mouse tumors and enables the sensitive detection of metabolic alterations following chemotherapy.

Another niche spectroscopic technique applied in this context is stimulated Raman scattering (SRS) imaging, which is a label-free vibrational spectroscopic method that can achieve high spatiotemporal resolution imaging of metabolic processes in living cells by detecting characteristic chemical bond vibrations, such as the C–D (carbon–deuterium) stretch at 2120 cm^{-1}. In 2014, Cheng and Li *et al.* used deuterium-labeled glucose **29** (glucose-d$_7$, Fig. 20a) as a tracer to observe metabolic reprogramming in individual living cells.[68] In this probe, the hydrogen atoms of glucose are replaced with deuterium, offering a key advantage over fluorescent analogs or FDG (fluorodeoxyglucose) since deuterium substitution does not significantly alter structure or physical and physiological properties. The Raman spectrum of **29** in aqueous solution features a distinctive peak around 2120 cm^{-1}, corresponding to the vibration of the C–D bond. This peak falls within the silent region of the Raman spectrum, a range free of interference from endogenous molecules, providing a unique opportunity for SRS imaging of target substances. Leveraging the high spatial and temporal resolution of SRS microscopy, the authors successfully monitored the dynamic metabolic processes of glucose in individual living cancer cells (Fig. 20b–f).

In 2015, Min and Hu *et al.* developed a novel glucose analogue **30** (3-*O*-propargyl-D-glucose, 3-OPG, Fig. 21a)[69] which contains an alkyne vibrational tag, which can also be observed by SRS. They successfully visualized glucose uptake activity in live cells and tissues. As with C–D stretches, alkynes exhibit a characteristic stretching vibration in the cell-silent spectral region, in this case around 2129 cm^{-1} (Fig. 21b). Cell imaging experiments confirmed that **30** could be efficiently visualized with high sensitivity and speed through SRS imaging of the alkyne Raman peak in HeLa cells (Fig. 21c). In a mouse subcutaneous tumor xenograft model **30** accumulated preferentially in the proliferative regions of the tumor, with low uptake in the necrotic areas (Fig. 21d and e). This research further highlights the potential of SRS microscopy, enabling the vibrational imaging of glucose uptake and metabolism using very simple glucose analogues with nearly identical structures to native glucose.

In 2018, inspired by the isotope-editing strategies employed in vibrational spectroscopy, the Min group synthesized ^{13}C-labeled 3-*O*-propargyl-D-glucose **31** (3-OPG-$^{13}C_3$, Fig. 22a).[70] Introduction of ^{13}C led to a significant shift in the vibrational frequency from 2129 cm^{-1} to 2053 cm^{-1} (76 cm^{-1}, Fig. 22b). This shift enabled the simultaneous use of both **29** (Fig. 20) and **31** (2060 cm^{-1} and 2250 cm^{-1}) with full spectral resolution for mapping glucose uptake and incorporation in individual living cells (Fig. 22c).

In 2019, Min and Zhang *et al.* developed a microscopic technique based on spectral tracing of deuterium (STRIDE), re-purposing deuterium-labeled glucose **29** (glucose-d$_7$) for high-resolution imaging of glucose metabolism (Fig. 23a and b).[71] Imaging studies confirmed that **29** can serve as an effective metabolic probe for monitoring macromolecule synthesis using

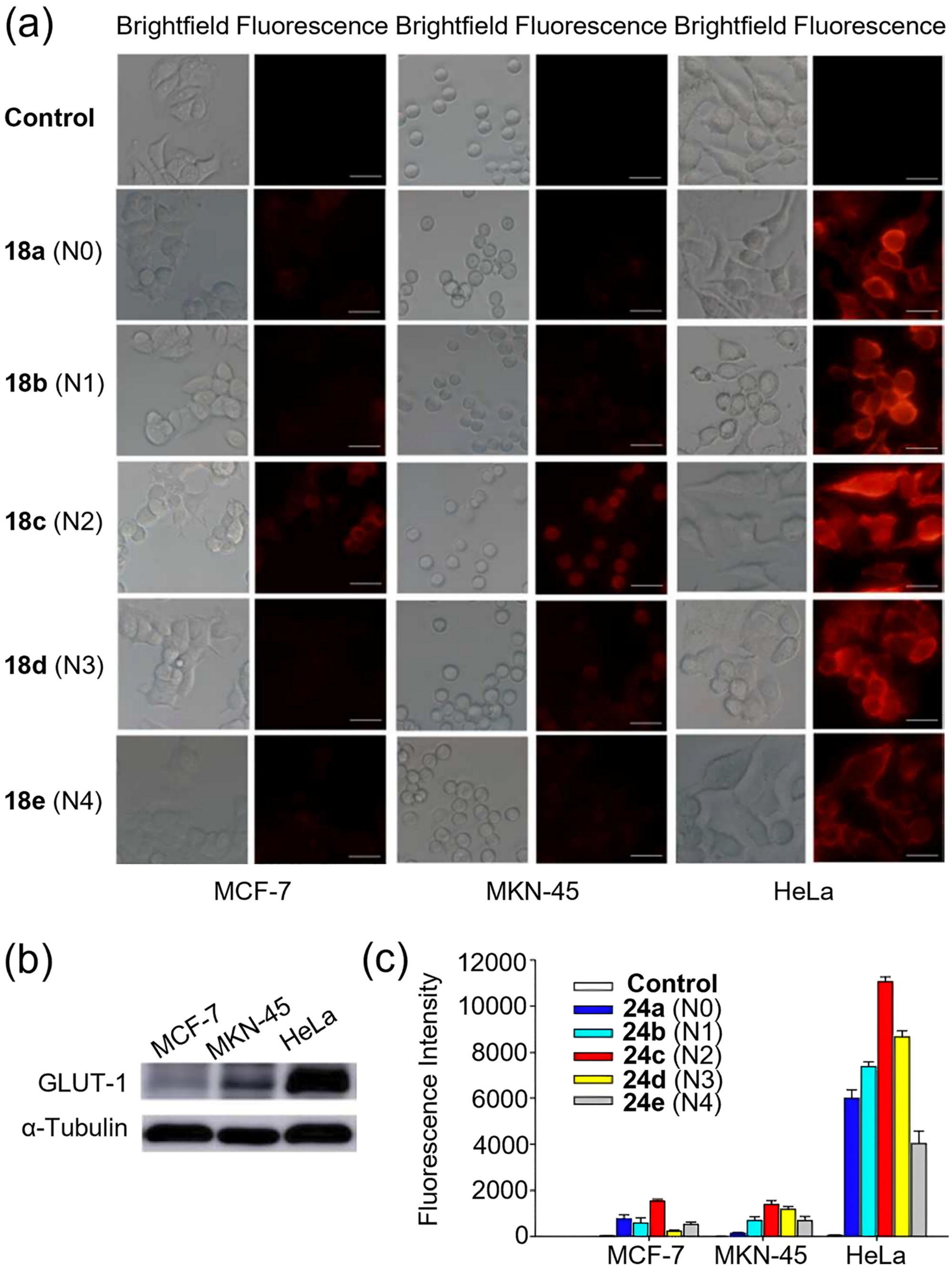

Fig. 16 Confocal microscopic imaging using **24a–e**. (a) Fluorescence imaging of MCF-7, MKN-45 and HeLa cells stained with different compounds (25 μM) for 24 h. (b) Western blots for the expression levels of GLUT-1 in different cancer cell lines. (c) Comparison of fluorescence intensity for **24a–e** uptake in MCF-7, MKN-45 and HeLa cells. Adapted with permission from ref. 63. Copyright (2016) Royal Society of Chemistry.

SRS microscopy as accumulation of C–D bonds was successfully quantitatively detected in both cells and mouse tissues using SRS (Fig. 23c). This study demonstrated that the STRIDE technique allows high-resolution metabolic imaging of macromolecules synthesized from glucose, offering significant insights into metabolic heterogeneity and dynamic metabolic processes.

Bioluminescence imaging is a powerful detection technique in which luciferase enzymes catalyze the oxidation of luciferin substrates, resulting in the emission of light. Which is characterized by exceptional sensitivity, a high signal-to-noise ratio, and strong suitability for non-invasive *in vivo* imaging. In 2019, Goun and Maric *et al.* introduced the bioluminescent glucose tracer BiGluc (CLP + **32** (GAz4)), designed for real-time, non-invasive, and longitudinal monitoring of glucose uptake both *in vitro* and *in vivo*.[55] BiGluc is composed of a caged luciferin triarylphosphine ester (CLP) and an azide-functionalized glucose derivative **32**. Once inside the cell, these two components undergo a bioorthogonal reaction (Staudinger ligation), releasing free luciferin, which produces a quantifiable light signal in the presence of luciferase (Fig. 24a and b). This

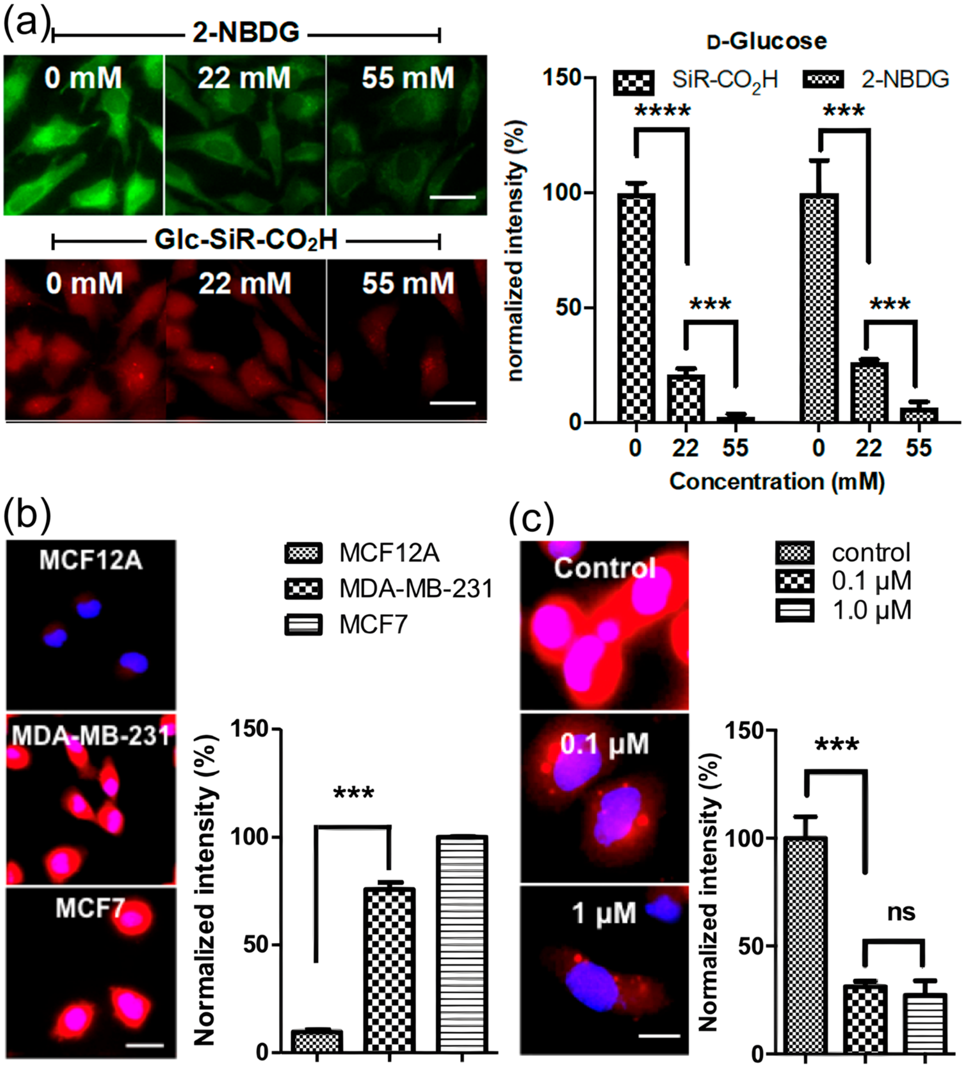

Fig. 17 (a) Comparison of fluorescence intensity for 2-NBDG and **25a** (Glc-SiR-COOH) in HeLa cells in the presence of various concentrations of D-glucose. (b) Confocal images of **25a** uptake in breast cancer cells (MDA-MB-231 and MCF7 cells) and normal breast cells (MCF12A cells). (c) Confocal images of **25a** uptake in MDA-MB-231 cells treated with various concentrations of combretastatin (0, 0.1 and 1.0 μM). Adapted with permission from ref. 64. Copyright (2018) American Chemical Society.

strategy allows BiGluc to effectively image and quantify glucose metabolic fluxes in live mice over extended timeframes without invasive procedures. BiGluc was shown to be reliable in assessing glucose uptake in disease models, such as cancer. Importantly, the performance of BiGluc was found to be comparable to that of the widely used tracer ^{18}F-FDG (Fig. 24c–f), indicating its broad applicability in metabolic research and pharmaceutical development.

In 2022, Chen and Liang *et al.* introduced a bioorthogonal light-up fluorescent probe (Glu-HT-Me + **33** (AzGlu2)), leveraging the arylphosphine-induced photoinduced electron transfer (PeT) and Staudinger ligation reaction to enable real-time, wash-free monitoring of cellular glucose uptake.[72] The probe is composed of two components: Glu-HT-Me and **33**. Glu-HT-Me incorporates an excited-state intramolecular proton transfer (ESIPT) fluorophore (HT-Me), along with a triphenylphosphine group, which are covalently linked by an ester bond (Fig. 25a). **33** is an azide-modified glucose derivative. These two reagents undergo a Staudinger ligation reaction, allowing for the detection of glucose uptake. Using a wash-free approach, it was demonstrated that this probe could effectively track glucose uptake in living cells in real time (Fig. 25b), with significantly higher fluorescence intensity observed in cancer cells compared to normal cells.

Radiolabeled probes (Table 1) such as **1** (^{18}F-FDG) offer high sensitivity, enabling quantitative *in vivo* metabolic imaging, and serve as the gold standard for clinical diagnosis of tumors and other diseases. When combined with CT or MRI, they provide anatomical-functional fusion information. Fluorescent probes, including **13** (2-NBDG) and SiR-glucose analogs **25a–b**, allow for real-time tracking of glucose uptake in living cells; their ease of operation makes them suitable for imaging in live cells and small animal models. NMR/SRS probes, exemplified by [1-^{13}C] glucose **27**, deuterium-labeled glucose **29** and **31**, minimally alter or even

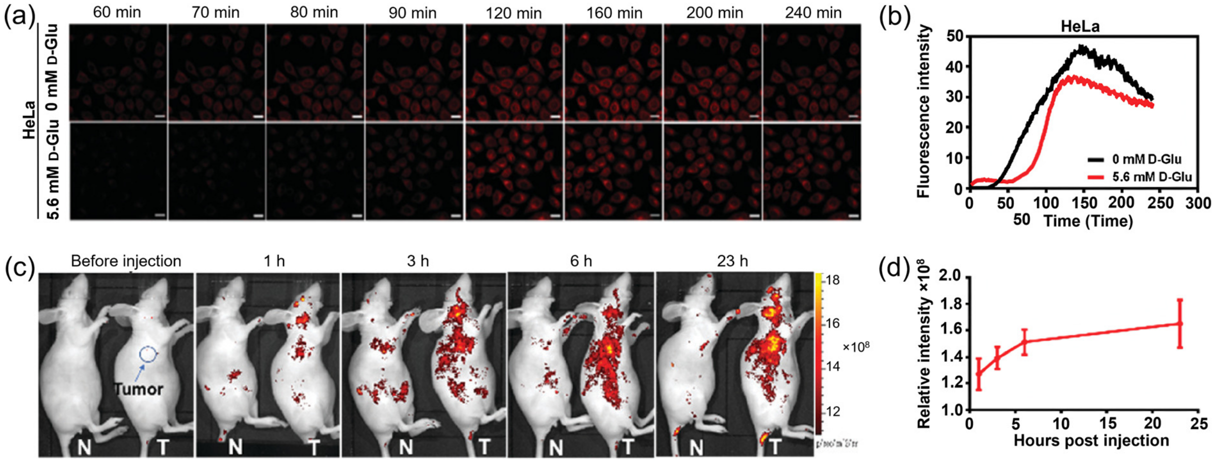

Fig. 18 Real-time fluorescence imaging (a) and quantitative analysis of uptake dynamics (b) of **26** in living HeLa cells under conditions of 0 mM and 5.6 mM D-glucose, respectively. (c) and (d) *In vivo* bioimaging of tumor-free mice (N) and tumor-bearing mice (T) following intravenous injection of **26**. The relative fluorescence intensity of the tumor was quantified using Living Imaging software (d). Adapted with permission from ref. 65. Copyright (2020) Royal Society of Chemistry.

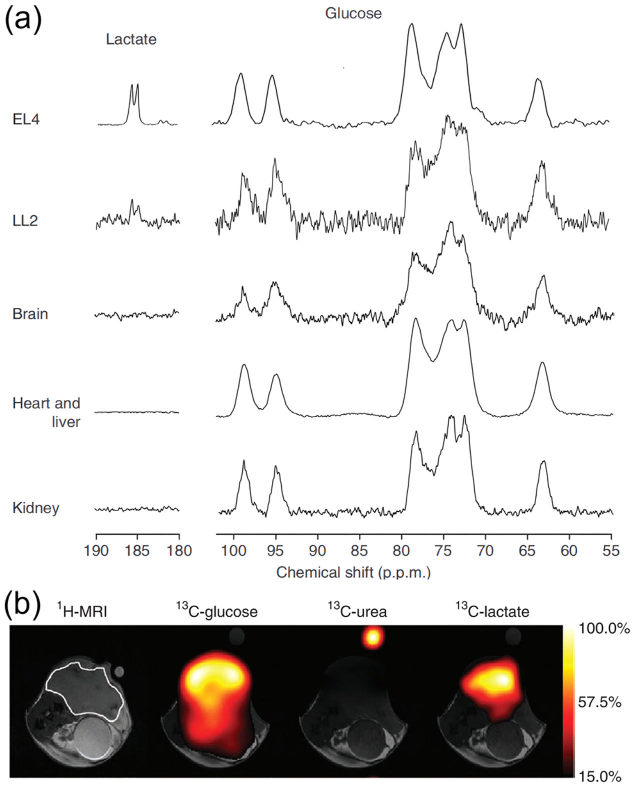

Fig. 19 (a) Representative ^{13}C MR spectra of subcutaneous EL4 and LL2 tumors, brain, heart, liver, and kidney tissue after the injection of 0.35 mL, 100 mM **28**. (b) Representative chemical-shift–selective images in an EL4 tumor-bearing mouse after IV injection of 0.4 mL, 200 mM **28**. Adapted with permission from ref. 67. Copyright (2014) Springer Nature America, Inc.

preserve the chemical structure and physiological function of glucose, thereby enabling the study of genuine endogenous glucose metabolism, and their high spatial resolution makes them ideal for studying metabolic heterogeneity at the single-cell and tissue levels. Bioluminescent probes like BiGluc (CLP + **32** (GAz4)) boast a high signal-to-noise ratio and low background interference, rendering them suitable for long-term non-invasive *in vivo* imaging.

However, these probes have distinct limitations. Radiolabeled probes depend on accelerators for isotope production (*e.g.*, ^{18}F), resulting in high costs, and their short half-lives (*e.g.*, $^{11}C_{t1/2}$ = 20 min) restrict imaging time windows, while their spatial resolution is also limited. Fluorescent probes suffer from typically poor tissue penetration, particularly in the visible light range, which hinders deep-tissue imaging; some exhibit phototoxicity, and molecular charge and steric bulk significantly affect cellular uptake efficiency. For NMR/SRS probes, NMR has low sensitivity, requiring high loading, with SRS relying on advanced microscopic equipment with complex operation, leading to low popularity. Additionally, most probes share some common drawbacks in that they act through metabolic trapping, disrupting normal glycolysis, therefore preventing real-time tracking of endogenous glucose dynamics.

The probes discussed throughout this section enable the study of glucose-dependent processes, but as clearly shown, they are all simply glucose-derivatives and so do not directly allow for the study of glucose itself. Probes designed to interact with or effect change upon interaction with glucose will be the primary focus of the remainder of this review, and as we shall see, many of the processes exploited by these probes are those demonstrated and characterized earlier in this section using glucose-derived systems.

3. Enzyme-based probes

As we shall see throughout this review, a number of technologies have been exploited for the detection of glucose. One key example is the use of glucose-specific enzymes for sensing. These systems generally rely on monitoring the formation or consumption of glucose-related metabolites, for example hydrogen peroxide or ascorbic acid, produced by glucose oxidase (GOx)

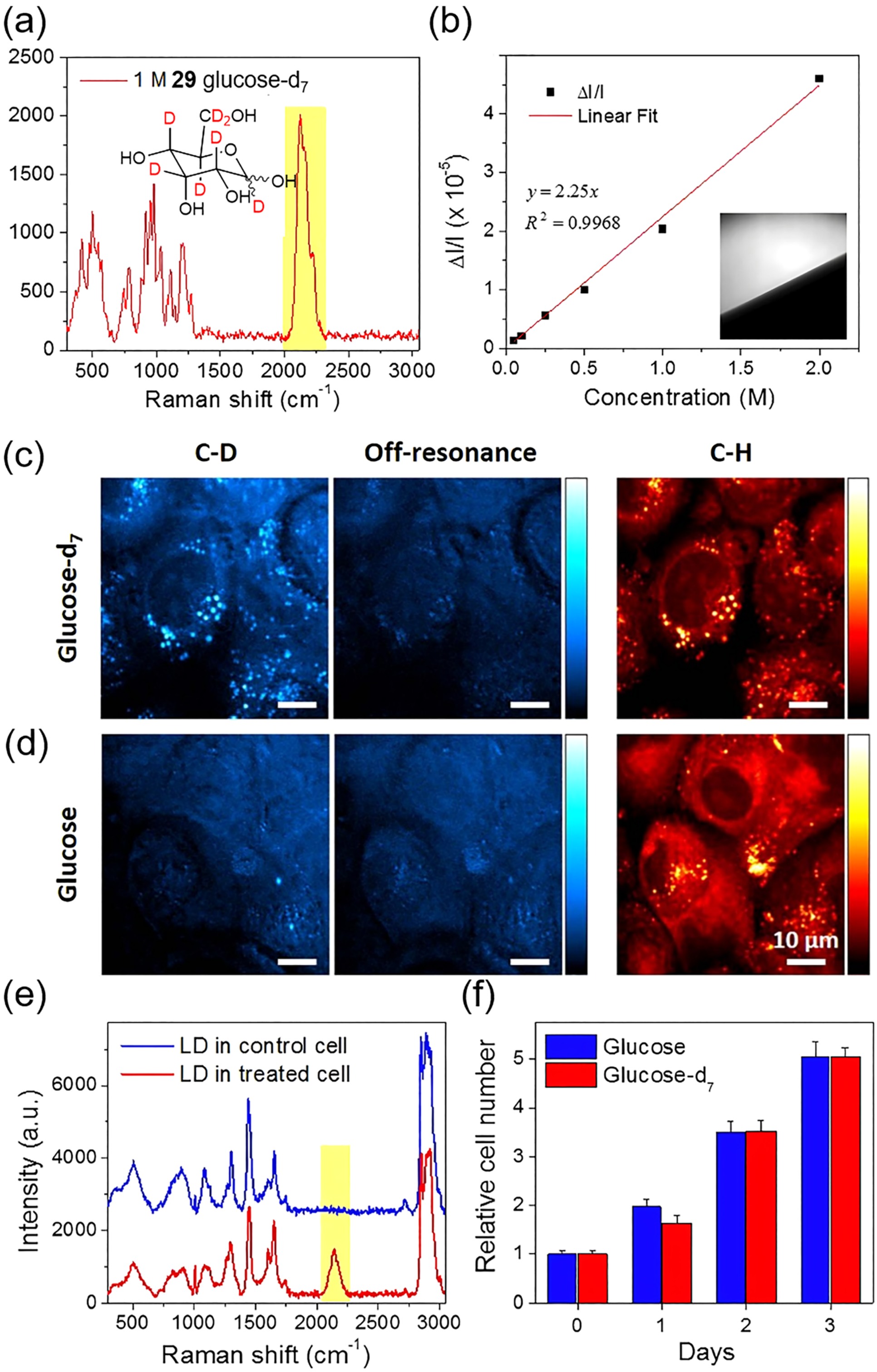

Fig. 20 (a) Structure of **29** (glucose-d$_7$) and its Raman spectrum showing a broad unique peak from C–D *ca.* 2120 cm^{-1}. (b) Linear relationship of the SRS signal *versus* concentration of **29**. (c) and (d) SRS imaging of PANC1 cells after incubation with (c) 25 mM **29** or (d) 25 mM glucose in glucose-free DMEM (Dulbecco's modified Eagle's medium) media. (e) Raman spectra were collected from lipid droplets in control and **29** treated cells. (f) Cell viability test of **29** when compared to regular glucose was achieved *via* an MTT (3-(4,5-dimethylthiazol-2-yl)-2,5-diphenyltetrazolium bromide) assay. Adapted with permission from ref. 68, published by Springer Nature.

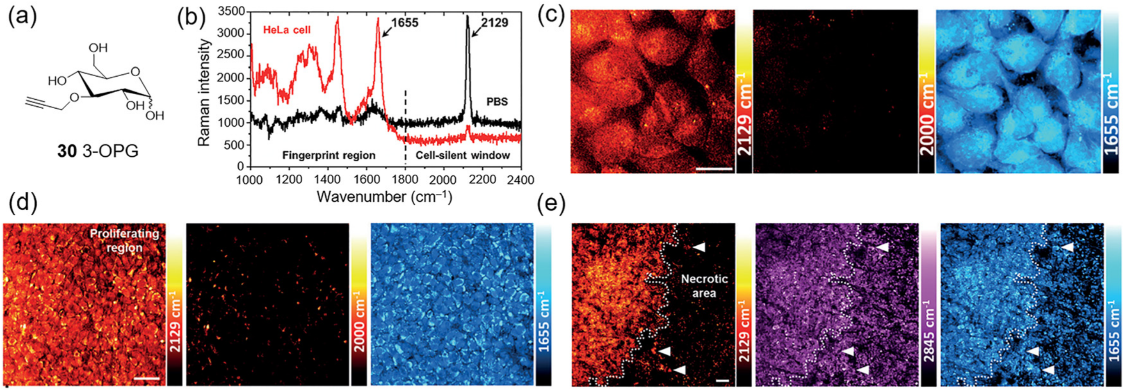

Fig. 21 (a) **30** (3-OPG). (b) Spontaneous Raman spectra of **30** solution in PBS (black) and HeLa cells incubated with **30** (red). (c) SRS imaging of **30** (2129 cm^{-1}) in live HeLa cells. SRS images acquired at 2000 cm^{-1} (off-resonance) and 1655 cm^{-1} (protein amide I) depict the same region of cells. (d) and (e) SRS imaging of **30** uptake in U-87 MG tumor xenograft tissues. Strong **30** signal in the proliferating region of the tumor (d). Sharp contrast of **30** signal at the interface of two tumor regions (e). Adapted with permission from ref. 69. Copyright (2015) Wiley-VCH Verlag GmbH & Co. KGaA, Weinheim.

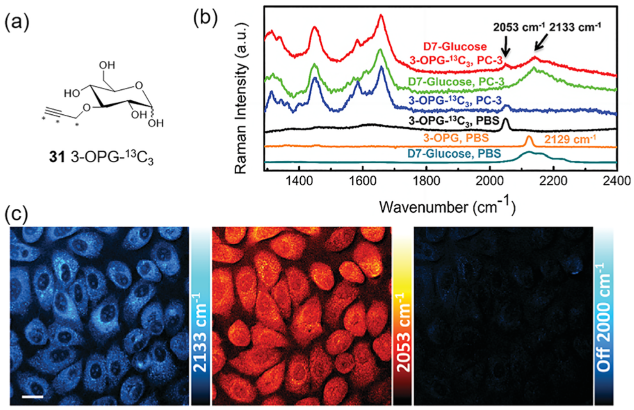

Fig. 22 (a) **31** (3-OPG-$^{13}C_3$). (b) Spontaneous Raman spectra of glucose-d_7 in PBS (dark cyan), PC-3 cells incubated with glucose-d_7 (green), 3-OPG in PBS (orange), **31** in PBS (black), PC-3 cells incubated with **31** (blue), PC-3 cells incubated with **29** and then incubated with **31** (red). (c) Two-color SRS imaging of PC-3 cells incubated with **29** and then with **31**, highlights glucose incorporation (2133 cm^{-1}, cyan hot), glucose uptake (2053 cm^{-1}, red hot) and off-resonance (2000 cm^{-1}). Adapted with permission from ref. 70. Copyright (2018) Royal Society of Chemistry.

enzymes. All the examples in this section will rely on this simple premise, using a range of approaches to detect these products and their local effects. GOx has been incorporated into electrochemical and fluorescent sensors, primarily solid-state/solid-supported systems, as well as a few more niche technologies that we will cover briefly at the end of this section.

Starting with electrochemical GOx-based glucose probes, in 1992 Ewing and Abe *et al.* constructed an ultra-small glucose probe **34** using platinum-deposited carbon ring microelectrodes containing glucose oxidase (Fig. 26a). These exhibited both a fast response time of just 270 ms, which was linear to the structural diameter of the electrode tip.[73] A key objective of the development of the probe was the dynamic measurement of glucose levels within the cytoplasm of single cells. To demonstrate this, the probe was implanted into a single large dopamine cell of the pond snail *Planorbis corneus* and used to detect transient concentrations of glucose. Following glucose injection (2 pL, 3 M) the implanted probe exhibited an increase in electrical response (Fig. 26b), confirming the desired application. The ability of the probe to detect glucose concentration changes in ultra-small environments provides a viable platform for the real-time monitoring of respiratory and metabolic activity of individual cells and their response to stimuli/chemical events, such as nerve cell stimulation or pharmacological manipulation.

In 2000 Kennedy and Jung *et al.* developed a micron-sized probe **35** to monitor glucose and oxygen levels in the extracellular space of a single islet of Langerhans (Fig. 27a–c), in the context of glucose-stimulated insulin secretion, which plays a critical role in glucose homeostasis.[74] This probe was fabricated based on a platinum microelectrode with GOx immobilized on its surface. Notable fluctuations in recorded glucose signals were observed, which seemingly oscillated with a periodicity of 2.4 min on reaching a concentration maximum. These oscillations were absent in controls, indicating genuine fluctuations in glucose levels rather than a system artifact (Fig. 27d). These fluctuations suggest real-time oscillations in pancreatic β-cell metabolism, as confirmed by simultaneous tracking of the fluctuations in oxygen consumption and calcium ion levels.

Along similar lines, Danielsson and Asif *et al.* introduced a ZnO nanorod-based electrochemical probe **36** for intracellular glucose detection in 2010 (Fig. 28a and b).[75] This probe consists of hexagonal ZnO nanorods grown on the tip of a silver-coated borosilicate glass capillary (0.7 μm diameter) and coated with GOx enzyme. As the enzyme is bound through strong electrostatic interactions with ZnO, rather than covalently, it retains full activity (Fig. 28c). This intracellular bioprobe exhibited a rapid response (<1 s), and a broad linear range from 0.5 to 1000 μM (Fig. 28d). Danielsson *et al.* employed this probe to measure intracellular glucose concentrations in human adipocytes and *Xenopus laevis* frog oocytes (Fig. 28e and f), demonstrating a glucose transport system that was significantly activated by insulin in both cell types. These results highlight the capability of the probe for biologically relevant glucose measurements within living cells. Compared to various other nanoprobe

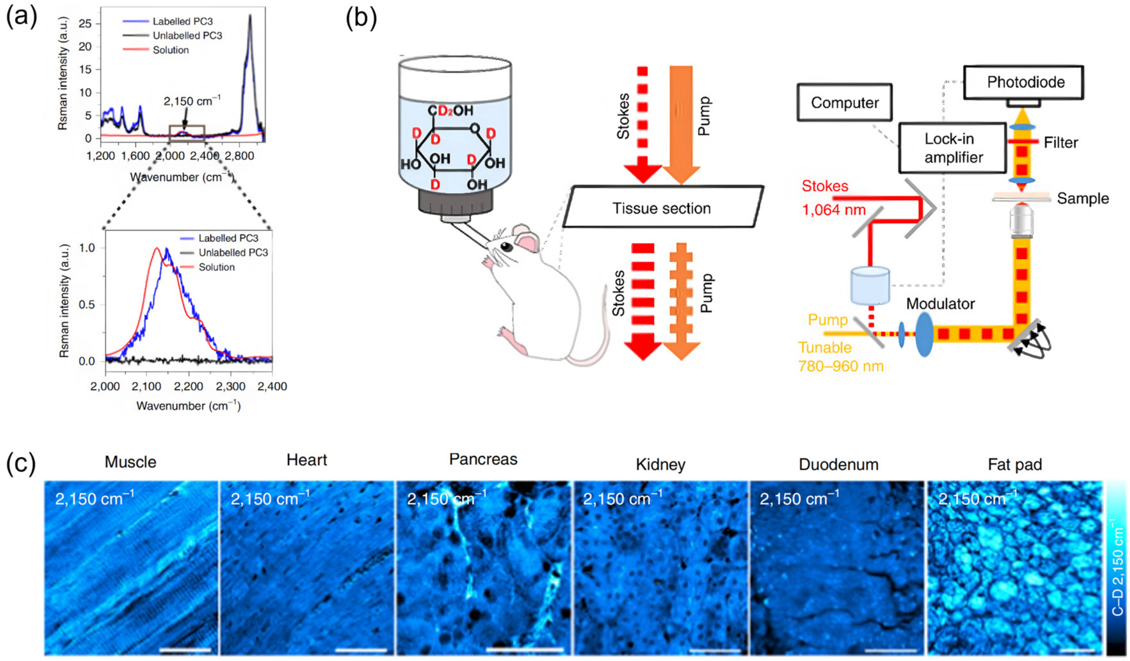

Fig. 23 (a) Raman spectra normalized to the intensity of the C–D peak, are presented for **29** solution (red), unlabeled PC3 cells (black), and PC3 cells labeled with **29** (blue). The boxed region, corresponding to the cell-silent area, is highlighted in the lower graph. (b) Experimental procedure of SRS imaging by **29** labelling. (c) SRS imaging at 2,150 cm^{-1} was performed to visualize C–D label incorporation in various tissues of a P30 mouse following 10-days consumption of 10% **29** solution or water. Adapted with permission from ref. 71. Copyright (2019) Springer Nature Limited.

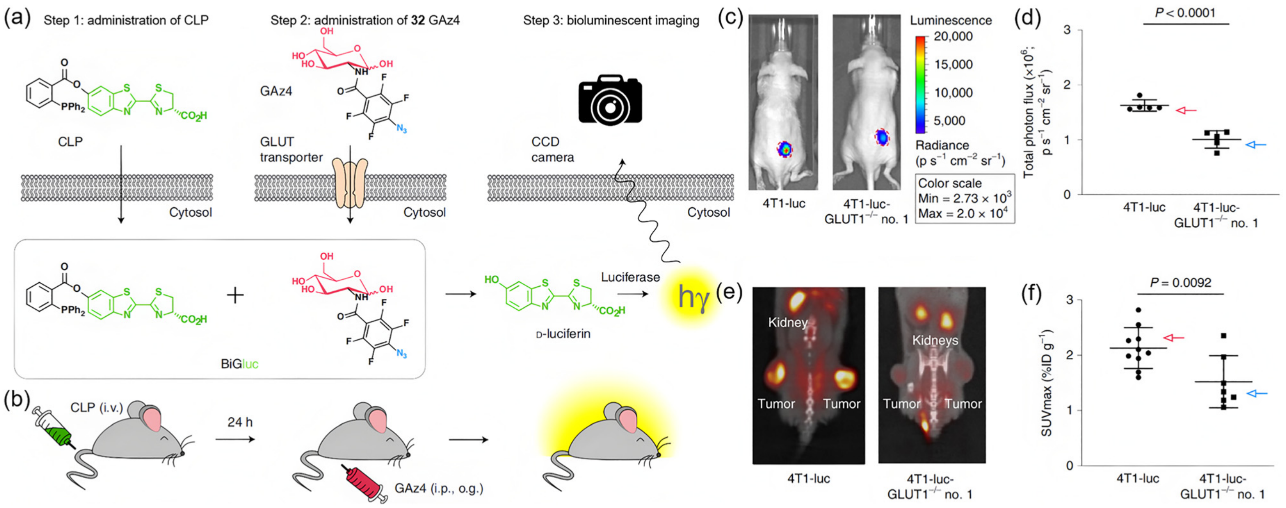

Fig. 24 (a) Schematic diagram of the bioluminescent-based probe for real-time imaging of glucose absorption *in vitro*. (b) Schematic representation of the BiGluc method for *in vivo* application. (c) Bioluminescent imaging of mice bearing 4T1-luc or 4T1-luc-GLUT1$^{-/-}$ no. 1 tumors. (d) Comparison of glucose uptake by subcutaneous tumors formed by 4T1-luc and 4T1-luc-GLUT1$^{-/-}$ no. 1 cells. A 38% reduction in signal intensity was displayed in the 4T1-luc GLUT1-deficient tumors compared to 4T1-luc controls. (e) Representative photos of ^{18}F-FDG PET/CT scans of mice bearing 4T1-luc or 4T1-luc-GLUT1$^{-/-}$ no. 1 tumors. (f) Glucose uptake by 4T1-luc and 4T1-luc-GLUT1$^{-/-}$ no. 1 tumors measured by PET. 4T1-luc-GLUT1$^{-/-}$ no. 1 is a derivative of the 4T1-luc cell line with the GLUT1 gene (Slc2a1) knocked out using gene-editing techniques such as CRISPR/Cas9. Adapted with permission from ref. 55. Copyright (2019) Springer Nature America, Inc.

systems, this nanostructured electrochemical probe offers superior sensitivity and real-time detection.

Enzyme immobilization and stability are two of the most critical factors in enzyme-based electrochemical bioprobes and so identifying support materials that offer a large surface area for enhanced enzyme loading, whilst also providing a compatible microenvironment to maintain enzyme activity is key. Building on the example above, Danielsson and Fulati *et al.* developed an intracellular glucose bioprobe **37** based on nano-honeycomb ZnO (Fig. 28g and h), using aluminum as a support instead of silver to encourage the honeycomb structure.[76] The nanoflake ZnO material exhibited 1.8 times higher

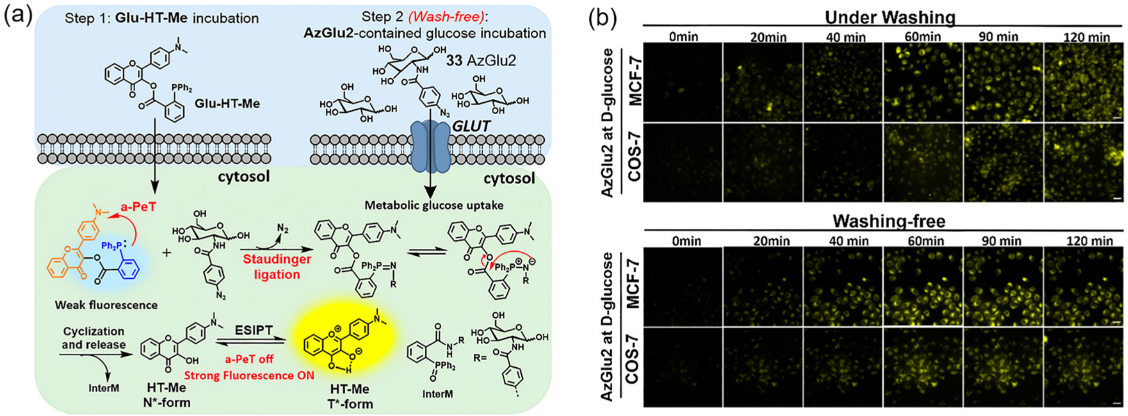

Fig. 25 (a) Schematic diagram of the bioorthogonal light-up fluorescent probe, Glu-HT-Me + **33**, for wash-free real-time dynamic monitoring and imaging of cellular glucose uptake. (b) Comparison of confocal fluorescence images by the probe (Glu-HT-Me + **33**) for real-time monitoring of glucose uptake with and without pre-imaging washing. Adapted with permission from ref. 72. Copyright (2022) American Chemical Society.

sensitivity compared to the above ZnO nanorods under identical conditions. A logarithmic linear glucose-dependent electrochemical potential difference was observed over a large range of glucose concentrations (500 nM–10 mM). This seemingly minor change, varying solely ZnO morphology, led clearly to significant improvement, overcoming the limitations of the previous microelectrode which demonstrated linear responses only below 1 mM. As before, this probe was successfully used for sensing glucose in both human adipocytes and frog oocytes, demonstrating a simple approach for improving the surface area available for GOx immobilization.

Intracellular investigations at the single-cell level pose significant challenges due to the absence of (i) nondestructive, metabolite-specific analytical sensors for in-cell measurements and (ii) precise cell-targeting technologies. In an attempt to overcome these limitations, in 2016 Pourmand and Nascimento *et al.* developed GOx-functionalized nanopipettes **38** (Fig. 29a and b), enabling the direct measurement of intracellular free glucose in single cells.[77] This nanoprobe is capable of detecting micromolar glucose, with a linear range of 0.1–8 mM, and sensitivity values of 20.40 and 13.89 mV mM^{-1} in PBS and DMEM, respectively. The nanopipettes were functionalized by covalently immobilizing GOx at the tip. On GOx-catalyzed oxidation of glucose, gluconic acid is produced, resulting in a drop in pH and a measurable change in impedance. Calibration studies demonstrated a direct correlation between impedance changes and glucose concentration in solution. This nanoprobe was employed to quantify intracellular glucose levels in human fibroblasts and metastatic breast cancer cell lines MDA-MB-231 and MCF-7 (Fig. 29c), demonstrating that cancer cells consistently exhibited significantly higher glucose levels than noncancerous cells. This innovative platform exhibits significant potential as a diagnostic tool for distinguishing cancer cells from non-malignant cells across various tissue samples, as well as for monitoring the progression of cancer *in situ*, enabling broad aspects of mechanistic research such as metabolic heterogenicity of cancer cells, processes relating to cellular transformation, and the correlation between glucose metabolism and cell proliferation and metastasis.

In 2016, Tong and Wang *et al.* developed a novel capillary electrophoresis (CE)-based biosensor **39** for detecting glucose in individual human stomach cancer cells (MGC80-3 cells).[78] The biosensors were fabricated by immobilizing a biocomposite of single-walled carbon nanotubes (SWNTs), glucose oxidase, and glutaraldehyde (GA) on a palladium nanoparticle (PdNPs)-modified platinum electrode (Fig. 30). SWNTs interact with GOx *via* their binding sites and enhance electron transfer, increasing the surface area of the biosensor and improving its catalytic activity when combined with PdNPs. Glucose concentrations ranging from 2.0 μM to 1.0 mM could be detected, with a detection limit of 0.5 μM. A mean glucose content in MGC80-3 cell extracts and single cells of 20.0 fmol and 20 ± 6 fmol (n = 10), respectively, was found, with a calculated mass detection limit of 1.0 fmol (injection volume of 2.0 nL). Compared to other CE-based electrochemical glucose probes, this biosensor **39** demonstrated superior sensitivity, stability, non-interference properties, and long-term operational reliability. Notably, glucose concentrations in both single MGC80-3 cells and cell extracts were determined without the need for complex pretreatment. This technique holds potential for broader applications in the analysis of other chemical species in single cells, using different enzymes or bioactive substances.

Concentrating on intracellular glucose monitoring, in 2019, Huang and Liao *et al.* developed a single-nanowire glucose probe **40** for the electrochemical detection of intracellular glucose by depositing platinum nanoparticles (PtNPs) on a SiC@C nanowire and the immobilization of glucose oxidase.[79] The H_2O_2 product of glucose oxidation by GOx is redox active, and is electro-catalytically reduced by the PtNPs to produce a current (Fig. 31a). Human umbilical vein endothelial cells (HUVECs) were used as a cell model to assess intracellular glucose levels under normal and hyperglycemic conditions (Fig. 31b). A distinct amperometric signal was observed (Fig. 31c, curve c) when the glucose nanowire probe was inserted into a HUVEC, with a marked increase in current when the cells were exposed to hyperglycemic conditions (Fig. 31c, curve d). A study of the response of HUVECs and control cells to treatment with 50 mM glucose using these

Table 1 Key properties of representative glucose analogue tracers

Probe	Label type	$\lambda_{ex}/\lambda_{em}$	Chemical properties	Biological applications
1–7	Radioisotope (^{18}F-labeled)	—/γ-ray (511 keV)	^{18}F-labeled (half-life 110 min), radiochemical purity >95%, glucose analogs, GLUT/SGLT-dependent transport, retained *via* phosphorylation/renal reabsorption	PET imaging (tumor glycolysis, brain metabolism), GLUT/SGLT function differentiation, diabetes/tumor research, drug efficacy monitoring
8–11	Radioisotope (^{99m}Tc-labeled)	—/γ-ray (140 keV)	^{99m}Tc-labeled (half-life 6.02 h), radiochemical purity ≥90%, hydrophilic ($\log P \leq -1.5$), primarily renal excretion, binds glucose transporters/proteins for retention	SPECT imaging (lung cancer/sarcoma/melanoma), tumor-inflammation differentiation, renal reabsorption evaluation, low-cost alternative to ^{18}F-FDG
12	NBD (fluorophore)	470/538 nm	Metabolizable *via* GLUT-mediated transport	Asymmetric glucose transport analysis, GLUT inhibitor screening
13	NBD (fluorophore)	475/550 nm	GLUT substrate, retained *via* C6 phosphorylation, hydrophilic	Live-cell glucose uptake imaging, cancer/normal cell differentiation, GLUT inhibitor screening
14a–b	Acedan (two-photon fluorophore)	780 nm (two-photon)/501 nm	Two-photon action cross-section (δ_{max}): 95 GM (14a)/155 GM (14b), pH-insensitive (pH 4.0–10)	Deep-tissue imaging, colon cancer tissue section diagnosis, anticancer drug efficacy monitoring
15	Pyropheophorbide a (fluorophore)	667/679, 720 nm	NIR emission, GLUT-binding ability, mitochondrial targeting, mitochondrial damage	Confocal analysis of GLUT-mediated uptake, NIR imaging of glioma, photodynamic therapy (mitochondrial damage)
16	Cypate (fluorophore)	780/810 nm	Polyvalent dendritic arrays, cypate as inner core, D-(+)-glucosamine as peripheral groups	Tumor targeting, blood flow monitoring and vascular imaging, tumor uptake mechanistic evaluations
17	Cy5.5 (NIR fluorophore)	675/694 nm	Conjugated with D-glucosamine, GLUT-independent uptake	Tumor cell imaging, long-term tumor retention, no glucose starvation required
18	Cy3 (fluorophore)	550/570 nm	Photostable, no glucose starvation required, competitive binding with D-glucose for GLUTs	Real-time cancer cell uptake imaging, anticancer drug screening, flow cytometry/confocal analysis
19	IRDye 800CW (NIR fluorophore)	785/794 nm	GLUT1 substrate, high NIR tissue penetration	*In vivo* tumor imaging, tumor viability monitoring, superior SNR *vs.* Cy5.5-2DG
20	CyNA (NIR fluorophore)	740/815 nm	Better cell permeability than IRDye 800CW 2-DG, stereoselective binding with D-glucose; stable in serum	NIR imaging of cancer cells, uptake difference evaluation between cancer and fibroblast cells
21a–c	Rhenium(I) poly-pyridine (fluorophore)	405/500–600 nm (MLCT emission)	α-D-glucose pendant, emission lifetime 0.22–4.32 μs, binds Con A ($K_a = 4.4 \times 10^5$–5.8×10^5 M^{-1})	Fluorescent sensor for Con A, *E. coli* adhesin binding assay, mito-chondrial localization imaging in HeLa cells
22	Cy3 (cyanine dye)	488/564–606 nm	GLUT substrate, 10-fold more sensitive than 2-NBDG	Glucose uptake imaging of myocytes *via* insulin/AMPK pathways, antidiabetic drug screening
23a–b	Cy3 (fluorophore)	488/564–606 nm	23a: Zwitterionic (net charge = 0), 23b: Anionic (net charge = −1), no GLUT dependence	*In vitro* cellular imaging to distinguish GLUT-mediated glucose uptake, zebrafish glucose uptake monitoring, anti-diabetic drug screening
24a–e	DCPO (NIR fluorophore)	580/670 nm	PEG-based linkers, GLUT1-dependent uptake	*In vitro* cancer cell imaging, GLUT1 expression assessment, potential *in vivo* tumor imaging
25a-b	Silicon rhodamine (NIR fluorophore)	25a: 648/676 nm; 25b: 650/676 nm	25a: Net charge = 0, GLUT-dependent uptake, 25b: Net charge = +1, no efficient cellular uptake	Live-cell glucose uptake imaging, cancer/normal cell differentiation, anticancer drug efficacy monitoring
26	DCI derivative (deep-red fluorophore)	530/685 nm	C1-type D-glucose conjugate, GLUT-dependent uptake, mitochondria-localized, low cytotoxicity	Live-cell glucose uptake imaging, tumor targeting, potential BBB crossing for brain disease imaging
27	NMR Tracer (^{13}C-labeled)	—/^{13}C NMR (glucose: 93.2/97.1 ppm)	99% ^{13}C enrichment, needs [1-^{13}C]-mannitol/Cr as standards, *in vivo* detection limit ∼0.07 mM	Non-invasive *in vivo* measurement of rat muscle intracellular glucose, differentiates glucose transport/phosphorylation impairment
28	NMR Tracer (^{13}C-labeled + deuterated)	—/^{13}C NMR (glucose: 63–99 ppm)	99% ^{13}C enrichment + full deuteration, polarization T1 $\sim 8.9 \pm 0.6$ s, detects 6-phosphogluconate (PPP intermediate)	*In vivo* tumor glycolysis imaging, pentose phosphate pathway activity assessment, potential brain/prostate tumor imaging
29	RS probe (Deuterium-labeled)	—/SRS (C–D bond vibration: ∼2120 cm^{-1})	Non-toxic, C–D signal in cell-silent region, tracks glucose-derived lipids/proteins/DNA/glycogen	*In vitro* single live-cell *de novo* lipogenesis metabolic imaging, distinguishes macromolecule-specific glucose utilization
30	SRS probe (Alkyne-tagged)	—/SRS ($C\equiv C$ stretching vibration: 2129 cm^{-1})	GLUT-dependent, non-toxic, detection limit 1.4 mM, no non-specific retention	*In vitro* live-cell glucose uptake imaging, *in vivo* tumor xenograft heterogeneity imaging, neuronal/mouse brain tissue imaging
31	SRS probe (^{13}C-labeled alkyne-tagged)	—/SRS ($^{13}C\equiv{}^{13}C$ stretching vibration: 2053 cm^{-1})	GLUT-dependent, no spectral crosstalk with D$_7$-glucose, non-toxic, ratiometric quantitation (C–D/$^{13}C\equiv{}^{13}C$)	*In vitro* two-color imaging of glucose uptake/incorporation in single live cells, *ex vivo* mouse tissue imaging
32	Bioluminescent Probe (Azido-labeled)	/Bioluminescence (luciferin-luciferase reaction)	GLUT-dependent, non-toxic, high reactivity with CLP, no thiol cross-reactivity	Live-cell glucose uptake imaging, non-invasive longitudinal imaging, distinguishes normal/cancer cells, sensitivity comparable to ^{18}F-FDG PET
33	Fluorescent Probe (Azido-labeled) glucose analog	437/560 nm	GLUT-dependent, reacts with Glu-HT-Me, no HNO interference, detection limit 96 nM, non-toxic	Wash-free real-time glucose uptake imaging, differentiates cancer/normal cells, superior to 2-NBDG in high-glucose environments

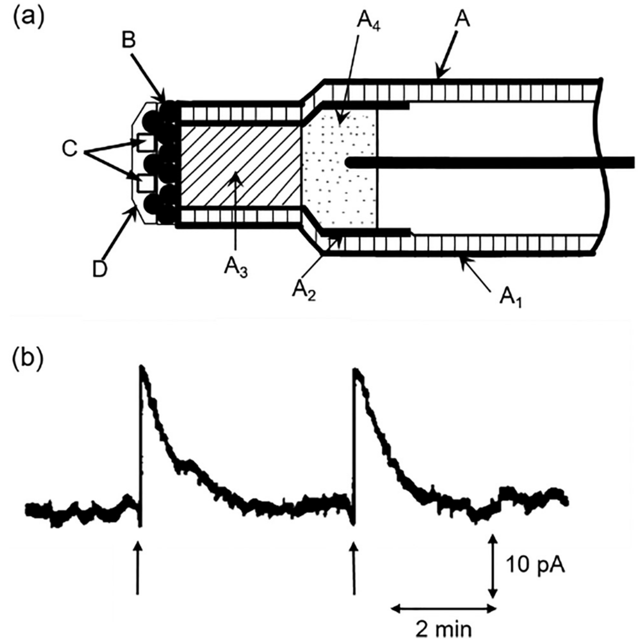

Fig. 26 (a) Schematic illustration GOx-based glucose microprobe **34**. A: Ultrasmall carbon ring electrode (A_1, drawn quartz capillary; A_2, thin carbon film; A_3, epoxy resin; A_4, mercury); B: Platinum coating; C: Incorporated glucose oxidase; D: Albumin film coating. (b) Current observed at electrode placed in the large dopamine neuron of *Planorbis corneus*. Adapted with permission from ref. 73. Copyright (1992) American Chemical Society.

nanowires showed intracellular glucose concentrations in the former were on average 1.6–1.7 times higher (Fig. 31c and d, $n = 5$). Using this probe, real-time monitoring of intracellular glucose levels was successfully achieved.

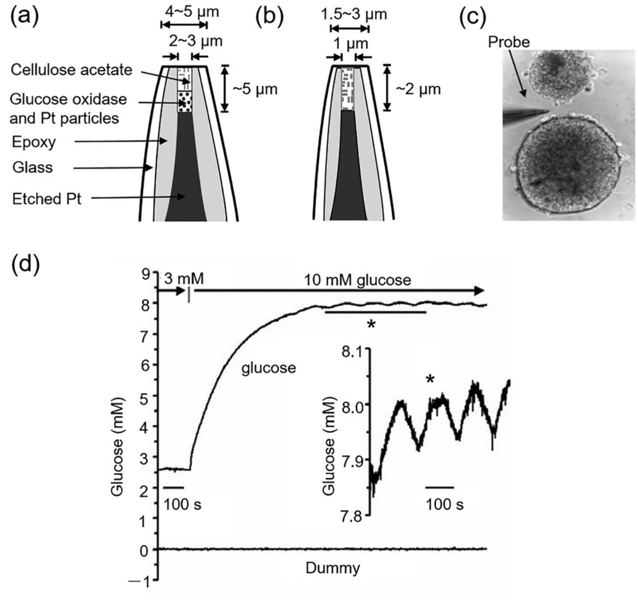

Fig. 27 Schematic illustration of the micron-sized probe **35** comprising a glucose microprobe (a) and an oxygen microprobe (b). (c) Photomicrograph displays a glucose probe near two individual islets for a size comparison, with a picture width of 150 μm. (d) Glucose measurements in single islets. The upper trace records the data from a glucose sensor implanted 70 mm inside an islet as the glucose concentration changes from 3 to 10 mM *via* perfusion at 32 mL s^{-1}. Inset: Oscillation in glucose level that occur after the glucose concentration increases to 10 mM. Adapted with permission from ref. 74, published by Elsevier.

Another common technology employed with GOx-based sensors is fluorescence-based sensing. An early example of this is Kopelman and Xu *et al.*'s 2002 PEBBLE (Probes Encapsulated By Biologically Localized Embedding) enzyme-based bioprobes **41** designed for real-time intracellular glucose measurements.[80] This probe employed co-immobilization of GOx alongside an oxygen-sensitive dye and a reference dye. GOx catalyzes the glucose oxidation reaction, leading to local oxygen depletion, which is itself detected by the O_2-sensitive dye. The fluorescent output from the O_2-sensing dye is measure (against the reference). This system's small size (approx. 45 nm diameter) and inert matrix allows insertion into living cells with minimal physical or chemical disruption to biological functions. These PEBBLEs offer a robust means for optically measuring intracellular glucose, avoiding the typical issues associated with free enzymes and fluorescent dye systems, offering a more versatile and more reliable tool for intracellular measurements.

In 2005, Strano and Barone *et al.* reported a solution-phase NIR probe **42** which used single-walled carbon nanotubes for β-D-glucose sensing.[81] They used non-covalent modification with electro-active $K_3Fe(CN)_6{}^{3-}$ species to create electron transfer sites. Reversible reduction of the ferricyanide by GOx-produced H_2O_2 facilitating use in sensing applications (Fig. 32a). A 200 μm × 1 cm microdialysis capillary (13 kDa cutoff) was filled with the nanotube solution, allowing glucose to diffuse through the membrane into the sensing medium. When placed beneath human skin, the resulting fluorescence was clearly mapped in two dimensions (Fig. 32b). The fluorescence emission of the (6,5)-nanotube ($\lambda_{\max}$ = 994 nm) exhibited an 80 s response lag to changes in local glucose concentration (Fig. 32c). This delay was attributed to glucose diffusion through the 200 μm dialysis membrane, followed by the GOx-catalyzed reaction and downstream electron transfer that modulates nanotube fluorescence. The response followed a type I adsorption isotherm with suitable sensitivity within the typical range of blood glucose in diabetic patients (1 to 8 mM), and a detection limit of 34.7 μM (Fig. 32d). The use of near-infrared signaling in such a capillary device offers the advantage of potential implantation into thick tissue or whole-blood media, where the signal can penetrate several centimeters. This passive, optically responsive substrate could enable continuous *in vivo* analyte detection with an external, miniaturized excitation and detection system. This approach offers clear advantages over electrochemical and photoelectrochemical sensing methods.

Unfortunately, the H_2O_2 product of glucose oxidation can induce oxidative stress by reacting with biomolecules *in situ*, potentially resulting in cellular damage, and so GOx-based sensing systems can be unsuitable, causing damage or dysregulation and hence unreliable results. The development of fully biocompatible enzyme-based systems is therefore of interest, including for instance the 2013 work of Tang and Li *et al.* Using apo-GOx (an inactive form of glucose oxidase), they modified gold nanoprobes to develop a biofriendly and highly sensitive nanoprobe **43** for the quantitative analysis and imaging of

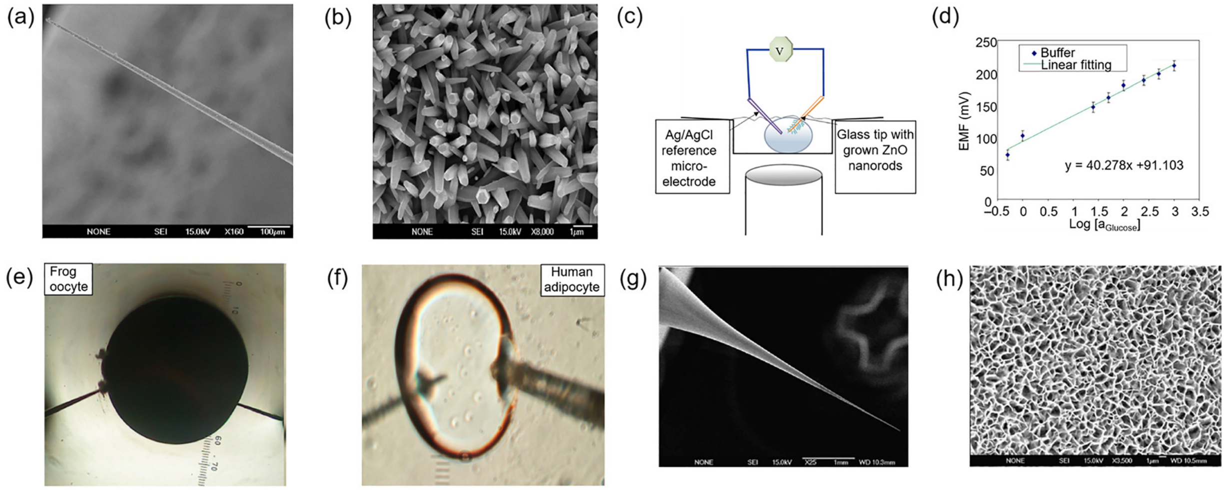

Fig. 28 (a) and (b) Scanning electron microscopic images of the ZnO nanorods grown on Ag-coated glass capillaries *via* low-temperature growth, captured prior to enzyme immobilization. (c) Schematic illustration of the ZnO-nanorod-based electrochemical probe **36** for intracellular glucose measurement. (d) Relationship between the electrochemical potential difference and glucose concentration (0.5–1000 μM) plotted using ZnO nanorod-coated probe. (e) and (f) Microscopic images of a single frog (*Xenopus laevis*) oocyte and a single human fat cell (adipocyte) during measurements. (g) and (h) Scanning electron microscopic images of nanoflake ZnO grown on an aluminum-coated glass capillary before enzyme coating. Panel a–f: Adapted with permission from ref. 75. Copyright (2010) Elsevier B.V. Panel g and h: Adapted with permission from ref. 76. Copyright (2010) Elsevier B.V.

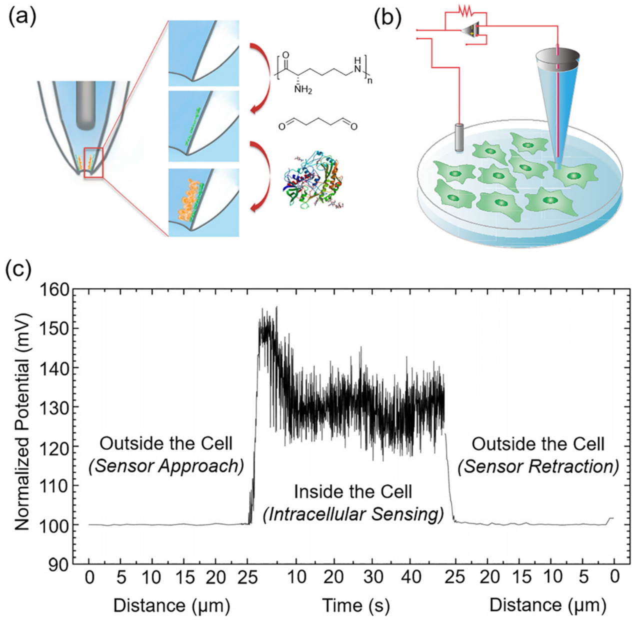

Fig. 29 (a) Schematic illustrating surface modification process of nanopipette tips **38** with immobilized glucose oxidase. (b) Diagram of the glucose nanoprobe utilized for intracellular glucose detection. (c) Intracellular dynamic glucose sensing using glucose nanoprobe. Adapted with permission from ref. 77. Copyright (2016) American Chemical Society.

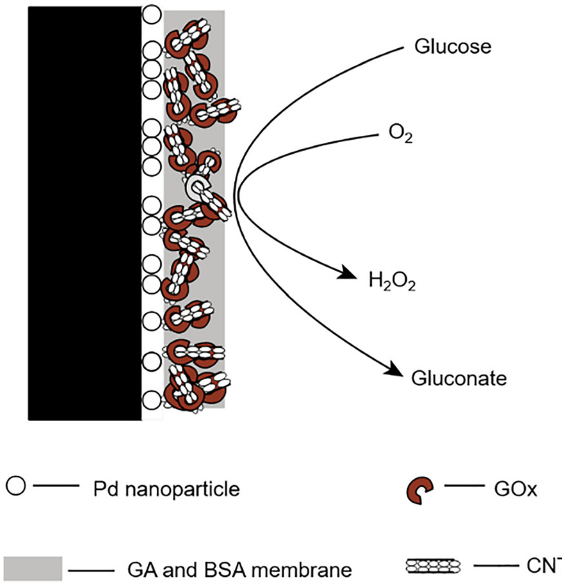

Fig. 30 Capillary electrophoresis-based micro-biosensor **39** for glucose detection. Adapted with permission from ref. 78. Copyright (2016) Elsevier B.V.

glucose consumption in living cells.[82] This probe system is based on fluorescence/Förster resonance energy transfer (FRET) between apo-GOx-modified gold nanoparticles (AuNPs) and dextran-FITC (fluorescein isothiocyanate, an amine-appended fluorescent dye) (Fig. 33a). On detection of glucose, the quenched fluorescence of FITC is restored due to the higher affinity of apo-GOx for glucose over dextran. The nanoprobe exhibits excellent selectivity for glucose over other monosaccharides and other biomolecules, as well as fantastic sensitivity with a detection limit as low as 5 nM. Owing to its low toxicity and the reliable cellular uptake ability of AuNPs, this system successfully enabled imaging of intracellular glucose consumption in cancer cells (Fig. 33b and c).

Using fluorescence to monitor H_2O_2 production rather than electrochemical methods as before, in 2008, Willner and Gill *et al.* constructed an integrated quantum dot (QD) ratiometric fluorescent nanoprobe **44** (Fig. 34),[83] modulating their photophysical properties, and therefore output, through oxidation by

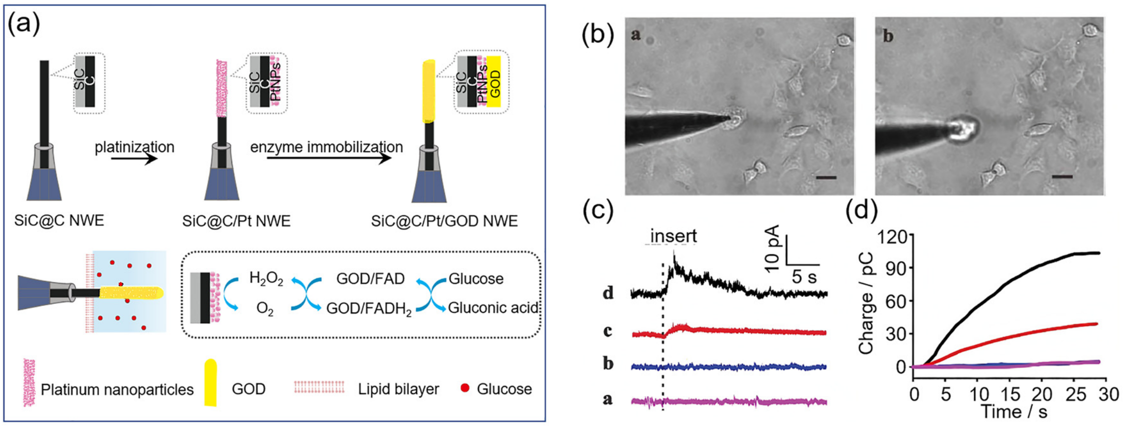

Fig. 31 (a) Fabrication processes of glucose nanowire probe **40** and intracellular glucose sensing mechanism. (b) Microscopic images of a HUVEC being inserted **a** and picked up **b** by a nanowire electrode. (c) Amperometric traces from HUVECs acquired by the SiC@C/Pt NWE (**a**: normal incubation, **b**: 50 mM glucose incubation), or by the glucose nanowire probe (**c**: normal incubation, **d**: 50 mM glucose incubation). (d) Charge chart of these amperometric curves. Adapted with permission from ref. 79. Copyright (2019) Royal Society of Chemistry.

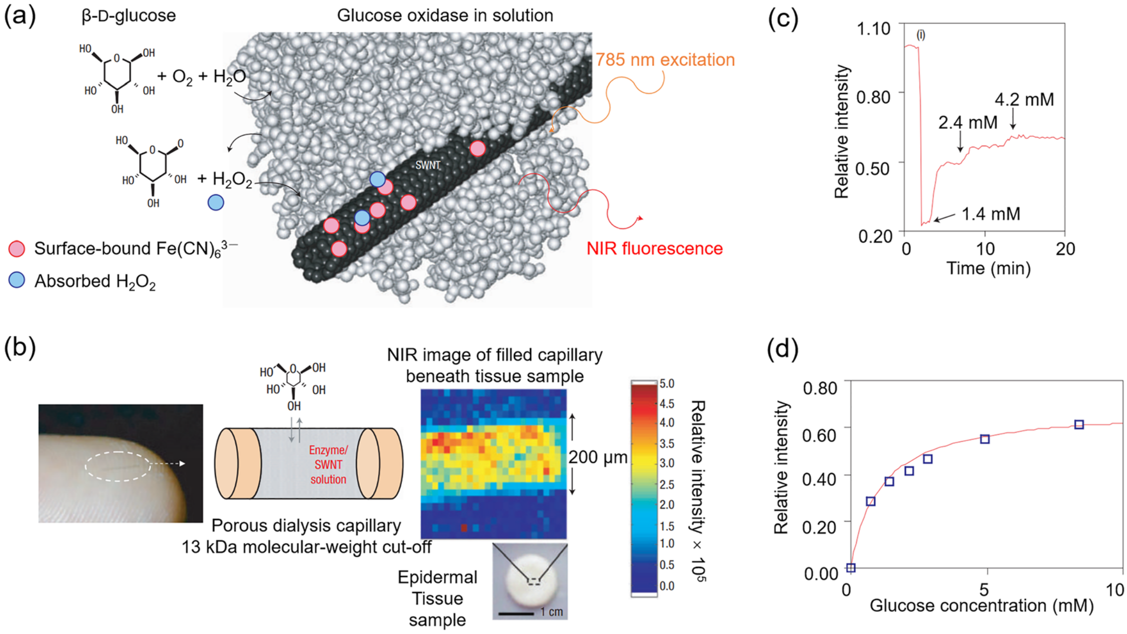

Fig. 32 (a) Working principle for carbon-nanotube optical probe **42**. (b) Microdialysis capillary on a finger (left), diagram illustrating porous structure enabling glucose diffusion (center) and glucose sensing using the carbon-nanotube optical probe (right). (c) Fluorescence response of the carbon-nanotube optical probe to the addition of glucose. (d) The response function connects the normalized intensity of the carbon-nanotube optical probe to the local glucose concentration within the blood glucose detection range. Adapted with permission from ref. 81. Copyright (2005) Springer Nature Limited.

H_2O_2. Biotinylated GOx (B-GOx) was conjugated to FITC-avidin-modified QDs, and the enzymatic production of hydrogen peroxide was tracked by observing its effect on QD fluorescence. As the biocatalytic oxidation advanced, the as-produced H_2O_2 quenches QD luminescence, and so the extent of QD fluorescence quenching correlates directly to glucose concentration. Willner and Gill were able to demonstrate both high sensitivity (0.1 mM) and selectivity against structurally-related ascorbic acid, demonstrating an effective new glucose-sensing QD-GOx platform.

Continuing with the trend of glucose sensing by the detection of H_2O_2, in 2015 Liu and colleagues explored DNA and CeO_2 nanoparticle (nanoceria) as a hydrogen peroxide sensor **45**.[84] Starting from CeO_2 nanoparticles, a well-known class of nanozymes, fluorescently labelled DNA was adsorbed onto their surface, that was displaced by H_2O_2 to produce a 20-fold fluorescence enhancement (Fig. 35a). Addition of nanoceria to DNA quenched the fluorescence near-completely, indicating DNA adsorption, while H_2O_2 promptly restored the fluorescence by releasing DNA (Fig. 35b). This system showed a high sensitivity for detecting H_2O_2, with a detection limit as low as 130 nM (Fig. 35c). When coupled with GOx, glucose could be detected with a sensitivity as low as 8.9 μM in buffer solution. Glucose in serum was also successfully detected, with results comparable to those obtained from a commercial glucose meter, demonstrating

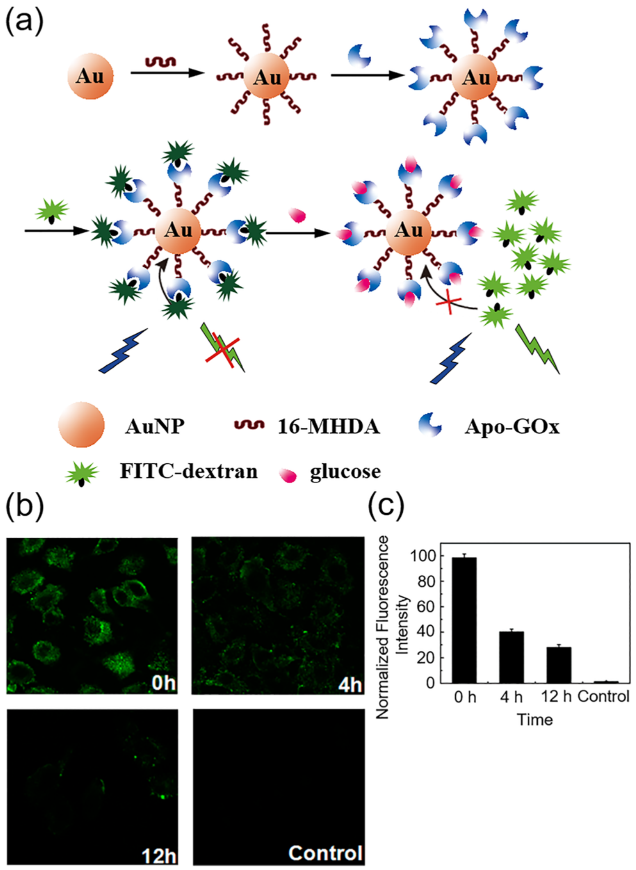

Fig. 33 (a) Glucose sensing using AuNPs-apo-GOx-Dextran-FITC nanoprobe **43**. (b) and (c) Confocal fluorescence images (b) and normalized fluorescence intensity (b) of HepG2 cells incubated with nanoprobe after treatment with glucose-free RPMI 1640 medium for 0, 4, and 12 h, respectively. Adapted with permission from ref. 82. Copyright (2013) American Chemical Society.

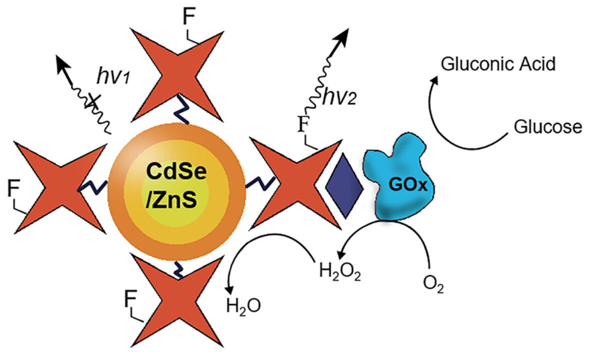

Fig. 34 Schematic structure and sensing mechanism of Willner and Gill's H_2O_2-sensing CdSe/ZnS QDs **44** for ratiometric analysis of glucose concentration. Adapted with permission from ref. 83. Copyright (2008) Wiley-VCH Verlag GmbH & Co. KGaA, Weinheim.

the potential use of DNA-based biosensors for the indirect monitoring of glucose *via* hydrogen peroxide.

Silver nanoparticles (AgNPs) have been shown to serve as highly effective quenchers for a variety of fluorescence-based probes, including organic dyes and quantum dots. In 2015, Yu and Li *et al.* reported a novel AgNP-perylene probe **46** for glucose sensing using AgNPs and a perylene probe (Fig. 36).[85] The perylene probe was non-covalently bound to the AgNP surface, quenching its fluorescence. On addition of glucose, exogenous GOx catalyzes glucose oxidation, production of H_2O_2, and thus etching of the AgNPs to eventually release the perylene fluorophore. The induced fluorescence turn-on enables glucose quantification, affording a simple, selective, and sensitive glucose-sensing system. The applicability of this assay was demonstrated in human blood serum samples.

In 2019, Lin and Jiang *et al.* put forward a signal-amplification strategy for glucose detection by synthesizing GOx-conjugated silver nanocubes (AgNC-GOx) **47** and an ultrasensitive Ag^+ fluorescence probe Ag^+-FP (Fig. 37a).[86] The usual H_2O_2 production leads to conversion of the AgNC into Ag^+, which in turn activates the fluorescence of the Ag^+-FP probe. Signal amplification arises from a doubling effect, where each molecule of H_2O_2 produces 2 Ag^+ ions. As a result, the AgNC-GOx/Ag^+-FP system significantly amplifies the fluorescence signal, thereby achieving high sensitivity, down to 50 μM. This approach exhibits excellent specificity and selectivity toward glucose and H_2O_2 (Fig. 37b), as demonstrated in a range of different cell lines (Fig. 37c and d).

Traditional fluorescent probes often rely on a single-signal response (''off/on'' model), making them susceptible to interference from analyte-independent factors, such as variations in probe concentration, light scattering within the sample, fluctuations in excitation light intensity, and inconsistencies in emission collection efficiency. Dual-emission can overcome many of these issues and so has become a stalwart of recent fluorescent sensing research. In 2020, Ni and Hu *et al.* developed a highly sensitive fluorescent microfluidic probe **48** incorporating carbon quantum dots (CQDs), cadmium telluride quantum dots (CdTeQDs) aerogel, and glucose oxidase for glucose detection in urine (Fig. 38a).[87] The CQDs, which emit green fluorescence at 520 nm, and CdTe QDs, which emit red fluorescence (λ_{em} = 620 nm, λ_{ex} = 365 nm) were synthesized specifically for this purpose. A ratiometric fluorescence mechanism was exploited through the selective quenching of the red fluorescence by H_2O_2, while the green fluorescence remained

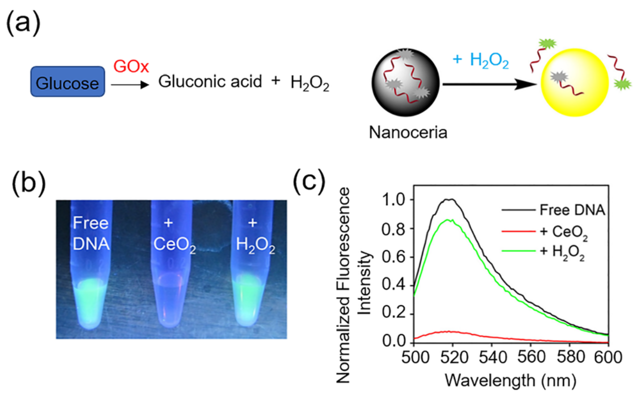

Fig. 35 (a) Sensing of H_2O_2 by displacement of fluorescent DNA adsorbed from nanoceria. (b) Fluorescence photos of free FAM-A_{15} DNA, after addition of nanoceria, and after addition H_2O_2. (c) Fluorescence spectra of the solutions diluted from (b). Adapted from ref. 84, published by American Chemical Society.

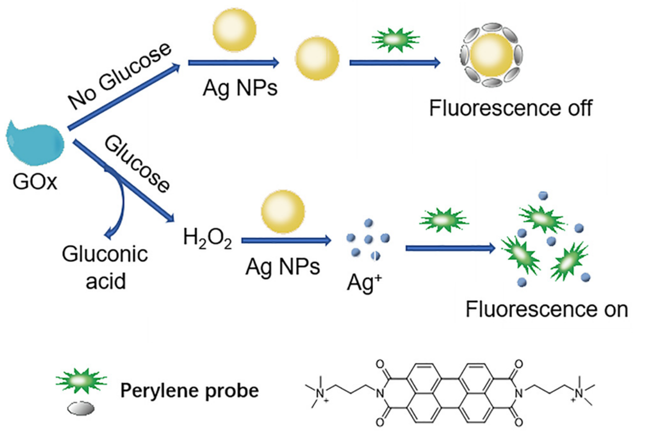

Fig. 36 Glucose detection using AgNP-perylene probe **46**. Adapted with permission from ref. 85. Copyright (2015) Royal Society of Chemistry.

constant. This change in fluorescence ratio produced a distinct shift in the probe's color, easily visible to the naked eye under 365 nm irradiation. The microprobe exhibited a clear transition in fluorescence color from red to green as the glucose concentration increased (Fig. 38b). Furthermore, glucose concentrations could be quantified using the red to green fluorescence ratio (R/G value). Within the biologically relevant glucose concentration range of 0–13 mM, the R/G value exhibited a strong linear correlation, achieving a detection limit of 0.223 mM, satisfying the requirements for urine glucose testing. These findings highlight the potential of this microfluidic probe for developing a portable, cost-effective, and real-time device for rapid urine glucose testing.

Continuing in the dual-emission arena, Wang and Guo *et al.* designed a dual-emission ratiometric fluorescent probe **49** for simultaneous sensing of glucose and cholesterol based on the inner filter effect (IFE) in 2021.[88] This probe **49** was developed by combining silver nanoparticles AgNPs/UiO-66-NH_2 and *o*-phenylenediamine (OPD) (Fig. 39). AgNPs/UiO-66-NH_2 were synthesized *in situ* by the reduction of $AgNO_3$ by sodium borohydride onto UiO-66-NH_2, with OPD serving as the chromogenic substrate. In the presence of glucose oxidase and cholesterol oxidase (ChOx), glucose and cholesterol are both oxidized to H_2O_2. The generated H_2O_2 causes the AgNPs to be etched into silver ions (Ag^+), which converts OPD into a fluorescent product 2,3-diaminophenazine (DAP) *in situ*. Thanks to the overlap of the emission spectrum of Ag NPs/UiO-66-NH_2 and the absorption/excitation spectrum of DAP, the fluorescence intensity ratio ($F_{555\text{ nm}}/F_{425\text{ nm}}$) increases with increasing concentrations of glucose and cholesterol, accompanied by a noticeable color transition from blue to yellow-green. Conveniently, the fluorescent probe-loaded composite films could be incorporated into a portable, smart color variation device employing a smartphone at its core, enabling real-

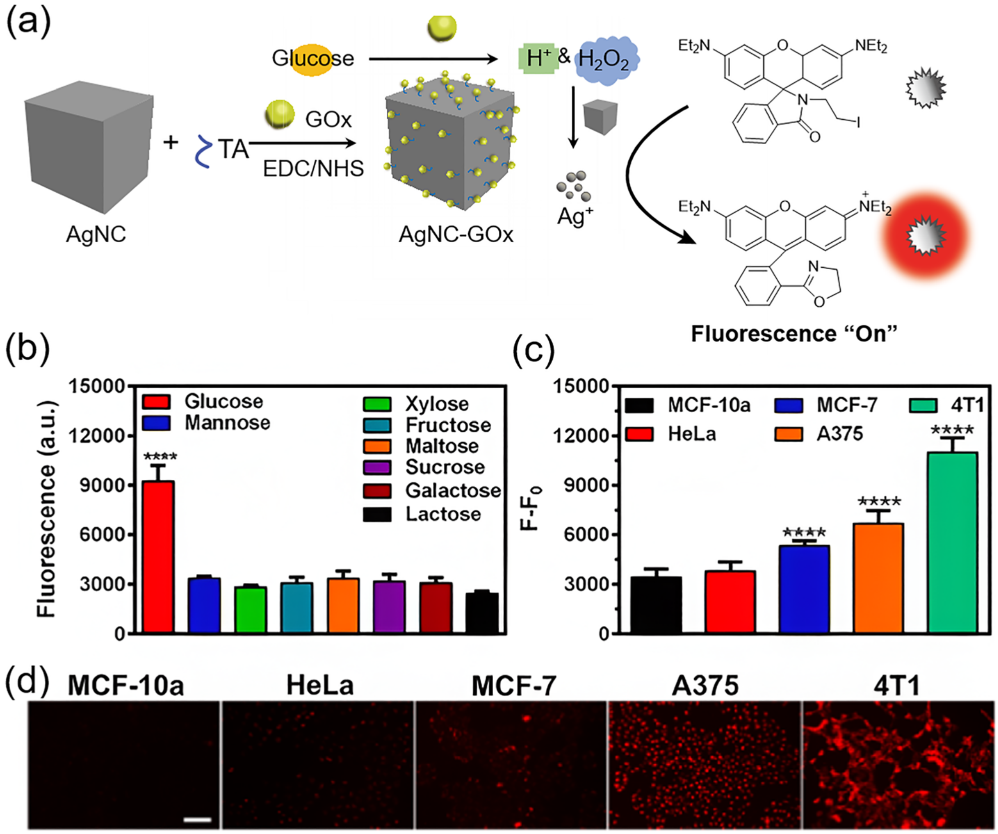

Fig. 37 (a) Fluorescence amplification mediated by AgNC-GOx/Ag^+-FP for glucose sensing. (b) Fluorescence response of AgNC-GOx/Ag^+-FP to various saccharides (final concentrations 2.5 mM). The final concentrations of (c) normalised fluorescence changes and (d) fluorescence images of AgNC-GOx/Ag^+-FP in different cell types. Adapted with permission from ref. 86. Copyright (2019) American Chemical Society.

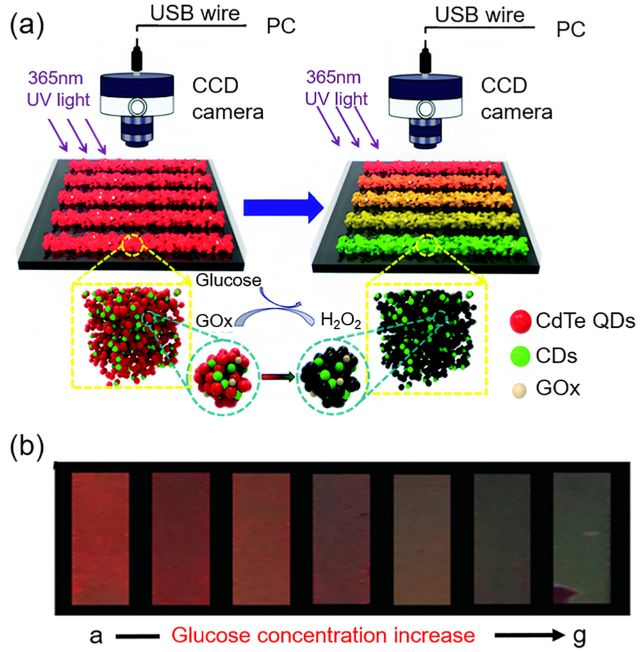

Fig. 38 (a) C/CdTe-GOx aerogel microsensor **48** for glucose detection. (b) Fluorescence images acquired by microprobes detecting urine containing different glucose concentrations (from left (a) to right (g) glucose concentration increased from 0 mM to 26 mM). Adapted with permission from ref. 87. Copyright (2020) Royal Society of Chemistry.

time on-site monitoring of glucose and cholesterol levels in human serum. This device demonstrates comparable analytical performance to standard testing methods. Given the cost-effectiveness and convenience of the fluorescent probe-loaded composite films, along with the widespread availability of smartphones, this method holds great potential for quantitative point-of-care testing of various biomarkers, contributing to improved human health monitoring.

Fluorescent metal–organic framework (MOF) nanomaterials exhibit numerous advantages over classical fluorescent sensors, including abundant active sites, high porosity, large specific surface area, and excellent chemical stability. These features make MOF platforms a prominent new player in the field, potentially enabling a tailored approach to *in situ* fluorescence imaging and detection. In 2022, Jiang and Liang *et al.* developed an iron-based MOF nanosol **50**, which was successfully applied for glucose detection.[89] This material was demonstrated to exhibit peroxidase-like activity under weakly acidic conditions, enabling the oxidation of 3,3′,5,5′-tetramethylbenzidine (TMB) by hydrogen peroxide, resulting in the generation of fluorescent TMBox (Fig. 40). This nanocatalytic process causes the solution's color to change from colorless to blue. To exploit this reaction, 0.25 mg mL^{-1} of GOx and glucose solutions at varying concentrations were introduced into the system. When glucose concentrations between 0.2 and 20 μM were added, the fluorescence emission intensity increased constantly, with a detection limit of 0.1 μM, and an expected transition from colorless to light blue.

In 2016, Zhang and Wang *et al.* developed an optical glucose biosensor **51** using glucose-sensitive hydrogel films as both the glucose-sensing material and the Fabry–Perot cavity.[90] The film was constructed using a layer-by-layer assembly process using partially oxidized dextran (PO-Dex), chitosan, and GOx. This sensor responds to glucose *via* GOx, with oxidation to gluconic acid decreasing the local pH within the film, thereby inducing swelling of the pH-sensitive hydrogel. As the film exhibits Fabry–Perot fringes in its reflection spectra, the glucose-induced swelling is detected as a shift in the fringes. This sensor exhibits high resistance to interference, as it does not respond to common interferents such as diols (as for boronic acid-based probes, see Section 6) or electroactive compounds, even at high concentrations. Additionally, the sensor demonstrates reversible response

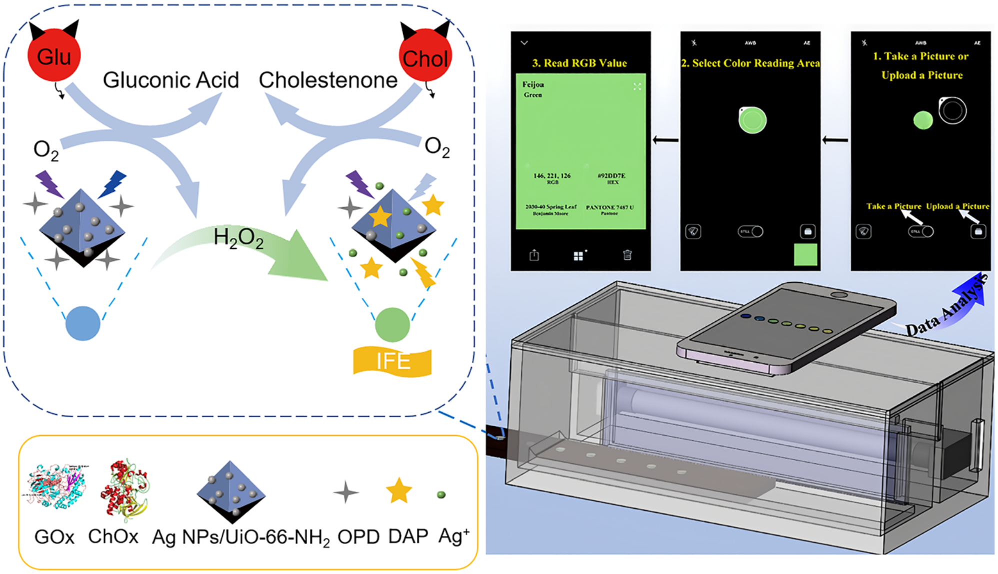

Fig. 39 Schematic diagram of the smartphone optical device for the detection of Glucose (Glu) and Cholesterol (Chol) using AgNPs/UiO-66-NH_2-based ratiometric fluorescent probe **49**. Adapted with permission from ref. 88. Copyright (2021) American Chemical Society.

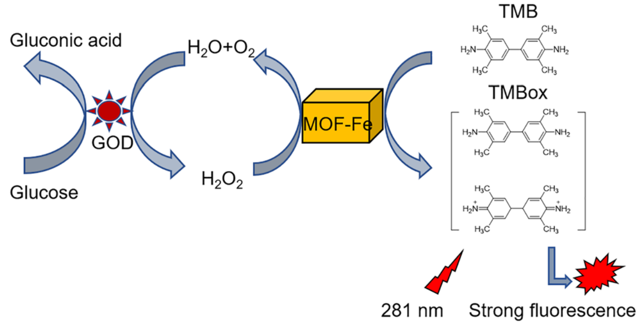

Fig. 40 The mechanism of the nanosol **50** for glucose detection *via* hydrogen peroxide, based on MOF-Fe catalytic oxidation of TMB. Adapted with permission from ref. 89. Copyright (2022) Elsevier B.V.

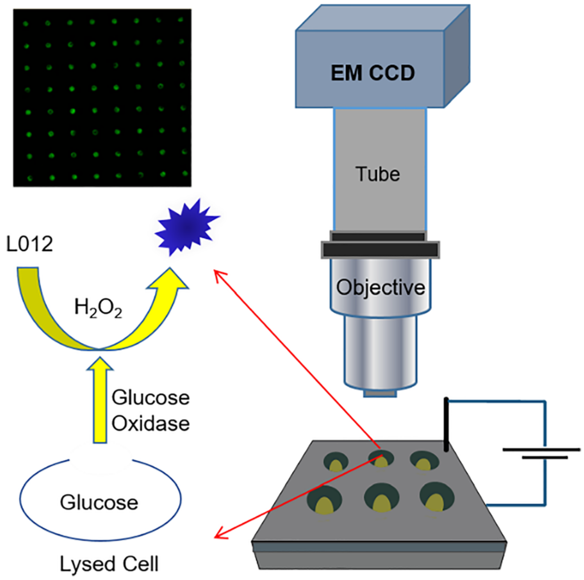

Fig. 41 Schematic illustration of the electrochemical luminescence imaging device **52** and detection method for fast analysis of intracellular glucose of single cells. Adapted with permission from ref. 91. Copyright (2016) American Chemical Society.

over a broad glucose concentration range, with a linear response within the clinically relevant range (0–20 mM). The thin film design allows for rapid response, making the sensor suitable for real-time, continuous glucose monitoring.

Stepping away from fluorescence-based systems, electrochemiluminescence (ECL) can also be employed as a sensing manifold. As a combination of electrochemical and spectroscopic methods, ECL offers several distinct advantages, such as improved overall control over and separation of the applied potential from light emission. Additionally, in contrast to fluorescence, ECL does not require excitation by light, which minimizes interference and can enable higher sensitivity. In 2016, Chen and Xu *et al.* developed an electrochemiluminescence imaging device **52** to analyze intracellular glucose in single cells.[91] As illustrated in Fig. 41, individual cells were confined in cell-sized microwells on a gold-coated indium tin oxide (ITO) slide, then simultaneously treated with luminol, Triton X-100, and glucose oxidase. The presence of Triton X-100 disrupts the cellular membrane, releasing intracellular glucose into the wells, where it is free to react with GOx to produce hydrogen peroxide. This in turn, induces luminol luminescence under positive potential. The luminescence from 64 individual cells on a single ITO slide is captured within 60 s using a charge-coupled device. Enhanced luminescence in all microwells following the addition of Triton X-100 and glucose oxidase indicated successful detection of intracellular glucose at the single-cell level. When cells were starved to reduce intracellular glucose levels, the luminescence intensity decreased, confirming the correlation between glucose and luminescence. The observed variations in glucose levels among individual cells highlighted the high cellular heterogeneity of intracellular glucose.

Brain glucose is widely recognized as a critical biomarker for Alzheimer's disease (AD), with particularly high specificity in early-stage AD. Activatable MRI contrast agents represent a powerful diagnostic tool for various diseases. In 2022, Zhao and Liu *et al.* developed a glucose-specific MRI contrast agent **53** termed ZIF-8/GOx@MnO_2@PEG (ZGMP).[92] This agent is constructed from a porous zeolitic imidazolate framework-8 (ZIF-8), functionalized with GOx, and further modified with MnO_2 and PEG (poly(ethylene glycol)). In this system, glucose detection proceeds indirectly by reduction of Mn(I) in MnO_2 to Mn(II) by the H_2O_2 product of GOx glucose oxidation. The newly generated Mn(II) impacts adjacent hydrogen atoms in water, shortening their relaxation time and enhancing the MRI signal (Fig. 42a). Experimentally, they demonstrated that these glucose-driven cascade reactions in **53** enhanced both T_1 and T_2 MRI signals, with T_1-weighted imaging (T_1WI) showing superior performance for visualizing brain glucose in AD models. To further verify this, an early AD mouse model was established by injecting Aβ42 oligomers into the brain parenchyma (Fig. 42b–f). **53**-based MRI revealed significantly higher glucose uptake in these early AD mice compared to control mice, as evidenced by pronounced T_1WI signal enhancement at regions of interest (ROI). Notably, this study eliminates the reliance on specialized scanning sequences for glucose-specific MRI, offering a potentially streamlined approach for early AD diagnosis. Unfortunately, though promising, this method remains limited, due in part to the irreversibility of this imaging process, challenges in achieving accurate linear analysis of glucose concentration, and a relatively slow kinetic response.

Other than for AD, aberrant cerebral glucose metabolism is closely associated with many brain disorders, and in particular tumors. In 2022, Wu and Liu *et al.* introduced a near-infrared optical transducer **54** designed for real-time *in vivo* monitoring of glucose fluctuations in cerebrospinal fluid (Fig. 43a and b).[93] This transducer utilized Nile Red and a Pt complex as a FRET pair embedded within a polymer matrix to create a ratiometric oxygen-sensitive probe. GOx was also integrated into the polymer nanoparticles, enabling highly sensitive glucose-dependent NIR phosphorescence. The research team demonstrated the utility of their NIR transducer in continuous glucose monitoring over extended periods, demonstrating consistent tracking of blood glucose fluctuations for multiple weeks following subcutaneous implantation. Direct injection into the lateral ventricle *via* the skull enabled the observation of elevated cerebral

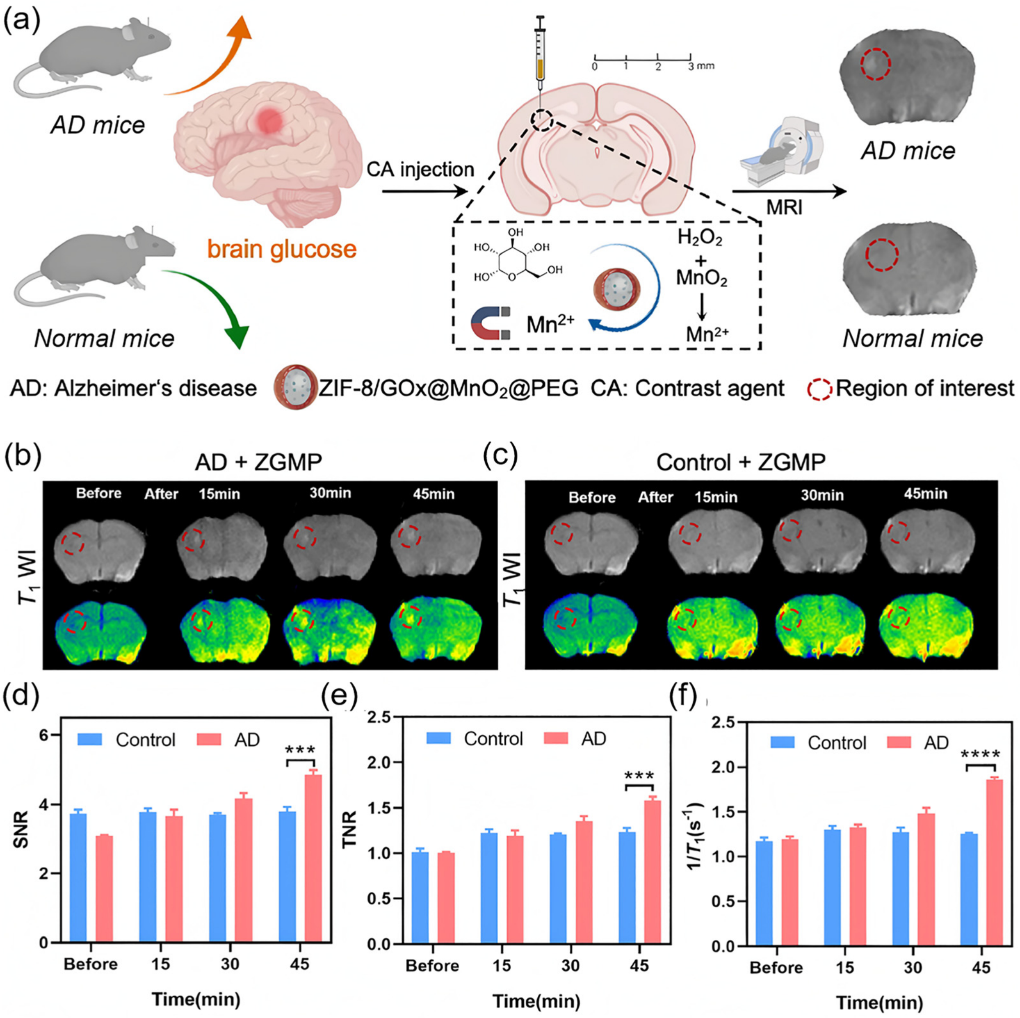

Fig. 42 (a) Glucose-activated MRI contrast agent **53** for diagnosing AD. (b) and (c) Brain MRI scans of (b) AD mice and (c) normal mice were carried out at 15, 30, and 45 min post **53** injection. (d)–(f) Comparison of (d) signal-to-noise ratio (SNR), (e) target-tissue-to-noise ratio (TNR), and (f) $1/T_1$ for MRI date form normal mice and AD mice. Adapted with permission from ref. 92. Copyright (2022) American Chemical Society.

glucose uptake rates in ND2:SmoA1 transgenic mice compared to wild-type controls, highlighting unique glucose uptake characteristics in tumor-bearing mice (Fig. 43c–e). This innovative approach offers a promising technique for dynamic imaging of glucose in the cerebrospinal fluid of small animal models, with clear potential for long-term glucose monitoring.

Enzyme-based probes based on GOx exhibit several notable advantages (Table 2). They possess high specificity thanks to the specific catalytic activity of GOx, enabling them to selectively target glucose and effectively distinguish structurally similar interferents such as ascorbic acid. These probes can achieve high sensitivity, with many achieving low-concentration detection. For example, DNA-ceria nanoparticle systems offer a glucose detection limit of 8.9 μM (Fig. 35), and MOF-Fe-based fluorescent probes have a detection limit of 0.1 μM (Fig. 40), both of which meet the requirements for trace glucose analysis in biological samples. They also demonstrate strong real-time and dynamic monitoring capabilities. Probes like PEBBLEs (45 nm) allow for real-time intracellular glucose measurement, while ZnO nanorod electrochemical probes, with a response time of less than 1 second, are well-suited for studying rapid metabolic processes (Fig. 28). These probes also benefit from compatibility with diverse detection platforms, covering electrochemistry, fluorescence, electrochemiluminescence, and magnetic resonance imaging, making them adaptable to various scenarios such as intracellular detection, serum analysis, and brain imaging. Furthermore, they have broad sample applicability, having been successfully applied to multiple sample types including single cells, serum, urine, and cerebrospinal fluid, thereby providing crucial metabolic information for the diagnosis of diseases like Alzheimer's disease and cancer.

However, these probes are not without limitations. A significant concern is the risk of oxidative stress from the H_2O_2 byproduct generated during GOx-catalysis. Insufficient enzyme stability is another; natural enzymes are prone to inactivation by environmental factors such as pH or temperature, which limits the long-term storage and reuse of the probes. Detection interference is also a common issue: H_2O_2-dependent detection

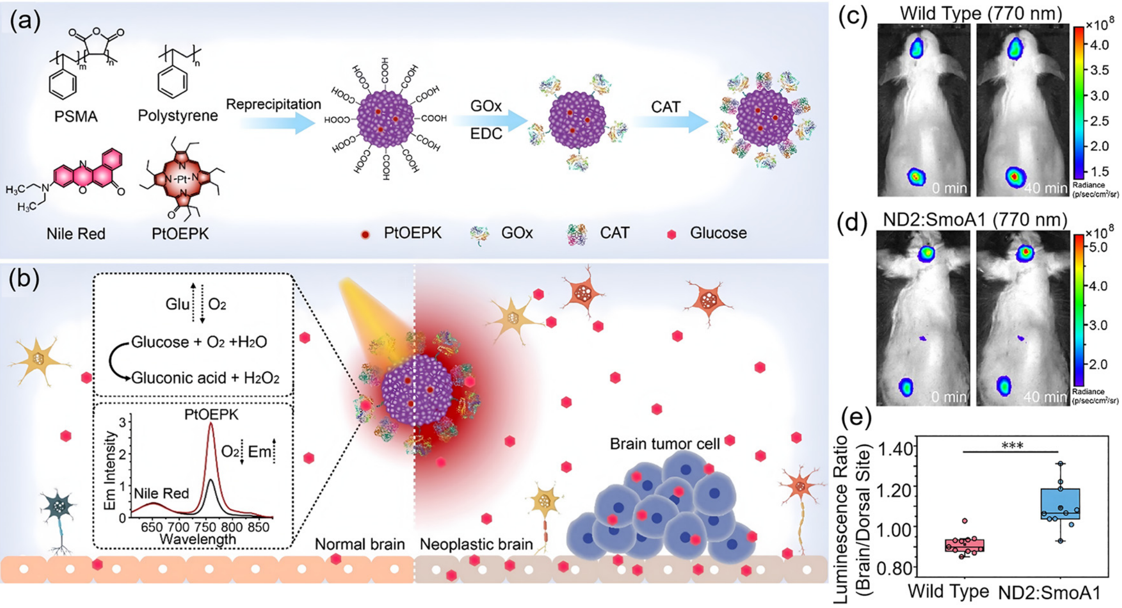

Fig. 43 (a) Structures and preparation of the nanoparticle transducer **54**. (b) Glucose sensing mechanism of the nanoparticle transducer in a normal brain and a neoplastic brain. (c) and (d) Optical images of a wild-type mouse and an ND2:SmoA1 mouse implanted with the nanoparticle transducer into the brain and dorsal site. (e) Ratios of the normalized luminescence intensities signals from both sites, assessed by a two-sided Student's *t* test (*$p < 0.001$). Adapted with permission from ref. 93. Copyright (2022) American Chemical Society.

mechanisms are susceptible to interference from other oxidizing substances, and some electrochemical probes are affected by electroactive species. Size and penetration limitations pose additional challenges: traditional electrochemical probes are often too large to enter cells, while fluorescence probes exhibit limited light penetration for deep tissues, hindering *in vivo* imaging. Finally, response range and kinetic constraints exist; some probes have a narrow linear range (*e.g.*, early ZnO nanorod probes only respond linearly to concentrations below 1 mM[75]), slow response (*e.g.*, ZGMP MRI probes[92]), or fail to cover the full range of physiological glucose concentrations.

Addressing the issue of H_2O_2-associated cytotoxicity is key, achievable for instance by using apo-GOx or nanozymes as alternatives to natural GOx. For instance, apo-GOx-modified gold nanoprobes which enable biofriendly detection by avoiding oxidative damage caused by H_2O_2.[82] Stability improvements can be achieved by improving enzyme immobilization efficiency through the use of nanocarriers such as ZnO nanoflakes[76] and MOFs.[89] A notable example is nano-honeycomb ZnO, which exhibits 1.8-fold higher sensitivity than nanorods due to its higher enzyme loading capacity, highlighting the effectiveness of optimized immobilization in stabilizing enzyme function. Broadening the response range of these probes is achieved by regulating the morphology of carriers. For example, ZnO nanoflakes, as a carrier, can expand the linear detection range to 500 nM–10 mM,[76] which covers the glucose concentrations encountered in both physiological and pathological states, making the probes more versatile for various biological and clinical scenarios.

To minimize detection interference, the development of ratiometric fluorescence or electrochemiluminescence systems has proven valuable. For example, CQDs/CdTe QDs ratiometric probes eliminate environmental interference through signal ratio correction, ensuring more reliable detection results.[87] Additionally, specific nanomaterials like carbon nanotubes can be used to shield electroactive interferents, further reducing unwanted signal disturbances in electrochemical detection.[81] Optimizing the size and penetration of probes is crucial for expanding their applicability. Designing ultrasmall probes, such as 45 nm PEBBLEs, facilitates intracellular detection by enabling efficient entry into cells.[80] For deep tissue imaging, adoption of NIR fluorescence probes or MRI probes (*e.g.*, **53**[92]) enhances penetration through tissues, overcoming the limitations of traditional probes in accessing deep biological structures.

Fluorescent protein-based probes emerge as a complementary paradigm, harnessing genetically encoded fluorophores and glucose-binding proteins to enable non-enzymatic, reversible glucose sensing. FRET-based fluorescent protein systems for glucose sensing offer advantages such as low cytotoxicity, genetic tractability, and subcellular localization capabilities—even in plant models *via* transgene-silencing-resistant designs. Yet, they face trade-offs: photobleaching in prolonged imaging, limited fluorescence dynamic range in early FRET probes, and reliance on complex microscopic setups. The next section of this review will present examples of this, looking at design innovations, mechanistic diversity, and biomedical applications of fluorescent protein-based probes, illustrating how they may address some of the limitations of enzymatic systems discussed thus far.

4. Fluorescent protein-based probes

Non-enzymatic proteins are also employed in sensing systems for glucose, exploiting for instance FRET properties of certain proteins. An outline of the development of these types of probes will be presented in this section, broadly illustrating the

Table 2 Key properties of representative enzyme-based probes

Probe	Probe type	Signal mechanism	Characteristics	Biological applications
34	Enzymatic electrochemical probe	Amperometric signal (glucose oxidase-catalyzed H_2O_2 detection)	Response time 270 ms, linear range 50 μM–5 mM	Real-time glucose monitoring in snail dopamine neurons
35	Enzymatic electrochemical probe	Amperometric signal (glucose oxidase-mediated H_2O_2 detection)	Response time 0.8 ± 0.1 s, linear ≤10 mM, glucose oxidation O_2-independent	Correlative detection of glucose/oxygen/Ca^{2+} in islet cells
36	ZnO nanorod electrode probe	Potential change (ionic distribution variation)	Tip diameter 0.7 μm, linear range 0.5–1000 μM, response time <1 s	Intracellular glucose detection in adipocytes/oocytes
37	ZnO nanoflake electrode probe	Potential change (ionic distribution variation *via* glucose metabolism)	Tip diameter 0.7 μm, linear range 500 nM, nanoflake 10 mM, strong anti-interference	Intracellular glucose detection in adipocytes/oocytes
38	Quartz nanopipette enzyme-based probe	Impedance change (pH- and ionic current-dependent glucose-enzyme interaction)	Tip diameter 90–100 nm, linear range 0.1–8 mM, reusable	Single-cell glucose detection, distinguishing cancer/normal cells
39	PdNPs/Pt microelectrode enzyme probe	Amperometric signal (catalytic oxidation of H_2O_2 generated from glucose oxidation)	LOD 0.5 μM, response time 2.5 s, good anti-interference	Glucose determination in gastric cancer cell extracts/single cells
40	Pt NPs/SiC@C nanowire electrode probe	Amperometric signal (GOx/Pt-catalyzed H_2O_2 detection)	Linear range 0.1–1 mM, LOD 41 μM, good stability	Real-time intracellular glucose monitoring in hepatocytes/endothelial cells
41	Fluorescent nano-PEBBLE sensor	Ratiometric fluorescence (oxygen-sensitive dye quenching *via* glucose oxidation)	Size ~45 nm, linear range 0.3–5 mM, photostable	Intracellular glucose imaging and real-time monitoring in live cells
42	SWNT-based NIR optical probe	NIR fluorescence modulation (charge transfer during glucose-enzyme reaction)	Emission wavelength ~994 nm, linear range 1–8 mM, good tissue penetration	Glucose detection in whole blood/serum, *in vivo* continuous monitoring
43	AuNP-apo-GOx FRET probe	FRET recovery (glucose-induced competitive binding to apo-GOx)	LOD 5 nM, high selectivity, good biocompatibility	Quantitative glucose detection and imaging in hepatoma cells
44	CdSe/ZnS QDs enzyme probe	Ratiometric fluorescence quenching (H_2O_2-generated from glucose oxidation)	Photostable, anti-ascorbic acid interference, stable for 3 weeks	Optical glucose detection in HEPES buffer
45	Fluorescent DNA/nanoceria probe	Fluorescence enhancement (glucose/H_2O_2-triggered DNA desorption and fluorescence recover)	LOD 8.9 μM, high selectivity, stable in serum	Serum glucose detection, H_2O_2 sensing in biological systems
46	Perylene/Ag NP composite probe	Fluorescence turn-on (glucose-induced AgNP etching and fluorescence recovery)	LOD 2.5 μM, linear range 0–200 μM, high selectivity	Human serum glucose detection, clinical blood glucose monitoring
47	AgNC-GOx/Ag^+ fluorescence probe	Fluorescence amplification (glucose/GOx-mediated Ag^+-enhanced fluorescence)	Linear range 0.05–5 mM, LOD 50 μM, low toxicity	Intracellular glucose detection in multiple cell lines, tumor cell distinction
48	C/CdTe QDs-GOx aerogel sensor	Ratiometric fluorescence color change (H_2O_2-induced quenching from glucose oxidation)	Linear range 0–13 mM, LOD 0.223 mM, stable for 30 days	Visual/quantitative urine glucose detection, diabetes screening
49	Ag NPs/UiO-66-NH_2 ratiometric probe	Ratiometric fluorescence (glucose-responsive inner filter effect)	LOD (glucose/cholesterol) 0.5/0.7 μM, smartphone-adaptable	Point-of-care testing of glucose/cholesterol in serum
50	MOF-Fe enzymatic fluorescence probe	Fluorescence enhancement (GOx-catalyzed TMB oxidation luminescence)	Linear range 0.2–20 μM, LOD 0.1 μM, high selectivity	Glucose detection in beverages, food sample analysis
51	PO-Dex/chitosan/GOD probe	Fringe shift (Glucose oxidation-induced pH drop)	Linear range 0–20 mM, fast response	Real-time glucose monitoring, diabetes management
52	Au NP-coated ITO microwell ECL probe	Electrochemiluminescence imaging (H_2O_2-induced luminol electrochemiluminescence from glucose oxidation)	Detection efficiency 64 cells/60 s, LOD 5 μM, AuNP-enhanced	Single-cell intracellular glucose analysis, revealing cellular heterogeneity
53	Glucose-activatable MRI contrast agent	T_1WI signal enhancement (enzyme-triggered Mn^{2+} release)	Relaxivity r_1 = 5.05 mM^{-1} s^{-1}, high selectivity, biocompatible	Early Alzheimer's disease diagnosis, cerebral glucose metabolism imaging
54	Glucose-responsive NIR nanoparticle transducer	Ratiometric NIR phosphorescence (glucose- and oxygen-sensitive)	Size ~19 nm, stable for 4 weeks, good penetration	Cerebrospinal fluid glucose imaging, brain tumor diagnosis

direction of progress in this field and the varied mechanisms of fluorescence that can be used.

4.1. First generation FRET-based fluorescent protein probes

Generally, FRET-based fluorescent protein systems employ a combination of different types of fluorescent proteins and glucose-binding protein (GBP), a periplasmic binding protein (PBP) with high selectivity for glucose. It consists of two globular domains connected by a flexible hinge region. On binding of the glucose substrate, a substrate-induced hinge twist occurs, causing appropriately placed chromophores to move apart, resulting in a concentration-dependent FRET-mediated fluorescent signal. As we shall see, these systems are predominantly based on the systems developed by Frommer and his group.

In 2003, Frommer and Fehr *et al.* developed a fluorescent protein probe **55** (FLIPglu-170n) by linking the mature *E. coli* periplasmic glucose/galactose-binding protein (GGBP) to both a cyan fluorescent protein (CFP) and a yellow fluorescent protein (YFP) at its N- and C-terminuses, respectively.[94] This enabled direct measurement of glucose levels in living cells (Fig. 44a), with a concentration-dependent reduction in FRET between the attached chromophores on glucose binding. A binding affinity of 170 nM, and a maximal change in the FRET ratio of 0.23 were measured (Fig. 44b). With a narrow glucose sensing range of only 0.02–1.5 μM, well outside of physiological concentrations. The affinity was successfully reduced to 0.59 mM through mutation of Phe-16 to an alanine, generating probe **56** (FLIPglu-600μ) with an improved glucose detection range of 0.07–5.3 mM (Fig. 44c). Using mutant probe **56**, the authors were able to monitor reversible glucose dynamics in COS-7 cells within the physiological range, and observed that removal of glucose from the extracellular medium led to an expected reduction in intracellular glucose levels, confirming the reversibility of these first-in-class FRET protein glucose sensors (Fig. 44d–f). This seminal work provided a foundation for further development of similar FRET-based protein probes, a selection of which will be detailed herein.

Building on this, in 2008, Ribalet and John *et al.* expressed probe **56** in four mammalian cell lines: COS-7, CHO, HEK293, and C2C12 to investigate intracellular glucose homeostasis.[95] Upon addition of extracellular glucose, the intracellular FRET ratio decreased rapidly as intracellular glucose levels increased. Conversely, when extracellular glucose was removed the FRET ratio returned to its initial value at a similar rate (τ = 15 to 40 s) across all cell types, as shown previously by Frommer. This is illustrated in Fig. 45, for instance, where undifferentiated C2C12 cells cultured in a high-glucose environment and subjected repeatedly to 10 mM extracellular glucose exhibited a baseline YFP/CFP emission ratio of 2.0 in the absence of glucose. 10 mM extracellular glucose decreased this to 1.75, reflecting glucose entry into the cells, returning to baseline 2.0 on glucose removal, signifying clearance of intracellular glucose.

Probe **56** has also proven valuable for imaging glucose fluctuations in COS-7 cells,[94] although a relatively limited dynamic range was observed, making it unsuitable for specialized applications such as high-throughput screening of small interfering RNA (siRNA) libraries for identification of glucose-regulating proteins. In 2005, Frommer and Deuschle *et al.* discovered that tighter allosteric coupling between PBPs and fluorophores could be achieved through either truncating linkers or targeted insertion of chromophores.[96] This was later employed by Frommer and Takanaga *et al.* in 2008 to develop probe **57** (FLIPglu-600μΔ13-M),[97] in which they removed the composite linker regions and replaced the pH- and chloride-sensitive fluorescent protein eYFP (enhanced yellow fluorescent

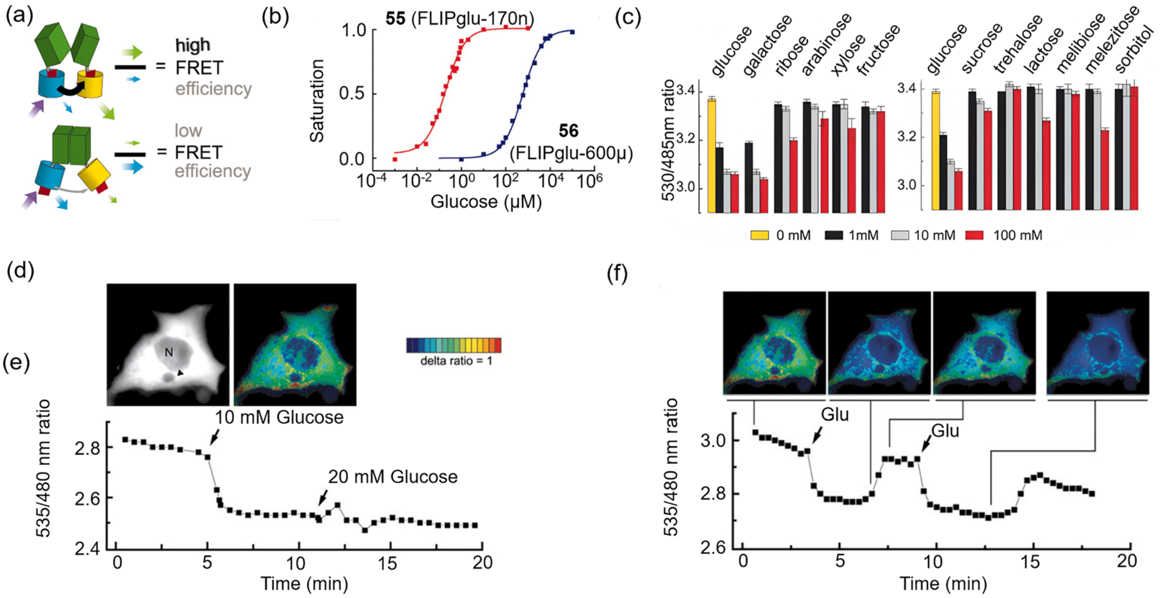

Fig. 44 (a) Working principle of FRET-based fluorescent protein probes. (b) Glucose titration curves for **55** (red) and **56** (blue). (c) Selectivity of **55** towards various saccharides. (d)–(f) *In vivo* characterization of **55** in COS-7 cells. (d) Averaged YFP-CFP emission image shows **55** in cytosol and excluded from nuclei (N) and lysosomes (▲). (e) Cell emission images were integrated to generate a single ratio value per cell over time, arrows mark glucose addition. (f) Following addition and detection of glucose, external glucose was removed by perfusion with glucose-free solution. Adapted from ref. 94, published by Elsevier.

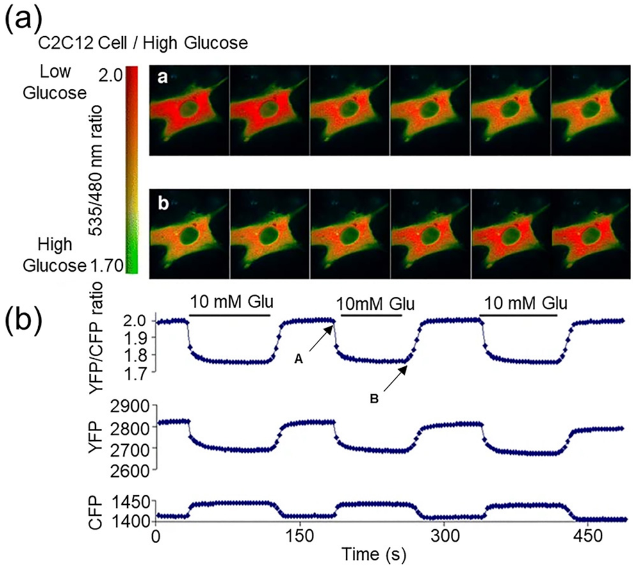

Fig. 45 (a) FRET ratio within a cell transfected with glucose probe **56**. Red signifies a high ratio or low glucose levels, while green denotes a low ratio or high glucose levels. (b) Average FRET ratio (YFP/CFP; upper trace), YFP emission (middle trace), and CFP emission (lower trace) across the entire cell. Adapted with permission from ref. 95. Copyright (2008) Springer Nature.

protein) with the yellow fluorescent protein citrine to improve robustness. This yielded a 4-fold increase in the ratio change on glucose addition, rising to 10-fold for related probe **58** (FLII^{12}Pglu-600μ), produced by insertion of a fluorophore into a surface-exposed loop. Further optimization was achieved through, truncation of amino acids from the given proteins *via* site-directed mutagenesis, as well as further truncation of the linkers. This produced highly optimized probes **59** (FLII^{12}Pglu-δ4) and **60** (FLII^{12}Pglu-δ6), amongst others (Fig. 46a). No direct correlation was observed between the length of the linker and the Δ ratio, suggesting that the composition of the linker is likely more influential than its length, supporting the premise that spatial arrangement of the fluorophores plays a crucial role in optimizing FRET efficiency. Glucose perfusion experiments in FLII^{12}Pglu-expressing HepG2 cell lines confirmed this (Fig. 46b and c), with probe **61** (FLII^{12}Pglu-700μδ6) demonstrating a significant improvement in sensitivity and dynamic range enabling reliable glucose analysis *in vivo* (Fig. 46d). The enhanced sensitivity of these glucose nanoprobes not only improves the accuracy of *in vivo* glucose fluctuation measurements but also offers potential platforms for screening siRNA libraries and drug compounds using high-content screening methods.

Glucose is the main physiological stimulus for insulin secretion in pancreatic β-cells. Its uptake and phosphorylation initiate and regulate many downstream pathways, ultimately leading to insulin secretion, a process that remains only partially understood. In 2012, Baltrusch and Kaminski *et al.* employed probe **61** to visualize changes in intracellular glucose concentrations in mouse pancreatic β-cells in response to the varying external glucose levels.[98] From time-dependent glucose concentration plots, they calculated the rates of glucose influx, efflux, and metabolism. Concurrently, real-time monitoring of glucose/calcium dynamics was carried out using probe **61** and fura-2 acetoxymethyl-ester (a fluorescent calcium indicator), which revealed that a glucose concentration threshold of 4 mM was required to trigger an increase in

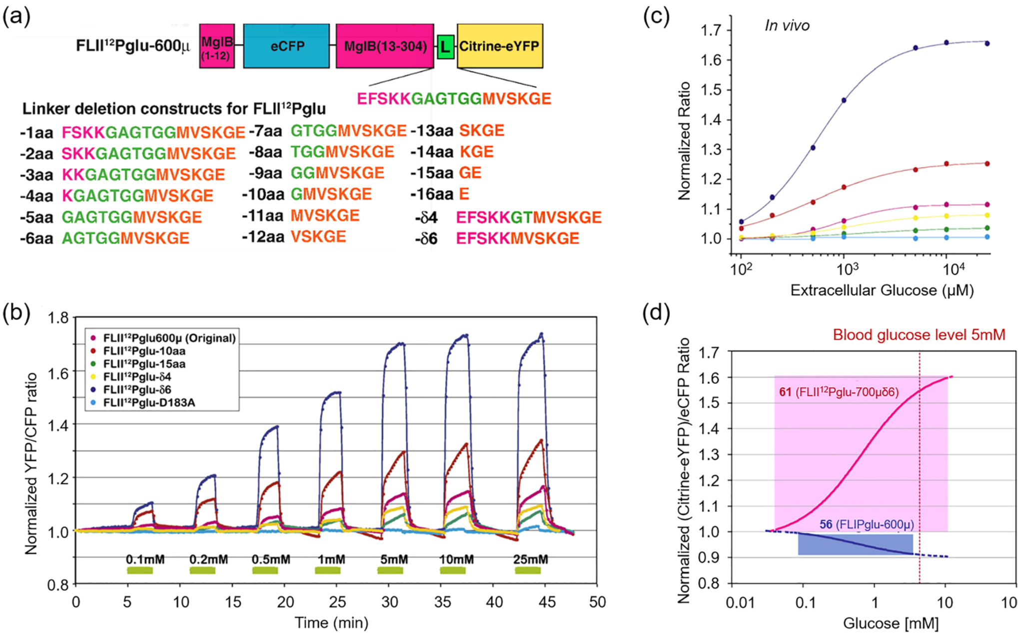

Fig. 46 (a) Domain structure of probe FLII^{12}Pglu, which encompasses N-terminal His-tag, N-terminal 12 amino acids of MglB (bacterial D-galactose-binding periplasmic protein), eCFP (enhanced cyan fluorescent protein), 13-304 amino acid of MglB, a C-terminal composite linker, and Citrine-eYFP. (b) Time-dependent ratio change of FLII^{12}Pglu-expressing HepG2 cells with increasing external glucose concentrations. (c) *In vivo* glucose apparent flux titration curve of FLII^{12}Pglu series nanoprobes. (d) *in vivo* detection range of (**56**, blue) and (**61**, pink). Adapted with permission from ref. 97. Copyright (2008) Elsevier B.V.

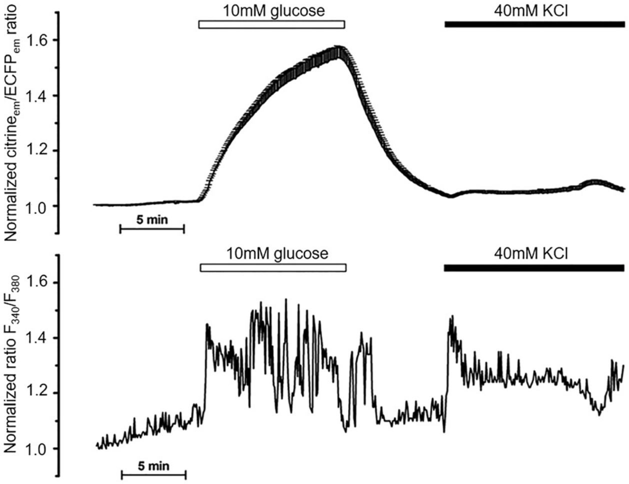

Fig. 47 Concomitant real-time sensing of both intracellular glucose concentration (top) and calcium dynamics (bottom) within MIN6 cells. MIN6-FLIPglu cells, which were loaded with fura-2 acetoxymethyl ester, during perifusion. As denoted by the bars, the perifusion was either in the presence or absence of glucose (10 mM) or KCl (40 mM). Adapted with permission from ref. 98. Copyright (2008) Elsevier B.V.

intracellular calcium concentration ([Ca^{2+}]$_i$) in β-cells, whilst large amplitude [Ca^{2+}]$_i$ oscillations required 7 mM glucose (Fig. 47). In the absence of glucose, the K$_{ATP}$ channel blocker glibenclamide was unable to induce substantial [Ca^{2+}]$_i$ oscillations, supporting the idea that glucose triggers [Ca^{2+}]$_i$ dynamics through a K$_{ATP}$ channel-independent mechanism. This study revealed that glucose must reach a critical concentration to trigger an increase in [Ca^{2+}]$_i$ and subsequently initiate oscillations in [Ca^{2+}]$_i$, demonstrating an elegant use of protein-based FRET-based glucose sensors such as probe **61**.

Probe **61** is now used widely as it provides an excellent platform for dynamic glucose sensing, in particular in the presence of other sensing motifs and analytes. This includes studies on the link between hippocampal and synaptic activity,[99] or neuronal excitotoxicity (excessive release of excitatory neurotransmitter glutamate) alongside other FRET-based probes for ATP and AMPK (AMP-activated protein kinase).[100] Recently, in 2023, probe **61** was employed by Schmachtenberg and García *et al.* in their studies of Müller cell metabolism where it relates to retinal function.[101] They employed probe **61** alongside the genetically encoded lactate probe Laconic to study the metabolite flux in retinal Müller cells (Fig. 48a and b). With this approach, a reduction in intracellular lactate was observed upon exposure to 0 mM extracellular lactate, confirming that lactate flux is governed by concentration gradients (Fig. 48c). When 10 mM glucose was introduced, fluorescence levels returned to baseline, indicating these cells are operating under a saturated intracellular glucose concentration under basal conditions (Fig. 48d).

In 2012, Polizzi and Behjousiar *et al.* expressed protein-based glucose and glutamine bioprobes in a Chinese Hamster Ovary cell model system for *in situ* monitoring.[102] The glucose biosensor FLIPglu600μΔ11Aphrodite (**62**) was again provided by

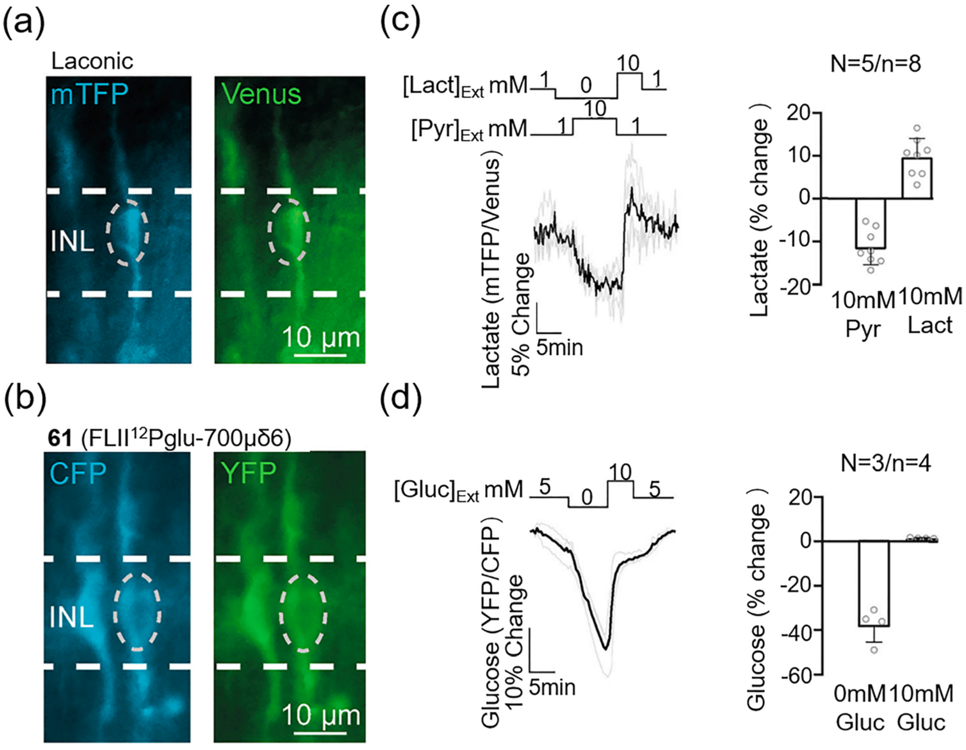

Fig. 48 (a) and (b) Representative images of the expression of the lactate probe (Laconic) and glucose probe **61**. (c) and (d) Dynamic range of the lactate and glucose probe in Müller cells. Adapted with permission from ref. 101. Copyright (2023) Elsevier B.V.

Frommer *et al.*,[96] while the glutamine probe was developed in-house based on *E. coli* glutamine PBP and citrine. These probes were chosen for their linear measurement range, which closely matched the intracellular metabolite concentrations observed for the study. These probes operated complementarily, with glucose binding disrupting alignment and causing a decrease in FRET, whilst glutamine binding caused the fluorophores to come together to increase FRET. Therefore, the model system constructed in this study enables *in situ* real-time monitoring of both glucose and glutamine, potentially providing support for the optimization of biopharmaceutical processes.

Glucose is of course not limited to mammalian systems, but unfortunately, the probes developed by Frommer and others above are not suitable for use in plants, as they were found to suffer from transgene silencing which reduced changes in FRET to undetectable levels. Therefore, Frommer and Deuschle *et al.* developed a set of FRET-based probes with enhanced sensitivity for glucose detection in epidermal cells and intact roots of *Arabidopsis* RNA-silencing mutants.[103] The design was based on a fusion protein consisting of eCFP translationally fused to an affinity mutant of the glucose-binding protein MglB and eYFP. Again, linker removal and site-directed mutagenesis were used to produce probes **63** (FLIPglu-600μΔ13-P), **64** (FLIPglu-170nΔ13-P), **65** (FLIPglu-2μΔ13-P), and **66** (FLIPglu-3.2mΔ13-P). These names indicate glucose affinity ("…μ", 600 μM, 170 nM, 2 μM, and 3.2 mM, respectively) and specific linker deletion ("Δ13") (Fig. 49a). By expressing these probes in *sgs3* and *rdr6* transgene silencing mutants, the silencing issues were overcome, producing strong fluorescence signals, with good reversibility (Fig. 49b and c). FRET evaluation revealed that **63** (FLIPglu-600μΔ13-P) exhibited a maximal ratio change of −0.26, significantly improving upon the original probe **56** (FLIPglu-600μ), also outperforming the ratio observed in initial mammalian cell systems.

4.2. "Off/On" mode protein switch-based fluorescent protein probes

Protein switches with optical properties are a prime example of designer bioprobes that exhibit altered responses to environmental stimuli, manifested as an "on/off" signal. These molecules have great potential for the development of bioprobes, the creation of allosteric enzymes, and as building blocks for tailored nanobiomaterials. In 2008, Daunert and Hamorsky *et al.* developed a bioluminescent molecular switch **67** by inserting GBP into the photoprotein aequorin (AEQ).[104] On addition of glucose, GBP undergoes a conformational change, bringing together the two segments of AEQ, "turning on" bioluminescence and enabling glucose detection (Fig. 50a and b). An impressive sensitivity of 100 nM was observed (Fig. 50c). This study marks the first time that AEQ was split into fragments, and that the AEQ fragments demonstrated "on" bioluminescence upon molecular recognition, providing valuable insight into and demonstrating the potential applications of genetically engineered chimeric proteins, paving the way for the design and production of a range of other unique designer bioprobes.

4.3. SWNT-based fluorescent protein probes

Although PBPs have been used to construct electrochemical and FRET probes as discussed throughout, their use as direct actuators for nanoscale devices remains relatively limited. In 2011, Strano and Yoon *et al.* combined GBP with single-walled carbon nanotubes to develop a novel glucose probe that exploits the NIR properties of SWNTs to achieve excellent tissue penetration and high sensitivity (Fig. 51a) (see earlier SWNT work in Section 3).[105] GBP was first heterologously expressed in *E. coli* and then covalently conjugated *via* amide bond formation to carboxylated poly(vinyl alcohol)-wrapped SWNTs (cPVA/SWNTs).

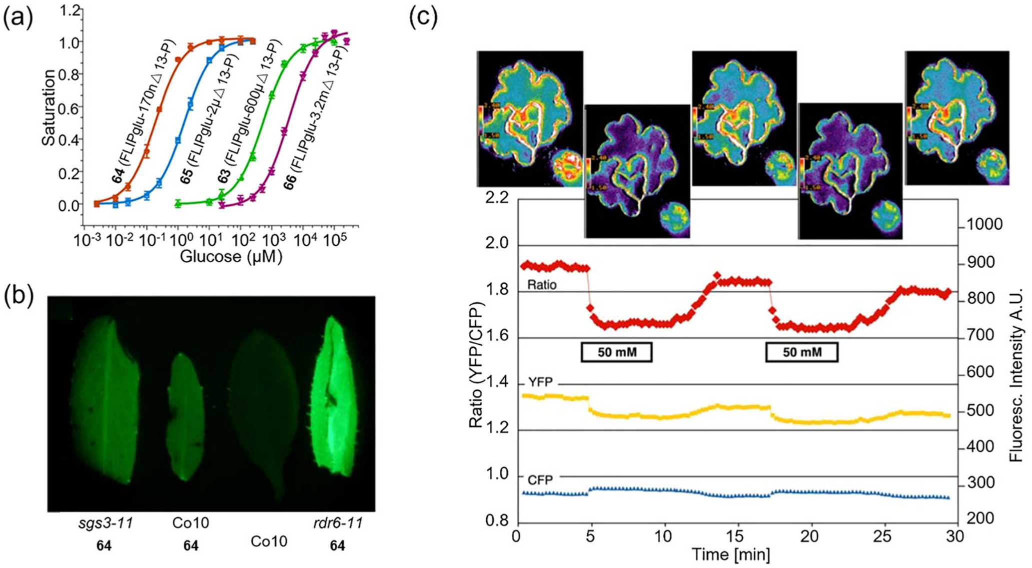

Fig. 49 (a) Glucose binding isotherms of **63–66**. (b) Representative fluorescent images of **64** in *Arabidopsis* wild type and silencing mutants. (c) Glucose-induced FRET changes of **63** in the cytosol of leaf epidermal cells. Adapted from ref. 103, published by Oxford Plant Cell.

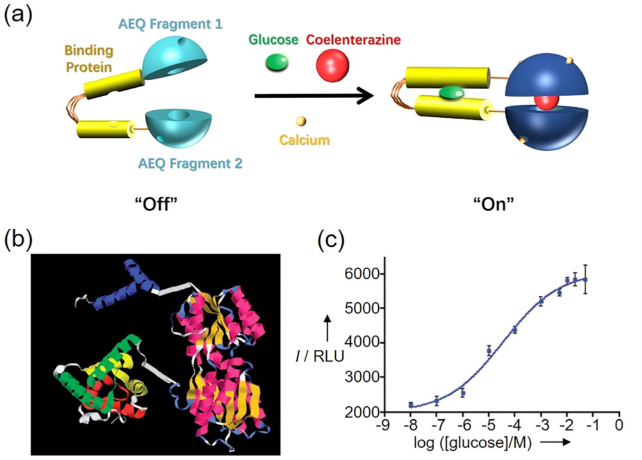

Fig. 50 (a) Schematic protein switch, illustrating the components and triggers responsible for transitioning from the "off" state to the "on" state. (b) Structure of **67** in solution. (c) Glucose response with intensity *I* in relative light units (RLU). Adapted with permission from ref. 104. Copyright (2008) Wiley-VCH Verlag GmbH & Co. KGaA, Weinheim.

The emission intensity of this probe **68** (GBP-PVA/SWNT) changed reversibly with different glucose concentrations (Fig. 51b and c), with a linear response below 10 mM, but a nonlinear behavior above 10 mM. The calculated equilibrium binding constant indicated that the complex was suitable for the detection of glucose in a physiological concentration range (2–30 mM). This new glucose probe **68** provides an innovative platform for the development of new probe types, building on prior enzymatic work, with potential applications in micro- and nanofluidic valves, and resonators, and is expected to be widely used in glucose monitoring in the biomedical field, in order to promote technological developments in related fields.

4.4. Frequency domain FLIM-based fluorescent protein probes

The intensity-based FRET fluorescence protein probes described above are well suited for real-time monitoring of intracellular glucose changes. They are not, however, suitable for continuous monitoring of glucose kinetics in living cells due to issues of photobleaching or crosstalk during repeated exposures of eCFP and eYFP. Addressing this in 2012, Jin *et al.* proposed a new approach using time-domain or frequency-domain fluorescence lifetime imaging microscopy (TD-FLIM/FD-FLIM).[106] FLIM changes in the FRET system are determined by measuring the donor fluorescence lifetime, which is independent of probe concentration, reflecting the chemical and physical properties of the local environment, relating to the energy transfer from the donor to the acceptor in FRET. This method is less susceptible to crosstalk between the donor and acceptor fluorophores. Whereas TD-FLIM is relatively slow for intracellular molecular dynamics visualization on a short timescale, FD-FLIM improves

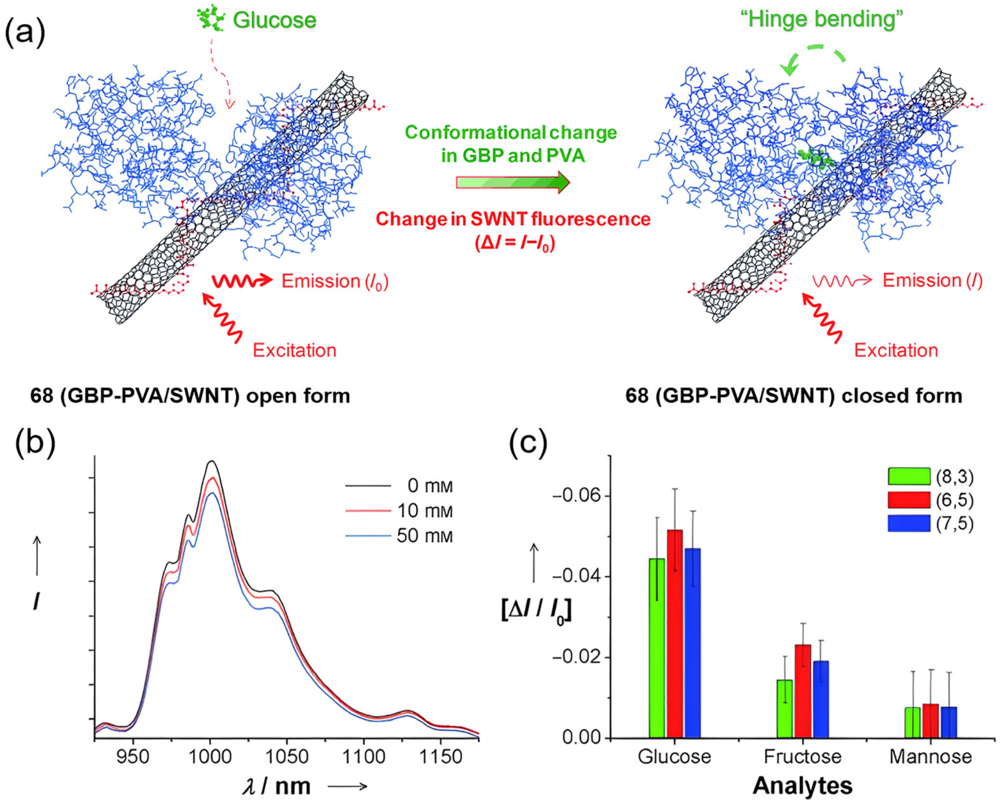

Fig. 51 (a) **68** for glucose recognition. (b) Fluorescence spectra of **68** before and after glucose addition (λ_{ex} = 785 nm). (c) Histogram illustrating the selectivity of **68** at 10 mM saccharide concentration. Adapted with permission from ref. 105. Copyright (2011) Wiley-VCH Verlag GmbH & Co. KGaA, Weinheim.

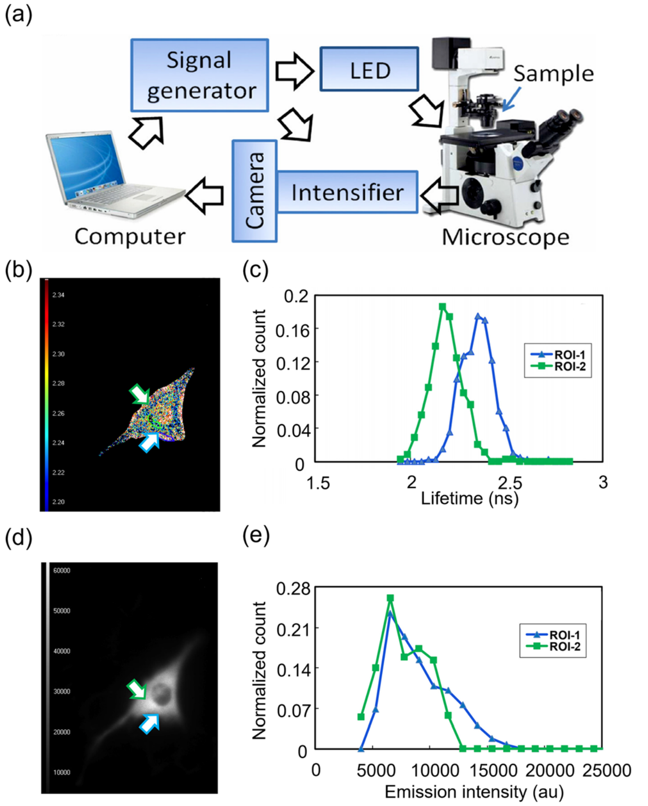

Fig. 52 (a) Workflow for FD-FLIM imaging. (b)–(e) FD-FLIM of glucose concentration gradients in the cytoplasm of C2C12 cells. (b) Pseudocolored lifetime map and (d) monochromatic intensity FRET image. Lifetime (c) and fluorescence intensity (e) of **69** were determined for two regions of interest in a single C2C12 cell. Adapted with permission from ref. 106. Copyright (2012) Sage Publications.

upon this by determining fluorescence lifetimes through measuring phase shifts and amplitude reductions in fluorescence (Fig. 52a). To minimize the impact of photobleaching on the probe's lifetime, the fluorescent proteins AcCFP1 and mCherry, known for their enhanced resistance to photobleaching, were selected and combined with GBP to design the fluorescent protein probe **69** (AcGFP1-GBPcys-mCherry). Jin and coworkers demonstrated that FD-FLIM can effectively monitor intracellular glucose concentrations and track changes in glucose dynamics with high spatial and temporal resolution in C2C12 cells. They showed high glucose concentrations were detected near the cell membrane, whilst low glucose concentrations were found near the nucleus (Fig. 52b and c), something FRET intensity imaging failed to achieve (Fig. 52d and e). Since FRET-FLIM is less affected by light scattering and the local concentration of probe proteins, it enables 3D imaging through rotating disk confocal microscopy. This can therefore enable continuous monitoring of intracellular glucose concentrations in animal models, providing a novel tool for studying the pathophysiology of diabetes.

4.5. Single fluorescent protein-based probes

Though functional, most FRET-based glucose probes exhibit relatively small fluorescence variations of only 10–70%, which limits their application in high-throughput screening and monitoring of subtle metabolic changes. Yang and Hu *et al.* therefore developed a series of ratiometric and highly responsive single fluorescent protein-based glucose probes in 2018.[107] To do this, they combined a circularly permuted yellow fluorescent protein (cpYFP) with a bacterial periplasmic glucose/galactose-binding protein (Fig. 53a and b), and developed mutants to optimize affinity. The result of this was four probes **70** (FGBP$_{27\,\mu M}$, original non-mutant), **71** (FGBP$_{380\,\mu M}$), **72** (FGBP$_{1\,mM}$), and **73** (FGBP$_{3.2\,mM}$) with measured K_d values of 27 μM, 380 μM, 1.0 mM, and 3.2 mM, respectively. Probe **72** exhibited a large dynamic range and was particularly useful for real-time tracking of subtle changes in cellular metabolism. The probe exhibited a roughly 700% fluorescence change *in vitro*, nearly 10 times greater than previously reported FRET-based probes, making it a highly responsive genetically-encoded probe. These probes were used to monitor glucose transport in living *E. coli.* cells (Fig. 53c and d). They found that the cells took up glucose within 10 min to maintain physiological glucose levels, and exhibited different glucose uptake profiles and metabolism between wild-types and Mlc knockouts. Compared with the first generation FRET-based fluorescent protein probes above, FGBP probes rely on only a single fluorescent protein and are intrinsically ratiometric, which allows for built-in normalization of fluorescence signals regardless of variations in indicator protein concentrations. These probes offer a specific, simple tool for glucose detection *in vitro* and provide a non-invasive approach for real-time monitoring of glucose metabolism *in vivo*.

In 2019 Kitaguchi and Mita *et al.* developed a series of glucose probes termed Green Glifons that can cover a wide range of glucose concentrations and applied them to multicolor imaging of living cells alongside Ca^{2+} probes to look at hierarchical relationships and interrelationships between glucose metabolism and Ca^{2+} signaling regulation.[108] Green Glifon probes are built around bacterial D-galactose-binding periplasmic protein (MglB, specific glucose/galactose binder) and Citrine GFP, bound by two leucine zipper peptides in the vicinity of its chromophore. Three probes (**74** Green Glifon50, **75** Green Glifon600, and **76** Green Glifon4000) were reported (EC$_{50}$s of 50, 600, and 4000 μM, respectively), producing a ~7-fold change in fluorescence intensity in response to glucose (Fig. 54a and b). These probes exhibited changes in fluorescence intensity corresponding to glucose concentration and were capable of detecting glucose in the range of 8.1 μM to 15 mM. Mechanistically, glucose binding leads to protonation/deprotonation of the chromophore, inducing the desired spectral change (decrease at *ca.* 400 nm, increase at *ca.* 500 nm) (Fig. 54c). The Green Glifon series was able to visualize glucose dynamics in various cellular compartments, including the cytoplasm, plasma membrane, nucleus, and mitochondria of living HeLa cells, and they were used *in vivo* to monitor glucose dynamics in the pharyngeal muscle of *C. elegans* and to measure blood glucose levels in mice. Furthermore, in MIN6 m9 β cells from mice, dual-color imaging of **76** and the Ca^{2+}-sensitive dye Rhod2 (Rhodamine 2) enabled the relationship

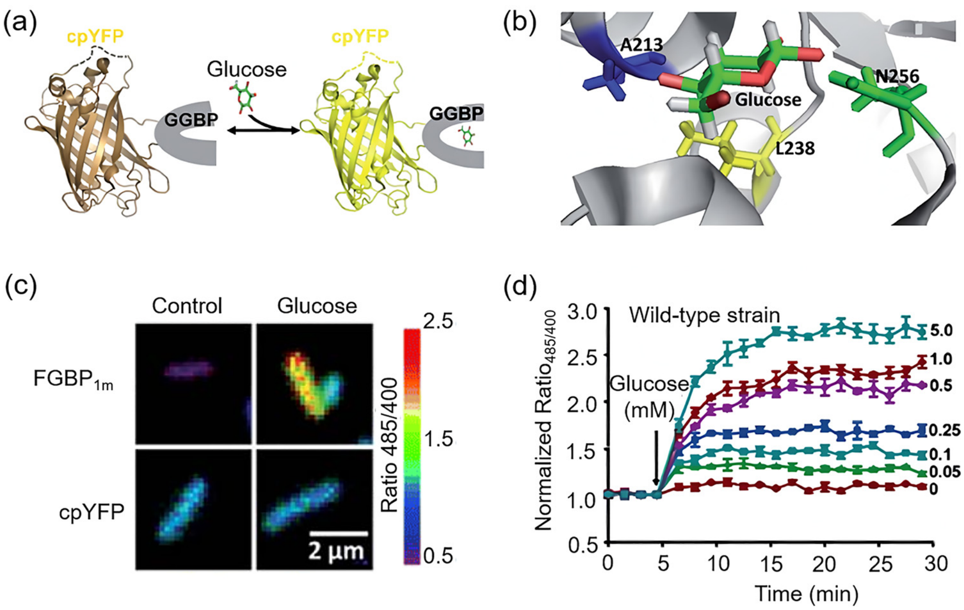

Fig. 53 (a) Structure and sensing mechanism of single fluorescent protein-based glucose probes. (b) Crystal structure of GGBP, highlighting the glucose-binding pocket. Three sites (A213, L238, and N256) for enhancing probe affinity are indicated. (c) Fluorescence images of **72** or cpYFP-expressing cells before and after incubation with 25 mM glucose. (d) Kinetics of **72** in *E. coli* JM109 (DE3) cells following glucose addition for 20 min. Adapted from ref. 107, published by Royal Society of Chemistry.

between glucose metabolism and Ca^{2+} dynamics to be monitored, providing a tool with high-spatiotemporal-resolution for studying the interaction between glucose and other molecules (Fig. 54d and e).

These approaches have led to a broadening of the field, with use of fluorescent protein glucose probes now widespread. In 2021, Looger and Keller *et al.* reported the single-wavelength probe 77 (iGlucoSnFR), for *in vivo* glucose imaging in multiple model organisms, including cells, larval flies, and zebrafish larvae.[109] The GBP from *T. thermophilus* was used as a scaffold, and circularly permuted green fluorescent protein (cpGFP) was inserted between residues 326 and 327. Binding site residues were mutated to reduce glucose affinity, affording 77 following screening. The probe exhibited a K_D of 2.3 mM and a fluorescence response ($\Delta F/F$) of 1.95 in PBS. A version fused with the red fluorescent protein mRuby2 was also developed for ratiometric measurements and cell typing, as well as a series of variants with affinities spanning four orders of magnitude (1 μM–10 mM). Fluorescence intensity imaging and time-domain fast Fourier-transform (FFT) imaging were performed on co-cultured rat astrocytes and neurons at the stimulation frequency, demonstrating glucose concentration changes (Fig. 55a and b). In this experiment, red fluorescence intensity correlated inversely with oscillation magnitude, illustrating the relative indifference of neurons towards glucose compared to astrocytes (Fig. 55c and d). Additionally, the probes were used for a range of applications such as characterization of glucose transporter function and inhibitor properties, discovering a potential glucose transport pathway in the fruit fly central nervous system (Fig. 55e and f), and tracking glucose transport in the muscles, liver, and brain of living larval zebrafish (Fig. 55g and h). Of particular interest were the effects of insulin and epinephrine on glucose metabolism. Zebrafish expressing 77 offer a tangible method for investigating mechanisms such as exercise-mediated glucose uptake in both muscle and liver, which is of significant medical relevance for addressing conditions such as obesity and diabetes.

In 2022, the range of colors available was expanded with the development of Red Glifons by Tsuboi and Mita *et al.*[110] These red glucose probes were designed by inserting the D-glucose/D-galactose binding domain from the bacterial D-galactose-binding periplasmic protein MglB near the chromophore of the red fluorescent protein mApple. As before, two linker peptides derived from the leucine zipper sequence were placed between mApple and the MglB domain, and then optimized through variant synthesis and screening, affording probe **78** (Red Glifon) capable of a three-fold F/F_0 change in the presence of 10 mM glucose. Subsequent mutation at F39 of MglB produced probes **79** (Red Glifon 300) and **80** (Red Glifon 3000), with different EC$_{50}$ values. Interestingly, they also discovered the mutant protein, **81** (Red Glifon nega), which does not respond to glucose and could therefore serve as a negative control for verifying and validating artifacts during time-lapse imaging (Fig. 56a). All three Red Glifon variants exhibited excitation peaks at 562 nm and emission peaks at 591 nm (Fig. 56b and c). When combined with green fluorescent indicators, Red Glifons enable the visualization of interactions between glucose and other metabolites, such as ATP, lactate, and pyruvate (Fig. 56d–g). Thus, these red glucose probes serve as a multi-color imaging toolkit for investigating complex interactions found in energy metabolism.

Fluorescent protein-based probes based on GBPs and their homologs (such as MglB) offer several distinct advantages

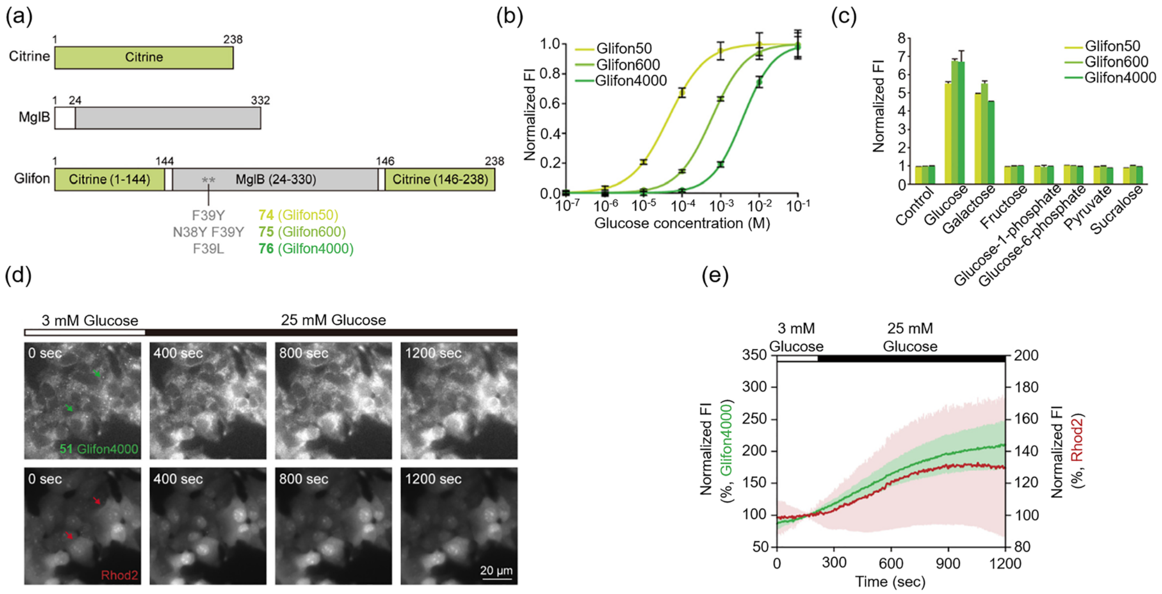

Fig. 54 (a) Domain structure for Citrine, MglB, and the Green Glifon series **74–76** (b) Dose–response plot of **74–76** (Green Gilfon-50, 600 and 4000) to glucose. (c) Specificity of Green Glifon series for glucose-related metabolites. (d) Sequential images of **76** expressing and Rhod2-loaded MIN6 m9 cells. (e) Time courses of fluorescence intensity (FI) of **76** green) and Rhod2 (red) in MIN6 m9 cells. Adapted with permission from ref. 108. Copyright (2019) American Chemical Society.

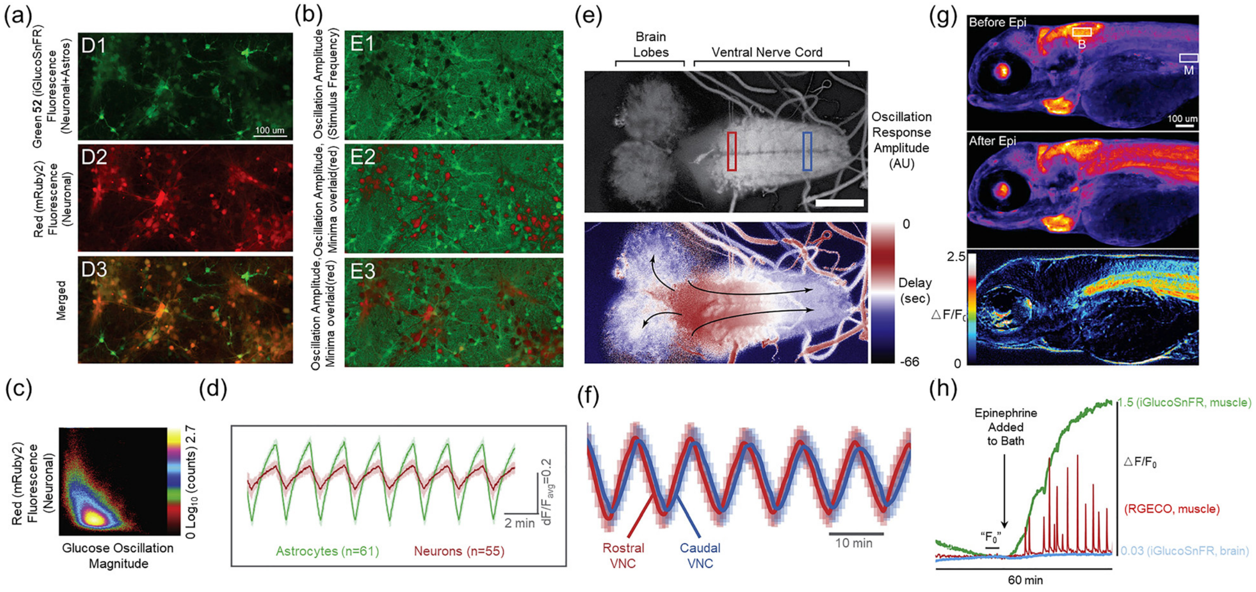

Fig. 55 Glucose imaging with **77** in multiple model organisms. (a)–(d) Cell culture. (a) Fluorescence images for each channel. (b) Pixelwise temporal FFT magnitudes at stimulus frequency, indicative of glucose concentration changes. (c) Correlation plot between FFT magnitude (*x* axis) and mRuby2 signal (*y* axis). (d) Averaged fluorescence responses ($\Delta F/F_{avg}$) to oscillating stimulus from astrocytes and neurons. (e) and (f) Intact larval fruit fly CNS explant. (e) FFT amplitudes of response (top). FFT phases/delays of response (bottom). (f) $\Delta F/F_{avg}$ traces from the ventral nerve cord. (g) and (h) Zebrafish muscle and brain *in vivo*. (g) Organism-scale responses of **77** to epinephrine addition. (h) Epinephrine-induced fluorescence changes. Adapted with permission from ref. 109. Copyright (2021) The Author(s).

(Table 3). Firstly, high specificity and targeting as they rely on the innate specific recognition of glucose to avoid interference from structural analogs. Their genetic encoding and live-cell compatibility are notable features, as they can be introduced into cells or organisms through genetic engineering for long-term stable expression, eliminating the need for external labeling. This makes them suitable for dynamic monitoring of live cells, tissues, and model organisms, including mice, zebrafish, and *Arabidopsis*, as we have seen. These probes also possess strong real-time dynamic monitoring capabilities. Their signal responses, which are typically based on FRET and conformational changes, are reversible, enabling the

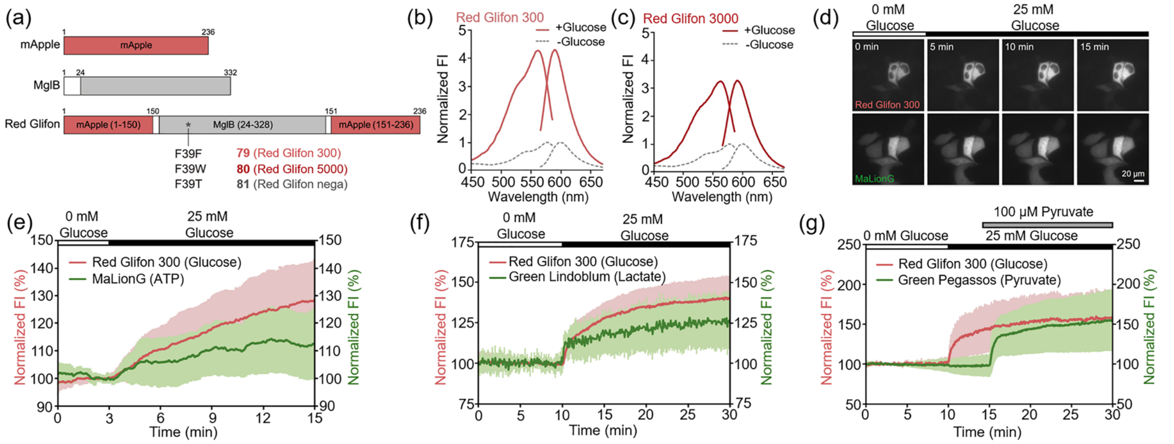

Fig. 56 (a) Domain structure for mApple, MglB, and resultant Red Glifon series **79**, **80**, and **81**. (b) and (c) Excitation and emission spectra of **79** (b) and **80** (c). (d) Sequential images of **79** and MaLionG co-expressed HeLa cells exposed to 0–25 mM glucose. The scale bar represents 20 μm. (e) Time course of fluorescence intensity (FI) of **79** and MaLionG co-expressing HeLa cells. (f) Time courses of FI of **79** and Green Lindoblum co-expressing HeLa cells. (g) Time course for the FI of **79** and Green Pegassos co-expressing HeLa cells. Adapted with permission from ref. 110. Copyright (2022) Elsevier Ltd.

tracking of rapid fluctuations in intracellular glucose. Additionally, they offer high spatiotemporal resolution; when combined with techniques like fluorescence lifetime imaging,[106] they can resolve subcellular glucose distribution, such as concentration gradients near the cell membrane and nucleus, overcoming the limitations of traditional intensity imaging. Their broad applicability is another key strength, as they have been successfully used in animal cells (*e.g.*, hepatocytes, neurons), plants (*e.g.*, *Arabidopsis* root cells), and microorganisms (*e.g.*, *E. coli*), providing a unified tool for cross-species glucose metabolism research. Moreover, they hold potential for multimolecular co-imaging: single fluorescent protein probes like Green Glifons[109] and Red Glifons[110] can be combined with other fluorescent probes (*e.g.*, calcium indicators, lactate probes) to reveal the role of glucose in related processes.

These probes are not without limitations of course, with for instance a limited dynamic range, or only a 10%–70% fluorescence signal change in early FRET probes. Insufficient affinity is another issue: the affinity of natural GBP (*e.g.*, 170 nM of **55**) is mismatched with physiological glucose concentrations (in the millimolar range), requiring complex mutation-based adjustments. Photostability and interference problems are also prevalent. FRET probes rely on dual fluorescent proteins such as CFP/YFP, which are susceptible to photobleaching and excitation crosstalk. Single fluorescent protein probes, on the other hand, may be disturbed by environmental pH. Species-specific limitations exist as well; mammalian-derived probes are prone to transgene silencing in plants like wild-type Arabidopsis, requiring expression in gene-silencing mutants. Finally, their tissue penetration is limited: visible light fluorescence (*e.g.*, green, yellow) scatters severely in deep tissues, hindering long-term imaging of deep organs such as the brain *in vivo*.

Some of the solutions to these drawbacks have been addressed already. To enhance the dynamic range of GBP-based probes, the development of single fluorescent protein probes, such as the FGBP series, has proven effective, with signal enhancement of up to 700%.[107] Optimizing affinity through site-directed mutagenesis, for example, *via* mutations at positions H66, L276, K312, and H348 in the thermophilic *Thermus thermophilus* GBP is also effective. This approach has for example enabled the generation of probe libraries (such as iGlucoSnFR variants) that cover a concentration range from 1 μM to 10 mM, making them suitable for different physiological environments (*e.g.*, intracellular, tissue and organismal levels).[109] Improving photostability and anti-interference capabilities can be achieved by using photobleaching-resistant fluorescent proteins like AcCFP1 and mCherry, combined with fluorescence lifetime imaging technology.[106] Quantification *via* fluorescence lifetime rather than intensity helps reduce interference from probe concentration and photobleaching. Addressing species-specific limitations can be accomplished by expressing probes in plant RNA-silencing mutants such as *sgs3* and *rdr6*,[103] or by developing plant-specific GBP homologs to avoid transgene silencing. Expanding tissue penetration involves developing near-infrared fluorescent protein probes, such as Red Glifons based on mApple,[110] or combining probes with nanomaterials like single-walled carbon nanotubes, leveraging their near-infrared emission properties for deep tissue imaging.[104]

5. Lectin-based probes

Building on enzyme and protein-based probes, this section will now consider systems built around the protein lectin, whose specific biological purpose is to bind carbohydrates. By virtue of their non-covalent glucose recognition mechanism, lectin-based probes are increasingly gaining popularity. A representative example is Concanavalin A (ConA), a lectin extracted from the jack-bean which contains four saccharide binding sites, binding glucose at 400 M^{-1}. Binding of ConA is typically used as the reference throughout lectin research. As ConA is non-reactive, merely binding glucose, it presents a range of benefits over GOx, in that it does not produce by-products, nor does it require O_2, with the added inherent feature of reversibility. This section will begin with an outline of ConA-based probes, highlighting their limitations (*e.g.*,

Table 3 Key properties of representative fluorescent protein-based probes

Probe	Fluorescent protein pair/component	Glucose dissociation constant (K_d)	$\lambda_{ex}/\lambda_{em}$	Biological applications
55	CFP/YFP-GGBP	0.17 μM	436/480, 535 nm	Glucose quantification, COS-7 cell glucose dynamics
56	CFP/YFP-GGBP mutant	0.59 mM	436/480, 535 nm	Multicellular glucose imaging, intracellular glucose homeostasis monitoring
57	eCFP/Citrine-eYFP-MglB	600 μM	433/485, 528 nm	HepG2 cell glucose flux analysis, GLUT function study
58	eCFP/Citrine-eYFP-MglB	583 ± 8.0 μM	433/485, 528 nm	High-throughput siRNA screening, glucose homeostasis monitoring
59	eCFP/Citrine-eYFP-MglB	600 ± 64 μM	433/485, 528 nm	Glucose sensing in multiple physiological buffers (*e.g.*, Hanks' balanced buffer), HepG2 cell metabolism assay
60	eCFP/Citrine-eYFP-MglB	660 ± 160 μM	433/485, 528 nm	High-sensitivity glucose detection, GLUT-related gene screening
61	eCFP/Citrine-eYFP-MglB	600 μM (*in vivo* $K_{0.5}$)	433/485, 528 nm	Pancreatic β-cell glucose-Ca^{2+} dynamic analysis; diabetes-related metabolic research
62	ECFP/EYFP-GGBP mutant	—	430/465, 520 nm	Non-invasive monitoring of intracellular glucose in CHO cell cultures
63	eCFP/eYFP-MglB	600 μM	433/485, 528 nm	Glucose flux analysis in Arabidopsis leaf epidermis/roots
64	eCFP/eYFP-MglB	170 nM	433/485, 528 nm	Detection of low glucose levels in Arabidopsis roots
65	eCFP/eYFP-MglB	2 μM	433/485, 528 nm	Glucose monitoring in Arabidopsis roots, leaf glucose flux studies
66	eCFP/eYFP-MglB	3.2 mM	433/485, 528 nm	High glucose range detection in Arabidopsis leaf epidermis
67	GBP-AEQ bioluminescent switch	—	—/469 nm (bioluminescent)	Sensitive glucose detection, clinical blood glucose monitoring
68	GBP-PVA/SWNT optical modulator	—	658, 785/973, 1001, 1041 nm	Physiological glucose sensing, near-infrared continuous monitoring
69	AcGFP1-GBPcys-mCherry	0.13 mM	485/525, 610 nm	Intracellular glucose dynamics monitoring; quantification of glucose uptake/clearance rates
70	cpYFP/GGBP fusion, non-mutant	27 μM	400, 485/528 nm	*In vitro* glucose detection, subtle metabolic change tracking
71	cpYFP/GGBP fusion, N256S mutant	380 μM	400, 485/528 nm	Physiological glucose range sensing
72	cpYFP/GGBP fusion, L238S mutant	1.0 mM	400, 485/528 nm	Real-time glucose monitoring in *E. coli*, wild-type *vs.* Mlc knockout cell metabolism comparison
73	cpYFP/GGBP fusion, A213R mutant	3.2 mM	400, 485/528 nm	Wide-range glucose detection, physiological glucose sensing
74	Citrine/MglB fusion, F39Y mutant	44 μM	460, 495/510–550 nm	Mouse blood glucose measurement, low-glucose range sensing
75	Citrine/MglB fusion, F39Y N40Y mutant	590 μM	460, 495/510–550 nm	HeLa cell organelle-specific glucose imaging (cytoplasm/nucleus/plasma membrane)
76	Citrine/MglB fusion, F39L mutant	3800 μM	460, 495/510–550 nm	*C. elegans* pharyngeal muscle glucose imaging, MIN6 m9 cell glucose-Ca^{2+} dual-color imaging
77	cpGFP/TtGBP fusion, L1-PA/L2-NP linker variant	7.7 mM	485/515 nm	Glucose imaging in muscle, brain, and liver of zebrafish larvae
78	mApple/MglB fusion, wild-type linker	—	562/591 nm	Intracellular glucose dynamics visualization in live cells, dual-color imaging compatibility
79	mApple/MglB fusion, F39F mutant	320 μM	562/591 nm	HeLa cell glucose flux monitoring, dual-color imaging with ATP/lactate/pyruvate indicators
80	mApple/MglB fusion, F39W mutant	3000 μM	562/591 nm	*C. elegans* pharyngeal muscle glucose imaging
81	Apple/MglB fusion, F39T mutant	—	562/591 nm	Artifact validation (temperature/osmolarity/cell movement) in glucose imaging experiments

low glucose sensitivity), before discussing opportunities for the development of biomimetic lectin-type probes suitable for imaging in biological systems.

5.1. Concanavalin A-based probes

In 1998, Ye developed an enzyme-based glucose biosensor **82** utilizing a ConA complex of glucose oxidase.[111] This GOx-ConA-based system was found to be suitable for incorporation into enzyme electrode systems. Ye found that enzyme electrodes prepared with the GOx-ConA complex maintained long-term stability at room temperature thanks to improved thermal stability over simple GOx systems, and were suitable for glucose sensing, with the response current remaining nearly constant over a 12-day period. In contrast, existing GOx electrodes exhibit poor stability, with a 10% reduction in response current after just 7 days, clearly demonstrating the leap forward on using GOx-ConA complexes.

Using a different approach, Schultz and Ballerstadt introduced a novel fluorescence affinity hollow fiber sensor **83** for continuous transdermal glucose monitoring in 2000 (Fig. 57),[112] employing a competitive binding mechanism between a mobile fluorophore-labeled ConA and glucose residues immobilized within Sephadex beads (polysaccharide dextran support). The beads are stained with Safranin O and Pararosanilin, whose absorption spectra overlap with the excitation wavelength (490 nm) of Alexa488-ConA. In the absence of glucose, this absorption quenches fluorescence by preventing the excitation of ConA bound within the beads. On addition of glucose, competition for the ConA binding sites occurs, displacing it from the bead, triggering an increase in fluorescence at 520 nm. This assembly exhibited a wide glucose detection range (0.15–100 mM), with the highest dynamic

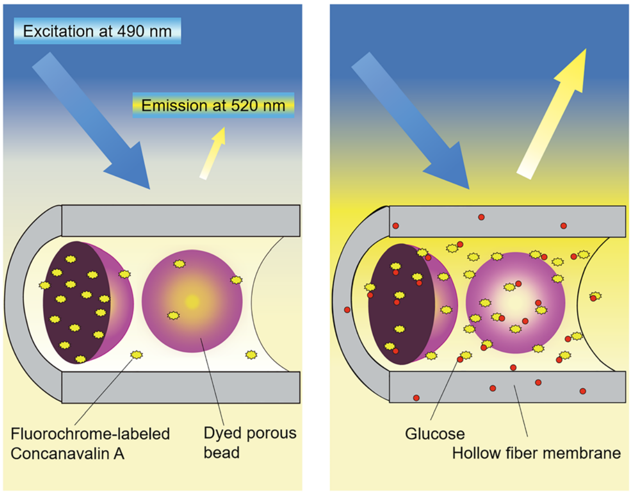

Fig. 57 Schematic illustration of the fluorescent affinity-based hollow fiber sensor **83** for glucose detection. Adapted with permission from ref. 112. Copyright (2000) American Chemical Society.

response occurring between 0.2 and 30 mM glucose (clinically relevant range). This further demonstrates the huge potential for the use of fluorescent ConA-based systems for *in situ* glucose measurements, including potential continuous monitoring applications, an increasingly important area of research.

In 2001, Birch and McCartney *et al.* described a serum glucose detection probe **84** based on NIR FRET-based fluorescence lifetime measurements using ConA labeled with allophycocyanin as the donor and malachite green-labelled dextran as the acceptor.[113] In this system, ConA and dextran are held together in the absence of glucose. However, on addition of glucose, competition occurs, resulting in a decrease in FRET efficiency. This change in FRET was monitored through time-correlated single-photon counting, which measures fluorescence lifetime. This approach was found to be effective for glucose concentrations ranging from 2.5 to 30 mM, offering yet another strategy for glucose sensing in the clinically relevant range.

In 2004, Frye and Ballerstadt *et al.* introduced a NIR fluorescence sensor **85** based on ConA conjugated with the fluorescent dye Alexa647$^{\text{TM}}$, bound to functionalized Sephadex beads (*vide supra*).[114] Which shifted the fluorescence emission of the sensor to the near-infrared range (670 nm). In the absence of glucose, only minimal fluorescence is observed thanks to absorbance of the excitation light by the beads. In the presence of glucose, competitive binding of ConA occurs, releasing the ConA-dye conjugate from the beads, sharply increasing the fluorescence intensity to enable the detection of glucose. Studies on the long-term stability of the sensor under simulated *in vivo* conditions indicated that this system could operate for over three months under continuous glucose cycling at 37 °C, clearly demonstrating the potential for clinical applications and continuous glucose monitoring.

In 2007, McNichols and Ballerstadt *et al.* introduced an affinity-based turbidity sensor **86** for glucose monitoring using optical coherence tomography (OCT) (Fig. 58), spawning a series of OCT-based ConA probes.[115] This sensor has ConA bound to macroporous hydrogel particles through glucose residues, with the entire system encapsulated in a glucose-permeable membrane, creating a high scattering coefficient. Introduction of glucose causes competitive binding, resulting in the release of ConA, and a decrease in the scattering coefficient of the sensor. OCT measures changes in the scattering coefficient, enabling precise glucose quantification. *In vitro* evaluation confirmed stability and reversibility, with good accuracy over a physiological glucose range of 2.5–20 mM. Unfortunately, storage at 37 °C for 100 days led to a decrease of 40–60% in turbidity response of the sensor. Response times were found to be variable across different sensor configurations. Their disk-shaped sensors had a response time of 23 min, while the hollow-fiber-based sensor had a response time of less than 5 min, demonstrating the viability of this type of affinity-based turbidity sensor for sensitive and rapid glucose detection.

Building on MchNicholls *et al.*'s 2007 work,[115] in 2013, Larin and Wang *et al.* developed an implantable probe **87** for continuous glucose monitoring based on optical coherence tomography (Fig. 59).[116] This method employs a competitive binding mechanism where glucose dynamically displaces dextran-coated microparticles from ConA immobilized on a gold mirror surface, with the resulting variation in microparticle density on the surface tracked by OCT. Specifically, ConA is immobilized on a gold mirror, and its reversible interaction with glucose influences the density of dextran-labeled microparticles, which leads to detectable changes in the reflected OCT signals. This work exhibits exceptional sensitivity in detecting individual microparticles, with a signal change of 2.9% ± 0.5%, confirming its applicability in both clear media and subcutaneous tissue. Using OCT, the probe successfully monitored the dynamics of microparticles in subdermal regions at a depth of 0.7–1.0 mm under the skin of mouse ears. This research presents a promising approach for developing highly sensitive, enzyme-free implantable glucose sensors and underscores its potential for clinical applications in diabetes management.

Finding another avenue for the development of his 2007 work,[115] in 2014 Ballerstadt *et al.* developed a label-free fiber-optic turbidity affinity probe **88** for continuous glucose monitoring, this time employing light scattering changes induced by glucose.[117] This sensor employs a semipermeable hollow fiber to encapsulate dextran microparticles and ConA, diffusing glucose then competitively binds ConA, altering the turbidity of the suspension. Moving away from the OCT method used previously, here the intensity of light was used, which was proportional to glucose concentration. A strong response was observed over a 50–400 mg dL^{-1} range (approx. 3–22 mM), with a response time of approximately 4 min, with stable operation for up to 8 days at 37 °C. Accuracy was comparable to commercially available devices, and this system benefits from a straightforward design, large signal amplitude, and does not require complex optical components, making it a promising candidate for miniaturized, implantable glucose monitoring devices.

One of the obvious and most popular applications of these types of sensors is of course in the management of diabetes, as demonstrated by the recent rise in commercial continuous

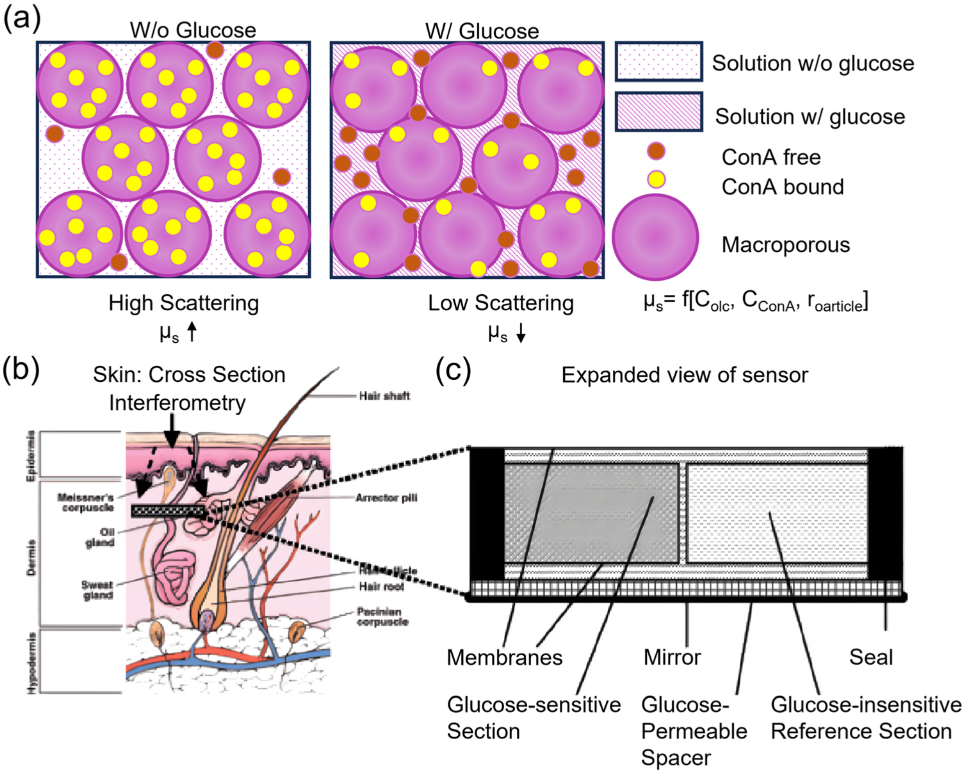

Fig. 58 (a) Schematic illustration of turbidity change in response to glucose for an affinity-based turbidity sensor **86**. (b) Schematic representation of the sensor implanted in the dermis. (c) Component diagram of the affinity-based turbidity sensor. Adapted with permission from ref. 115. Copyright (2007) American Chemical Society.

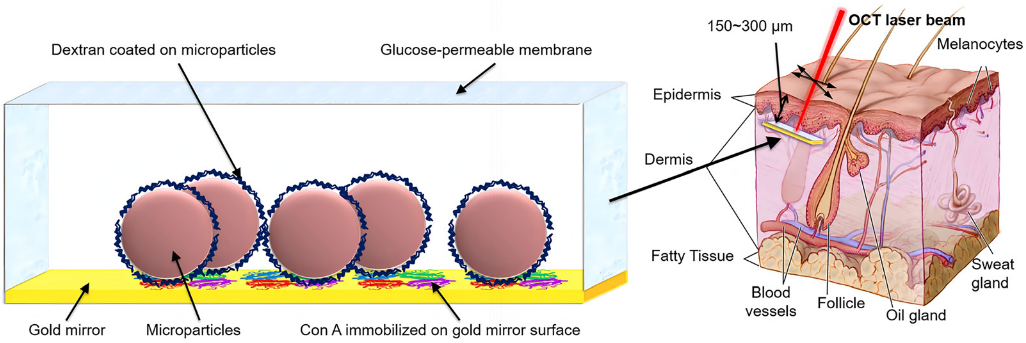

Fig. 59 Schematic representation of the optical coherence tomography-based probe design (left) and its implantation site (right). Adapted with permission from ref. 116. Copyright (2013) IEEE.

glucose monitoring systems. Building on the *in vitro* work above in 2007, McNichols and Ballerstadt developed an implantable, fiber-coupled fluorescence affinity sensor (FAS) **89** for glucose detection in hairless rats and pigs (Fig. 60a–c).[118] FAS **89** utilizes a fluorescence-based system for glucose detection, with ConA serving as the glucose-binding agent, glucose competing with dextran for ConA to modulate fluorescence intensity. During *in vivo* experiments, the FAS **89** exhibited excellent performance, reaching equilibrium within 60 min after implantation, and exhibiting a rapid response time of less than 5 min. The correlation coefficients between the sensor's output and known blood glucose changes ranged from 0.88 to 0.94, indicating a high degree of reliability in tracking glucose changes. In long-term experiments, FAS **89** demonstrated good stability, with correlation coefficients stable in an acceptable range during the 3-day monitoring period. This approach was then explored by the McNichols group in 2012,[119] with a clinical trial of 12 diabetic patients (2 with type 1 and 10 with type 2) involving subcutaneous implantation of the sensor **90** in the abdomen (Fig. 60d and e). The sensor **90** was connected to a fluorescence monitor *via* optical fibers. A correlation coefficient of 0.84 was measured between the FAS **90** measurements and blood glucose levels, with 97% of the data points falling within clinically acceptable zones on the Clarke error grid. The average warm-up time for the sensor

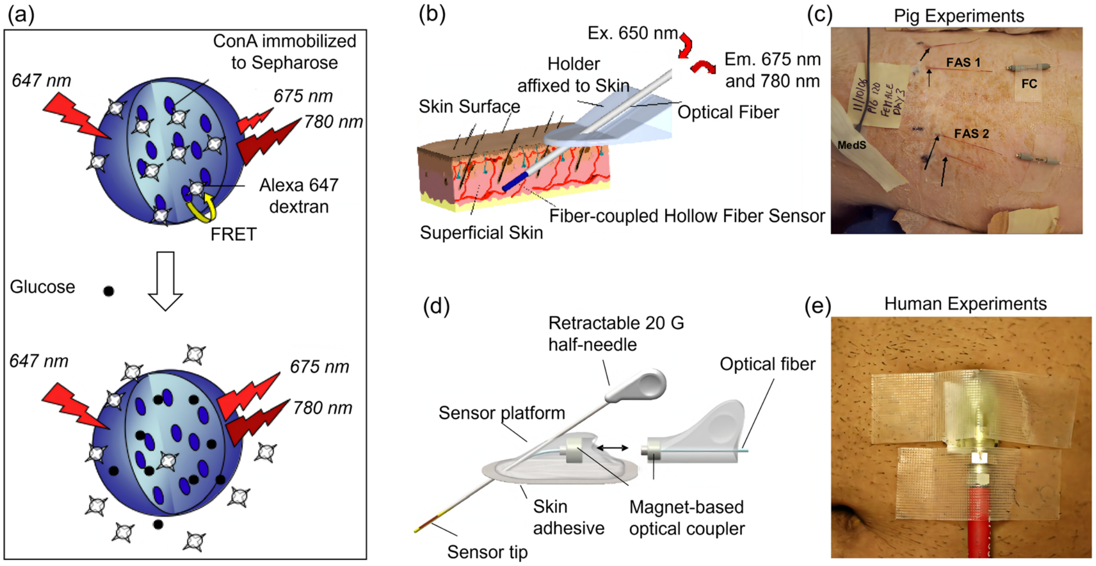

Fig. 60 (a) Fluorescence sensing mechanism of the fiber-coupled fluorescence affinity sensor (FAS) **89** for glucose. (b) Illustration of the FAS **89** for the interstitial glucose detection in skin tissue. (c) Photo of the FAS **89** implantation site in a pig after 3 days. (d) Schematic illustration of the second-generation lectin-based fluorescence affinity sensor **90**. (e) Image of the FAS **90** implanted in the abdomen for glucose sensing. Panel a–c: Adapted with permission from ref. 118. Copyright (2007) Sage Publications. Panel d and e: Adapted with permission from ref. 119. Copyright (2012) Sage Publications.

was 65 min, and it exhibited a response delay of 4 min, with comparable results to the earlier work by FAS **89** in rats and pigs, which showed an equilibration time of 60 min and a response time of less than 5 minutes. Optical signals remained stable throughout measurement and were not influenced by external light sources. Insertion and removal of the sensor reportedly caused minimal discomfort, with only minor bleeding observed, ensuring a good safety profile. This study affirmed the accuracy and safety of the FAS **90**, emphasizing its potential application in continuous glucose detection for monitoring diabetes. This work supports the clinical potential of fiber-coupled FAS technology as an effective and reliable glucose monitoring platform for short-term applications.

In 2008, Yu and Tang *et al.* developed an innovative quantum-dot-based nanobiosensor **91**, QDs-AuNPs, for the direct detection of glucose in serum based on the principle of FRET (Fig. 61).[120] This sensor is composed of quantum dots conjugated to ConA and gold nanoparticles functionalized with thiolated β-cyclodextrins (β-CDs). Upon specific binding between ConA-conjugated QDs and thiolated β-CDs-modified AuNPs, the QD fluorescence is quenched by the AuNPs through FRET. When glucose is present, it competes with β-CDs for ConA binding which leads to the displacement of the AuNPs-β-CDs complex and restoration of fluorescence. Fluorescence recovery is directly proportional to glucose concentration, with a detection range of 0.10–50 μM and a remarkably low detection limit of 50 nM. Notably, this sensor **91** showed high selectivity for glucose, readily distinguishing it from other sugars and serum biomolecules. Under optimized experimental conditions, the biosensor exhibited excellent recovery rates and precision when applied to the detection of glucose in human serum samples.

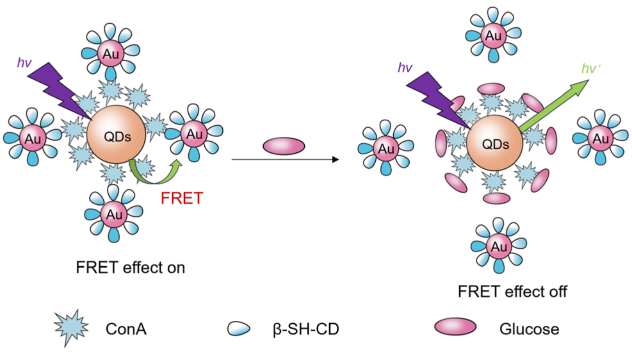

Fig. 61 Structure and sensing mechanism of the nanobiosensor **91** for the detection of glucose. Adapted with permission from ref. 120. Copyright (2008) Wiley-VCH Verlag GmbH & Co. KGaA, Weinheim.

In 2010, Battaglini and Pallarola *et al.* introduced a novel functionalized redox-active complex **92** of ConA and Os(II), immobilized onto gold electrodes through carbohydrate-lectin interactions (*via* mannose).[121] GOx is then bound to these complexes, allowing eventual glucose detection by GOx to create a current of electrons that passes through the Os(II) complexes before being transferred to the electrode, producing a glucose-dependent current (Fig. 62). This interesting design leads to a mixed GOx/lectin probe, spanning several approaches discussed throughout this review. Rather than employing ConA to detect glucose, ConA serves as a linker/modifier, with its carbohydrate-binding properties used exclusively to bind the sensing system to the electrode to enable current production.

In 2011, Coté and Cummin *et al.* developed a novel glucose sensing system **93** based on ConA and glycodendrimers encapsulated in microporated PEG microspheres (Fig. 63).[122] Through

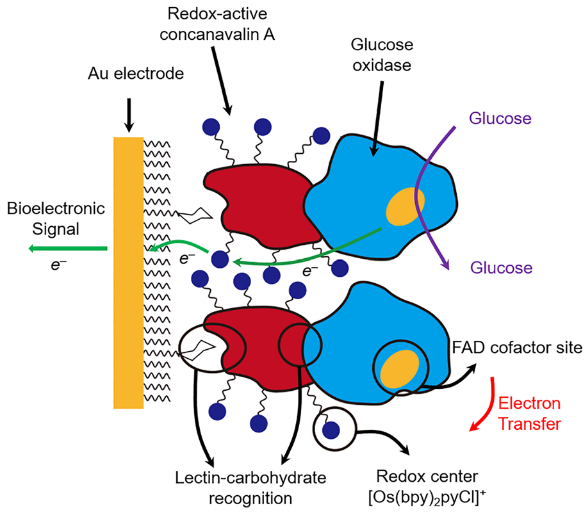

Fig. 62 Schematic illustration of the glucose-responsive interfacial supramolecular bioconjugate **92** based on redox-active ConA and GOx. Adapted with permission from ref. 121. Copyright (2010) American Chemical Society.

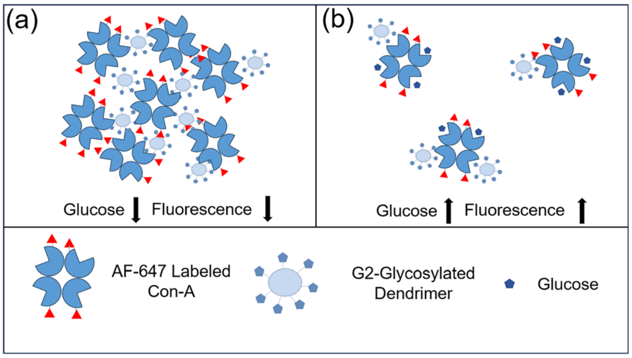

Fig. 63 Schematic illustration of the aggregative nature used in the ConA/dendrimer system **93** for glucose sensing at low (a) and high (b) glucose concentrations.

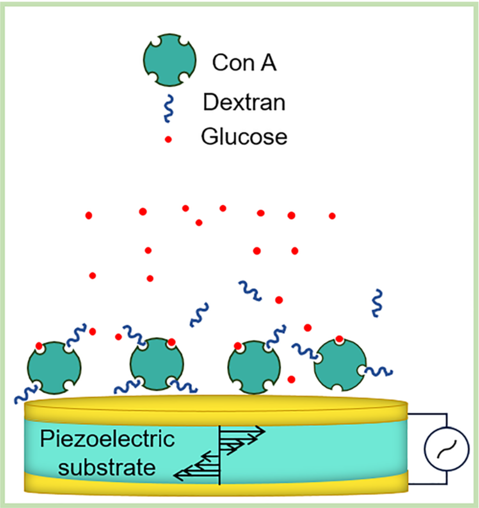

Fig. 64 Schematic illustration of the gravimetric glucose biosensor **95** based on the ConA-dextran affinity assay.

an innovative microporation technique, assay-filled pores (fluid-filled microsphere pores within the hydrogel) were created, containing the sensing assay, which allows glucose to diffuse into the interior pockets while effectively preventing the leakage of the encapsulated sensing components. The crosslinked PEG hydrogel used in the system ensures both biocompatibility and structural stability, making it suitable for potential subcutaneous implantation. As in previous examples, competitive binding is employed, with ConA and glycodendrimers forming aggregates that are disrupted on the addition of glucose. This sensor demonstrated a sensitive fluorescence response over a 3–11 mM glucose range, with a sensitivity of 1.3% fluorescence change per 10 mg dL^{-1} (0.555 mM) glucose.

In 2011, Chen and Tang *et al.* developed a quartz crystal microbalance (QCM, measures minute mass variations) probe **94** for sensitive glucose sensing using the usual glucose/dextran displacement approach.[123] The probe **94** was composed of a phenoxy-derived dextran (DexP) on a graphene-coated QCM, with ConA bound to the dextran. Again, using the principle of competitive binding, glucose displaces the ConA, leading to a change in the QCM frequency. Under optimal conditions, the frequency change relative to the basic resonant frequency was proportional to glucose concentrations, exhibiting a linear response in the range of 0.01–7.5 mM, with a detection limit of 5 μM. Compared to other enzyme-based and enzyme-free glucose sensors, this sensor **94** achieved signal amplification and sensitive detection through the high surface area of graphene and the macromolecular displacement effect of ConA, achieving reliable measurements at remarkably low concentrations.

In 2021, Johannessen and Hoang *et al.* developed another QCM-based gravimetric glucose biosensor **95** which amplifies the glucose signal through competitive binding of ConA with dextran (Fig. 64).[124] This sensor **95** utilizes thiol-immobilized ConA on a gold-coated QCM electrode to measure glucose concentration by measuring mass changes. A detection range of 2–40 mM was reported, with a minimum resolution of ±0.4 mM, exhibiting particularly high sensitivity at concentrations below 10 mM.

In 2013, Wu and Hsieh *et al.* developed another gravimetric probe **96**, this time a label-free approach using cantilever sensor technology, which leverages gravimetric detection principles to achieve highly sensitive and specific glucose measurement (Fig. 65).[125] The cantilever was chemically modified with aminopropylsilatrane and functionalized with ConA, therefore in the presence of glucose a measurable shift in the cantilever's resonance frequency was achieved, allowing for the quantification of glucose concentrations. This sensor exhibited high specificity, effectively distinguishing glucose from structural isomers such as galactose. This study underscores the potential of cantilever technology as a high-sensitivity glucose detection tool, offering a stable and enzyme-free platform for blood glucose monitoring in diabetes management.

In 2011, Ryser and Boss *et al.* introduced a viscosity-dependent affinity sensor **97** designed for continuous glucose monitoring in biological fluids (Fig. 66).[126] Fundamentally, this

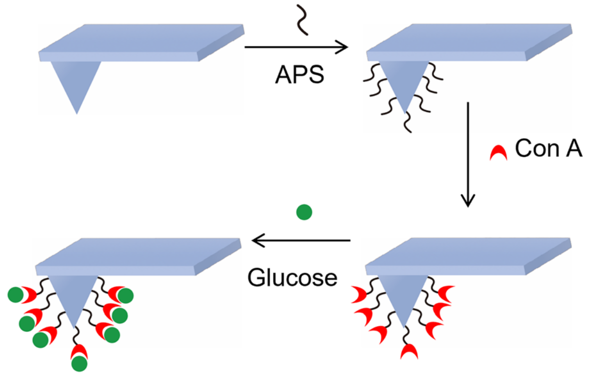

Fig. 65 Schematic illustration of the probe **96** based on gravimetric detection principles for label-free glucose sensing.

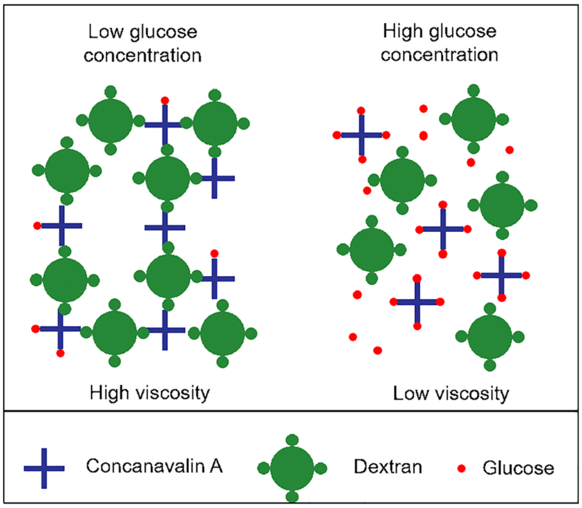

Fig. 66 Schematic illustration of the viscosity-dependent affinity sensor **97** for glucose sensing: competitive binding of glucose and dextran on ConA under low and high glucose concentrations. Adapted with permission from ref. 126. Copyright (2011) Elsevier B.V.

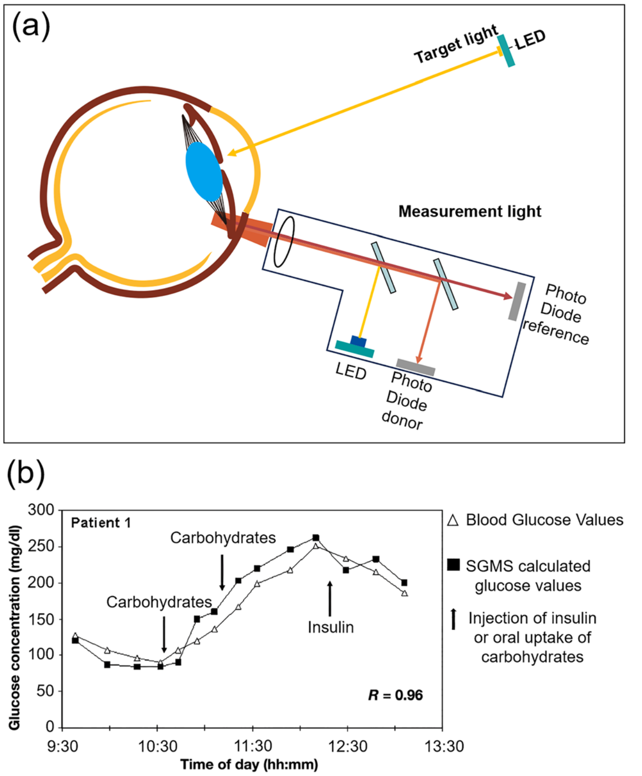

Fig. 67 (a) Schematic illustration of the implantable subconjunctival glucose monitoring probe **98**. (b) *In vivo* performance of the ocular mini implant in human eyes after implantation. *R* represents the correlation coefficient between blood glucose concentration and detection signal. Adapted with permission from ref. 127. Copyright (2012) Sage Publications.

remains a competitive binding system, exploiting the disruption of ConA-dextran binding by glucose. In this instance, disruption of the network releases ConA and dextran into solution, decreasing the viscosity of the medium. The researchers demonstrated that this sensing system exhibited excellent sensitivity within the physiological glucose range (2–20 mM), and in particular in the hypoglycemic range (2–4 mM), with an accuracy of ±1.7%. Additionally, this sensor featured good reversibility and stability over a period of up to 3 days.

In 2012, Herbrechtsmeier and Müller *et al.* developed an implantable subconjunctival glucose monitoring probe **98** (Fig. 67),[127] comprising of an ocular mini implant and a hand-held fluorescence photometer for data collection. The probe **98** utilizes a ConA displacement and FRET mechanism of the types seen throughout this section and is integrated into a nelfilcon polymer hydrogel disk (same material as contact lenses). This probe was evaluated in a clinical trial with five patients over two weeks, yielding promising results: where it demonstrated a strong correlation with blood glucose fluctuations (correlation coefficient >0.88 against a commercial GOx sensor), consistent performance for up to two weeks was observed, with a delay of 5–10 min, with 98% of readings within clinically acceptable limits. Additionally, the probe is reportedly straightforward to implant, well-tolerated by patients, and provides non-invasive readings. By its nature, it is oxygen and cofactor-independent and the reversible binding, making it a promising, minimally invasive, and stable option for continuous glucose monitoring in diabetes management.

In 2014, Wang and Song *et al.* developed a pH-switchable electrochemical probe **99** based on chitosan-reduced graphene oxide (CS-rGO) and ConA for the simultaneous measurement of both glucose and urea (Fig. 68).[128] This probe **99** leverages the large specific surface area of CS-rGO to immobilize a large concentration of ConA, whose surface net charge varies with pH, thus exhibiting a pH-dependent response to $Fe(CN)_6^{3-}$. At low pH, positively charged ConA interacts with $Fe(CN)_6^{3-}$, whereas at high pH, the now negatively charged ConA does not. Addition of GOx or urease adjusts the pH of the solution enzymatically and enables the detection of glucose and urea. Experimental results exhibit good linear response to glucose concentrations ranging from 1.0–10.0 mM and urea concentrations from 1.0–7.0 mM, with accuracy validated in serum and urine samples. Compared to conventional methods, this probe offers advantages

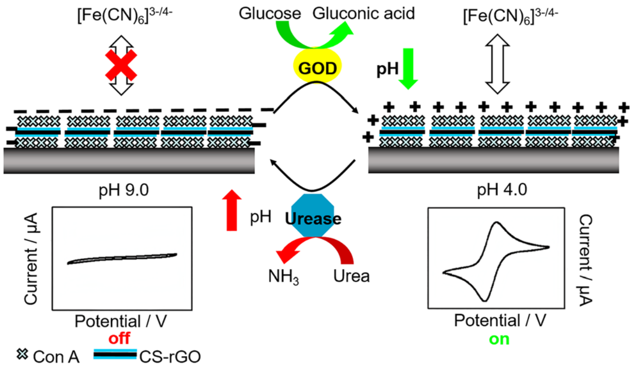

Fig. 68 Schematic illustration of the pH-switchable electrochemical probe **99** based on CS-rGO and ConA for glucose sensing. Adapted with permission from ref. 128. Copyright (2014) American Chemical Society.

such as simple sample preparation, high selectivity, and excellent reproducibility, thereby offering a novel approach for the design of probes for electrochemically inactive species.

In 2014, Pachpinde and Peng reported a longitudinal plasmon resonance sensor **100** based on gold nanorods and ConA (Fig. 69).[129] Gold nanorods were modified using dextran sulfate, adjusting the refractive index, which was then used to bind the ConA. ConA-binding promotes aggregation of the nanorods, producing a red shift in the longitudinal plasmon resonance wavelength from 701 nm to 718 nm. Therefore, on addition of glucose, competitive binding causes the nanorods to disperse, causing a blue shift in the UV-Vis (ultraviolet-visible) wavelength, from 718 nm back to 714 nm (a small but measurable change). Thus, glucose concentrations could be accurately detected within the range of 1 to 30 mM by monitoring the wavelength shift, adding to the myriad uses of gold nanorods and nanoparticles, some of which have been illustrated throughout this review already.

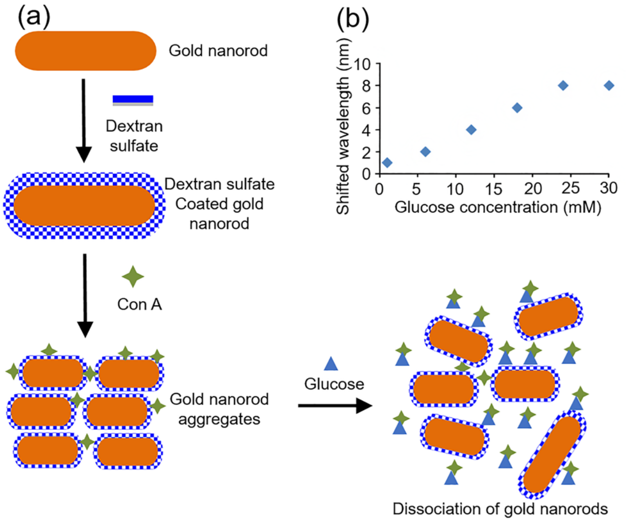

Fig. 69 (a) Schematic illustration of the longitudinal plasmon resonance sensor **100** based on gold nanorods and ConA for glucose sensing. (b) Longitudinal plasmonic peak shift of the sensor as a function of glucose concentration. Adapted from ref. 129, published by SAGE Publications Ltd under CC-BY 3.0.

In 2015, Coté and Locke *et al.* developed a ConA-based competitive binding probe **101** for long-term glucose detection.[130] To improve its thermal stability *in vivo*, ConA was modified with polyethylene glycol, and a fluorescently labeled mannotetraose was employed as a competing ligand. Concentration-dependent binding of glucose can therefore be monitored through fluorescence changes, thanks to competitive mannotetraose/glucose binding. This method exhibited a strong linear response to glucose concentration ranging from 0 to 400 mg dL^{-1} (up to 22 mM), and maintained stability for 30 days at 37 °C, although the mean absolute relative difference increased slightly from 6.13% to 7.6%. This probe demonstrated both high sensitivity and long-term stability (thanks to PEG-ylation), offering significant potential for the development of implantable probes for continuous glucose detection *in vivo*, although the lack of commercial mannotetraose does present a challenge to potential adoption more widely.

In 2015, Wei and Fan *et al.* developed a novel non-enzymatic electrochemiluminescence glucose sensor **102**, based on the competitive binding of glucose and phenoxy dextran with ConA.[131] The sensor **102** employs a hybrid of graphitic carbon nitride and 3,4,9,10-perylenetetracarboxylic acid as the probe, immobilized on a glassy carbon electrode. ConA is then attached to the electrode through interactions with DexP. On exposure to glucose, competitive binding displaces ConA, reducing hindrance to electron transfer at the interface, to produce an enhanced electrochemiluminescent signal. Results indicated that the sensor exhibited a strong linear response to glucose concentrations ranging from 1.0×10^{-10} M to 5.2×10^{-10} M (0.1–0.52 nM), although relative errors up to approximately 30% were seen in blood serum samples.

Glucose detection in tears offers a promising non-invasive approach for monitoring blood glucose levels. In 2017, Zhang and Chen *et al.* developed a nanostructured ConA sensor **103** based on the FRET quenching mechanism for the rapid and non-invasive detection of glucose concentrations in tear fluid (Fig. 70).[132] The sensor **103** employs quantum dots (CdSe/ZnS) as the donor and malachite green-labeled dextran (MG-dextran) as the acceptor, where the fluorescence signal recovered upon glucose binding to ConA. This sensor is assembled on a ZnO nanorod array deposited on a silicone hydrogel, allowing glucose detection within a concentration range of 0.03–3 mM, which covers the typical tear glucose levels in both healthy and diabetic individuals. Experimental validation indicated that the sensor provides detection within 30 s, with results correlating well with measured blood glucose concentrations. Furthermore, the sensor **103** exhibited high sensitivity, good selectivity, and excellent reliability, offering a valuable new approach for the advancement of highly non-invasive glucose monitoring devices.

With rapid advancements in 3D printing technology and its applications in biomedicine, its integration into glucose sensing has emerged as a promising research direction. In 2023, Thielemann and Krstić *et al.* developed a 3D-printed fluorescent glucose sensor **104** specifically engineered for continuous glucose monitoring in cell cultures (Fig. 71).[133] The sensor's architecture

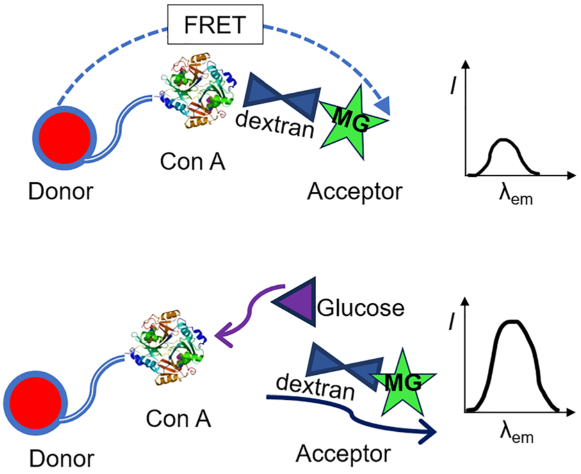

Fig. 70 Schematic illustration of the FRET sensor **103** consisting of ConA-conjugated quantum dots (donor) and malachite green (acceptor) for glucose sensing. Adapted with permission from ref. 132. Copyright (2017) Elsevier B.V.

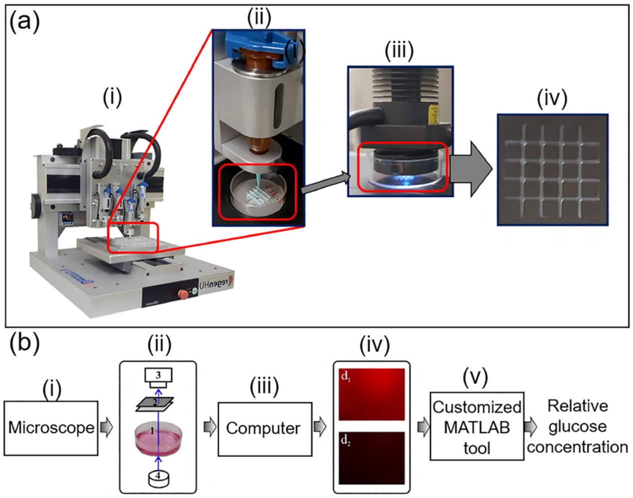

Fig. 71 (a) Printing workflow for FRET-based 3D-printed glucose: (i) bioprinter, (ii) printing of sensor ink onto plasma-treated Petri dish, (iii) UV curing, and (iv) printed structure. (b) Schematic illustration of glucose detection in cell culture medium based on the FRET-based sensor **104**: (i) fluorescence microscope, (ii) glucose detection system, (iii) computer/software; (iv) glucose imaging, (v) image analysis using MATLAB. Adapted with permission from ref. 133. Copyright (2023) Elsevier B.V.

features a UV-curable polyvinyl alcohol (PVA) hydrogel as the primary matrix, with its rheological properties optimized by tuning PVA solid content (37.0 wt% in the optimal formulation) to enable extrusion-based printing of stable, customizable 3D structures (*e.g.*, grids, pillars). Within this PVA matrix, alginate microspheres encapsulate the sensing core: fluorescently labeled ConA (acceptor fluorophore) and dextran (donor fluorophore), which operate *via* a FRET-based competitive binding mechanism. In the absence of glucose, ConA and dextran form a complex that quenches donor fluorescence, while glucose displacement of dextran increases the fluorophore distance, restoring fluorescence intensity in a linear manner (0–2 g L^{-1}, 11.1 mM). In HEK cell experiments, the sensor **104** not only tracked glucose depletion driven by cellular metabolism over 10 days but also maintained excellent biocompatibility. This work addresses the unmet need for miniaturized continuous glucose sensors tailored to complex 3D cell models, laying a foundation for their integration into tissue engineering platforms and expanding the utility of 3D-printed biosensors in preclinical drug screening and regenerative medicine.

In 2023, Huth and Pfützner *et al.* developed an osmotic pressure-based sensor **105** for continuous intraperitoneal and subcutaneous glucose monitoring, which adopts a ConA/dextran system as the core glucose-sensing chemistry.[134] The sensor **105** achieves glucose detection by relying on osmotic pressure variations. Its sealed chamber contains an active fluid composed of glucose-binding molecules (GBM, *e.g.*, ConA) and glucose-like ligands (GL, *e.g.*, dextran). In a glucose-free environment, GBM and GL form stable complexes *via* specific interactions (Fig. 72a). When glucose penetrates the chamber through a semipermeable membrane, it displaces GL from GBM-binding sites due to its stronger binding affinity for GBM, thereby elevating the internal osmotic pressure. Conversely, when external glucose concentration decreases, glucose dissociates from GBM, allowing GBM and GL to reassociate leading to a decline in osmotic pressure. Traditional osmotic pressure-based glucose sensors were plagued by size issues, and failed to meet clinical implantation requirements. To tackle this challenge, the research team replaced the conventional piezoresistive pressure transducers with nano-granular tunneling resistive pressure sensors (sized at 4000 × 400 × 150 nm^3) fabricated *via* focused electron beam-induced deposition technology (Fig. 72b). By leveraging this nanotechnology, precise structural control of the sensor **105** was achieved, reducing the core chamber volume from 70 μL to 750 nL (a reduction of over 95%). Results of dynamic glucose testing showed that under dynamic glucose concentrations ranging from 0 to 300 mg dL^{-1}, the miniaturized sensor generated a stable osmotic pressure variation of 40–50 mBar. Moreover, its output signal exhibited a linear relationship with glucose concentration, which fully met the clinical performance requirements for continuous glucose monitoring devices (Fig. 72c and d).

5.2. Synthetic lectin biomimetic probes

The body of work detailed above clearly highlights community interest in developing lectin-based (*i.e.*, ConA) probes for glucose detection, utilizing the entire range of sensing technologies at its disposal, and often coupling ConA with existing FRET or GOx approaches. Alongside this work, many groups have worked to chemically replicate lectin/ConA activity through biomimetic probes, starting in 1988 with the seminal work of Ogoshi and Aoyama *et al.* (Fig. 73).[135] This work investigated the host–guest interactions of functionalized resorcinol oligomer **106** and various polar substrates, including glycerol, D-glucose, D-ribose, riboflavin (vitamin B_2), vitamin B_{12}, and hemin. They found that **106** had different extraction abilities for different substrates, for instance extracting D-ribose more effectively than D-glucose.

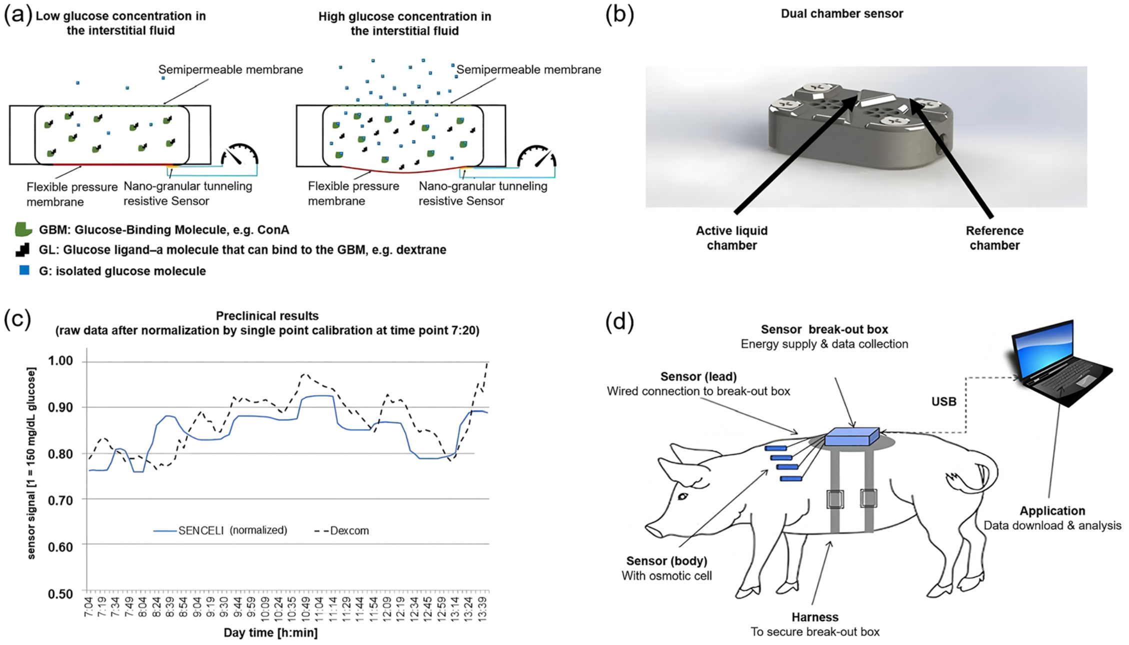

Fig. 72 (a) Schematic diagram of the osmotic pressure-based glucose sensor **105** demonstrating detection states under low and high glucose levels within interstitial fluid. (b) Sketch of the dual chamber sensor **105**. (c) One-point calibration measurement outcomes of dual chamber sensor *versus* a commercial CGM system. (d) Sketch of the dual chamber sensor on the animal study setup. Adapted with permission from ref. 134 published by MDPI AG.

While their calixarene framework was too small to fully encapsulate a saccharide, it was well-suited for "face-to-face" H-bonding interactions between the calixarene hydroxyl groups on the upper rim and those of the saccharide. However, the formation of saccharide-**106** complexes in aqueous solution required exceedingly high saccharide concentrations (100 mM–1 M), falling well short of a functional sensor or lectin mimic, but the system provides a foundation for biomimetic research to come.

In 1995, Diederich's team designed a series of macrocycles featuring internal phosphate groups.[136–138] Among them, probe **107** (Fig. 73) exhibited remarkable selectivity towards saccharides such as octyl β-D-glucopyranoside **109** thanks to a calculated distance between phosphate groups of 7.2 Å that was deliberately designed to be complementary to the size of monosaccharides. It was reported that the stability constant K_a for the complex formed between probe **107** and octyl β-D-glucopyranoside **109** in a 98 : 2 mixture of deuterated acetonitrile and deuterated methanol reached 5200 M^{-1}. Despite this significant step forward, these synthetic receptors still suffered from solvent competition, rendering them incapable of measuring glucose in aqueous media (*e.g.*, blood, urine, tear fluid, beverages...). This limitation in aqueous media means that in many cases, the performance of these sensors is assessed in aprotic solvents such as chloroform, which is not representative of clinically-relevant conditions.

Shortly afterwards in 1998, as part of seminal research from the Davis group, Davis and Wareham developed an octaamide-based receptor **108** (Fig. 73) inspired by carbohydrate-binding proteins,[139] which typically create hydrophobic "CH-accepting" pockets using aromatic residues, whilst binding carbohydrate hydroxyl groups using hydrogen bonding motifs. Molecular modelling of the analogous tetramethyl ester indicated that the cavity created by the biphenyl and benzene-1,3-dicarboxamide units was sufficiently large to accept a β-D-glucose molecule. The planar hydrophobic surfaces of the dual diphenyl groups provide apolar contacts, and the array of amides provides favorable hydrogen-bonding interactions with hydroxyls of the saccharide. The impressive reported stability constant of 300 000 M^{-1} of **108** in $CDCl_3$ for β-D-glucopyranoside **109** is unfortunately significantly reduced as soon as competitive cosolvents are introduced, dropping to only 1000 M^{-1} on addition of just 2% methanol-d_4. Modification of external functionalities in 2005 led to probe **110**,[140] which binds D-glucose in aqueous solution with a stability constant of 9.5 M^{-1}. Although this represents an improvement on previous systems, its binding strength remains insufficient in water, seriously limiting the practical applicability of the system for detecting saccharides in biological environments.

To further improve the binding performance of **110**, Davis and Barwell *et al.* synthesized a range of carbohydrate receptors **111a–d** (Fig. 73) in 2009 by adding ether substituents to the framework of the core structure.[141,142] The binding properties of **111a–d** were evaluated by ^1H NMR spectroscopy through titrations in D_2O, measuring association constants (K_a) with D-glucose of 35, 41, 60, and 47 M^{-1}, respectively. The receptors exhibited low affinity for glucose in water but exhibited significantly stronger binding to β-GlcNAc, with good selectivity and nearly millimolar affinity. A range of other modifications were also investigated, identifying other key modifications that could be made to improve binding, and in particular characterizing the role of CH–π (Carbon-hydrogen···π) interactions in carbohydrate recognition, which could be modulated through electronic modulation of the aromatic cage.

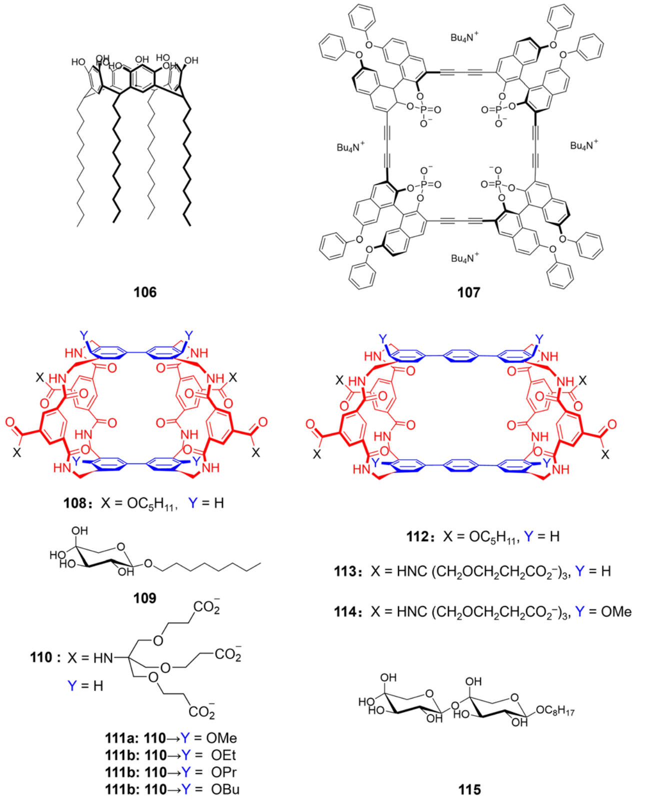

Fig. 73 First generation early biomimetic saccharide receptors designed to operate in organic solvents and water.

Alongside this work, Davis and Lecollinet *et al.* developed a tricyclic octaamide cage receptor **112** (Fig. 73) in 2002, essentially an "extended analogue" of receptor **108** designed to accommodate disaccharide substrates.[143] The binding of **112** and octyl-β-D-cellobioside **115** was investigated by ^{1}H NMR, revealing a 1 : 1 binding mode with a binding K_a of 7000 M^{-1} in $CDCl_3/CD_3OH$ (92 : 8). Selectivity studies involving various glycosides indicated that only compound **115** induced significant changes in the NMR spectrum, fluorescence emission, and circular dichroism of the receptor, confirming high selectivity. Compound **112** is generally recognized as the first receptor capable of distinguishing between disaccharides using solely non-covalent interactions.

Though promising, these early biomimetic probes clearly suffer from some key limitations around selectivity and sensitivity. Continuing their work, Davis and Ferrand *et al.* in 2007 employed an alternative biomimetic recognition strategy to design receptor **116** (Fig. 74),[144] moving away from the tricylic cages discussed so far. **116** is composed of a *meta*-terphenyl motif top and bottom which binds carbohydrates through the usual hydrophobic and CH–π-interactions, while the isophthalamides act as structural pillars and the isophthalamide units form hydrogen bonds with the carbohydrate hydroxyls. The addition of outward-facing carboxylates increased aqueous solubility and prevents aggregation. Receptor **116** was found to be extremely selective towards cellobiose in D_2O, with a binding constant of 560–650 M^{-1}, while its binding constant K_a for D-glucose was only 11 M^{-1}. Taking these lessons and applying them to probe **112**, Davis and Sookcharoenpinyo *et al.* reported two new synthetic receptors **113** and **114** (Fig. 73) in 2012, featuring carboxylate side-chains, but retaining the decreased preorganization of the first generation of probes, which makes them more accessible.[145] The binding constant of receptor **114** for methyl cellobioside reached an impressive 4500 M^{-1}. Tricyclic lectins **113** and **114** demonstrated superior effectiveness compared to **116** in binding all-equatorial disaccharides under biomimetic conditions. These findings suggest that the "induced fit" or "conformational selection" approach that serves enzymes and proteins so effectively can also be employed for synthetic biomimetic receptors, providing a new route for receptor modification and improvement.

Building on the hypothesis that aromatic units play a critical role in the design of synthetic lectin-type receptors, Davis and Ke *et al.* developed the bis-anthracenyl monocyclic receptor **117** (Fig. 74) in 2012.[146,147] ^{1}H NMR titration experiments revealed

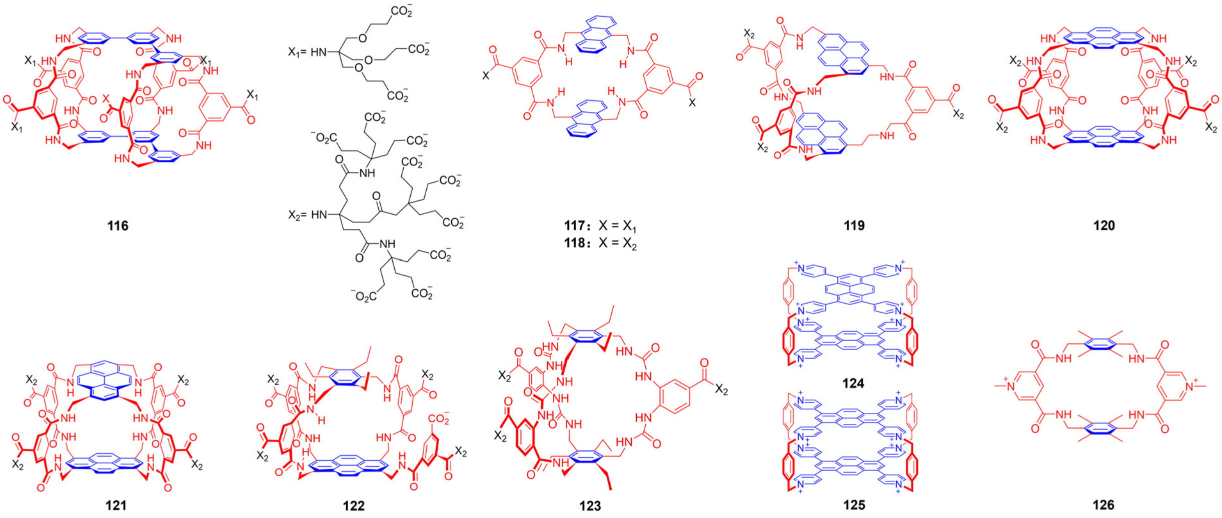

Fig. 74 Synthetic receptors based on condensed aromatic roof/floor units.

that the addition of glucose induced significant spectral changes in receptor **117**, with an average K_a of 56 M^{-1} for glucose. Fluorescence spectroscopy further indicated that the addition of glucose led to a substantial increase in emission intensity, with a maximum enhancement factor of 2.5. Receptor **117** exhibited remarkable selectivity for glucose, for instance with a selectivity ratio of approximately 50 : 1 relative to galactose. The relative structural simplicity of receptor **117** means it is easily synthesized, and exhibits excellent glucose recognition, coupled with an integrated fluorescence signaling system, offering a promising foundation for effective blood glucose monitoring.

Further exploring side-chain modulation, dendritic side chains can be used to modulate the binding microenvironment within anthracene-based synthetic carbohydrate receptors. In 2015, Davis and Destecroix *et al.* engineered a series of synthetic receptors featuring diverse side-chain architectures.[148] When tested for glucose, the binding affinity displayed a noticeable increase from 56 M^{-1} (receptor **117**) to approximately 90 M^{-1} (receptor **118**, Fig. 74). In addition, the fluorescence response to glucose binding was influenced by the nature of the side chains. The emission intensity of receptor **116** increased by as much as 3.7 upon titration with glucose, compared to a 2.5 for receptor **115**. This work demonstrated that controlling the length, charge, and branching of the side chains allowed the positioning of carboxylate groups in a manner that improved substrate binding instead of obstructing the receptor cavity. Together with improved glucose-binding affinities, these findings suggest an approximate two-fold enhancement in receptor **118**'s sensitivity to glucose concentration changes in the 0–10 mM range. Given that this concentration range is highly relevant to diabetes-related glucose monitoring, these receptor systems hold major potential practical implications in the medical field.

The first pyrene-based bicyclic template **119** (Fig. 74) was reported in 2016, Davis and Mooibroek *et al.*, which consists of pyrene and isophthalamide spacers.[149] This structure features two parallel aromatic surfaces and rigid polar spacers, complementing the structure of polysaccharides. Dendritic nonacarboxylate units were incorporated to enhance the water solubility of the receptor. Binding of receptor **119** was shown to be selective for all-equatorial carbohydrates, with stronger binding to glucose and glucosides compared to mannose and galactose. While its performance with monosaccharides was moderate (*e.g.*, K_a for glucose 120 M^{-1}), significantly improved results were obtained with all-equatorial oligosaccharides such as cellodextrins (cellulose fragments). Cellotetraose, for instance, demonstrating a binding constant of K_a = 12 000 M^{-1}.

In 2016, Davis and Rios synthesized two novel receptors by combining a pyrenyl tetraamine with an isophthaloyl spacer, **120** and its isomer **121** (Fig. 74).[150] These receptors are composed of parallel aromatic units (pyrenes) and polar spacers, which are specifically intended to enhance carbohydrate interactions. The issue of pyrene self-aggregation in water was solved by the strong water-solubilizing dendritic side-chains previously discussed. These isomers exhibited moderate affinities for glucose (120 and 190 M^{-1}, respectively), while their binding with β-*N*-acetyl-D-glucosaminosides (O-GlcNAc) showed promising results. Specifically, receptor **121** exhibited a binding constant K_a of 18 200 M^{-1} for the GlcNAc-β-OMe, which is approximately 30 times greater than that of 1st generation receptor **110** and 25 times higher than the natural lectin wheat germ agglutinin (WGA, K_a = 730 M^{-1}).

Enantioselective recognition of carbohydrates in water is also of interest and has been explored using Davis' lectin biomimics. In 2017, Davis and Ríos *et al.* introduced chiral receptor **122** (Fig. 74).[151] Chirality was achieved by linking tetra-aminopyrene and a C_3-symmetric triamine *via* isophthalamide spacers. Binding experiments with *N*-acetylglucosamine (GlcNAc) showed an enantioselectivity ratio of 16 : 1, which is on par with the highest enantioselectivity reported for monosaccharide binding by synthetic receptors in any medium. Additionally, its K_a for GlcNAc was determined to be as high as 1280 M^{-1}, surpassing that of earlier synthetic lectins and three times greater than the value observed for WGA. For glucose, the association constant was found to be K_a = 250 M^{-1}, also exceeding previous synthetic lectins. This report represents a breakthrough in the development of efficient methods for incorporating chirality into these frameworks, marking the first instance of synthetic receptors achieving enantioselective carbohydrate recognition in water through purely non-covalent interactions.

In 2019, Davis and Tromans *et al.* developed the bicyclic hexaurea receptor **123** (Fig. 74) featuring a simple symmetrical core structure.[152] Through elaborate design, this receptor provides a binding cavity that closely complements the all-equatorial β-pyranoside substrate, with the six urea groups providing a robust hydrogen-bonding network for binding to glucose. Receptor **123** was found to bind glucose strongly, with a K_a of approximately 18 000 M^{-1}, and a selectivity for glucose roughly 100 times higher than for most other saccharides, and 1000-fold higher than for non-binding substrates. Furthermore, receptor **123** exhibited good performance in diverse media, including near-identical affinities in phosphate-buffered saline and water. Additionally, receptor **123** exhibited excellent thermal stability and low toxicity. The exceptional performance and tunable characteristics of this system indicate significant potential for clinical medical applications.

Creating glucose-responsive insulin analogs that can reversibly adjust their biological activity according to circulating blood glucose concentrations has become a prominent research direction in the domain of glucose molecular recognition. In 2024, Slaaby, Hoeg-Jensen, and Davis *et al.* engineered a novel insulin conjugate NNC2215 using **123** as the glucose probe, which exhibits reversible bioactivity tailored to the glucose concentration ranges relevant to diabetes both *in vitro* and *in vivo* trials.[153] NNC2215 was constructed by conjugating two key moieties to the insulin backbone: a glucose-specific macrocycle and a glucoside group (Fig. 75a). This dual-modification strategy introduced an intelligent molecular switch that undergoes conformational opening and closing in response to fluctuations in ambient glucose levels, thus dynamically balancing the insulin molecule between a biologically active conformation and a low-potency state (Fig. 75b and c). Biochemical assays demonstrated that the binding affinity of NNC2215 to insulin receptors increased 3.2-fold when ambient glucose concentrations rose from 3 mM to 20 mM – a key glycemic

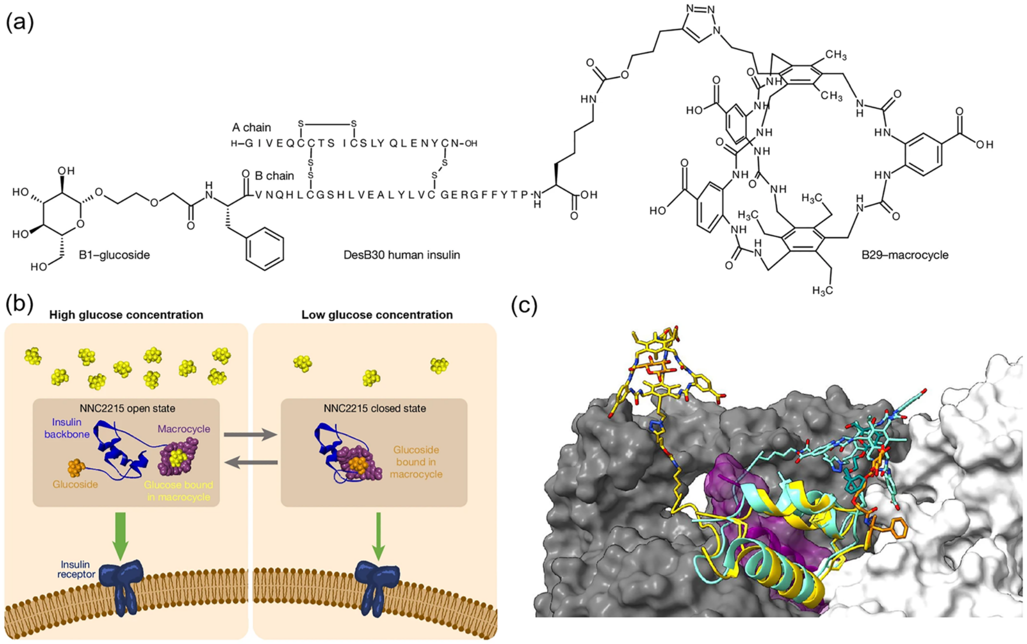

Fig. 75 (a) Chemical structure of NNC2215. (b) Functional principle of NNC2215. NNC2215 is a glucose-sensitive insulin with a molecular switch. At high glucose levels, the switch opens, boosting its insulin receptor affinity to prevent hyperglycemia; at low glucose levels, the switch closes, impairing receptor binding and thus reducing hypoglycemia risk. (c) Open-state and closed-state 3D structural models of the NNC2215 insulin conjugate. Adapted with permission from ref. 153, published by Springer Nature.

interval for patients with diabetes. In preclinical animal tests, the glucose-dependent bioactivity of NNC2215 was proven to deliver two pivotal therapeutic advantages: it significantly reduced the likelihood of hypoglycemic episodes and partially suppressed postprandial blood glucose surges. These findings highlight NNC2215's potential to strike a balance between precise glycemic regulation and treatment safety in diabetes management.

In 2021, Stoddart and Liu *et al.* designed two pyrene-based, temple-shaped receptors **124** and **125** (Fig. 74).[154] The pyrene panels act as the roof and floor of the cage, providing flat, electron-rich surfaces that are ideal for binding with the all-axial C–H bonds of the glucose ring in its chair conformation. The polarized C–H bonds act as hydrogen-bond donors, forming multiple [C–H···O] hydrogen bonds with the hydroxyl groups on the glucose. Four *para*-xylylene pillars play a critical role in maintaining the optimal distance between the roof and floor of the receptor. Nonlinear fitting of the titration isotherm using a 1 : 1 receptor-substrate binding model yields an association constant of 286 M^{-1} for the interaction between **124** and glucose. In the presence of 45 mM glucose, the fluorescence intensity increases by up to 65%. **125** exhibits a similar fluorescence enhancement upon glucose binding, with the association constant estimated to be 96 M^{-1} for the interaction between **125** and glucose. The fluorescence intensity can be increased by as much as 85% upon glucose binding to **125**. Both **124** and **125** exhibit strong fluorescence responses to glucose at physiological concentrations (1–10 mM).

In 2023, Liu and Zhai *et al.* developed a glucose receptor **126** (Fig. 74), which incorporates two durene panels and two pyridinium residues, based on the electrostatic potential map of glucose.[155] The durene panels interact with the hydroxyl groups of glucose by virtue of their electropositive edges, while the methyl groups introduce steric hindrance to preserve structural rigidity. The pyridinium residues contribute to aqueous solubility, and their polarized C–H bonds act as hydrogen bond donors, strengthening the interaction with glucose. To assess the binding affinity of carbohydrates to **126**, ^{1}H NMR titration experiments were conducted, resulting in a binding constant K_a of 845 M^{-1}, significantly higher than that observed for conventional amide-based molecular templates. Further work replacing the durene groups with pyrenes led to a further increase to 3001 M^{-1}, in part thanks to the increased contact surface.[156] These receptors also exhibited a strong selectivity for glucose. The synthetic accessibility and good performance of this glucose-binding lectin analogue underscores its potential for advancing glucose-responsive materials and sensors.

Lectin-based glucose probes utilizing non-enzymatic recognition mechanisms possess several notable advantages (Table 4). Their operation relies on non-covalent interactions, such as the competitive binding between ConA and glucose, which produces no by-products like H_2O_2 and does not require oxygen. This avoids interference with normal cellular metabolism and inherently enables reversible detection. High stability and long-term efficacy are also key strengths: ConA complexed with carriers, including GOx and nanomaterials, exhibits enhanced stability. For instance, GOx-ConA composite electrodes maintain stable response currents for 12 days at room temperature, significantly outperforming standalone GOx systems.[111] Additionally, some sensors, such as NIR fluorescence sensors, can operate continuously for over 3 months at 37 °C under simulated *in vivo*

Table 4 Key properties of representative lectin-based probes

Probe	Sensing component	Signal type	Detection range	Biological applications
82	ConA-GOD/ConA-GOD-GA	Amperometric signal	4–10 mM	On-line fermentation monitoring, *in vivo* glucose assay for diabetics
83	ConA-Alexa488	Fluorescence quenching/recovery	0.15–100 mM	Continuous transdermal glucose monitoring, subdermal implantable sensing
84	ConA-APC/Dextran-MG	FRET reduction	2.5–30 mM	Serum glucose monitoring for diabetes, potential subcutaneous sensing
85	ConA-Alexa647	Fluorescence enhancement	2.5–20 mM (half-saturation: 15 mM)	Long-term transdermal glucose monitoring, subcutaneous implantable sensing
86	ConA-Sephadex	Turbidity change	2.5–20 mM (physiological range)	Implantable glucose monitoring, OCT through-tissue imaging
87	ConA-dextran-coated microparticles	OCT intensity change	—	Subcutaneous continuous glucose monitoring, implantable OCT-based imaging
88	ConA-Sephadex G100	Turbidity change	2.8–22.2 mM	Continuous interstitial glucose monitoring, implantable fiber-optic sensing
89	ConA-Sepharose/Dextran	FRET	0–30 mM	3-day continuous interstitial glucose monitoring, implantable fiber-coupled sensing
90	ConA-dextran	FRET	5.6–19.4 mM	Acute human continuous glucose monitoring, subcutaneous implantable sensing
91	ConA-CdTe QDs/β-CD-modified AuNPs	FRET	0.10–50 μM	Direct serum glucose detection, single-cell/bacterial glucose sensing
92	ConA (C_8/PEG linker)/Os (bpy)$_2$Clpy	Electrochemical redox signal	—	Electrode-immobilized glucose detection
93	ConA-Alexa Fluor 647/glycodendrimer	Fluorescence intensity enhancement	2.8–11.1 mM	Subcutaneous interstitial glucose sensing, invasive continuous glucose monitoring
94	ConA/DexP-graphene	Quartz crystal frequency shift	0.01–7.5 mM	Glucose detection in biological fluids, clinical serum glucose sensing
95	ConA-dextran/thiol-immobilized QCM	Quartz crystal frequency shift	2–40 mM	Gravimetric glucose sensing, implantable continuous glucose monitoring
96	ConA-APS-modified AFM cantilever	Cantilever resonance frequency shift	—	*In vitro* glucose detection in artificial sugar solutions
97	ConA-dextran	Phase shift/relaxation time change	2–20 mM	Continuous glucose monitoring in blood/serum, clinical glycemic control
98	Fluorescent dye-labeled ConA-dextran	FRET	2.8–25.0 mM	Human subconjunctival glucose monitoring, diabetic long-term glycemic control
99	ConA-chitosan-reduced graphene oxide	Electrochemical signal change	1.0–10.0 mM	Simultaneous glucose/urea assay in human serum/urine, clinical biochemical detection
100	ConA-dextran sulfate-coated gold nanorods	Longitudinal plasmon resonance peak shift	1–30 mM	Glucose plasmonic detection, optical glucose sensing
101	PEGylated ConA/APTS-labeled mannotetraose	Fluorescence anisotropy change	0–22.2 mM	Long-term *in vitro* glucose sensing, continuous glucose monitoring assay
102	ConA-phenoxydextran/g-C_3N_4-PTCA hybrid	Electrochemiluminescence intensity increase	0.1 nM–0.052 mM	Non-enzymatic glucose detection in biological fluids, serum/urine/glucose sensing
103	ConA-CdSe/ZnS QD/MG-dextran	FRET	0.03–3 mM (tear glucose range)	Non-invasive tear glucose detection, diabetic glycemic monitoring
104	Fluorescently labeled ConA-dextran	FRET	0–11.1 mM	Continuous glucose measurement in cell cultures, 3D tissue engineering metabolic monitoring
105	ConA-dextran	Osmotic pressure change	0–16.7 mM	Continuous intraperitoneal/subcutaneous glucose monitoring, diabetic CGM

conditions.[114] These probes offer a broad detection range, covering physiological and pathological glucose concentrations, and are applicable to diverse biological samples including serum, interstitial fluid, and tear fluid. Certain sensors, like 3D-printed fluorescent sensors, are also adaptable to cell culture environments.[133] Moreover, they benefit from diversified detection platforms, integrating fluorescence, electrochemistry, optical coherence tomography, and quartz crystal microbalance technologies, thus enabling applications ranging from *in vitro* analysis to *in vivo* implantation.

These probes are not without limitations of course. A primary drawback is their low affinity and moderate selectivity: natural ConA has low affinity for glucose and only moderate selectivity, making it easily interfered with by other sugars such as mannose. Another is the typically limited binding ability of biomimetic probes in aqueous media; early synthetic receptors like calixarene derivatives exhibit weak binding in aqueous solutions, with stability constants far below physiological requirements, and their performance is highly affected by solvent competition. Kinetic and environmental adaptability problems also exist: some sensors have long response times, such as disk-shaped turbidity sensors with a response time of 23 min,[115] and suffer from signal drift in complex matrices like bacterial culture media. Furthermore, there are barriers to clinical translation; despite applications in animal and clinical trials, some implantable sensors exhibit similar long response delays (5–10 min) (consistent with the timing issues noted earlier), and their long-term stability requires further improvement.

In terms of improvement strategies, optimizing natural lectins has shown promising results. PEG-modified ConA exhibits enhanced thermal stability, enabling operation for 30 days at 37 °C, while fluorescently-labeled ligands such as mannotetraose strengthen competitive binding signals, improving detection sensitivity.[130] Sensor design optimization is also possible, for example 3D-printed PVA hydrogel-based sensors combined with FRET technology.[133] On the other hand synthetic lectin mimics (Table 5) can be improved through structural modification such as introduction of aromatics, ureas, or dendritic side chains to improve water solubility, affinity, and binding. For example, the bicyclic hexaurea receptor **123** achieves a stability constant (K_a) of 18 000 M^{-1} for glucose in physiological saline, with 100-fold selectivity over other sugars.[152]

6. Boronic acid-based probes

Having covered the breadth of macromolecular glucose detection systems in Section 2–5, this review will conclude with small-molecule-based probes, a field dominated by boronic acids, and phenylboronic acids (PBAs) in particular. Both mono- and di-boronic acid systems are common, as will be detailed herein. Boronic acid motifs readily and reversibly form boronic acid esters (boronate esters) on condensation with 1,2-diols or 1,3-diols of the type found in saccharides. Binding between boronic acids and substituted *cis*-diols is much stronger than with *trans*- or linear diols (*e.g.*, ethylene glycol), and so these covalent reversible interactions can be readily exploited for sugar binding, recognition, and differentiation. The binding and recognition of saccharides (and diols more generally) is a well-described and thoroughly reviewed topic, and so a detailed account of historical work in this area will not be reported here.[157–159]

Broadly speaking, the recognition and binding of diols is covered by the equilibria shown in Fig. 76a, showing the different mechanistic pathways for the interconversion of PBA **127** and the associated boronate ester anion **130** which ultimately forms in aqueous solution, as originally studied by Edwards and Lorand in 1959.[160] Due to the complexity of these systems, the general equilibrium shown in Fig. 76b is typically considered, describing more broadly the equilibrium between boronic acids and esters as K_{eq}. Key to the reactivity, stability, and selectivity of boronic acids in binding diols is the ability of the boron center to switch between its low-valent neutral sp^2 hybridized state and an anionic tetravalent sp^3 configuration.

6.1. Monoboronic acid-based probes

Monophenylboronic acid derivatives can be exploited for glucose sensing using a range of structural modifications and sensing manifolds/devices of the type seen already. This includes combination with existing fluorescent groups to create fluorescent probes, incorporation into quantum dots, gels, microgels, or nanodiamonds polymerization with functional monomers, incorporation into/onto electrode surfaces to prepare electrochemical probes.

The use of PBAs for glucose sensing can be traced back to a handful of seminal fluorescent anthracene-based examples: the very first boronic acid saccharide probe reported by Yoon and Czarnik in 1992 (probe **131**, Fig. 77),[161] and Shinkai and James' 1994 *ortho*-aminomethylphenylboronic acid probes **132** (Fig. 77)[162] and **133** (Fig. 95, see Section 6.2).[163,164] Czarnik and Yoon's original systems were based on an intramolecular charge transfer (ICT) fluorescence mechanism, whereby heteroatoms or strong electron-withdrawing groups induce electron density imbalance in excited states, causing quenching through enhanced dipole–dipole interaction between fluorophores and the surrounding solvent shell. In the case of probe **131**, this meant that binding of fructose would cause a decrease in fluorescence through formation of a boronate ester anion, also observed on simple exposure to basic aqueous media. This probe was found to selectively recognize D-fructose in aqueous solution at pH 7.4. Subsequently in 1993, Czarnik and Yoon synthesized another anthracene-based boronic acid probe **134** (Fig. 77),[165] an isomer of probe **131**. Although it displayed similar chelation and quenching effects to probe **131** on addition of saccharides, reduced selectivity was observed.

Based on earlier mechanistic work by Edwards and Lorand[160] and Wulff,[166,167] it was already understood at the time that incorporation of an *o*-aminoalkyl (methyl) substituent onto a phenylboronic acid markedly improves diol affinity under neutral conditions. Later, Shinkai and James' 1994 report introduced *ortho*-aminomethylphenylboronic acid-based anthracene probes **132**[162] and **133** (see Section 6.2).[163,164] Unlike previous systems, probe **132** exhibited a significant turn on fluorescence with the addition of glucose, which at the time was believed to be

Table 5 Key properties of representative synthetic receptors

Probe	Structural feature	Sensing mechanism	Glucose binding constant (K_a)	Binding selectivity	Solvent system
106	Resorcinol-dodecanal cyclooligomer	Hydrogen bonding	—	D-ribose > D-glucose (weak)	CCl_4/C_6H_6
107	Chiral binaphthyl-derived cyclophane	Hydrogen bonding	—	β-D-glucoside > α-anomer, weak mannose binding	Dry $CDCl_3$
108	Tricyclic polyamide receptor	Hydrogen bonding + $[\text{C–H}\cdots\pi]$ interactions	—	β-D-glucoside ≫ α-anomer (45 : 1)	$CHCl_3$, $CDCl_3/CD_3OH$ (92 : 8)
111	Alkoxy-substituted tricyclic polyamide	Hydrogen bonding + $[\text{C–H}\cdots\pi]$ interactions	111a: 35 $\mathrm{M^{-1}}$; 111b: 41 $\mathrm{M^{-1}}$; 111c: 60 $\mathrm{M^{-1}}$; 111d: 47 $\mathrm{M^{-1}}$;	β-glucose > galactose (20 : 1) > GlcNAc (9 : 1)	D_2O, human plasma
112	Tricyclic octaamide cage receptor	Hydrogen bonding + $[\text{C–H}\cdots\pi]$ interactions	—	Octyl β-D-cellobioside ≫ others	$CDCl_3/CD_3OH$ (92 : 8)
113	Tricyclic polyamide receptor	Hydrogen bonding + $[\text{C–H}\cdots\pi]$ interactions	2 $\mathrm{M^{-1}}$	D-cellobiose ≫ D-glucose (1300 : 1)	H_2O/D_2O
114	Tricyclic polyamide receptor	Hydrogen bonding + $[\text{C–H}\cdots\pi]$ interactions	3 $\mathrm{M^{-1}}$	D-cellobiose ≫ D-glucose (1300 : 1)	H_2O/D_2O
116	Tetracyclic polyamide synthetic lectin	Hydrogen bonding + $[\text{C–H}\cdots\pi]$ interactions	11 $\mathrm{M^{-1}}$	D-cellobiose ≫ lactose/maltose (∼50 : 1)	H_2O/D_2O
117	Bis-anthracenyl monocyclic synthetic lectin	Hydrogen bonding + $[\text{C–H}\cdots\pi]$ interactions	56 $\mathrm{M^{-1}}$	Glucose ≫ galactose/mannose (50 : 1)	H_2O/D_2O, PBS buffer (pH 7.1)
118	Bis-anthracenyl receptor with dendritic side chains	Hydrogen bonding + $[\text{C–H}\cdots\pi]$ interactions+ electrostatic attraction	90 $\mathrm{M^{-1}}$	Glucose≫ galactose/mannose	H_2O/D_2O, PBS buffer (pH 7.1)
119	Pyrene-based bicyclic threading receptor	Hydrogen bonding + $[\text{C–H}\cdots\pi]$ interactions+ threading complexation	120 $\mathrm{M^{-1}}$	Glucose ≫ mannose/galactose	H_2O/D_2O
120	Pyrene-based tricyclic receptor	Hydrogen bonding + $[\text{C–H}\cdots\pi]$ interactions	120 $\mathrm{M^{-1}}$	O-GlcNAc glycopeptide ≫ GlcNAc derivatives	H_2O/D_2O (pH 7)
121	Pyrene-based tricyclic receptor	Hydrogen bonding + $[\text{C–H}\cdots\pi]$ interactions	190 $\mathrm{M^{-1}}$	GlcNAc-β-OMe ≫ α-anomer (12 : 1)	H_2O/D_2O (pH 7)
122	Chiral pyrene-based macro-bicyclic receptor	Hydrogen bonding + $[\text{C–H}\cdots\pi]$ interactions	250 $\mathrm{M^{-1}}$	Glucose ≫ mannose	H_2O/D_2O (pH 7)
123	Bicyclic hexaurea biomimetic receptor	Hydrogen bonding + $[\text{C–H}\cdots\pi]$ interactions	18 200 $\mathrm{M^{-1}}$ (ITC)	Glucose ≫ galactose/mannose (∼100 : 1)	H_2O/D_2O, PBS buffer (pH 6–8), human blood serum
124	Pyrene-based tricyclic octacationic receptor	Hydrogen bonding ($[\text{C–H}\cdots\text{O}]$) + $[\text{C–H}\cdots\pi]$ interactions	286 $\mathrm{M^{-1}}$ (fluorescence titration)	Glucose ≫ mannose/fructose (∼40 : 1)	H_2O/D_2O (pH 7)
125	Pyrene-based tricyclic octacationic receptor	Hydrogen bonding ($[\text{C–H}\cdots\text{O}]$) + $[\text{C–H}\cdots\pi]$ interactions	96 $\mathrm{M^{-1}}$ (fluorescence titration)	Glucose ≫ sucrose/mannose (∼20 : 1)	H_2O/D_2O (pH 7)
126	Durene-based dicationic tetralactam receptor	Hydrogen bonding ($[\text{N–H}\cdots\text{O}]$ + $[\text{C–H}\cdots\text{O}]$) + $[\text{C–H}\cdots\pi]$ interactions	684 $\mathrm{M^{-1}}$ (ITC)	Glucose ≫ mannose (211 : 1) ≫ galactose (37 : 1)	H_2O/D_2O (pH 7)

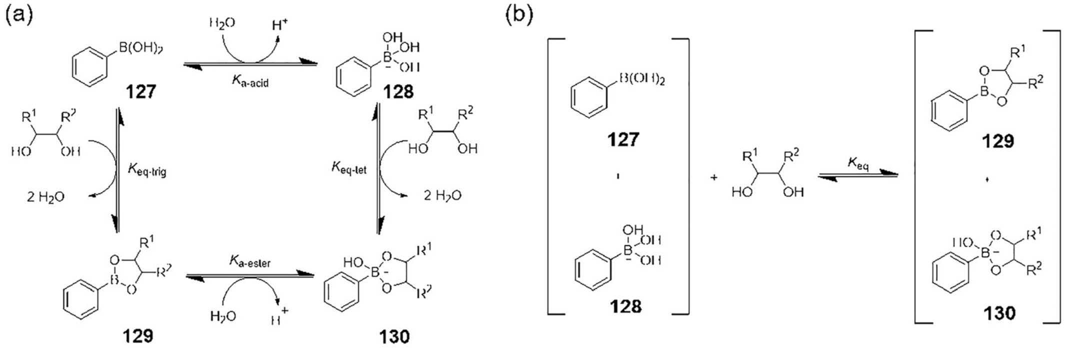

Fig. 76 (a) Reaction of phenylboronic acid with diols. (b) Simplified system for the reaction of phenylboronic acid with diol compounds.

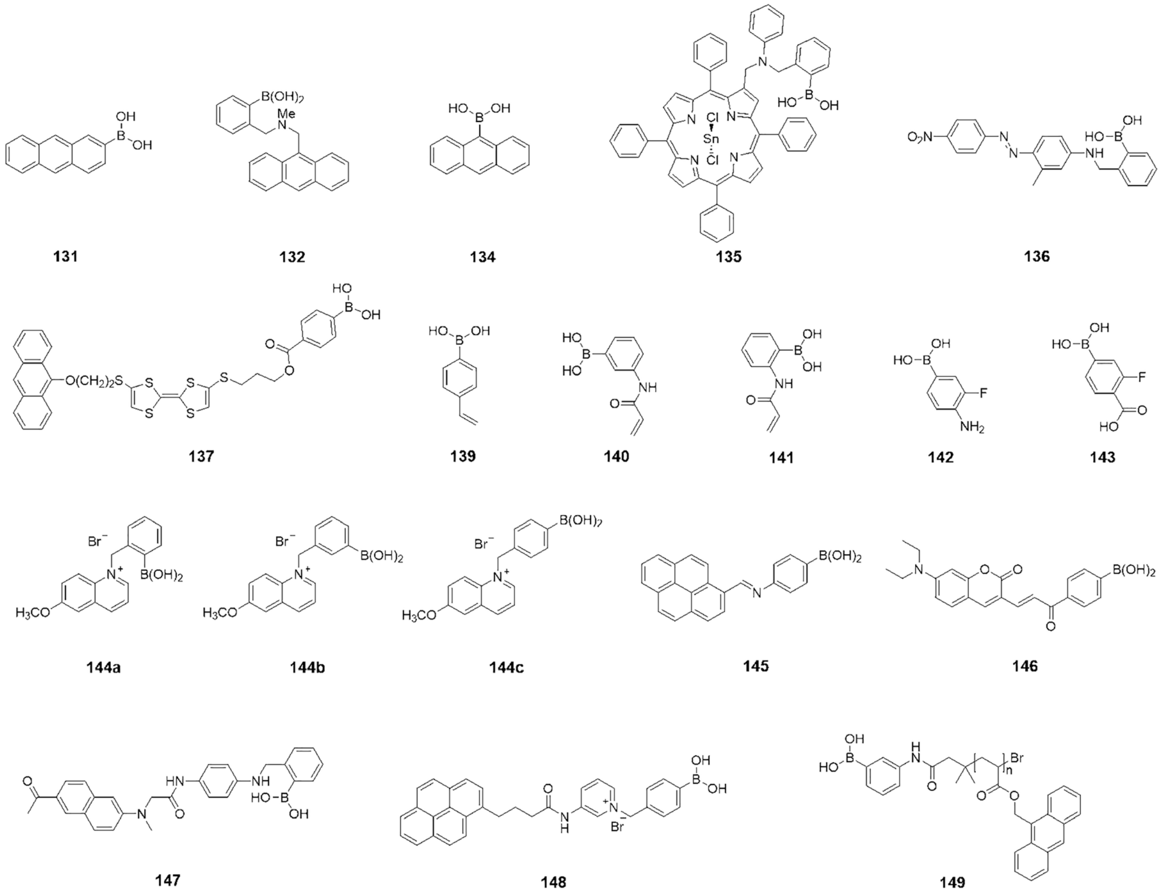

Fig. 77 Representative examples of monoboronic acid-based probes.

controlled by photoinduced electron transfer (PeT) from the tertiary amine to the anthracene to quench fluorescence in the glucose-unbound state. On binding of glucose, probe **132** undergoes "off–on" activation to produce a new fluorescent output, initially believed to be caused by N → B coordination triggered by the increased Lewis acidity of the boronate ester, and thus loss of PeT quenching (Fig. 78a).[158,168] Since this report, however, a better mechanistic understanding has been developed, with an initial alternative proposal made by Wang and Franzen in 2003 who observed this N–B bond to be weak, indicating boronate ester formation could cause a "pK_a switch", protonating the amine to quench PeT (Fig. 78b).[169,170] This was further supported in 2006 when Anslyn and Zhu confirmed that the expected N → B only readily forms in aprotic solvents.[171] A decade later in 2017, Anslyn and Chapin *et al.* found that the fluorescence enhancement of probe **132** based on the PeT quenching was potentially caused by de-aggregation on binding (Fig. 78c).[172]

Shortly after in 2018 Anslyn, Sun, James *et al.* established a unified theory for the fluorescence profile of *o*-aminophenylboronic acids.[173,174] They proposed a $-B(OH)_2$-induced internal conversion mechanism (Fig. 78d). This was achieved by determining key properties of probe **132**. First, it did not aggregate. Second, they

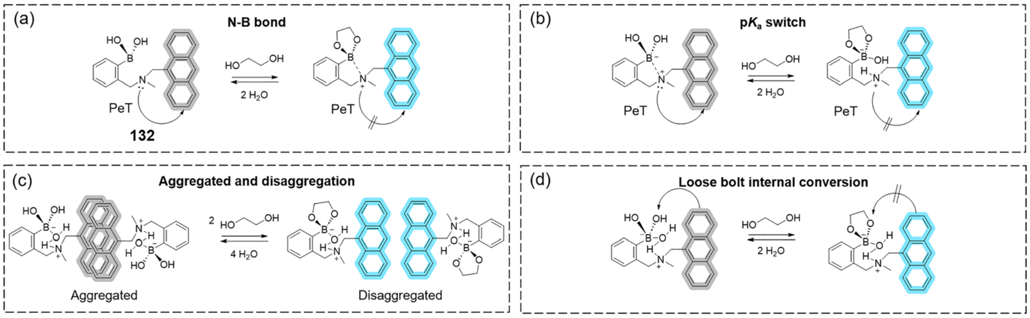

Fig. 78 Proposed mechanisms for emission "turn-on" of *ortho*-aminomethylphenylboronic acids: (a) N–B bonding; (b) pK_a switching; (c) disaggregation; (d) loose bolt internal conversion.

confirmed that no B → N bonds were observed in aqueous solution, including in the presence of fructose. Third, in pure methanol solution, the boronic acid $-B(OH)_2$ was converted to a methoxy boronate ester, which exhibited no fluorescence response on fructose binding. Thus, Anslyn *et al.* showed that $-B(OH)_2$-induced internal conversion mechanisms can explain how *o*-aminomethylphenylboronic acid fluorescent probes recognize saccharides, which the authors termed the "loose bolt" effect.

Building on James and Shinkai's original "on–off" sensor, in 1999, James and Kijima *et al.* developed a fluorescence "on–off" probe **135** (Fig. 77) using tetraphenyl porphyrin tin(IV) as the fluorophore and 2-aminomethylphenylboronic acid as the saccharide binding site.[175] Excitation at 417 nm produced a distinct fluorescence emission peak λ_{em} = 605 nm that decreased on addition of fructose. In this instance, it is believed that the change in fluorescence profile is caused by steric factors, with formation of the boronate-sugar complex causing rotation of the aminoboronic acid motif, thus distancing it from the porphyrin fluorophore.

In 2000, James and Ward *et al.* reported another *o*-aminophenylboronic acid probe **136** (Fig. 77), this time a colorimetric system relying on ICT.[176] At basic pH 11.32, probe **136** is purple, shifting to red when saccharides are added. Mechanistically, once the saccharide-sensor boronate ester complex is formed, B → N bond interactions are promoted, significantly increasing the acidity of the benzylic amine to allow its deprotonation. Formation of the anionic species causes the observed color change. The stability constants ($\log K$) of boronic acid-saccharide complexes were calculated from the corresponding UV-Vis absorption-concentration curves, in which D-fructose was 3.75, D-glucose was 1.85 and ethylene glycol was 0.66, illustrating a marked selectivity for the former. Though clearly not suitable for *in situ* testing due to the high pH required, these types of sensors are highly suitable for specific testing applications, for example the development of glucose diagnostic test papers.

Beyond anthracene-boronic acid and *o*-aminophenylboronic acid systems, many different fluorescent and functional approaches to the detection of glucose *via* boronic acids have been developed. In 2005, Zhu and Wang *et al.* employed a tetrathiafulvalene (TTF) derivative as an electron donor to synthesize a tetrathiafulvalene-anthracene compound **137** containing a boronic acid recognition group (Fig. 77).[177] Thanks to the strong electron-donating capability of tetrathiafulvalene, the interaction between this probe and saccharides elicited a significant fluorescence response, with the fluorescence intensity increasing 5-fold when the fructose concentration reached 50 mM, demonstrating high selectivity in detecting fructose. Subsequently, in 2006, Zhu and Tan *et al.* synthesized diboronic acid probe **138** (Fig. 96, see Section 6.2) by adding a boronic acid group to probe **137**.[178] The binding constants of probe **138** with various saccharides followed the order: D-glucose > D-mannose > D-fructose > D-galactose, demonstrating good selectivity for D-glucose (see Section 6.2–6.4 for more on diboronic acids probes). Under physiological conditions (pH 7.3), the fluorescence intensity of probe **138** exhibited a 6-fold enhancement on exposure to 1500 equivalents of D-glucose. While fluorescence enhancement was also observed with D-galactose, D-mannose, and D-fructose, the response was notably weaker compared to D-glucose (< 3-fold).

In 2004, Lowe and Kabilan *et al.* successfully fabricated a holographic sensor capable of glucose detection using 4-vinylphenylboronic acid **139** (Fig. 77) as the glucose probe,[179] which exhibited excellent reversibility in its response to glucose under pH 9 conditions. When glucose binds to **139** in the sensor to form charged boronate groups, a Donnan potential is generated, driving water to infiltrate the hydrogel, inducing swelling. This swelling increases the spacing between holographic fringes, leading to a red shift in the diffraction wavelength. Upon the removal of glucose, the sensor reverts to its initial diffraction wavelength, demonstrating the reversibility of the binding interaction between phenylboronic acid and *cis*-diols. Unfortunately, at pH 7.4 and pH 8, the sensor showed no significant change in diffraction wavelength in the presence of 2 mM glucose. This is attributed to the pK_a of **139** being approximately 8.9; hence below pH 9 the proportion of its tetrahedral boronate configuration is low, resulting in weak glucose-binding capacity and thus a reduction in the sensor's sensitivity.

3-Acrylamidophenylboronic acid **140** (AAPBA, Fig. 77) can be integrated into acrylamide copolymers and has been validated to bind glucose under physiological pH conditions. Thus, in the same year, the Lowe group utilized **140** as the glucose probe to construct a glucose-sensitive holographic sensor integrated into contact lenses for minimally invasive glucose detection.[180] In pH 7.4 PBS the sensor exhibited a reversible response to 2 mM glucose, reverting to its original diffraction wavelength after rinsing with buffer, thereby demonstrating its suitability for physiological environments. Moreover, preliminary results from human trials indicated that the sensor was capable of tracking blood glucose fluctuations, laying a solid foundation for subsequent *in vivo* validation and device optimization. Later in 2008, the Lowe group constructed holographic glucose sensors with reduced interference from lactate and pH by using 2-acrylamidophenylboronic acid **141** (Fig. 77) as the glucose probe.[181]

In 2004, Asher and Alexeev *et al.* constructed a novel photonic crystal glucose sensor using 4-amino-3-fluorophenylboronic acid **142** and 4-carboxy-3-fluorophenylboronic acid **143** (Fig. 77 and 79) as glucose probes.[182] The pK_a of 4-acetamido-3-fluorophenylboronic acid was 7.81, while that of 3-fluoro-4-*N*-methylcarboxamide phenylboronic acid was 7.28; both values compatible with physiological pH. At physiological pH and ionic strength, the sensor achieved highly sensitive and selective detection of glucose in tear fluid, featuring a detection limit as low as 1 μmol L^{-1} and visually distinguishable diffraction color changes in response to varying glucose concentrations.

Another approach was demonstrated by Geddes and Badugu in 2004, who reported a series of quinolinium-based systems for the detection of glucose in tears. The high solubility and lower-than-usual pK_a (6.70–7.90 in buffer, 6.10–6.95 upon glucose binding) of this motif enabled its use in the acidic medium (pH 5.5–6.5) of a contact lens, for potential development of wearable diagnostics. In this instance, probes **144a–c** were reported (Fig. 77),[183] their fluorescence modulated by charge-neutralization on coordination of glucose to produce the corresponding anionic tetrahedral boronate (*vide supra*). With an absorption of 345 nm and an emission wavelength of 450 nm, these systems were suitable for fluorescence sensing, and were demonstrated in contact lenses, performing suitably for continuous monitoring of tear glucose levels over a concentration range from 50–500 μM.

Fig. 79 Pictorial representation of boronic acid-based contact lens sensors for glucose concentration determination in tear fluid. Adapted with permission from ref. 182. Copyright (2004) The American Association for Clinical Chemistry.

Pyrene can also be employed as the fluorophore, as in probe **145** developed by Pitchumani and Tharmaraj *et al.* in 2013 (Fig. 77).[184] On reaction with glucose, the fluorescence signal at 512 nm is markedly enhanced thanks to the suppression of pyrene-boronic acid PeT quenching, making this an ''off–on'' probe. Probe **145** exhibited a strong linear correlation between its fluorescence intensity and glucose concentrations within the range of 0–50 mM with a correlation coefficient (R^2 = 0.9998), and an impressive detection limit of 5.0 × 10^{-7} M.

Coumarin, a classic chromophore, can also be employed. In 2013, Zhang and Bai *et al.* designed and synthesized the monoboronic acid probe **146** with coumarin serving as the fluorophore (Fig. 77).[185] This probe utilizes an α,β-unsaturated ketone linker to extend conjugation across the coumarin and phenylboronic acid and achieve an extended maximum absorption and emission wavelengths of 463 nm and 616 nm, respectively. Probe **146** possessed good water solubility, and its selectivity for glucose in a 1% DMSO (dimethyl sulfoxide)-PBS showed an affinity towards saccharides as follows: D-fructose > D-sorbitol ≫ D-galactose ≈ D-glucose ≈ D-mannose. This work offers a valuable design perspective for the development of glucose-based fluorescent probes possessing good water solubility, large Stokes shifts, and longer emission wavelengths.

As in previous applications, these traditional single-photon fluorescence probes suffer from short excitation wavelengths and shallow tissue penetration, issues that can be in part addressed using two-photon microscopy (TPM) (*vide supra*). In 2012, Cho and Lim *et al.* designed and synthesized monoboronic acid probe **147** with λ_{ex} of 780 nm (Fig. 77).[186] Its dissociation constants for D-glucose, D-galactose, and D-fructose were determined to be 0.60 ± 0.03 M, 0.35 ± 0.01 M, and 0.048 ± 0.002 M, respectively, showing fair selectivity towards glucose. After incubating HeLa cells and primary cortical neurons with **147** and LysoTracker Red (acidic vesicle-specific fluorescent probe), it was found that probe **147** was predominantly located in the cytoplasm, with only a small fraction in the lysosomes. Upon addition of 20 mM D-glucose, intracellular fluorescence initially increased and subsequently decreased, with no such changes observed with either galactose or fructose (Fig. 80a–h), confirming good selectivity. Similarly, in the imaging of rat hippocampal tissue slices, probe **147** was able to monitor the uptake of glucose in the tissue, showing no response to the uptake of other sugars.

The monoboronic acid small-molecule systems discussed so far all rely on simple binding between a boronic acid and the diols of glucose to elicit a response. An interesting switch in manifold exploited by Jiang and Huang *et al.* in 2013[187] is the idea that glucose can link two boronic acid-containing molecules, by virtue of its two sets of *cis*-diols. The reported ''amphiphilic monomer'' probe **148** employed a highly lipophilic pyrene as both the fluorophore and the lipophilic ''tail'', complementing the polar boronic acid ''head'' (Fig. 77 and 81). The premise of this system was to facilitate the formation of excimer aggregates that would emit at longer wavelengths under high glucose concentrations. This was indeed observed, with the monomer emitting *ca.* 390 nm, whilst the glucose-bridged excimers were seen at a longer emission wavelength *ca.* 510 nm in pH 10.0

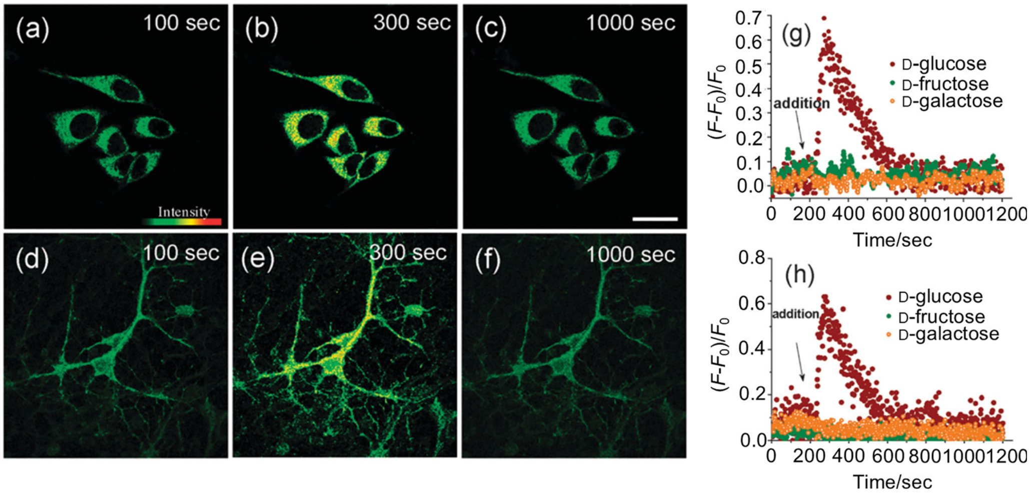

Fig. 80 Pseudocolored TPM images of **147**-labeled (a)–(c) HeLa cells and (d)–(f) primary cortical neuronal cells captured at time points of (a) and (d) 100, (b) and (e) 300, and (c) and (f) 1000 s. (g) and (h) Temporal variation in TPEF (two-photon-excited fluorescence) intensity for (g) HeLa cells and (h) primary cortical neuronal cells. 20 mM saccharides (D-glucose, D-fructose, and D-galactose) introduced after 200 s. TPEF signals recorded in the 500–620 nm range following 780 nm excitation with a femtosecond pulsed laser. Adapted with permission from ref. 186. Copyright (2012) Royal Society of Chemistry.

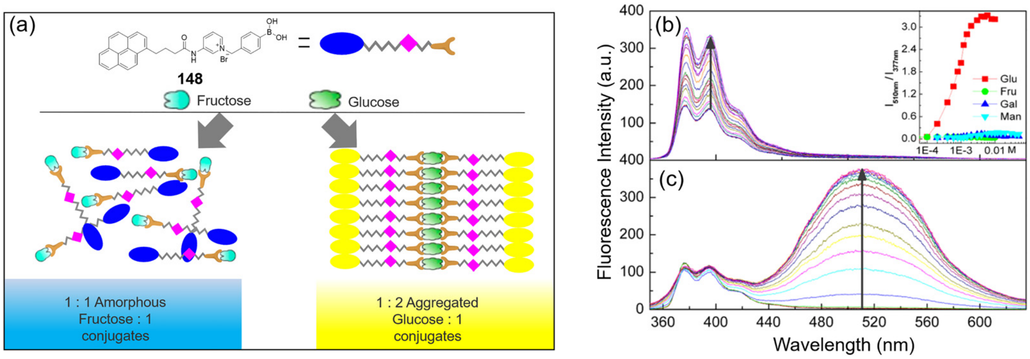

Fig. 81 (a) Schematic illustration of probe **148** forming a 1 : 1 complex with fructose and a 1 : 2 aggregate with glucose. (b) Fluorescence spectra of **148** in a pH 10.0 carbonate buffer containing 2% (v/v) methanol, recorded in the presence of D-fructose (b) and D-glucose (c) across concentrations of 0–10 mM. (b) inset shows excimer-to-monomer intensity ratio as a function of saccharide concentration. The concentration of probe **148** was 0.1 mM, with excitation at λ_{ex} = 328 nm. Adapted with permission from ref. 187. Copyright (2013) American Chemical Society.

carbonate buffer. In contrast, only a moderate increase was observed on addition of fructose, with no new signal at 510 nm, as dimer formation was not possible. The lowest detectable concentration of glucose was determined to be 10 μM, and the sensitivity of the pyrene aggregates was greater than that of most monoboronic acid small-molecule probes, providing an interesting new approach to small-molecule probe design.

Moving away from in-solution small-molecule probes, incorporation into polymers and use in micellar and gel-based systems is also now commonplace. For instance, in 2016, Wei and Wang *et al.* synthesized monomeric fluorescent probe **149** (Fig. 77 and 82).[188] As in the amphiphilic system **148** above, each glucose molecule can bind two boronic acids, causing boronic-acid terminated polymeric chains to cross-link which amplifies the fluorescent signal. Fluorescence spectra revealed that probe **149**'s response showed a good linear relationship with the logarithm of the glucose concentration in the range 0.003–3.0 mM (R^2 = 0.992), and a detection limit of 0.8 μM. Furthermore, outstanding glucose selectivity was observed, with negligible fluorescence enhancement for all other tested biomolecules (including fructose and lactose). The application of this system was demonstrated in human serum albumin, where it accurately detected a normal glucose concentration of 8.0 ± 0.1 mM. The accuracy of the method was verified using a spike-recovery method, ranging from 90.5% to 100%, and a relative standard deviation between 1.2% to 3.8%, indicating that this method can accurately determine the glucose content in complex biological samples.

Moving away from classical cyclic chromophores briefly, in 2014, Liu and Zhang *et al.* fabricated a photobleaching-resistant microgel probe **150** using 3-acrylamidophenylboronic acid (AAPBA) as the glucose recognition site and poly(amido amine) (G1.0 PAMAM) acting as the fluorophore (Fig. 83).[189] The fluorescence intensity at 425 nm increased markedly with increasing

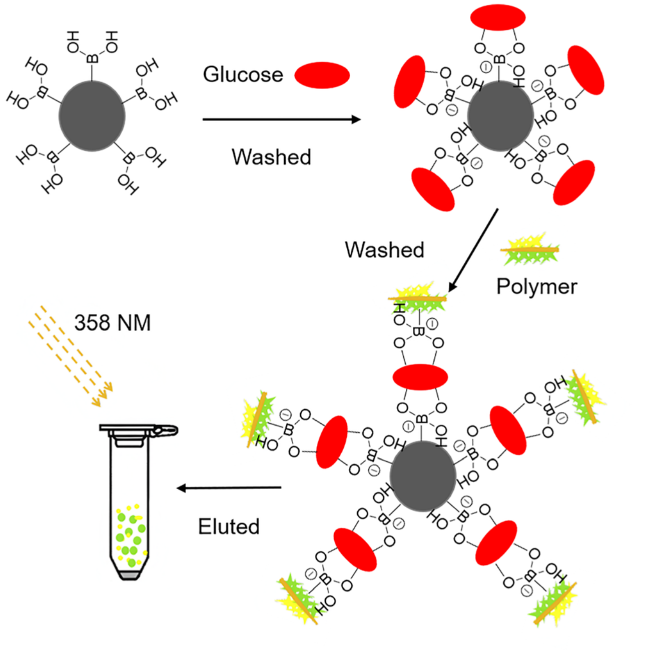

Fig. 82 Schematic diagram of compound **149** for glucose detection. Adapted with permission from ref. 188. Copyright (2016) Elsevier B.V.

glucose, caused by a corresponding change to the microgel network and increase in hydrogen bonding. The microgel probe **150** was able to detect glucose concentrations as low as 10 μM, demonstrating rapid response and excellent photostability, outperforming the reference organic dye DAPI (4′,6-diamidino-2-phenylindole), and proving suitable for longer-term and continuous blood glucose monitoring. In HepG2 cell experiments fluorescence gradually increased as the glucose concentration increased, and an MTT assay indicated that there was no significant cytotoxicity to HepG2 cells up to 100 μg mL^{-1}. For *in vivo* mouse experiments the microgel was injected into the dermal layer of the mouse ear, and the PAMAM-functionalized microgel probe **150** emitted blue light upon excitation by a 365 nm light source, confirming that the microgel probe **150** can enable wireless transdermal glucose detection. This research has the potential to be developed into smart multifunctional continuous glucose monitoring sensors, thereby providing an accurate detection method for diabetes management and clinical medicine.

Incorporation into hydrogels is also common, for instance Sakata and Kajisa *et al.* polymerizing 4-vinylphenylboronic acid with 2-hydroxyethyl methacrylate (HEMA) to synthesize a phenylboronic acid-based hydrogel **151** (Fig. 84), with a view of constructing a glucose-responsive hydrogel for use in a field effect transistor (FET) biosensor.[190] When the glucose concentration increases from 10 μM to 40 mM, the gate surface potential of the hydrogel FET shifts in the negative direction. In addition, hydrogel coated on the gate suppresses noise caused by non-specific adsorption of proteins such as albumin. The experimental data indicated that the surface potential change is linear with the logarithm of glucose concentration in the range of 10 μM–40 mM, and the detection limit of this hydrogel FET is 5 μM. This study holds the promise of being applied in the fabrication of wearable devices dedicated to glucose detection in biological fluids.

In 2017, Yun and Yetisen *et al.* developed a novel glucose-sensitive hydrogel optical fiber sensor **152** using AAPBA to introduce boronic acids (Fig. 85).[191] This work opted for poly(acrylamide-*co*-poly(ethylene glycol)diacrylate) (p(AM-*co*-PEGDA)) as the core material of the optical fiber and calcium alginate as the cladding. The AAPBA boronic acid was covalently incorporated into the hydrogel optical fiber core. Complex formation with AAPBA occurs upon glucose diffusing into the hydrogel, altering the Donnan equilibrium of the system, which in turn affects its density and refractive index. Therefore, by measuring changes in

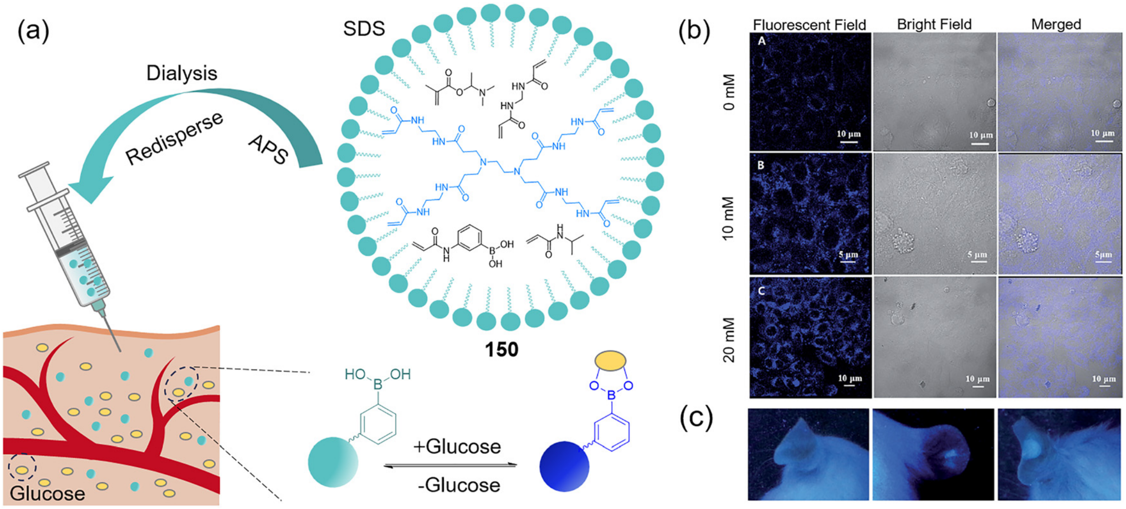

Fig. 83 (a) Schematic diagram of PAMAM-functionalized microgel probe **150** for glucose detection *in vivo*. (b) Fluorescence response of microgels exposed to varying glucose concentrations *in vitro*. (c) *In vivo* mouse experiment with microgel implantation beneath the dermis of the ear. Left-site before injection; middle-after introducing 1 mg mL^{-1} G1.0 PAMAM; right-after administering 1 mg mL^{-1} PAMAM-functionalized microgel probe **150**. Adapted with permission from ref. 189. Copyright (2014) Royal Society of Chemistry.

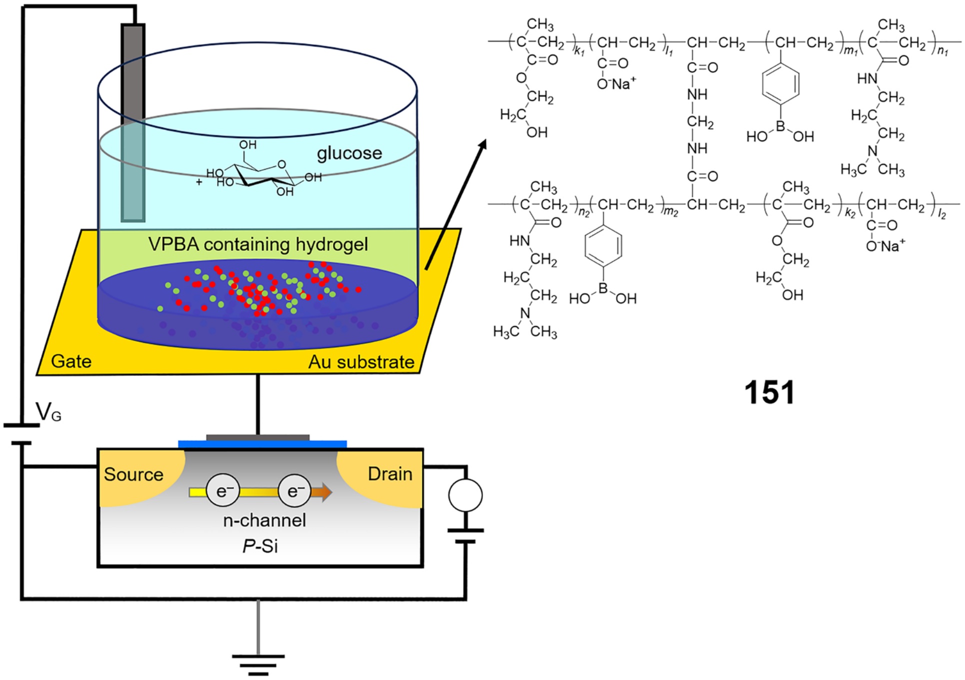

151

Fig. 84 Schematic diagram of boronic acid hydrogel-based FET for glucose sensing. Adapted from ref. 190, published by Taylor & Francis.

the output light intensity glucose concentration can be monitored. This hydrogel optical fiber sensor **152** enables rapid, sensitive, and reversible glucose detection, thus exhibiting great potential for continuous blood glucose monitoring in diabetic patients, which may contribute to more effective diabetes management.

As one would expect, the success of small-molecule boronic acid-based probes in solution, gels, and self-assembled systems has led to their incorporation into heterogeneous saccharide recognition systems, such as quantum dots. This was demonstrated for instance in 2010 by Zhou and Wu *et al.* whose nanoprobe employed 3-aminophenyl boronic acid (APBA)-modified CdTe/ZnTe/ZnS quantum dots **153** (APBA-QDs) for intracellular glucose imaging (Fig. 86a).[192] TEM indicated that as glucose concentrations increased APBA-QD assemblies increased through close-packing of individual APBA-QDs, consistent with the proposed bridging/cross-linking mechanism discussed in previous systems. *In vitro* experiments indicated that **153** exhibited a sensitive response to glucose within the physiological concentration range of 0.4–20.0 mM, with a detection limit of 50 μM. Cellular imaging of mouse melanoma B16F10 cells demonstrated that **153** could enter cells and were mainly distributed in specific regions of the cytoplasm (Fig. 86b–d), confirming APBA-QDs as a viable platform for glucose-sensing nanoprobe development.

The same approach was employed using graphene quantum dots (GQDs) by Shi and Qu *et al.* in 2013 (nanoprobe **154**, Fig. 87).[193] In this study, GQDs were synthesized from

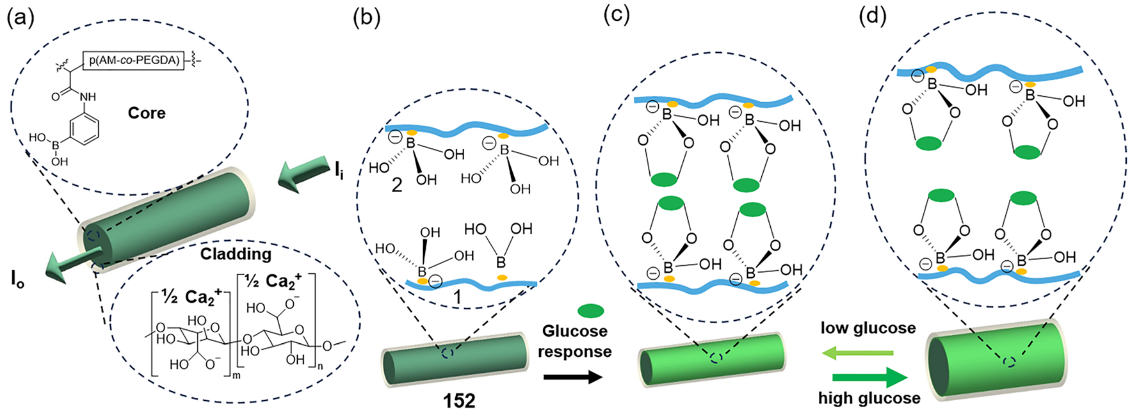

Fig. 85 (a) Structural composition of the glucose-responsive p(AM-*co*-PEGDA-*co*-3-APBA) fiber core, coated with calcium alginate. (b) The hydrogel matrix **152** is functionalized with 3-APBA which is in its charged tetrahedral form. (c) PBA derivative interacts with glucoses *cis*-diols, resulting in a change in the refractive index of the hydrogel fiber. (d) Glucose concentration increases can be quantified by monitoring the variation in the intensity of the output light. Adapted from ref. 191, published by Wiley-VCH Verlag GmbH & Co. KGaA, Weinheim.

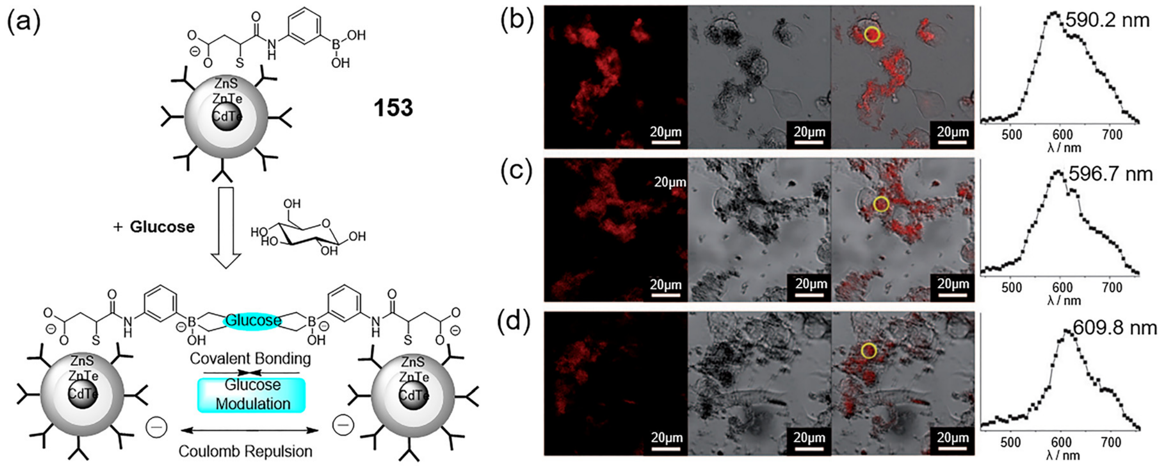

Fig. 86 (a) Schematic illustration of PBA-modified CdTe/ZnTe/ZnS QDs **153** for glucose detection. (b)–(d) Scanning confocal fluorescence microscopic images (left), transmission electron microscopic images (center), and merged images (right) were obtained from mouse melanoma B16F10 cells incubated with **153** (5.0 mg mL^{-1}). Glucose was added at concentrations of (b) 0 mM, (c) 2.0 mM, and (d) 20.0 mM. Local photoluminescence spectra were recorded from specific areas marked by the yellow circles. Adapted with permission from ref. 192. Copyright (2010) Wiley-VCH Verlag GmbH & Co. KGaA, Weinheim.

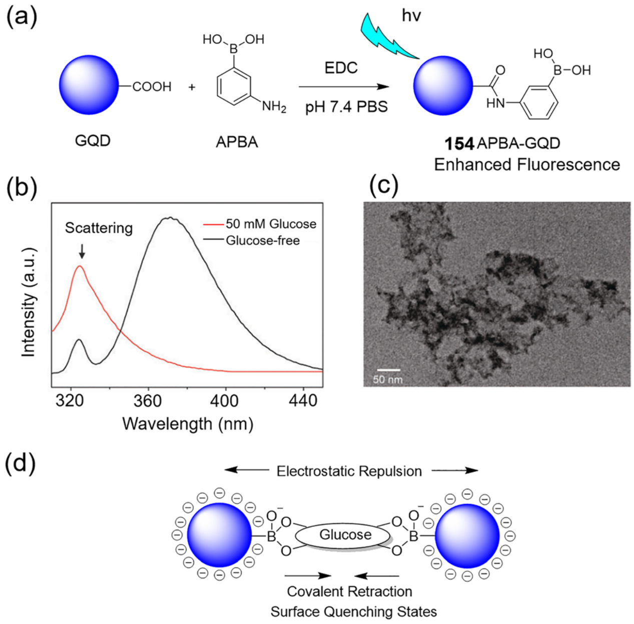

Fig. 87 (a) Functionalization of GQDs with APBA to synthesize quantum dots APBA-GQDs **154**. (b) Fluorescent spectra of probe **154** with or without the addition of glucose. (c) TEM image showing the close packing of probe **154** when exposed to 20 mM glucose. (d) Proposed mechanism of surface quenching states (SQS) in the recognition of glucose. Adapted with permission from ref. 193. Copyright (2013) Royal Society of Chemistry.

carboxyl-functionalized graphene oxide coupled with APBA using 1-ethyl-(3-dimethylaminopropyl) carbodiimide (EDC, a common amide coupling agent). In aqueous solution, probe **154** exhibited a rapid and sensitive response to glucose, whose binding, as before, led to aggregation through cross-linking, resulting in a change in the fluorescence profile. This enabled a detection range of 0.1–10 mM, with a detection limit of 5.0 μM, with Stern–Volmer analysis showing a good linear relationship (correlation coefficient *R* = 0.999). Excellent selectivity for glucose over other saccharides was observed, with only glucose enabling the cross-linking of GQDs. The application of probe **154** was successfully demonstrated for measuring glucose levels in rat brain microdialysates.

Further developments include a report in 2016 by Zhou and Hao *et al.* who employed BA (boronic acid)-modified QDs to develop a ratiometric glucose probe **155** (Fig. 88) using a hybridized combination of red- and green-emitting CdTe quantum dots (r-QDs and g-QDs, respectively).[194] Use of a dual-fluorophore system enables the use of ratiometric fluorescence technology, and both visual colorimetric and fluorescent glucose detection. In this case, only the g-QD components were APBA-modified, and so on addition of glucose cross-linking aggregation occurred solely at g-QD sites, leading to green fluorescence quenching, whilst r-QD output remained unchanged. This ratiometric color change from green to red on increase of glucose concentration could then be used to quantify glucose concentrations, with a functional range of 0.1–2.0 mM, and a calculated detection limit

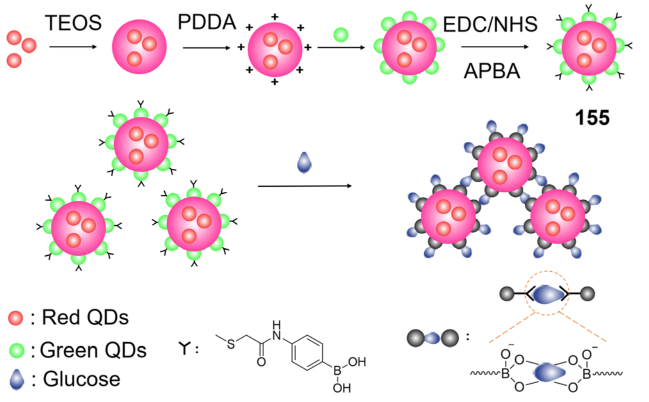

Fig. 88 Schematic diagram of the synthesis of the ratiometric fluorescence probe **155** and the mechanism for glucose detection.

of 4.5 μM. Application of probe **155** was illustrated by detecting glucose levels in human serum samples, demonstrating an efficient and simple ratiometric fluorescent probe for the rapid, sensitive, and specific visual identification of glucose without the need for complex equipment.

Other non-QD optical solid-supported/based boronic acid glucose detection manifolds are also in development, with PBAs also being used with SWNTs, as shown by Strano and Yum *et al.*'s 2012 arylboronic acid system **156** using BA-SWNTs composites.[195] Through high-throughput screening, the authors tested 30 different arylboronic acids, finally identifying 4-cyanophenylboronic acid as a viable reversible partner for glucose sensing, demonstrating the largest response in fluorescence on addition of 45.5 mM glucose (75% of the original SC/SWNT fluorescence level) (Fig. 89, see Section 6.4 for work on functional/electronic modification of PBAs). Complexation onto the SWNT surface causes fluorescence quenching due to PeT. On binding of glucose with the SWNT-complexed boronic acid, the expected sp^2/sp^3 neutral/anion switch occurs, decreasing the boronic acid's reduction potential. This shift reduces potential difference between the boronic acid and the SWNT, diminishing electron transfer potential, reducing the magnitude of PeT quenching, and causing recovery of the nanotube fluorescence. This 4-cyanophenylboronic acid BA-SWNT exhibited a sensitive fluorescence response at physiological glucose concentrations from 0–30 mM, offering a novel platform for the near-infrared optical sensing and recognition of saccharide and glycoproteins.

Alternatively, Guan and Cai *et al.* reported in 2022 a photonic nanochain probe PNCs **157** capable of glucose detection through colorimetry (Fig. 90).[196] This probe consist of a one-dimensional, array of magnetic nanoparticles encapsulated by a phenylboronic acid-functionalized hydrogel with a thickness of tens of nanometers. When the glucose concentration increases from 0 to 20 mM, the color of the solution changes from green to yellow/orange, as the wavelength of the probe PNCs **157** is red-shifted by 130 nm. This research resulted in the development of a rapid, continuous, and reversible glucose-sensing photonic nanochain probe using a unique synthetic approach. This probe exhibits significant potential for enabling real-time continuous glucose monitoring and facilitating the miniaturization of glucose diagnostic devices.

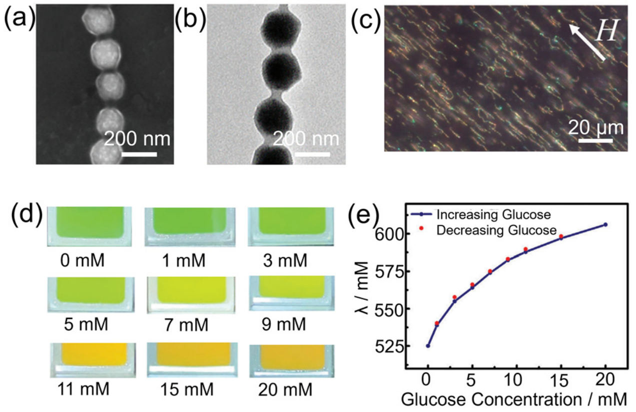

Fig. 90 Characterization and glucose-sensing performance of the Fe_3O_4@PVP@poly(AAPBA-*co*-HEAAm) PNCs **157**. (a) SEM and (b) TEM images (c) dark-field optical microscopy images with a horizontal magnetic field, (d) digital photographs, and (e) diffracted wavelengths during a cyclic sweep with varying glucose concentrations. Adapted from ref. 196, published by Wiley-VCH Verlag GmbH.

More recently in 2023, Mei and Lu *et al.* developed a glucose-responsive upconversion nanoprobe **158** (UCNP@$mSiO_2$/FITC-BA) with phenylboronic acid-modified fluorescein isothiocyanate **158a** (FITC-BA) serving as the glucose-sensing unit (Fig. 91).[197] This nanoprobe **158** was successfully employed for the real-time *in vivo* detection and regulation of blood glucose levels in mice. Preparation of this probe required initial coating of mesoporous silica onto $NaYF_4$:Yb/Tm nanoparticles, after which boronic acid **158a** could be introduced into the pores. On evaluation, the fluorescence intensity of nanoprobe **158** increased and decreased proportionally to glucose concentration, with the magnitude of response remaining unchanged after multiple cycles, demonstrating good reversibility and stability. For *in vivo* mouse experiments, upon irradiation with 980 nm near-infrared light, nanoprobe **158** emitted blue light at 470 nm. This emission-activated photosensitive proteins, leading to an increase in intracellular calcium ions, which in turn

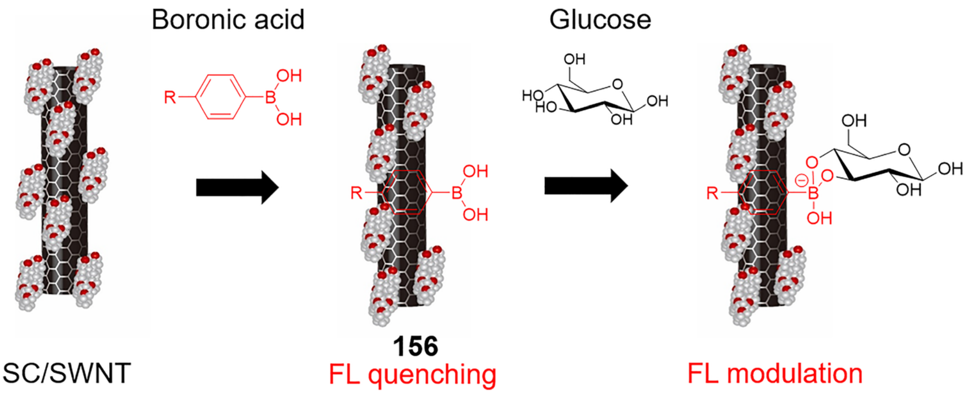

Fig. 89 Schematic diagram of the complexation **156** of boronic acids with sodium cholate suspended SWNTs and the sensing mechanism of the subsequent boronic acid SWNT complex to glucose. Adapted with permission from ref. 195. Copyright (2012) American Chemical Society.

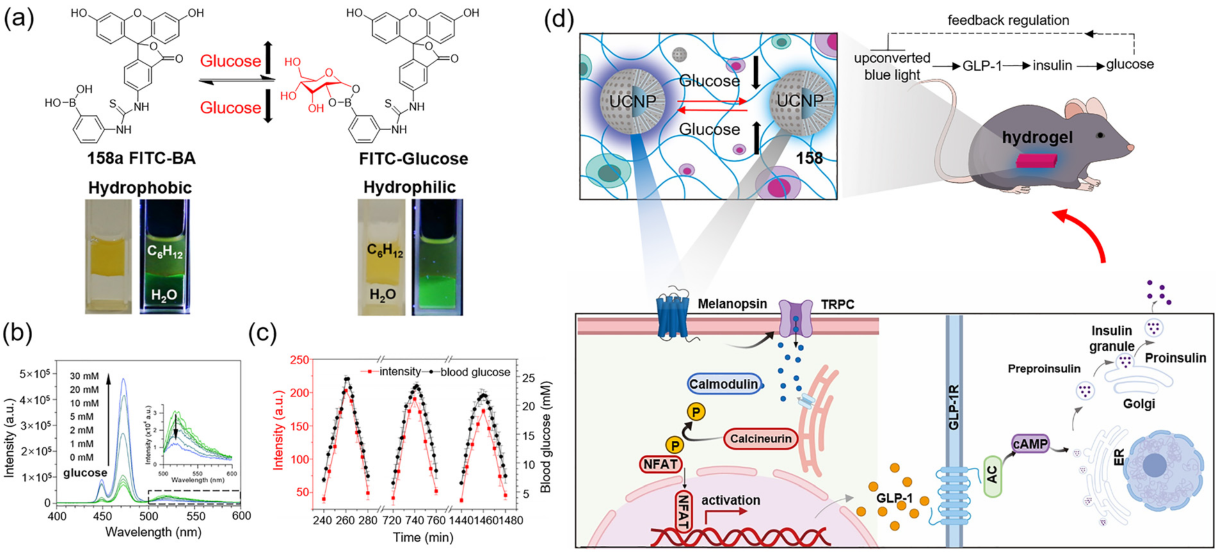

Fig. 91 (a) Variations in hydrophobic properties of **158a** (FITC-BA) before and after glucose binding. (b) Luminescence recovery of the nanoprobes **158** upon the addition of varying glucose concentrations. (c) Comparison of the luminescence intensity of the hydrogel with measured blood glucose levels from a commercial glucose meter. (d) Upconversion nanoprobes **158** for reversible glucose detection and glucose-feedback optogenetic therapy of diabetic mice. Adapted with permission from ref. 197. Copyright (2023) American Chemical Society.

stimulated transcription factors to promote the secretion of GLP-1 (glucagon-like peptide-1) from engineered HEK293 cells. Ultimately, this process stimulated insulin secretion from pancreatic islet cells, lowering blood glucose levels. Furthermore, the induced reduction in blood glucose provided feedback regulation of the fluorescence intensity of nanoprobe **158**, suppressing gene activation and establishing a feedback mechanism that helped diabetic mice maintain blood glucose homeostasis. This research illustrates real-time feedback regulation of blood glucose concentrations using a fluorescein isothiocyanate-based boronic acid glucose probe. Boronic acid-based systems have also been used to achieve direct, glucose-triggered insulin release. In 2025, Egawa *et al.* reported a fully dissolvable glucose-responsive insulin delivery system composed of GOx and a *p*-borono-phenylmethoxycarbonyl (BPmoc)-modified insulin aspart prodrug.[198] Under high glucose conditions, GOx generates hydrogen peroxide, triggering BPmoc cleavage and the release of active insulin. Both *in vitro* and *in vivo* studies showed glucose-dependent insulin activation and selective glucose lowering under hyperglycaemic conditions, reducing hypoglycaemia risk.

The monoboronic acid systems discussed thus far have relied exclusively on optical outputs. We are not limited to such techniques, and so the remainder of this subsection will conclude with a few non-optical boronic acid-based glucose sensors. A notable example is the 2016 work by Zhao and Awino *et al.*, whose boronic acid-functionalized molecularly imprinted nanoparticles (MINPs) **159** enable enzyme-like glucose detection (Fig. 92).[199] Combining surfactant **159a** with diazide **159b** using Click chemistry, alkynyl-functionalized surface-crosslinked micelles were prepared, which

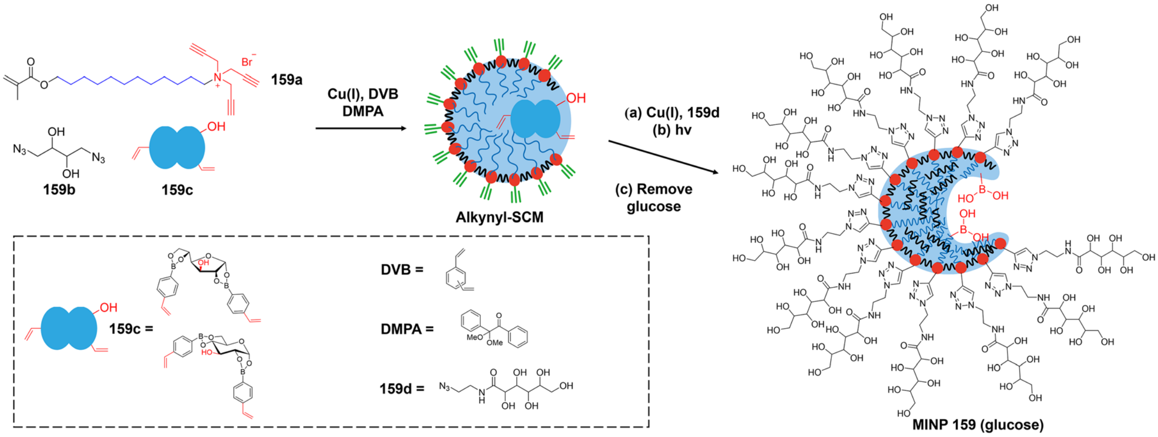

Fig. 92 Preparation of boronic acid-functionalized MINP **159** for glucose detection. Adapted with permission from ref. 199. Copyright (2016) American Chemical Society.

were then functionalized with a 4-vinylphenylboronic acid-glucose complex "template". Sequential washing was then used to remove the glucose, affording an enzyme-like glucose-specific recognition site containing two boronic acid motifs. Binding studies in HEPES (4-(2-hydroxyethyl)piperazine-1-ethanesulfonic acid)-buffered solution (pH 7.4) showed satisfactory binding affinity of K_a = 1.18 × 10^3 M^{-1} (*cf.* Davis' lectin-mimic systems 7–19 × 10^3 M^{-1}, Section 5.2),[150–152] selectivity for glucose, and only minimal binding affinity for other D-hexose and non-hexose aldehydes. This research lays a strong foundation for the development of molecularly imprinted nanoparticles for saccharide recognition and provides a promising general design strategy for the selective recognition of monosaccharides and polysaccharides.

Employing a completely different micelle-based manifold, in 2020, Qi and Qiao *et al.* designed and synthesized a highly sensitive glucose nanoprobe **160** (P(MAn-St-NIPAm-PBA) (Fig. 93).[200] Use of block copolymer P(MAn-St-NIPAm) as the support enabled a high density of PBA sites at the micelle surface for selective formation of PBA–glucose–PBA complexes. As a result, glucose could be selectively bound, whilst other sugars were not strongly bound. Following glucose capture, controllable detection was achieved through pH-triggered release and further detection using analyte-specific enzymatic reactions. In rat brain samples, this method, based on cascade enzyme reactions and changes in the UV intensity of quinone, enabled the detection of glucose in a range of 0.30–10.0 mM, with a detection limit of 0.20 mM.

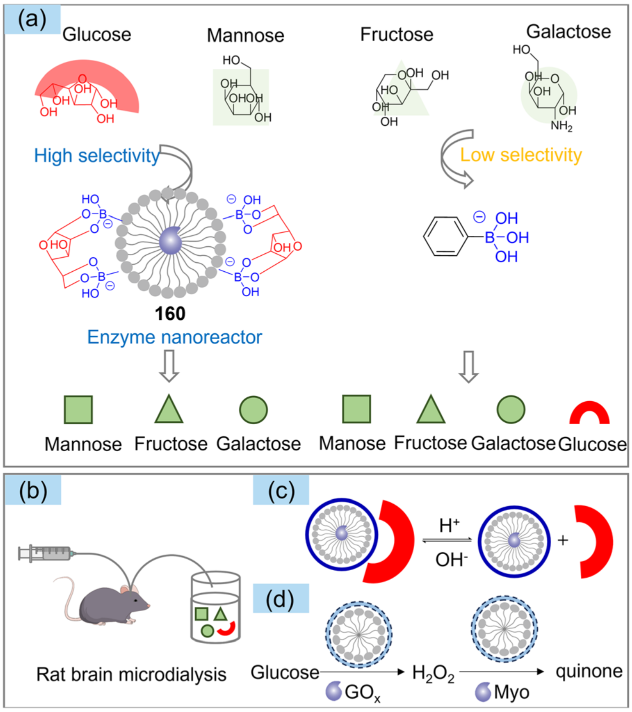

Fig. 93 (a) Schematic diagram of the selective and controllable detection nanoreactor **160** for glucose. (b) Schematic illustration of the microdialysis process in the rat brain. (c) The procedure for capturing and releasing glucose using the hollow nanoreactor. (d) Hollow nanoreactors, equipped with a GOx enzyme and myoglobin (Myo)-based catalyst, enable controlled monitoring of glucose in the rat brain through temperature modulation. Adapted with permission from ref. 200. Copyright (2020) American Chemical Society.

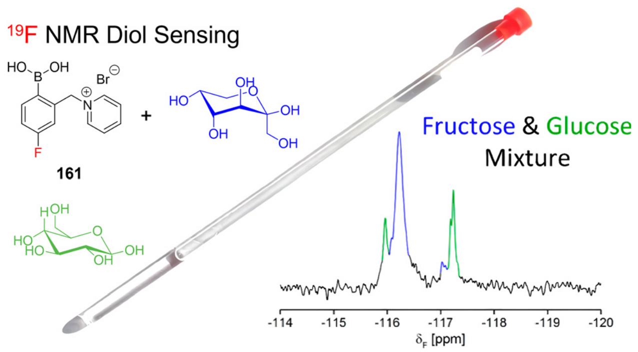

Fig. 94 Probe **161** for use in ^{19}F NMR spectroscopy. Adapted with permission from ref. 201. Copyright (2017) American Chemical Society.

Experimentally, glucose concentration exhibited a linear relationship with the UV intensity of the produced quinone at 470 nm, affording an innovative new non-fluorophore-derived boronic acid-based platform for glucose detection.

Developed in 2017 by Schiller and Axthelm *et al.*, fluorinated boronic acid pyridinium salt **161** allows for the detection of glucose (and differentiation from other diols) using ^{19}F NMR spectroscopic methods (Fig. 94).[201] Using this probe, a library of 59 bionalaytes was studied, demonstrating **161**'s ability to differentiate between a range of monosaccharides (*e.g.*, glucose, fructose) and their isomers, as well as other analytes including polyols, carboxylic acids, nucleotides, amines, and catechols based on representative ^{19}F NMR chemical shifts. Notably compared to other NMR-based probes, the cationic nature of **161** affords it good water solubility, while the incorporation of fluorine for ^{19}F NMR confers high sensitivity to chemical/magnetic environmental changes, a broad chemical shift range (preventing signal overlap), and minimal background interference, thus ensuring reliable and resolved signals. Moreover, the characteristic ^{19}F NMR analyte fingerprint exhibits good stability under different pH conditions, rendering it particularly suitable for medical applications.

6.2. Diboronic acid-based probes

As mentioned at the start of this section, early work by James and Shinkai proved a seminal contribution to the development of sugar-recognition systems. This includes monoboronic acid **132**, discussed in depth in Section 6.1, and diboronic acid probe **133** (Fig. 95).[163,164] Probe **133** represents the first boronic acid-based probe with high glucose selectivity, enabled by the ability of glucose to bind two boronic acids, as seen in many of the systems above. In this case, the bridging occurs intramolecularly, initially believed to be forming the 1 : 1 pyranose complex **133a**. However, in 1999, Norrild and Bielecki *et al.* confirmed that **133a** exists only under anhydrous conditions, and that the furanose 1 : 1 form **133b** is preferred in the presence of water.[202] This was determined using ^1H and ^{13}C NMR spectroscopic analysis, in particular $^1J_{cc}$ coupling constants, providing evidence that all five free hydroxyl motifs are bound to boron centers in **133b**, hence the binding preference. The binding constant K_a of probe **133** towards glucose in 1 : 2

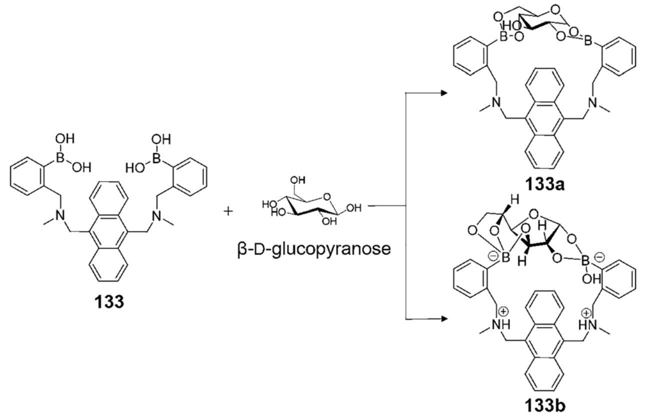

Fig. 95 Probe **133** binding D-glucose in its β-pyranose form in CD_3OD and in the α-furanose form in basic aqueous media.

methanol/water solution at pH 7.77 is 3981 M^{-1}, much higher than those for fructose (316 M^{-1}) and galactose (158 M^{-1}).

This work has since spawned a broad field of diboronic acid saccharide probes, with the bidentate nature of their binding to glucose enabling impressive selectivity over other saccharides like galactose and fructose. Broadly, diboronic acid systems can be classed as non-Shinkai- and Shinkai-type, the latter being specifically anthracene-*o*-aminomethylphenylboronic acid-based.

6.3. Non-Shinkai type diboronic acid probes

The earliest reports of diboronic acids predates the seminal 1994 glucose-selective report, as Shinkai and Murakami *et al.* reported the first diboronic acid probe **162** in 1993 (Fig. 96),[203] consisting of a porphyrin motif and two APBA substituents. Due to the aggregation of porphyrin in aqueous media, probe **162** initially exhibited no fluorescence. However, upon saccharide addition boronate formation was found to disrupt this aggregation by increasing hydrophilicity, thereby restoring fluorescence. Consequently, saccharides with higher affinity for boronic acid exhibited higher deaggregation efficiency, and a stronger output. The fluorescence output therefore correlated with the binding constants of monosaccharides with boronic acid, specifically: D-fructose > D-arabinose > D-mannose ≈ D-glucose.

One type of application not yet discussed in this review is chiral recognition. An early example of this comes from Shinkai and James' 1995 report of diboronic acid probe **163** (Fig. 96),[204] which can distinguish between the enantiomers of monosaccharides. When excited at 289 nm, probe **163** exhibits a strong fluorescence emission at 358 nm. As it is built around a BINOL (1,1′-bi-2-naphthol)-derived chiral backbone, **163** can be either (*R*)- or (*S*)-chiral, each enantiomer binding the enantiomers of saccharides differently, and *vice versa*. Experiments demonstrated that probe (*S*)-**163** exhibited remarkable recognition ability for L-fructose, with (*R*)-**163** exhibiting a strong preference for D-fructose.

Adding to their work in 1995, Shinkai and Linnane *et al.* synthesized the phthalocyanine diboronic acid probe **164** (Fig. 96).[205] At glucose concentration below 1.0 mM the fluorescence signal was weak, whilst at concentrations in excess of 1.0 mM a significant emission peak appeared at 365 nm (λ_{ex} = 275 nm), increasing 20-fold up to 100 mM. Structural investigations using Corey–Pauling–Koltun models and binding studies found that probe **164** formed a 1 : 2 complex with glucose rather than a 1 : 1 complex, likely due to the distance between the two boronic acids, deviating from the mechanism discussed above. Due to this monoboronic acid-type binding, this probe exhibited poor selectivity, with the stability constants for glucose, fructose, and galactose all in a similar range ($\log K_a$ = 1.96, 2.24, 1.86, respectively). This clearly highlights the incredibly effective cooperative binding enabled by suitable oriented pairs of boronic acids, a trend we shall explore throughout this section.

Exploring the effect of the distance between the two boronic acids, in 1997 Shinkai and James *et al.* designed the diboronic acid probe **165** (Fig. 96) with a narrow binding pocket using naphthalene as the fluorophore.[206] Unfortunately, this significant reduction in distance was found to exclude "large" sugars such as D-glucose, instead tightly binding "small" saccharides such as sorbitol in a 1 : 1 complex. Binding causes the benzylamine-phenylboronic acid to generate an increase in fluorescence intensity at 347 nm. Probe **165** was shown to be effective for detecting important small molecule saccharides such as sorbitol, indicating that careful tailoring of the boronic acid spacing is key to selectivity, and could enable tuning of such systems to the desired saccharide.

In 1999, Norrild and Eggert *et al.* synthesized a diboronic acid compound **166**,[207] selective for D-glucose and with good water solubility, adapted from Shinkai and James' research with probe **133** where the benzene ring linkers were replaced with cationic pyridinium rings (Fig. 96). ^1H and ^{13}C NMR spectroscopic data confirmed that probe **166** binds to glucose in a 1 : 1 ratio in its furanose form at physiological pH. The pK_as of probe **166** were determined to be 3.7 and 4.7 (unbound, bound), enhancing its ability to bind saccharides in neutral aqueous solutions. The binding constant of probe **166** with D-glucose was a promising 2512 M^{-1}. Although probe **166** exhibited lower glucose selectivity than probe **133**, its ionic nature solves the critical issue of aqueous solubility that often prevents the use of such fluorescence-based probes.

Shortly after in 2001/2002, James, Bosch and Arimori *et al.* reported probes **167** and **168** (Fig. 96) based on ICT fluorescence.[208,209] Monoboronic acid probe **167** was developed first, and exhibited the following order of saccharide stability constants: D-fructose > D-galactose > D-glucose. In methanol/water buffer solution (52.1 wt% methanol at pH 8.21) the fluorescence intensity of probe **167** increased and its emission wavelength shifted from 404 nm to 362 nm with the increase of fructose concentration. On the other hand, probe **168**, a "dimeric" version of this probe, was found to be D-glucose selective under the same conditions, with near-identical emission wavelengths (405 nm to 360 nm on glucose addition). This simple structural change now produced the following selectivity order: D-glucose > D-fructose > D-galactose > D-mannose, further illustrating how crucial boronic acid spacing is, as well as the key role played by tandem boronic acid binding.

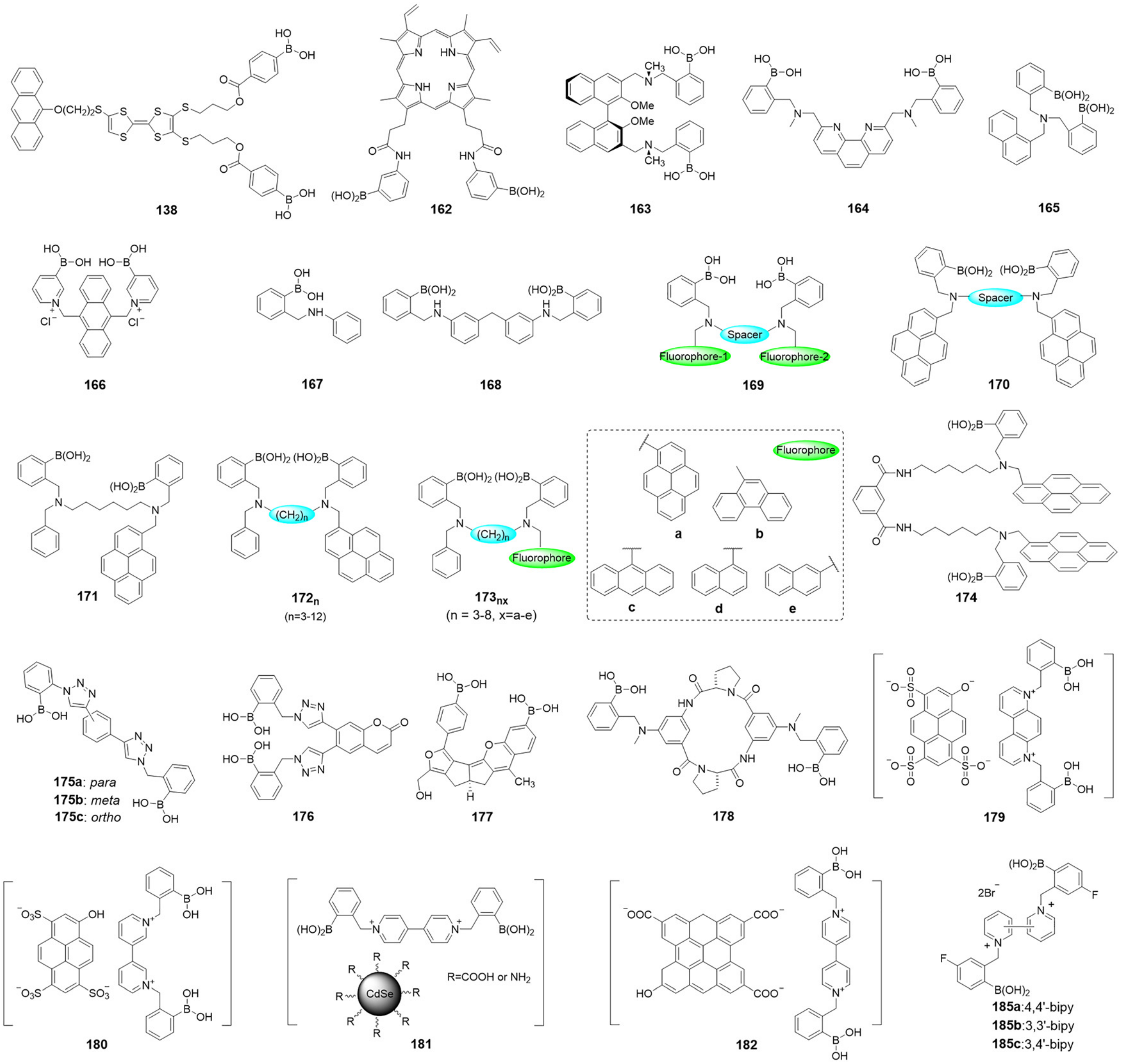

Fig. 96 Representative examples of non-Shinkai type diboronic acid probes.

This bis-*ortho*-amino phenylboronic acid motif is now ubiquitous, and many of the bis-boronic acids developed since the 1990s follow a simple modular pattern, as illustrated in model structure **169** (Fig. 96). These probes typically retain the diboronic acid motif and the tertiary amine structure, varying the spacer and fluorophore to tailor selectivity and the fluorescence profile as desired. This specific approach is well illustrated by the work of Gibson and Appleton *et al.* in 2000, who synthesized a series of diboronic acid derivatives **170** (Fig. 96) in which the alkyldiamine spacer length was varied.[210] Up to a two-fold difference in fluorescence output was observed, with 6- and 7-carbon spacers conferring the best glucose selectivity, whilst longer 8- and 12-carbon spacers favored fructose, again highlighting the crucial nature of boronic acid spacing.

Similarly, James and Arimori *et al.* designed and synthesized glucose probe **171** (Fig. 96) in 2001,[211] incorporating two boronic acid groups, a single pyrene fluorophore, and a hexamethylene spacer. In line with Gibson and Appleton's concurrent work, probe **171** showed some selectivity towards glucose, with the stability constant trend: D-glucose (962 ± 70 M^{-1}), D-fructose (784 ± 44 M^{-1}), D-galactose (657 ± 39 M^{-1}), and D-mannose (74 ± 3 M^{-1}). Using the same mono-pyrene framework in 2002 they screened the spacer length from C_3 to C_8, looking closely at saccharide selectivity.[212] Interestingly, sensors **172**$_{4-6}$ (Fig. 96) exhibited a high affinity for D-glucose, whereas **172**$_{7-8}$ showed higher affinity for D-galactose, conflicting somewhat with the previous studies, but primarily highlighting the importance of the entire structure of the sensor, as variation in the fluorophore seemingly also impacted saccharide selectivity (*cf.* **170** and **172**).

Further studying this in 2004, James and Phillips *et al.* reported a family of probes **171**, varying both the spacer and the fluorophore (Fig. 96).[213] The same C_3–C_8 spacers were studied, this time in conjunction with five common polyaromatic carbocycles: pyrene (a), phenanthrene (b), anthracene (c), 1-naphthalene (d), and 2-naphthalene (e). Some additional dual-fluorophore systems were also studied (not shown here for clarity). This study revealed that the probes containing a single pyrene fluorophore **173_{4a}**, **173_{a}** and **173_{6a}** exhibited the highest affinity for D-glucose, while **173_{7a}** and **173_{8a}** demonstrated the strongest binding to D-galactose. The modification of fluorophores in the probe design also affected binding selectivity: **173_{6a}**, **173_{6b}**, and **173_{6c}** displayed selectivity for D-glucose, while **173_{6d}** and **173_{6e}** showed selectivity for D-galactose. Notably, binding affinity decreased in probes containing two fluorescent moieties.

In 2009, James and Phillips *et al.* designed and synthesized a diboronic acid tweezer-type probe **174** (Fig. 96).[214] They found that probe **174** formed a 1 : 1 complex with D-glucose, D-mannose, and D-galactose (at low concentration, 2 : 1 at high concentration) and a 2 : 1 complex with D-fructose. The fluorescence intensity of probe **174** at 377 nm was enhanced on saccharide binding, while the fluorescence intensity at 470 nm varied depending on the specific monosaccharide. The binding stability of probe **174** with the saccharides followed the order: D-glucose > D-galactose > D-mannose.

A variation on this is the 2017 work by Fossey and Zhai *et al.*, who developed four novel diboronic acid compounds **175a–c** and **176** with bis-triazole cores (Fig. 96).[215] These could be assembled combinatorially by rapid derivatization using a copper-catalyzed azide–alkyne cycloaddition (CuAAC). Probes **175a–c** were used to quickly screen regioisomers to optimize boronic acid spacing. The binding constants of these newly synthesized compounds with fructose and glucose were determined using isothermal titration calorimetry, revealing an expected higher affinity for fructose than glucose by probes **175a** and **175b**. Conversely, **176c** exhibited over twice the binding affinity for glucose compared to fructose, carrying on the trends discussed above. Based on this structural screening, they developed a coumarin-based "on–off" glucose-selective fluorescent probe **176**, which upon the addition of 5 mM glucose exhibited a gradual decrease in fluorescence intensity (I/I_0 = 0.79).

These are by no means the only diboronic acid modular systems to have been developed, with many innovative analogues reported. For example, in 2001 Drueckhammer and Yang *et al.* employed computational methods to design diboronic acid probe **177** to be specifically selective towards glucopyranose (Fig. 96).[216] Following synthesis, evaluation of the probe revealed an apparent binding constant with glucose of $K_a = 40\,000\ \mathrm{M^{-1}}$, with a 400-fold higher affinity for glucose over other monosaccharides, including the often problematic fructose. Despite this incredible selectivity profile, probe **177** had certain limitations, such as poor water solubility and low sensitivity, requiring 30% methanol as a co-solvent and fluorescence response value (F/F_0) of only 0.5 when the glucose concentration was 0.1 M.

Another study in 2006 by Kubik and Heinrichs *et al.* reported an "on–off" type diboronic acid probe **178** (Fig. 96) with a cyclic tetrapeptide scaffold.[217] On excitation at 285 nm probe **178** produced an emission peak at 480 nm which was reduced by 50% on glucose addition. The K_a value for D-glucose ($24\,800 \pm 1200\ \mathrm{M^{-1}}$) was measured at over twice that for L-glucose ($11\,900 \pm 1600\ \mathrm{M^{-1}}$), and only a very low response was seen with mannose and galactose. Probe **178** therefore has high affinity, selectivity and enantioselectivity in glucose recognition, and could be used as an optical probe for glucose in aqueous solution, although an unfortunately high pH is required. This highlights the broad range of backbones employed, enabling selectivity to be tailored significantly to suit the desired application.

Throughout this review, a number of ionic probes, often pyridinium-based, have already been discussed, typically designed for improved solubility, specific applications (*e.g.*, use in contact lenses), or specific targeting strategies (*e.g.*, triphenylphosphonium mitochondria-targeting groups).[218] However, the charged nature of ionic systems can be explicitly exploited beyond this, as in the case of Singaram and Suri *et al.*'s 2003 glucose probe system **179** (Fig. 96).[219] Where they paired a bis-cationic diboronic acid 4,7-phenanthrolinium viologen with a hydroxypyrene trisulfonic acid trisodium salt pyranine. The complementary nature of these bis-cationic and tri-anionic species enables both electrostatic attraction and electron transfer, resulting in quenching of the pyranine fluorophore, which acts as the reporter unit. These electrostatic interactions are suppressed on addition and binding of glucose, resulting in restoration of the fluorescence emission. Thanks to the ionic nature of both components, the sensing system exhibits excellent water solubility and can effectively detect glucose concentrations in the range of 0–20 mM. Subsequently in 2007, the same group developed probe **180** (Fig. 96) using a similar pyranine approach but using a different viologen isomer. By using this system, they observed high binding affinity for glucose ($K_b = 1900\ \mathrm{M^{-1}}$), with a corresponding glucose/fructose selectivity value of 1.7.[220]

Bis-cationic viologens can also be used to facilitate binding of probes to a charged surface. An example of this is that of Singaram and Cordes *et al.*, who in 2006 synthesized the glucose selective system **181** based water-soluble quantum dots (Fig. 96).[221] The working principle of this system is based on bonding of the cationic pyridiniums to the QD surface *via* electrostatic binding through polar surface groups (carboxylic acid, amine), quenching the QDs' innate fluorescence. In the presence of glucose, the viologen quencher binds to glucose, resulting in the dissociation of the complex and the subsequent release of the fluorescent quantum dots. Quantitative detection of glucose concentrations can then be achieved by monitoring the fluorescence increase. Alternatively, this same boronic acid motif can be used in the preparation of GQD systems, as illustrated in 2013 by Qiu and Li *et al.* with probe **182** (Fig. 96).[222]

A vast multitude of diboronic acid systems exist, and so a brief overview of a selection of mechanisms and applications will now be presented. In 2011, Tang and Liu *et al.* designed and synthesized a tetraphenylethene (TPE)-cored diboronic acid glucose probe **183** based on aggregation-induced emission (AIE) effects (Fig. 97).[223] In an aqueous solution, the fluorescence of probe **183** is quenched due to intramolecular rotation. When glucose is added, probe **183** forms a 1 : 1 complex with glucose, in the form of an oligomeric bridged structure in which glucose binds to boronic acids. This inhibits the rotation of TPE and triggers the AIE effect to turn on the fluorescence signal. Since saccharides such as fructose, galactose, and mannose only

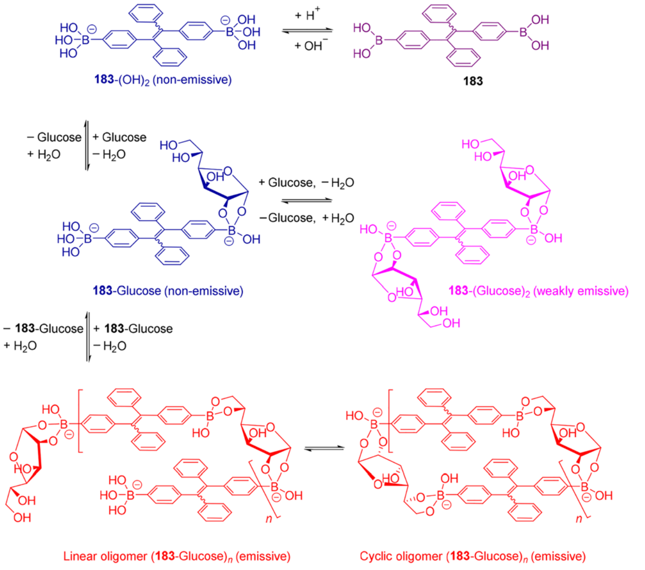

Fig. 97 Probe **183** and its glucose sensing through formation of oligomeric complexes.

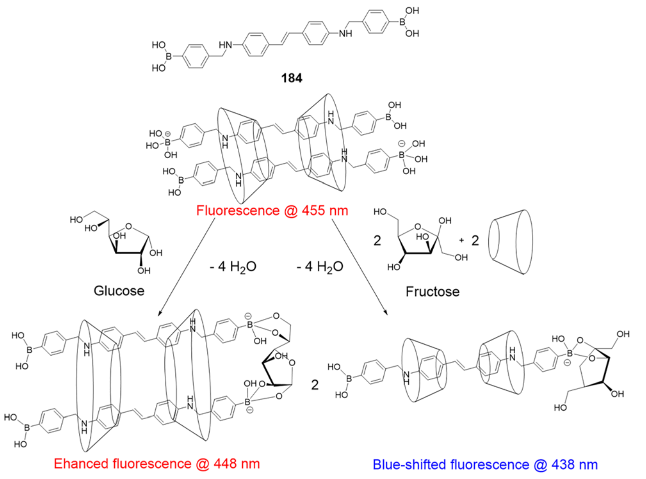

Fig. 98 Probe **184** and the interaction of 2 : 2 **184-γ-CyD** complexes with glucose and fructose.

present one *cis*-diol, only glucose is able to produce large complexes, resulting in outstanding selectivity. Probe **183** exhibits good glucose selectivity and ultimately successfully realizes the sensitive detection of glucose in artificial urine.

In 2012, Jiang and Wu *et al.* developed a fluorescent supramolecular ensemble probe **184-γ-CyD** (Fig. 98) combining a stilbene diboronic acid (STDBA) with γ-cyclodextrin (γ-CyD) for selective glucose recognition.[224] Probe **184-γ-CyD** exhibited higher binding affinity for glucose (K_a = 1048 ± 64 M^{-1}) compared to fructose (K_a = 789 ± 47 M^{-1}). In 1% DMSO-buffer (pH 10.5), fluorescence was significantly enhanced on addition of glucose, and the spectral band narrowed, possibly due to fluorophore rigidity within the cavity enhanced by the binding of glucose. When fructose was added, the fluorescence emission peak at 455 nm was quenched, alongside a blue shift to 438 nm. This was accompanied by a change in the CD signal, indicating that the STDBA dimer depolymerizes. Evaluation of glucose binding demonstrated that the relative error of the probe **184-γ-CyD** for glucose detection in the presence of 0.1 mM fructose, galactose, or mannose was below 30%. Furthermore, the deviation for glucose detection in artificial urine was less than 25%, indicating that the **184-γ-CyD** probe possesses good selectivity and can effectively quantify glucose in complex systems.

As part of the same general family of ^{19}F NMR spectroscopic probes already discussed above,[201] in 2015 Schiller and Axthelm *et al.* designed and synthesized fluorinated boronic acid-appended bipyridinium salts **185a–c** as saccharide probes (Fig. 96).[225] Using these saccharide probes, they developed a method to convert the ^{19}F NMR spectra of their complexes with diol analytes into two-dimensional barcodes, enabling the detection and identification of nine diol-containing bioanalytes under physiological aqueous conditions (50 mM HEPES or phosphate buffer, 10% D_2O, pH 7.4), again enabled by their ionic nature. Thanks to slow boronic acid/boronate ester equilibrium on the NMR timescale, each analyte generates a unique set of ^{19}F signals arising from the unique structures and distributions of all the equilibrium species. These signals combine to form a ''two-dimensional barcode'', enabling analyte identification without requiring multivariate analysis. This NMR fingerprint can distinguish most analytes intuitively, and benefits from the usual advantages of ^{19}F NMR spectroscopy: high resolution, low/no background signal, high sensitivity, and resistance to pH interference.

In 2021, Galan and Ramos-Soriano *et al.* reported a vibration-induced emission (VIE)-based fluorescence probe **186** for glucose detection by both fluorescence and visual colorimetry (Fig. 99a).[226] When excited at 350 nm, probe **186** exhibited a strong broad fluorescence emission peak at 592 nm, along with a smaller emission peak at approximately 432 nm. On the addition of D-glucose, a new and intense fluorescence peak emerged at 452 nm (Fig. 99b), while the original 592 nm signal decreased. Simultaneously, the emission spectrum of the solution changes from orange-red (free probe) to bright blue-green (glucose-coordinated probe), a change visible to the naked eye. In contrast, the fluorescence of probe **186** was quenched by fructose, with no associated visible color change, highlighting excellent selectivity. Again, the effect of individual monosaccharides could be seen colorimetrically with the naked eye (Fig. 99c).

6.4. Shinkai-type diboronic acid probes

This final section will look specifically at Shinkai-type diboronic acid probes, namely those based on the anthracene *ortho*-aminomethylphenylboronic acid fluorescent probes **132** and **133** reported by Shinkai and James in 1994 (*vide supra*).[162–164] These early Shinkai-type probes are now widely recognized as the start of boronic acid-based glucose probes, and constitute a significant milestone in the research annals of boronic acid glucose probes.[168] Through the combination of *ortho*-aminomethylphenylboronic acid with assorted fluorophores, researchers have successfully fabricated a range of fluorescent ''turn-on'' probes.[227,228]

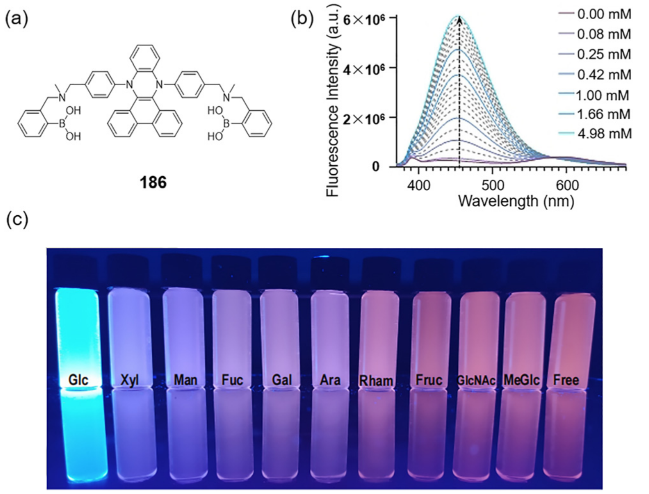

Fig. 99 (a) Chemical structure of probe **186**. (b) Fluorescence changes of **186** upon the addition of increasing quantities of D-glucose. (c) Fluorescent images of **186** in the presence of various monosaccharides under irradiation with 365 nm UV light. Adapted from ref. 224, published by Wiley-VCH GmbH.

In 1995, Shinkai and James *et al.* reported saccharide probe **187** featuring an allosterically-coupled system consisting of two boronic acid groups and two crown ether groups (Fig. 100).[229] This design enables the formation of a "sandwich" structure *via* coordination of metal ions by the crown ethers, altering the distance between the two boronic acid groups to regulate glucose binding and release. Allosteric coupling effects occur when saccharides and salts dissolve together and can be monitored by changes in fluorescence intensity. In the presence of cations such as lithium (Li^+), both crown ethers participate in cation coordination, forming a 1:1 saccharide:probe pseudo-macrocyclic complex. Larger cations such as Na^{2+}, K^+, and Sr^{2+} disrupt the formation of the 1:1 complex, leading to loss of fluorescence from probe **187**. This innovative strategy provided a new approach for the design of molecular probes for specific saccharide recognition. In 2004, James and Zhao *et al.* reported a Shinkai-type anthracene diboronic acid fluorescent probe **188** with improved enantio- and chemo-selectivity for sugar acids such as tartaric acid.[230] This method introduces a stereocenter at each of the alkylamine side-chains, leveraging both stereogenic centers to better distinguish between different sugars and enabling the differentiation of chiral sugars based on binding constants.

In 2002, Wang and Karnati *et al.* designed and synthesized a series of diboronic acid fluorescent probes **189a–c** containing two anthracene fluorophores (Fig. 100).[231] Of these, probe **189a** exhibited the highest selectivity toward glucose, its K_a value for glucose, fructose, and galactose being 1472, 34, and 30 M^{-1}, in 1:1 MeOH/phosphate buffer—showing 43-fold and 49-fold higher selectivity for glucose over fructose and galactose, respectively. ^1H NMR studies revealed that probe **189a** binds to α-D-glucofuranose in a 1:1 stoichiometric ratio *via* the expected bidentate coordination mode. As before, this modular synthesis and screening of analogous probes **189a–c** further highlights the importance of subtle changes to distance and angle between the two boronic acid recognition groups, reinforcing the principle that these systems can be finetuned for selectivity and sensitivity.

To further explore structural effects, in 2006 Wang and Kaur *et al.* synthesized related monoboronic **190a–c** and diboronic acids **191a–c** by introducing either cyano or nitro electron-withdrawing groups or fluorine at the *para*-boronic acid position (Fig. 100).[232] This study demonstrated that monoboronic acids **190a–c** exhibited significant selectivity for fructose, while the diboronic acid derivatives **191a–c** were selective for glucose. Mildly electron rich fluorinated **191c** bound glucose the weakest (K_a = 630 M^{-1}), while electron-poor **191a** and **191b** exhibited K_a values of 2540 M^{-1} and 1808 M^{-1}, respectively, which were significantly higher than those of the original compound **191d** (K_a = 1472 M^{-1}). However, selectivity in probes **191a–c** decreased relative to the parent system **191d**, a trend that was

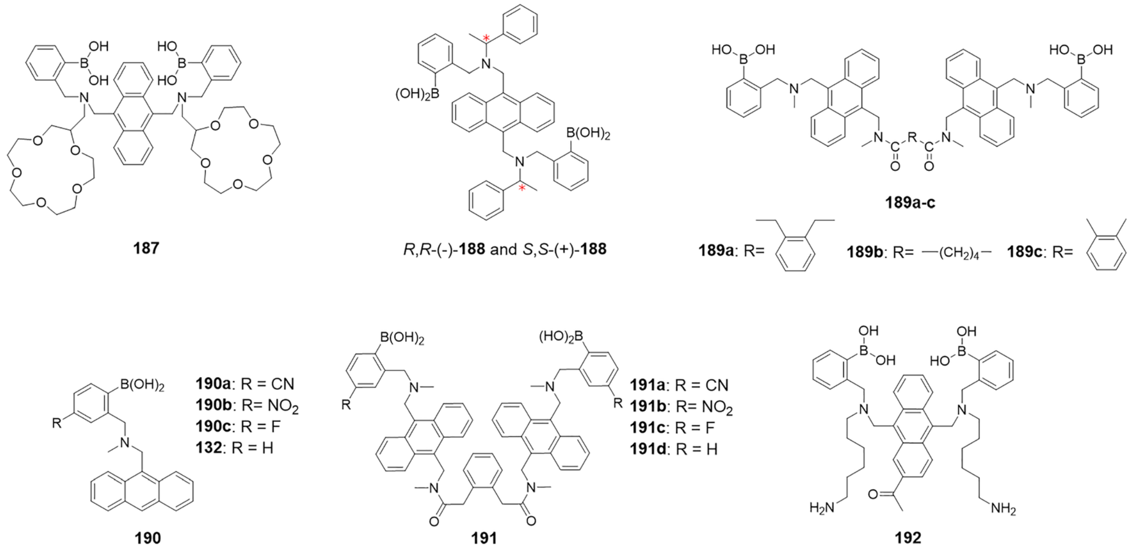

Fig. 100 Representative examples of Shinkai-type diboronic acid probes.

also observed in monoboronic acids **190a–c**, clearly illustrating the typical tradeoff between sensitivity and selectivity.

In 2010, Takeuchi and Shibata *et al.* developed an injectable hydrogel microbead-bead based glucose fluorescence sensor using diboronic acid probe **192** reported by Shinkai[233] as the probe (Fig. 101a–d).[234] Highly uniform and reproducible injectable microbeads were produced using microfluidic techniques, allowing minimally invasive implantation and transdermal transmission for effective blood glucose monitoring without the need for external power sources or implantable electronics or wiring. These diboronic acid-based microbeads exhibited high sensitivity toward glucose. By implanting these microbeads into the ear skin of mice, continuous *in vivo* blood glucose monitoring was successfully achieved (*vide supra*). The results demonstrated that these microbeads could dynamically monitor blood glucose concentrations ranging from 0 to 1000 mg dL^{-1} (0–5.55 × 10^{-3} mol L^{-1}). Subsequently, in 2011, Takeuchi and Heo *et al.* found that the fluorescent hydrogel beads exhibited problems for long-term blood glucose monitoring *in vivo*, including easy dispersion from the implantation site and removal was difficult, and inflammatory reactions were caused by poor biocompatibility.[235] To address these issues they improved the polymerization techniques and constructed a novel hydrogel fiber-based glucose sensor using PAM (polyacrylamide) hydrogels conjugated with PEG (Fig. 101e). This new glucose sensor enabled effective monitoring of blood glucose fluctuations for up to 140 days, showcasing superior stability and sensitivity in blood glucose monitoring. These novel glucose sensors enabled minimally invasive implantation, long-term stable monitoring, and easy removal, providing a new approach for the long-term blood glucose monitoring. More recently, in 2025, Ichiki *et al.* further advanced this concept by developing an optical microneedle sensor with a fluorescent boronic acid-functionalized hydrogel embedded at its tip.[236] The device can sample sub-nanoliter volumes of interstitial fluid, enabling minimally invasive glucose measurement with high accuracy across physiologically relevant concentrations.

This class of diboronic acid probe has also found application in dual analyte sensing, for instance glucose and oxygen, both of which are crucial to cellular metabolism. In 2013, Meldrum and Zhang *et al.* developed a dual-responsive polymer film sensor **193** for glucose and oxygen sensing (Fig. 102).[237] This dual-responsive sensor consists of three components: a blue-emitting glucose probe **193a** (GS-COOH); a red-emitting oxygen probe **193b** (OS); and an internal reference probe Rhod-MA, which is unresponsive to the analytes and emits yellow light. All three components were incorporated into a polymer film and deposited on a TMSPA (trimethoxysilylpropyl methacrylate)-treated quartz glass. Selectivity tests indicated that glucose exhibited higher selectivity than fructose, mannose, or galactose. This dual-responsive sensor was successfully applied for the sensitive detection of glucose and oxygen consumption in bacterial cells (including *E. coli* and *B. subtilis*), mouse macrophage J774, and human cervical cancer HeLa cells.

Following this, in 2014 Meldrum and Tian *et al.* designed a polymer-based sensor **194** (G-PS) for intracellular glucose monitoring (Fig. 103).[238] This sensor utilized poly(*N*-(2-hydroxypropyl) methacrylamide) (PHPMA) as a biocompatible polymer matrix and included a small proportion of poly([2-(methacryloyloxy)-ethyl]trimethylammonium chloride) (PMAETMA) to ensure cell permeability. As a monomer, the glucose probe **194a** (GS-MA) could be easily copolymerized with HPMA and MAETMA. To alleviate the impact of the complex cellular environment on measurements, a rhodamine-based glucose non-responsive probe Rhod-MA was integrated into the polymeric sensor to produce a ratiometric sensor **194**. In PBS, the blue fluorescence emission of **194** at 445 nm increased with rising glucose concentrations, up by 4.5-fold at 50 mM glucose concentration. Comparison of the glucose probe and rhodamine emissions (blue 445 nm and red 580 nm emissions, respectively) allowed more accurate measurement of glucose concentration changes, thus improving the accuracy and reliability of the probe in real applications. HeLa cells were used as a test environment, intracellular glucose concentrations equilibrated within 5 min with high

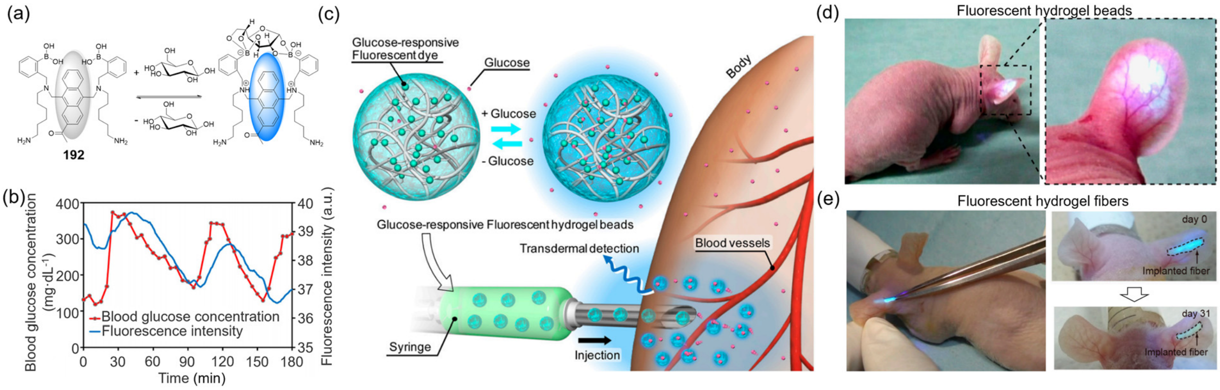

Fig. 101 (a) Probe **192** for glucose reversible recognition. (b) Fluorescence intensity of **192**-beads and measured blood glucose concentrations *versus* time. (c) Schematic illustration of the injectable fluorescent microbeads for *in vivo* continuous glucose monitoring. (d) *In vivo* CGM in a mouse using injected **192**-beads. (e) Mouse ear with implanted **192**-fiber: the fiber remained at the implantation site for one month. Panel a–d: Adapted with permission from ref. 234. Copyright (2010) National Academy of Sciences. Panel e: Adapted with permission from ref. 235. Copyright (2011) National Academy of Sciences.

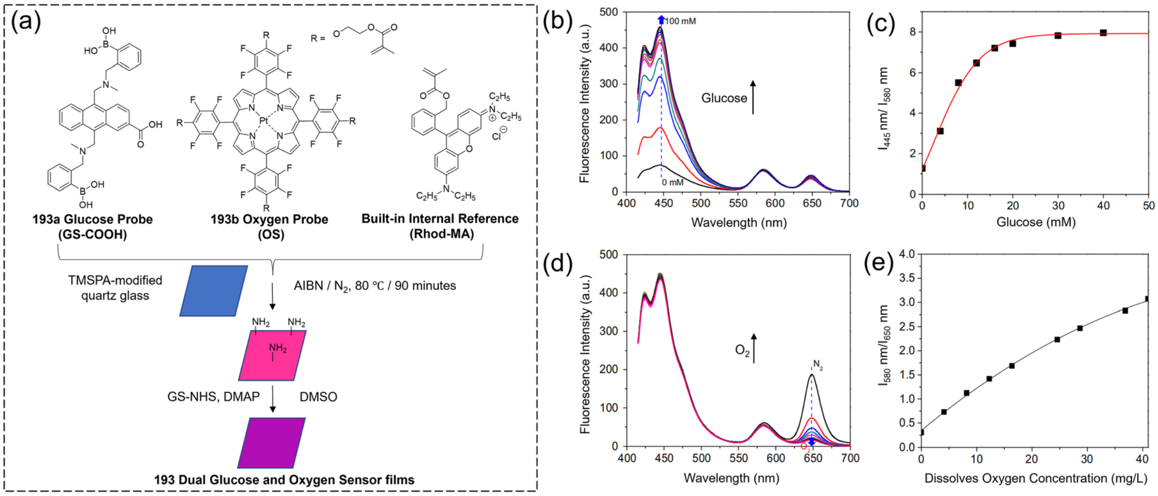

Fig. 102 (a) Components of probe **193**: probes **193a** (Glucose Probe), **193b** (Oxygen Probe), Rhod-MA (Built-in Internal Reference) used for the preparation of dual probe **193**. (b)–(e) Responses of the dual probe **193** to glucose (b) and (c) and to oxygen (d) and (e). (b): fluorescence responses to glucose; (c): ratiometric fluorescence changes for glucose using the ratio of fluorescence signals at 445 and 580 nm; (d): fluorescence response to oxygen; (e): ratiometric fluorescence changes for oxygen using the ratio of fluorescence signals at 580 and 650 nm. Adapted with permission from ref. 237. Copyright (2013) Elsevier Ltd.

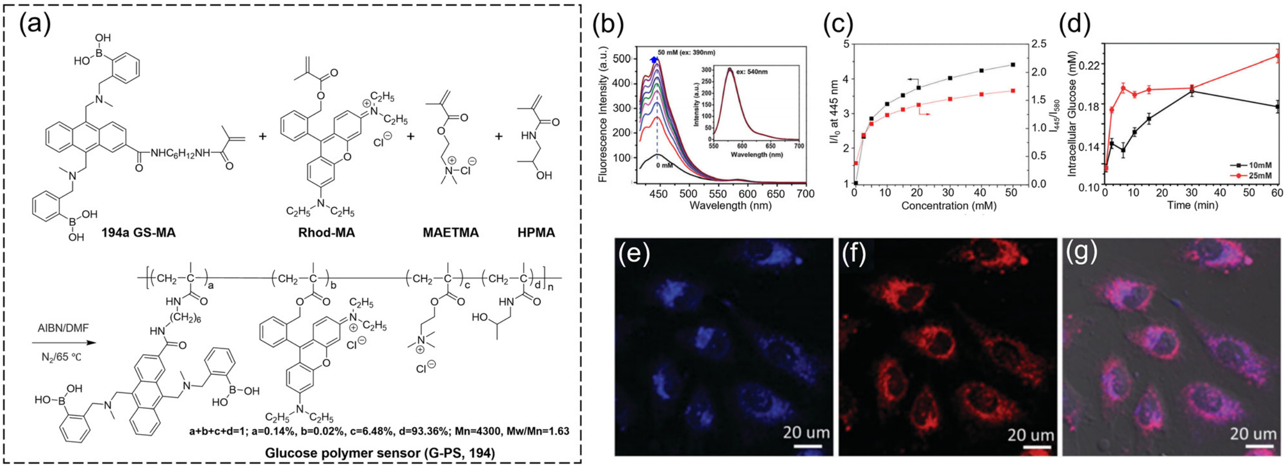

Fig. 103 (a) Synthesis of glucose probe **194**. (b) Fluorescence response of probe **194** to glucose in PBS buffer. (c) Changes in fluorescence intensity ratio as a function of glucose concentration. (d) Measurement of intracellular glucose concentration using probe **194**. (e) and (f) Cellular images of probe **194** in HeLa cells. (e) Blue channel showing glucose probe fluorescence excited at 405 nm. (f) Red channel showing rhodamine internal reference fluorescence excited at 561 nm; (g) Overlay of (e) and (f) with the bright field image. Adapted from ref. 238, published by Royal Society of Chemistry.

concentrations (25 mM) of extracellular glucose, but equilibration took 30 min at normal concentrations (10 mM), indicating that the sensor **194** could effectively measure dynamic change of intracellular glucose concentrations although somewhat slower than desired.

Building on this, the same group (Tian *et al.*) reported a wearable fluorescent smart contact lens for real-time glucose detection in tear fluid in 2022, which represents a paradigm shift from intracellular sensing to transdermal/ocular wearable sensing (Fig. 104).[239] The smart contact lens sensor was constructed by grafting two key components–a boronic acid-modified ultrasensitive glucose probe **195** (GS-NHS) and a rhodamine-based reference probe RDMA–into a poly(2-hydroxyethyl methacrylate) (PHEMA) hydrogel network. PHEMA hydrogel was selected for its inherent suitability as a contact lens material: its soft, transparent nature and high-water content ensure comfort during prolonged wear and facilitate the rapid diffusion of tear glucose to the immobilized probes. Glucose binding to the boronic acid moiety of **195** suppresses the "loose bolt effect", which refers to a rotational energy loss mechanism of the fluorophore. This suppression results in a concentration-dependent increase in blue fluorescence emission at 440 nm. Meanwhile, the reference probe RDMA emits stable red fluorescence at 595 nm, and this emission is unaffected by glucose or tear components (*e.g.*, Na^+, K^+, albumin). This ratiometric design yielded a low detection limit of 9.3 μM (*via* fluorescence spectroscopy) and 23 μM (*via* smartphone-based analysis), and it has a linear response range of 0.1–1 mM, which perfectly matches the physiological

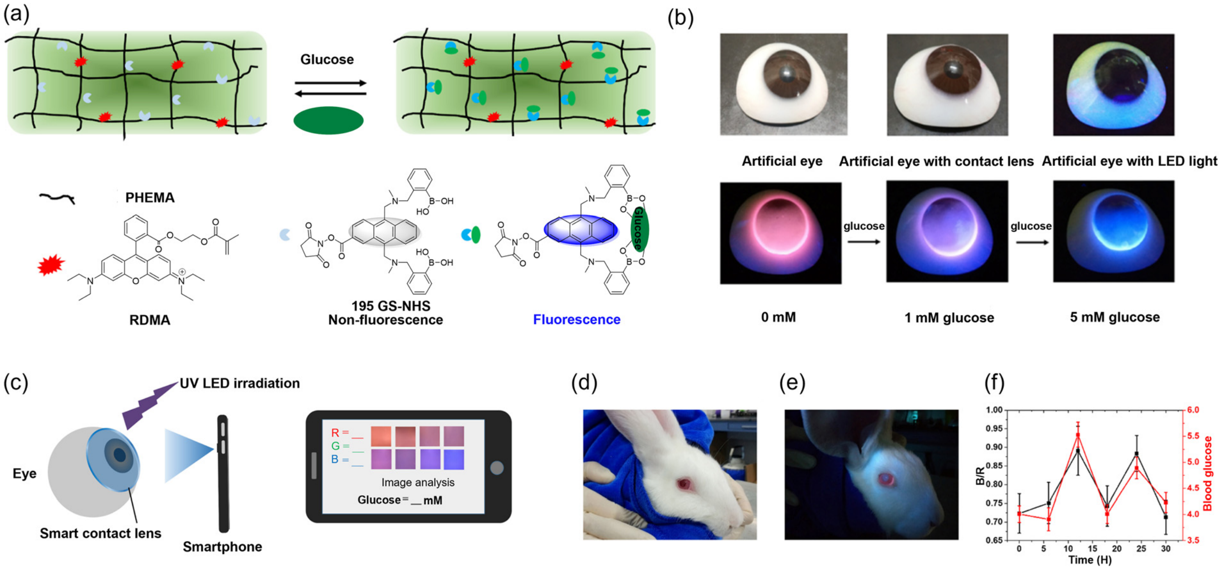

Fig. 104 (a) Components of smart contact lenses for detecting glucose. The network of HEMA hydrogels contains a highly sensitive glucose probe **195** and a reference probe for calibration. (b) Photos of the contact lenses worn on artificial eyes and their fluorescent images in artificial tears with varying glucose concentrations. (c) Schematic illustration of smart contact lenses for monitoring glucose *via* a smartphone. (d) and (e) Images of rabbits fitted with the smart contact lenses: (d) without UV LED illumination; (e) under UV LED illumination. (f) Time-dependent fluorescence analysis of the contact lenses on rabbits and corresponding blood glucose levels measured *via* a commercial glucometer. Adapted with permission from ref. 239. Copyright (2022) Elsevier B. V.

concentration of glucose in human tears. Fluorescent images of the contact lens can be captured *via* a smartphone under illumination from a portable UV LED (light-emitting diode), and glucose concentrations are quantified by analyzing the blue-to-red (B/R) RGB intensity ratio. *In vivo* validation in New Zealand white rabbits confirmed the sensor's biocompatibility (with no ocular irritation observed after 7 days of wear) and reliability: fluctuations in the B/R ratio correlated with changes in blood glucose levels measured by a commercial glucometer.

In 2014, DeHennis and Tian *et al.* developed a wireless subcutaneously implantable glucose sensor using Shinkai derived **196** as the glucose probe combined with wearable sensors to form a novel continuous glucose monitoring system (Fig. 105).[240] The diboronic acid probe **196** is coated onto a miniature optical detection system which connects to an external transmitter *via* wireless communication, itself connected to a smartphone app *via* Bluetooth to enable CGM. Testing has demonstrated that the accuracy of this system is comparable to that of traditional venous blood glucose measurement methods. Preliminary clinical work indicated that during a 28-day implant period in 12 type 1 diabetic patients, the glucose measurement accuracy of this sensor was comparable with that of existing commercial CGM devices.

Following this development, several companies aimed to commercialize the copolymer-based diboronic acid CGM sensor, leading to Eversense CGM.[241,242] Human studies lasting 90 days demonstrated the device's safety and effectiveness,

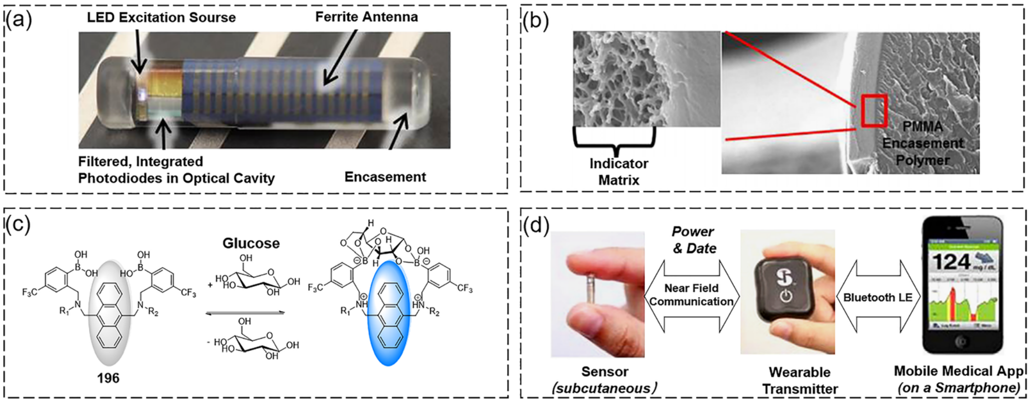

Fig. 105 (a) Photograph of the implantable glucose sensor. (b) Scanning electron microscope (SEM) images showing the glucose indicator hydrogel grafted onto the exterior of the PMMA sensor casing. (c) Glucose-binding probe **196**. (d) Components of the continuous glucose monitoring system. Adapted with permission from ref. 240. Copyright (2014) Elsevier B.V.

resulting in its CE mark approval in Europe and South Africa in 2016, followed by USFDA clearance in 2018.[243,244] In these trials, the compact sensor was implanted in the subcutaneous tissue of the upper arm—rather than the wrist—thereby enhancing patient comfort and allowing the detachable receiver/power supply to be worn on the arm.

Furthermore, the PRECISE[245] and PROMISE[246] trials assessed the performance of the Eversense CGM system over a 180-day (6-month) period. In line with previous findings, the device was found to be both safe and effective, with only a small proportion of sensors requiring replacement prior to the end of the 180-day period, as indicated by alerts from the sensor in combination with the smartphone application. The latest 365-day long-term CGM system has been made accessible to consumers in the United States.[246] In 2022, the Eversense E3 180-day sensor received both CE mark certification in Europe and FDA approval. Following its clinical success, the Eversense System became the first long-term CGM to gain FDA approval as an integrated continuous glucose monitoring system (iCGM) under the FDA's *De Novo* pathway in April 2024.[247] Integrated with insulin pumps, iCGM systems use algorithms to predict and address hypo- and hyperglycemic events and trends without requiring intervention from the patient.

In 2017, Yang and Tang *et al.* developed a novel non-invasive, highly selective nanosensor **197** incorporating the original Shinkai probe **133** (Fig. 106),[248] which successfully achieved sensitive detection of intracellular glucose using a two-step recognition method. This nanosensor employs liposomes encapsulating aptamer-functionalized gold nanoparticles (AuNPs), Shinkai probe **133**, and complementary oligonucleotides labeled with rhodamine dye conjugated to the AuNPs. Once this nanosensor enters the cell, probe **197** is bound by glucose, inducing a conformational change in the nanosensor. This conformational change triggers the release of the rhodamine-labeled oligonucleotides from the gold nanoparticles. As the rhodamine dye is no longer subject to quenching by the gold nanoparticle the fluorescence signal is restored, thereby reflecting the changes in glucose concentration dynamically. By combining glucose-specific probe **133** with nucleic acid recognition mechanisms, this nanosensor achieves high selectivity for intracellular glucose. However, the method requires the use of cetyltrimethylammonium bromide as a cell membrane permeabilizer to facilitate the entry of the nanoprobe into cells, which may interfere with the glucose metabolism of the cells, limiting the ability of the nanosensor to accurately reflect intracellular glucose fluctuations.

In 2019, Bazan and Wang *et al.* developed an electrochemical glucose sensor based on Shinkai probe derivative **198** DBA2+ with high affinity for glucose ($K_d \approx 1$ mM) and excellent selectivity. (Fig. 107).[249] probe **198** incorporates two *ortho*-aminomethylphenylboronic acid groups, a design that provides the chemical basis for maintaining selectivity for glucose. In phosphate buffer, glucose reacts with **198** to reduce the pK_a of the probe from 9.4 to 6.3, thereby initiating deprotonation of the probe, and the released protons are neutralized by HPO_4^{2-}. When glucose is present, **198** and HPO_4^{2-} in the system (with higher ionic conductivity, left, red) are converted to **198**/glucose complex (DBA-G) and HPO_4^{-} (low ionic conductivity, right, blue), and the proton release rate of **198** shows a good linear relationship with glucose concentration (0–30 mM). In addition, the electrochemical probe exhibits no interference with other sugars (such as maltose, fructose, sucrose, lactose, and galactose) during glucose detection, indicating that the

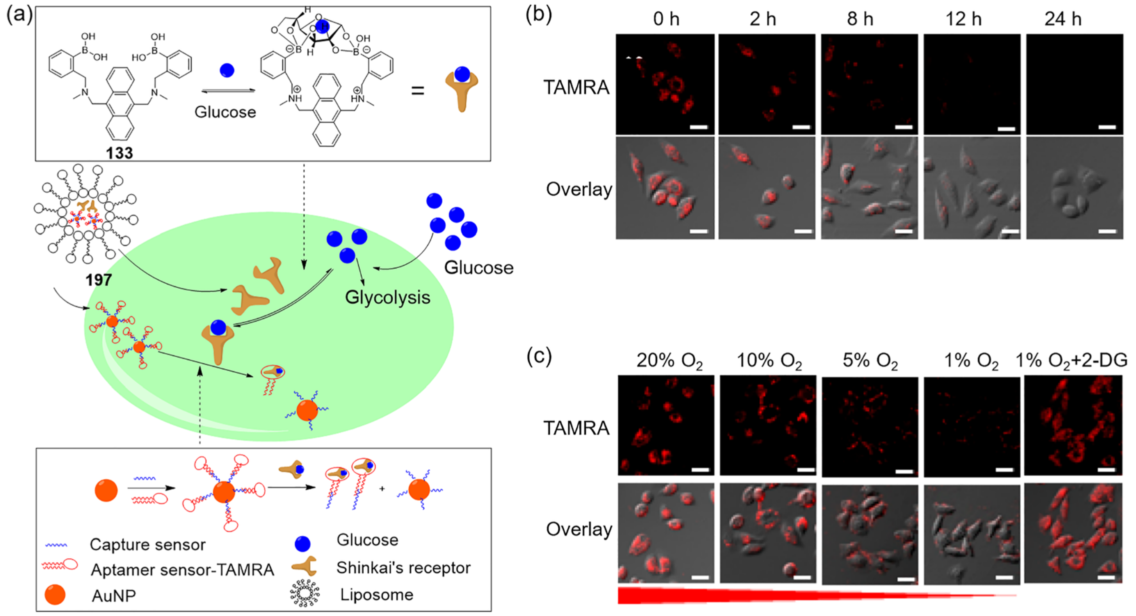

Fig. 106 (a) Schematic illustration of the intracellular glucose monitoring *via* a smart nanosensor **197** based on gold nanoparticles-functionalized aptamers and the Shinkai probe **133**-coencapsulated liposome. (b) Dynamic detection of intracellular glucose consumption in HeLa cells by **197** under normoxia at 0, 4, 8, 12, and 24 h. (c) Fluorescence images of glucose in HeLa cells under different oxygen concentrations (20%, 10%, 5%, 1% O_2) and upon 2-DG addition (5 mM). Adapted with permission from ref. 248. Copyright (2017) American Chemical Society.

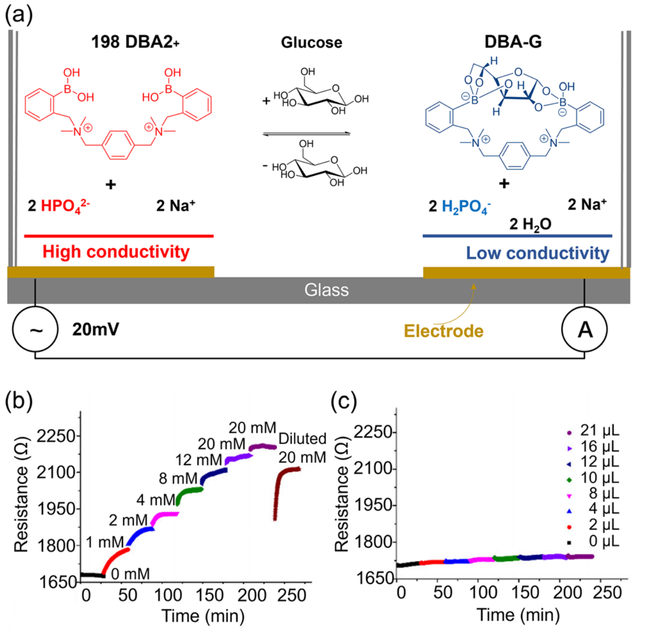

Fig. 107 (a) Schematic illustration of the binding interaction between **198** DBA2+ and glucose in a PBS buffer solution. (b) and (c) Variation in the solution resistance (*R*) of 1 mL of test solution with continuous additions of 0.5 M or 2 M glucose concentration (b), or with the addition of an equivalent volume of water as a control (c). Adapted with permission from ref. 249. Copyright (2019) Wiley-VCH Verlag GmbH & Co. KGaA, Weinheim.

electrochemical sensor **198** has good application prospects for the quantitative detection of glucose.

In 2019, Tian and Deng *et al.* developed the ratiometric nanosensors **199** based on a tricolor core–shell polymer with dual responsiveness to glucose and oxygen (Fig. 108).[250] Nanosensors **199** were constructed by covalently embedding the red emitting oxygen probe **199a** (OS1) and yellow emitting reference probe RDMA into a hydrophobic core and covalently grafting blue emitting glucose probe **195** GS-NHS onto hydrophilic shells. Sensors **199** can simultaneously and sensitively detect glucose in the range of 0.01 to 5.0 mM and dissolved oxygen in the range of 0.05–39.3 mg L^{-1}. HeLa cells stained with the nanosensors **199** displayed an increase in blue emission when glucose was added, and an increase in red emission when oxygen was reduced, while retaining a constant yellow emission to allow ratiometric interpretation. The ratiometric luminescent nanosensors **199** developed in this study offer simultaneous monitoring of intracellular glucose and oxygen concentrations with good cellular permeability and low cytotoxicity, making it a promising tool for cellular imaging and real-time dynamic monitoring.

In 2021, Meng and Wang *et al.* synthesized phenylboronic acid-modified diboronic acid probes **200a–d** by introducing fluorine, chlorine, methoxy, or cyano substituents at the *para* position of phenylboronic acid of Shinkai probe **133** (Fig. 109).[251] Consistent with the work of Wang and Kaur[231] above, the electron-poor cyano-substituted probe **200d** exhibited the highest glucose binding affinity (6489.5 M^{-1} in 33% MeOH). More importantly, it exhibited excellent aqueous solubility, ultra-sensitive recognition of glucose with a detection limit of 1.51 μM, and stability and sensitive fluorescence response over a pH range of 6.0–9.0. Thanks to these properties, probe **200d** was successfully deployed for glucose detection in cell lysates and plasma samples. **200d** was found to be highly sensitive and accurate for glucose detection in complex biological systems. Building on this in 2023, James and Wang *et al.* synthesized anthracene-modified diboronic acid probes **201a–b** by introducing carboxylate and methyl ester substituents onto the anthracene of **200d.**[252] **201a** (CO_2Me derivative) exhibited high sensitivity toward glucose (F/F_0 = 47.8, LOD = 1.37 μM), while probe **201b** showed high glucose affinity (K_a = 4.5 × 10^3 M^{-1}). Probe **201a** was successfully employed to distinguish glucose heterogeneity between normal and tumor cells. Additionally, both probes **201a** and **201b** were effectively used for fluorescence imaging of glucose in zebrafish larvae. This study provides a novel strategy for designing highly efficient boronic acid-based glucose probes and offers a reliable detection tool for the diagnosis and treatment of glucose-related diseases.

Boronic acid-based probes clearly offer distinct advantages over the other manifolds discussed in Sections 2–5 of this review (Table 6). One key feature is their reversible recognition mechanism: they form reversible covalent boronate esters with the *cis*-diols of glucose, generating no by-products. By their nature, they can be readily modified structurally to control the wavelength, solubility, fluorescence mechanism, or conjugated with other functional motifs such as fluorophores, nanomaterials, and polymers, enabling the construction of diverse detection platforms. These probes exhibit broad applicability, covering physiological glucose concentrations and facilitating detection in various samples, including serum, interstitial fluid, and intracellular fluid. Additionally, they demonstrate excellent stability: they are chemically stable, resistant to degradation during storage, and some probes, for example, PEG-bonded polyacrylamide hydrogel fibers, can function stably *in vivo* at physiological temperature for up to 140 days (with longer trials ongoing),[235] outperforming enzyme-based probes in long-term application.

However, boronic acid-based probes are also limited in several key aspects. Insufficient selectivity is a primary concern, as they are easily interfered with by other *cis*-diol-containing sugars like fructose and galactose. pH dependence is another key consideration, as phenylboronic acid have a relatively high pK_a (~8.8), leading to reduced binding affinity at physiological pH (7.4) which impairs detection sensitivity in biological environments. While diboronic acid probes have shown improved selectivity, further optimization is still required. Limited water solubility and biocompatibility remain significant challenges, as many probes incorporate hydrophobic fluorophores (such as anthracene or pyrene). This hydrophobicity reduces aqueous solubility and restricts their suitability for *in vivo* applications.

Enhancing selectivity remains central to boronic acid probe development. Diboronic acid systems, such as Shinkai-type probes, look to address this by leveraging glucose's dual *cis*-diol structure for specific recognition. For instance, probe **133** demonstrates a 12-fold higher selectivity for glucose over fructose, highlighting the effectiveness of this design in distinguishing glucose

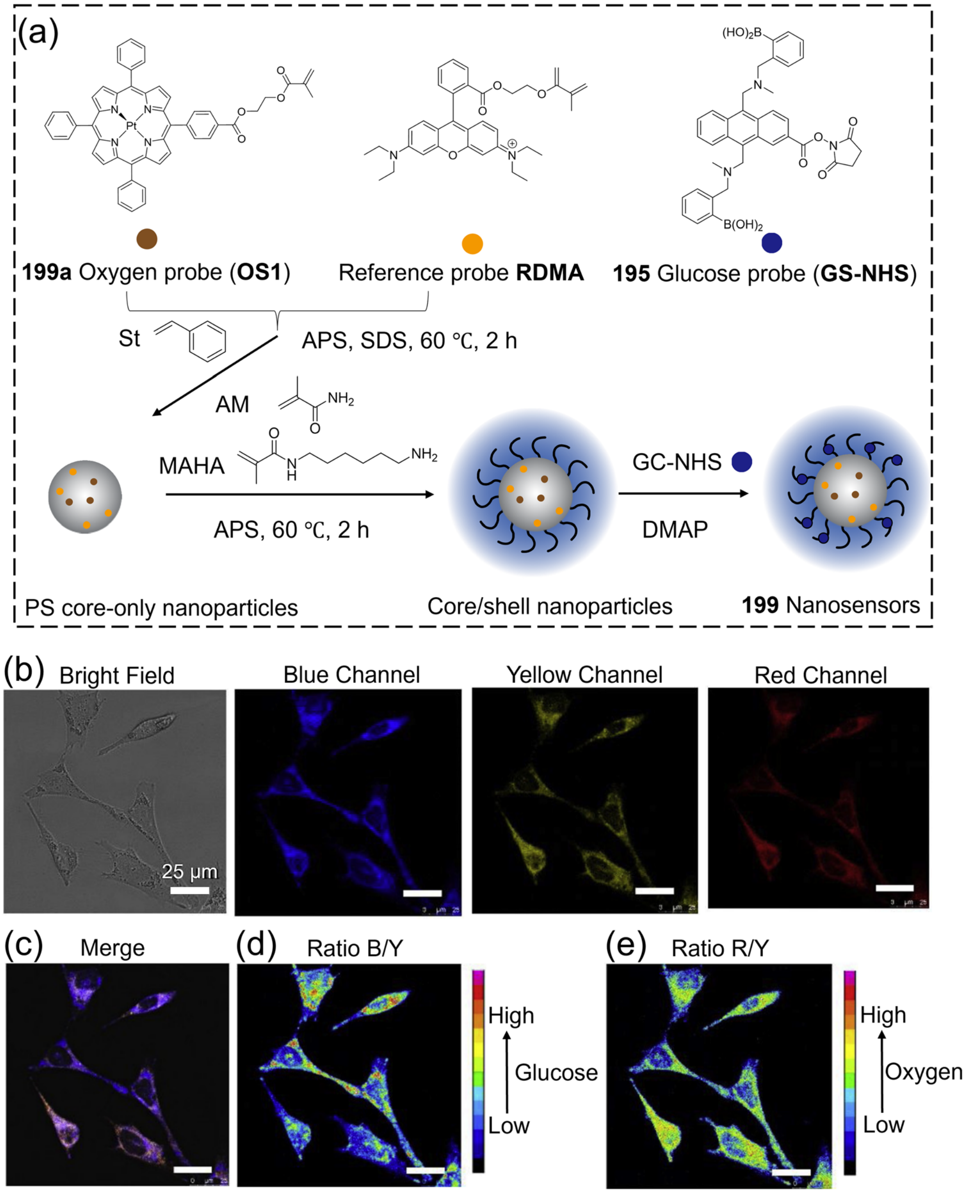

Fig. 108 (a) Components and synthesis of polymeric ratiometric nanosensors **199**. (b) Confocal luminescence images (λ_{ex} = 405 nm) of HeLa Cells incubated with nanosensors **199** (0.5 mg mL^{-1}) for 24 h. (c) Merged image of the confocal images. Ratio of pseudo color of blue channel/yellow channel (d) and red channel/yellow channel (e). Adapted with permission from ref. 250. Copyright (2019) Elsevier B.V.

from structurally similar sugars.[164] pH adaptability can be addressed by introducing electron-withdrawing substituents (*e.g.*, cyano, nitro, fluorine) to reduce the pK_a of boronic acids to the physiological range (6.5–7.5). *o*-Aminomethylphenylboronic acids also achieve this, stabilizing saccharide binding at neutral pH.[174] A notable example is the cyano-substituted diboronic acid probe **200d**, which has a pK_a of 4.8, significantly enhancing its ability to bind under physiological conditions.[251]

Improving water solubility and biocompatibility can be achieved through various modifications, including PEGylation, introduction of carboxyl groups, or conjugation with hydrophilic carriers such as PVA hydrogels and graphene quantum dots. For instance, APBA-functionalized quantum dot probe **154** shows improved water solubility and reduced toxicity, making it more suitable for biological applications.[193]

Accelerating response and sensitivity is facilitated by the use of nanostructures like gold nanorods and mesoporous silica, which increase the specific surface area and enhance interactions with glucose. Meanwhile, developing ratiometric fluorescent probes, such as the dual-emission quantum dot probe **155**, helps reduce environmental interference, enabling a detection limit as low as 4.5 μM.[194] The development of NIR-emissive glucose probes with high two-photon absorption cross-sections should also be encouraged, as these features reduce light scattering, enable deeper tissue penetration, and minimize photodamage by lowering the need for intense pulsed laser excitation during *in vivo* imaging.

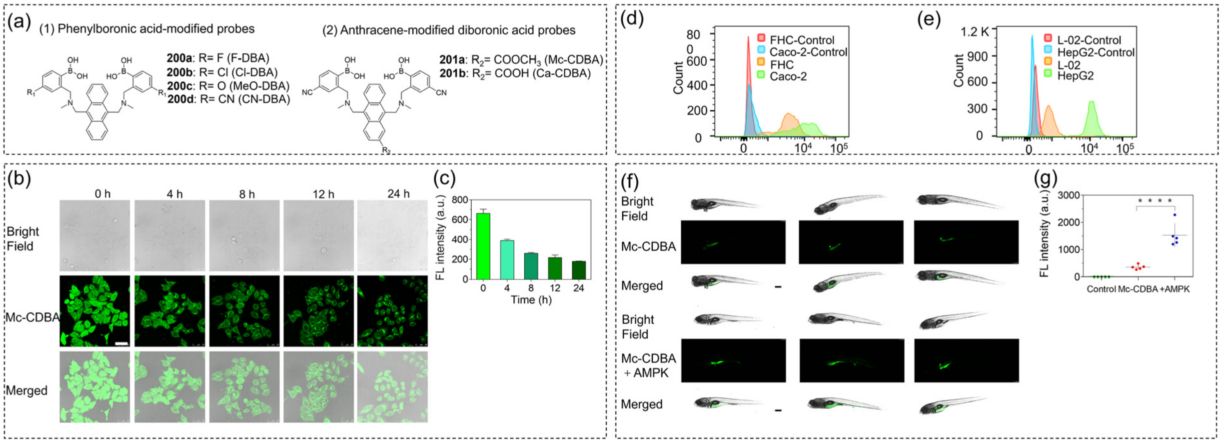

Fig. 109 (a) Structure of the phenylboronic acid-modified probes **200a–d** and anthracene-modified diboronic acid probes **201a–b**. (b) and (c) Confocal microscopy images (b) and fluorescence intensity (c) of HeLa cells preincubated with glucose-free DMEM for 0, 4, 8, 12, and 24 h, then incubated with 50 μM **201a** for 30 min. (d) Flow images of probe **201a** distinguishing Caco-2 cells from FHC cells. (e) Flow images of probe **201a** distinguishing HepG2 cells from L-02 cells. (f) and (g) Fluorescence confocal images (f) and fluorescence intensity (g) of 7 dpf zebrafish embryos preincubated with blank medium and 20 μM ampkinone medium for 4 h, then groups further incubated with 50 μM **201a** for 1 h. Adapted from ref. 252, published by American Chemical Society.

7. Conclusions and outlook

As a cornerstone of metabolic processes, the dynamic fluctuations of glucose demand precise, real-time monitoring in order to advance both biological understanding and clinical practice. Recent innovations in probe design have transformed our ability to visualize and quantify glucose in complex environments, leveraging strategies from glucose analogues to boronic acid sensors. These developments not only enhance analytical capabilities but also open new avenues for non-invasive diagnostics and mechanistic insights. To address this need, a range of innovative glucose probes have been engineered, incorporating versatile molecular design approaches and offering non-invasive detection capabilities. The broad range of designs have been extensively presented throughout this review, including: glucose analogue-based tracers; enzyme-based probes; fluorescent protein-based probes; lectin-based sensors; and boronic acid glucose probes.

Radiolabeled tracers such as ^{18}F-FDG and fluorescent derivatives have enabled sensitive metabolic visualization, but remain limited by radiation exposure, shallow penetration, and interference with glycolysis. Enzyme-based systems, primarily glucose oxidase, improved real-time sensing with high specificity, yet oxidative byproducts and enzyme instability restrict long-term use. Genetically encoded fluorescent protein probes advanced live-cell imaging but face photobleaching and modest dynamic range, underscoring the need for robust, non-enzymatic alternatives.

Lectin-based probes, exemplified by ConA, introduced reversible glucose recognition without oxidative stress, supporting diverse sensing platforms from fluorescence to quartz crystal microbalance. However, low affinity ($K_a < 1000$ M^{-1}), moderate selectivity, and susceptibility to biological interference limit their clinical viability. Recent biomimetic designs of the types reported by Davis *et al.* incorporating synthetic receptors and chiral architectures have improved specificity, though challenges in solubility and stability remain.

Boronic acid-based probes represent the most versatile and clinically impactful recent approach. Exploiting reversible covalent binding to glucose *cis*-diols, these systems deliver byproduct-free sensing and exceptional structural adaptability, enabling integration with fluorophores, polymers, and nanomaterials across optical, electrochemical, and fiber-based platforms. Their durability is exemplified by PEG-linked hydrogel fibers functioning *in vivo* for 140 days, while the Eversense continuous glucose monitoring system demonstrates successful clinical translation, offering long-term implantable sensing (>1 year lifetime so far). Despite limitations such as pH-dependence, hydrophobic fluorophores, and potential for cross-reactivity with other *cis*-diol bioanalytes, boronic acid-based designs combine stability, adaptability, and strong potential for next-generation glucose monitoring. Collectively, these advances provide a clear trajectory toward non-enzymatic, reversible recognition systems with high affinity and biocompatibility. Boronic acid-based probes, in particular, appear poised to dominate future development, bridging fundamental innovation with real-world clinical impact.

Given the remarkable pace of progress for glucose probes in biological imaging applications over recent years, we wish to conclude this review by highlighting several critical areas where further investigation remains urgently needed.

7.1. The future of glucose sensing research

Signal molecule monitoring has emerged as a research hotspot in the field of signal transduction.[253] Among them, Ca^{2+}, as a well-established second messenger, is one of the most conserved and ubiquitously present intracellular signaling molecules. The generation and termination of calcium signaling arise from the spatiotemporal dynamic fluctuations in intracellular calcium ion concentrations, giving rise to two classical phenomena in

Table 6 Key properties of representative boronic acid-based probes

Probe	$\lambda_{ex}/\lambda_{em}$	Glucose binding constant (K_a)	Characteristics	Detection systems
131	—/416 nm	—	Chelation-enhanced quenching (CHEQ)	20 mM phosphate buffer (1% DMSO, pH = 7.4)
132	370/420 nm	—	Photoinduced electron transfer (PeT) + loose bolt internal conversion	0.05 mol dm^{-3} NaCl aqueous solution
133	370/423 nm	3981 M^{-1}	Selectivity order: D-glucose > D-allose > D-fructose ≈ D-galactose > ethylene glycol	33.3% MeOH/H_2O buffer (pH = 7.77), physiological glucose level detection
134	348/416 nm	—	Selectivity order: Catechol > dopamine ≈ L-DOPA > glucose > guaiacol > phenol	20 mM phosphate buffer (pH = 7.4), 1% v/v DMSO, catechol/catecholamine chemosensing
135	417/605 nm	—	"On–off" type PeT sensors	Water + MeOH (1 : 1 v/v), pH = 10.0
136	—/—	70.8 M^{-1}	Selectivity order: D-fructose > D-glucose > ethylene glycol	MeOH–H_2O (1 : 2 w/w) with 0.05 mol dm^{-3} NaCl (pH 11.32), visual detection
137	370/420 nm	70 ± 7 M^{-1}	Selectivity order: D-fructose > D-mannose > D-glucose > D-galactose	THF/H_2O (1 : 1 v/v) with 0.033 M phosphate buffer (pH = 7.3), fructose-selective detection
138	370/420 nm	130 ± 2.8 M^{-1}	Selectivity order: D-glucose > D-mannose > D-fructose > D-galactose	THF/H_2O (1 : 1 v/v) with 0.033 M phosphate buffer (pH = 7.3)
139	—/—	—	Detection range ≥0.4 mM, fully reversible	0.1 M phosphate buffer (pH 7.4/8/9)
140	—/—	—	Fully reversible, physiological pH-compatible	PBS buffer (pH 7.4), tear fluid
141	—/—	—	Linear range 0–23 mM, glucose-selective, negligible lactate interference, pH-stable	PBS buffer (pH 6–7), artificial tear fluid (pH 7.4)
142	—/—	370 M^{-1} (for the anionic boronate form)	Glucose-selective, LOD 10 μM	Artificial tear fluid (pH 7.4)
143	—/—	284 M^{-1} (for the anionic boronate form)	Glucose-selective, LOD 1 μM	Artificial tear fluid (pH 7.4)
144a	345/457 nm	20.2 M^{-1}	Glucose-responsive, pK_a = 6.62 (with glucose)	Phosphate buffer (pH 7.5), tear fluid-mimetic environment
144b	345/457 nm	1.0 M^{-1}	Glucose-responsive, pK_a = 6.90 (with glucose)	Phosphate buffer (pH 7.5), tear fluid-mimetic environment
144c	345/457 nm	2.3 M^{-1}	Fructose-preferential but glucose-responsive, pK_a = 6.90 (with glucose)	Phosphate buffer (pH 7.5), tear fluid-mimetic environment
145	420/512 nm	—	Linear range 0–50 equiv. glucose	DMSO
146	463/616 nm	15 M^{-1}	Detection range 0–300 mmol L^{-1}, LOD 1.0 mmol L^{-1}	50 mmol L^{-1} phosphate buffer (pH 7.4)
147	366/500 nm	1.67 M^{-1}	Detection range 0–1.0 M, $\lambda_{ex}/\lambda_{em}$: 780 nm/500–620 nm (Two-photon)	30 mM PBS buffer (pH 7.4), live cells, deep tissue
148	328/390, 510 nm	1378 M^{-1}	Selectivity order: D-glucose > D-fructose > D-mannose > D-galactose, LOD 10 μM	0.1 M carbonate buffer (pH 10.0) with 2% (v/v) methanol
149	358/418 nm	—	Glucose-selective, linear range 0.003–3.0 mM	20 mM NH_3–NH_4Cl buffer, human serum
150	360/425 nm	—	Glucose-selective, linear range 0–20 mM, LOD 10 μM, low cytotoxicity	PBS buffer (pH 7.4), artificial tear fluid, HepG2 cells, mouse
151	—	—	Glucose-selective, linear range 10 μM–40 mM, LOD ∼5 μM, pH-stable	PBS buffer, tear, sweat, saliva simulates
152	532 nm (laser source)/-	—	Glucose-selective, linear range 1.0–12.0 mM	PBS buffer, gelatin phantom tissues, porcine tissue (*ex vivo*)
153	—/585–609 nm		Glucose-selective, linear range 0.4–20.0 mM, LOD 50 μM	Aqueous medium (pH 7.4), mouse melanoma B16F10 cells
154	290/370 nm		Glucose-selective, linear range 0.1–10 mM, LOD 5.0 μM, water-soluble	Aqueous solution (physiological pH), rat striatum microdialysate
155	330/530,660 nm	—	Glucose-selective, linear range 0.1–2.0 mM, LOD 4.5 μM, pH-stable	0.1 M PBS buffer (pH 7.4), naked-eye glucose detection, human serum samples
156	785/1000–1150 nm	—	Glucose-selective, linear range 5–30 mM, non-photobleaching, NIR fluorescence	2% sodium cholate aqueous suspension (pH 6–9, physiological range)
157	Visible light/532–655 nm	—	Glucose-selective, linear range 0–20 mM, naked-eye detectable, good dispersibility in PBS	PBS buffer (pH = 8.0, 150 mM ionic strength)
158	980/473,520 nm	—	Glucose-selective, linear range 0–30 mM, recyclable, deep tissue-penetrating, biocompatible	Aqueous solution, HEK293 cells + RIN-m5F cells, diabetic mice
159	—/—	1.18 × 10^3 M^{-1}	Glucose-selective, covalent molecular imprinting + boronate ester formation, pH-stable	D-Aldohexoses recognition in aqueous media, mimic natural lectin-sugar binding
160	—/—	—	Glucose-selective, linear range 0.30–10.0 mM, pH-controllable capture/release	Phosphate buffer (pH 4.0–6.0), rat brain microdialysate
161	—/—	132 ± 33 M^{-1}	Glucose-selective, LOD 1 mM, unique ^{19}F NMR fingerprint, pH-robust, water-soluble	100 mM HEPES buffer (pH 7.4, synthetic urine (30 mM HEPES)

Table 6 (*continued*)

Probe	$\lambda_{ex}/\lambda_{em}$	Glucose binding constant (K_a)	Characteristics	Detection systems
162	415/632 nm	—	Selectivity order: D-fructose > D-arabinose > D-mannose ≈ D-glucose	DMSO-water (1 : 30) buffer (pH 10.5)
163	289/358 nm	2000 M^{-1} (D-glucose), 1260 M^{-1} (L-glucose)	Chiral recognition of D/L-monosaccharides	33.3% MeOH/H_2O, pH 7.77, chiral discrimination in enantiomer mixtures
164	273/365 nm	91.2 M^{-1}	Glucose detection range 1.0–100 mM	33% MeOH/water buffer (pH 7.77)
164	296/347 nm	—	High selectivity for "small" saccharides	H_2O-MeOH (300 : 1 v/v), pH 8.0
166	377/427 nm	2512 M^{-1}	Glucose-selective, water-soluble, thermal stability	0.05 M phosphate buffer (pH 7.4)
167	274/404 → 362 nm	186 M^{-1}	Selectivity order: D-fructose > D-galactose > D-glucose > D-mannose	52.1 wt% MeOH-phosphate buffer (pH 8.21)
168	265/405 → 360 nm	140 ± 13 M^{-1}	Selectivity order: D-glucose > D-fructose > D-galactose > D-mannose	52.1 wt% MeOH-PBS (pH 8.21)
170	343/378 nm	—	6-carbon spacer: glucose-selective, spacer-length dependent specificity	33% (v/v) methanol: water (pH 7.77)
171	—/397 nm	962 ± 70 M^{-1}	Glucose-selective	52.1 wt% MeOH/PBS (pH 8.21)
174	342/377, 470 nm	2660 ± 200 M^{-1}	Dual-signal modulation (PeT + excimer)	52.1 wt% MeOH-phosphate buffer, pH 8.21
175c	—/—	6.19 × 10^3 ± 731 M^{-1}	Glucose-selective	pH 8.21 PBS buffer + 20% DMSO
176	330/432 nm	—	Glucose-selective (fluorescence "on–off")	Methanolic buffer (pH 8.21)
177	375/447 nm	4.0 × 10^4 M^{-1}	D-glucopyranose-selective	30% MeOH-PBS (pH 7.5)
178	285/480 nm	24 800 M^{-1} (D-glucose)	K_a = 11 900 M^{-1} (L-glucose), enantioselectivity	Water/methanol (1 : 1, v/v), pH = 11.7
179	470/510 nm	1800 ± 200 M^{-1}	Charge-modulated quenching/recovery	PBS (pH 7.4)
180	460/510 nm	1900 ± 200 M^{-1}	Glucose-selective (glu/fru = 1.7, glu/gal = 11)	PBS (pH 7.4)
181	460/604 nm	—	Glucose-selective (quenching/recovery specific to glucose)	PBS (pH 7.4)
182	310/445 nm		Linear range 0–60 mM, GQDs properties	PBS (pH 7.4)
183	365/485 nm	—	Glucose-specific (oligomerization-enabled), AIE-active	2 vol% DMSO/carbonate buffer (pH 10.5), artificial urine
184	376/448 nm	1048 ± 64 M^{-1}	Glucose-selective, supramolecular fluorescent ensemble	1 vol% DMSO/aqueous buffer (pH 10.5)
185a	—	45 M^{-1}	^{19}F NMR-based sensor, LOD 200 μM	50 mM phosphate/HEPES buffer
186	350/592 → 452 nm	816 M^{-1}	Vibration-induced emission (VIE), LOD 9.4 μM	80% MeOH/10 mM PBS (pH 7.4)
187	370/423 nm	53.7 M^{-1}	Glucose selectivity inherited from diboronic acid "cleft" design	33.3% MeOH-H_2O (pH7.77)
188	365/429 nm	28.2 M^{-1}	High enantioselectivity (up to 550 : 1) for sugar acids	52.1% MeOH/water, 0.05 M NaCl buffer
189a	370/423 nm	1472 M^{-1}	High glucose selectivity (43 × *vs.* fructose, 49 × *vs.* galactose)	50% MeOH/0.1 M phosphate buffer
190a	370/423 nm	101 ± 5.2 M^{-1}	Fructose-preferential, 13-fold fructose/glucose selectivity	50% MeOH/phosphate buffer (pH7.4)
191a	370/423 nm	2540 ± 90.1 M^{-1}	3-fold selectivity *vs.* fructose, 10-fold fluorescence enhancement	50% MeOH/phosphate buffer (pH7.4)
192	405/450 nm	—	Glucose-selective, PEG-modified for biocompatibility	Minimally invasive *in vivo* CGM *via* subcutaneous injection in mouse ears
193	390/445 nm		Linear range 1–30 mM, glucose-selective over fructose/galactose/mannose	Phosphate buffer (pH 7.4), *E. coli*, *B. subtilis*, HeLa, J774 cells
194	390/445 nm	—	Glucose-responsive, pH-stable, cell-permeable	PBS (pH 7.4), HeLa, CPA, U87-MG, J774.A1 cells
195	390/440	—	Linear range 9.3 μM–1 mM, LOD 9.3 μM, ratiometric, glucose-selective	PBS (pH 7.4), artificial tears, *in vitro* glucose solutions, *in vivo* rabbit tear fluid
196	—	—	Glucose-selective, abiotic (non-enzymatic), 28-day *in vivo* stability, anti-biofouling	Interstitial fluid, *in vivo* human (diabetes patients), subcutaneous implantation
197	405/425 nm	—	$\lambda_{ex}/\lambda_{em}$ = 568/570–680 nm (TAMRA), detection range 0–2 mM, LOD 33 nM	HEPES buffer (pH 7.4), cell lysate, HeLa cells
198	—	1000 M^{-1}	Glucose-selective, detection range 0–20 mM, pK_a shift (9.4 → 6.3) upon glucose binding	50 mM phosphate buffer (pH 7.4)
199	405/430–480 nm		Glucose-selective, linear range 0.01–5.0 mM, tricolor non-cross-interfering, pH-stable	PBS (pH 7.4), HeLa/J774 A.1 cells
200d	375/427 nm	3349.8 M^{-1}	Glucose-selective, linear range 6.1 μM–12.5 mM, LOD 1.51 μM, pH-stable	0.5% MeOH/PBS (pH 7.4), cell lysates, DMEM, plasma
201a	393/457 nm	710 M^{-1}	Glucose-selective, linear range 12.2 μM–12.5 mM, LOD 1.37 μM, pH-stable	0.5% MeOH/PBS (pH 7.4), DMEM, sheep plasma, HeLa/HepG2/Caco-2/L-02/FHC, zebrafish embryos (1–10 dpf)

calcium signal transduction: calcium oscillations[254,255] and calcium waves.[256–258] Experimental studies on glucose sensing in cells have demonstrated that intracellular glucose levels also undergo oscillatory fluctuations akin to calcium signaling. Increasing evidence suggests that glucose exhibits characteristics of a ‘‘messenger’’ molecule.[10,11] It is not only closely associated with the generation of signals such as Ca^{2+} and ROS, but also participates in signal transduction processes that regulate the functions of various metabolism-related proteins. However, current research on the real-time and dynamic detection of intracellular glucose remains in its infancy. The accuracy and sensitivity of different types of probes for detecting glucose dynamics in cells remain unclear, warranting further investigation.

With the growing global threat posed by major health conditions such as diabetes, cancer, and neurological disorders---all of which exhibit significant abnormalities in glucose metabolism and function—achieving specific recognition of glucose in complex biological environments has become a central challenge. Until recently, studies on intracellular glucose sensing has remained rather limited. Furthermore, research on the impact of blood glucose fluctuations on other signaling molecules remains scarce. In particular, enabling dynamic detection with high spatiotemporal resolution is crucial for elucidating the sensing mechanisms, signal transduction pathways, and biological functions of glucose as a signaling molecule. The development and application of highly efficient glucose probes hold promise for uncovering the functional roles and regulatory mechanisms of glucose abnormalities associated with disease. If the complete communication mechanisms of cells can be elucidated, it will provide new insights and strategies for addressing a range of severe human diseases (*e.g.*, diabetes, cancer, and psychiatric disorders) caused by cellular signal transduction disorders.

7.2. The future of glucose probe research

For the future development of glucose tracer probes, non-disruptive probes should be prioritized as a pivotal goal, with an emphasis on designing tracers that fully mimic endogenous glucose metabolism. Such tracers should avoid interrupting glycolysis or altering cellular physiology, thereby enabling the faithful tracking of glucose uptake and dynamics in biological systems. By closely resembling natural metabolic processes, these tools can provide more accurate insights into glucose utilization and regulation at the cellular and tissue levels. Meanwhile, developing reversible recognition mechanisms is essential to overcome the limitations of ‘‘metabolic trapping’’. Probes developed based on the reversible binding of glucose to glucose-binding proteins, ConA and boronic acids can respond to real-time changes in glucose concentration, allowing for dynamic monitoring of fluctuations rather than capturing only static snapshots. This reversibility is critical for understanding rapid metabolic shifts, such as those occurring in response to hormonal signals or environmental stimuli.

Boronic acid-based fluorescent probes represent a rapidly developing field in glucose recognition research. In this section, we outline a series of frequently encountered challenges that affect the performance and utility of most boronic acid-based fluorescent probes. To date, the majority of boronic acid-based glucose fluorescent probes possess relatively short emission wavelengths, which typically result in a low signal-to-noise ratio, thereby compromising the reliability and precision of the acquired data. Consequently, the design and development of NIR-based boronic acid probes represent a critical future direction for advancing fluorescence imaging technologies. Beyond advancing NIR probes, it is equally crucial to focus on developing ratiometric boronic acid fluorescent probes, as these systems enable more accurate and quantitative detection in biomedical contexts through internal signal calibration mechanisms. Equally important, when constructing high-performance boronic acid-based fluorescent probes, several key parameters—including aqueous solubility, fluorescence quantum yield (QY), photostability, cytotoxicity, and cellular permeability—must be carefully considered and optimized to ensure their effectiveness in biological applications.[259–261]

7.3. Multimodal detection systems

Although considerable progress has been made in the design and application of glucose probes over the past decade, a major drawback of relying on a single detection modality is its inherent limitation in capturing comprehensive, multidimensional biological information. In this context, integrating multiple glucose detection techniques has attracted growing attention, as it can reduce the risk of misdiagnosis and minimize the loss of critical data.[262–264] As summarized in this review, various strategies have been employed to detect glucose fluctuations in living systems, including glucose analogue-based tracers, enzyme-based probes, fluorescent protein-based probes, lectin-based sensors, boronic acid glucose probes, and other probes. Thus, in biological glucose detection, the development of multimodal glucose detection technologies is essential to effectively evaluate the accuracy and sensitivity of different glucose detection methods.

Promoting the integration of multimodal technologies with intelligent devices constitutes another important direction. Combining fluorescence-electrochemical or MRI-optical multimodal approaches *via* smart devices allows for the simultaneous acquisition of metabolic and anatomical information, thereby providing a more comprehensive understanding of glucose-related biological processes. Additionally, portable devices integrated with AI algorithms—such as smartphone-integrated sensors—enable real-time data analysis, enhancing the practicality and efficiency of glucose detection across various settings. In future research, the integration of multimodal glucose detection data will yield more comprehensive and accurate insights into dynamic glucose fluctuations within living cells and entire organisms.

7.4. Multichannel detection systems

Owing to the complexity and highly dynamic nature of biological systems, static single-signal acquisition methods are insufficient to capture the full spectrum of physiological and pathological alterations.[265–270] Herein, we highlight that robust detection systems possess the exceptional capability to simultaneously monitor multiple analytes in a single biological sample. This multiplex detection holds great promise for significantly enhancing our understanding of complex biological phenomena, as multiple molecular species typically act in concert to trigger specific physiological or pathological responses. This multiplexed approach offers powerful insights into the spatiotemporal coordination of cellular signaling cascades, thereby advancing our understanding of biological complexity and disease pathogenesis.

Accordingly, by monitoring information on glucose alongside multiple signaling molecules or physiological metabolic parameters, we can acquire *in situ*, dynamic and multi-source metabolic parameters of cells. For instance, a multi-channel fluorescent platform capable of simultaneously monitoring glucose and other key signaling molecules (such as Ca^{2+}, ROS, *etc.*) could be developed in the future. Subsequently, this multi-target molecule monitoring approach will provide comprehensive information for investigating the regulatory mechanisms of cellular glucose homeostasis, the interactions between glucose and signaling molecules as well as their spatiotemporal evolution patterns. It will facilitate a thorough analysis of dynamic correlations within cellular energy metabolism networks and ultimately offer new insights into the pathogenesis of metabolic diseases.

7.5. *In vivo* cellular imaging and detection

In vivo cellular imaging and detection is an emerging technique in biophotonic imaging that enables non-invasive, real-time, and dynamic monitoring of cellular target molecules within living small animals.[271–273] The key advantages of *in vivo* cellular imaging in live animals include: (1) reflection of true physiological states: monitoring can be performed while animals are freely moving and maintaining near-natural physiological conditions. This avoids the behavioral and functional alterations often introduced during *ex vivo* experiments, where cells are removed from their native environment. (2) long-term dynamic monitoring: This method enables continuous, longitudinal observation of the same individual animal, making it possible to track cellular processes such as development, differentiation, migration, and the progression or treatment response to diseases over extended periods. (3) reduction of inter-individual variability: repeated imaging within the same subject reduces variability caused by differences between individual animals, thereby improving the reliability and comparability of experimental data.

A comprehensive understanding of glucose metabolic heterogeneity necessitates the development of high-resolution imaging systems capable of single-cell and subcellular resolution.[274] In the realm of super-resolution cellular imaging, several advanced techniques are currently widely employed, including stimulated emission depletion (STED), structured illumination microscopy (SIM), and photo-activated localization microscopy/stochastic optical reconstruction microscopy (PALM/STORM). These imaging modalities overcome the diffraction limit of light and allow for nanoscale visualization of cellular structures and molecular events. By integrating super-resolution imaging with *in vivo* optical imaging approaches, researchers can achieve deeper and more precise insights into the behavior of intracellular molecules and cellular structures under physiological conditions in awake animals. For instance, in the future, high-resolution imaging of intracellular glucose dynamics could be combined with monitoring of systemic glucose levels to investigate the regulatory mechanisms between cellular glucose homeostasis and systemic glucose control. Such innovations are expected to provide a robust theoretical framework for the precise diagnosis and targeted treatment of these diseases.

Glucose probes have proven highly effective for both cellular studies and *in vivo* applications, with several successfully deployed in disease models to reveal critical links between glucose homeostasis and pathology. This review provides a clear overview of current probe technologies and the design principles shaping their development. By highlighting these advances, we aim to deepen understanding of glucose regulation in health and disease while driving innovation in sensing platforms. Such progress holds promise for clinical research, molecular imaging, and therapeutic discovery. Looking ahead, breakthroughs will require interdisciplinary collaboration and resource sharing across chemical biology, bioanalysis, and medical sciences. We hope this review serves as a catalyst for these efforts, inspiring the next generation of glucose-sensing tools and accelerating their translation into impactful applications.

Conflicts of interest

There are no conflicts to declare.

Abbreviations

AAPBA	3-Acrylamidophenylboronic acid
AD	Alzheimer's disease
ADP	Adenosine diphosphate
AEQ	Aequorin
AFM	Atomic force microscopy
AIE	Aggregation-induced emission
AMP	Adenosine monophosphate
AMPK	AMP-activated protein kinase
APBA	3-Aminophenylboronic acid
APS	Aminopropylsilatrane
ATP	Adenosine triphosphate
BA	Boronic acid
BINOL	1,1′-bi-2-naphthol
BPmoc	*p*-Boronophenylmethoxycarbonyl
C–D	Carbon-deuterium
CDP-DAG	Cytidine diphosphate diacylglycerol
CE	Capillary electrophoresis
CFP	Cyan fluorescent protein
CGM	Continuous glucose monitoring
CH–π	Carbon–hydrogen···π
CHEQ	Chelation-enhanced quenching
Chol	Cholesterol
ChOx	Cholesterol oxidase
CLP	Caged luciferin triarylphosphine ester
CoA	Coenzyme A
ConA	Concanavalin A
cpYFP	Circularly permuted yellow fluorescent protein
CQDs	Carbon quantum dots
CS	Chitosan
CT	Computed tomography

CTP	Cytidine triphosphate
Cy3	Cyanine 3
Cy5.5	Cyanine 5.5
CyNA	Amine-acetylated tricarbocyanine dye
DAP	2,3-Diaminophenazine
DAPI	4′,6-Diamidino-2-phenylindole
DBA	Diboronic acid
DCM	Dicyanomethylene-4*H*-pyran
DCI	Dicyanoisophorone
DexP	Phenoxy-derived dextran
DMEM	Dulbecco's modified Eagle's medium
DMSO	Dimethyl sulfoxide
DNP	Dynamic nuclear polarization
E. coli	*Escherichia coli*
ECL	Electrochemiluminescence
EDC	1-ethyl-(3-dimethylaminopropyl)carbodiimide
eCFP	Enhanced cyan fluorescent protein
ESIPT	Excited-state intramolecular proton transfer
ETC	Electron transport chain
eYFP	Enhanced yellow fluorescent protein
FAS	Fluorescence affinity sensor
FD-FLIM	Frequency-domain fluorescence lifetime imaging microscopy
FDG	2-Fluoro-2-deoxy-D-glucose
FET	Field effect transistor
FFT	Fast Fourier-transform
FI	Fluorescence intensity
FITC	Fluorescein isothiocyanate
FLIM	Fluorescence lifetime imaging microscopy
FRET	Förster resonance energy transfer
G-3-P	Glucose 3-phosphate
G-6-P	Glucose 6-phosphate
GA	Glutaraldehyde
γ-CyD	γ-Cyclodextrin
GBP	Glucose-binding protein
GBM	Glucose-binding molecule
GGBP	Glucose/galactose-binding protein
GL	Glucose-like ligands
GlcN	D-Glucosamine
GlcNAc	*N*-Acetylglucosamine
GLP-1	Glucagon-like peptide-1
GLUTs	Glucose transporter proteins
GMP	Guanosine monophosphate
GO	Graphene oxide
GOx	Glucose oxidase
GQDs	Graphene quantum dots
GSH	Glutathione
GSSH	Glutathione disulfide
H_2O_2	Hydrogen peroxide
HEMA	2-Hydroxyethyl methacrylate
HEPES	4-(2-Hydroxyethyl)piperazine-1-ethanesulfonic acid
HUVEC	Human umbilical vein endothelial cell
ICT	Intramolecular charge transfer
IL-6	Interleukin-6
IL-17	Interleukin-17
iCGM	Integrated continuous glucose monitoring
IFE	Inner filter effect
IMP	Inosine monophosphate
ITC	Isothermal titration calorimetry
ITO	Indium tin oxide
K_{ATP}	ATP-sensitive K^+ channel
LED	Light-emitting diode
LOD	Limit of detection
MCU	Mitochondrial calcium uniporter
MG	Malachite green
MINP	Molecularly imprinted nanoparticle
MglB	Bacterial D-galactose-binding periplasmic protein
MOF	Metal–organic framework
MRI	Magnetic resonance imaging
MRS	Magnetic resonance spectroscopy
MTT	3-(4,5-Dimethylthiazol-2-yl)-2,5-diphenyltetrazolium bromide
Myo	Myoglobin
NADPH	Nicotinamide adenine dinucleotide phosphate
NBD	7-Nitrobenz-2-oxa-1,3-diazol-4-yl
NBD-Cl	4-Chloro-7-nitrobenz-2-oxa-1,3-diazole
NCLX	Na/Ca/Li exchanger
NIR	Near-infrared
NMR	Nuclear magnetic resonance
OAA	Oxaloacetate
OCT	Optical coherence tomography
OPD	*o*-Phenylenediamine
PA	Phosphatidic acid
PALM	Photo-activated localization microscopy
PAM	Polyacrylamide
PAMAM	Poly(amido amine)
PBS	Phosphate-buffered saline
PBA	Phenylboronic acid
PC	Phosphatidylcholine
PDT	Photodynamic therapy
PE	Phosphatidylethanolamine
PEBBLE	Probes encapsulated by biologically localized embedding
PEG	Poly(ethylene glycol)
PEP	Phosphoenolpyruvate
6-P-GL	6-Phosphogluconolactone
PeT	Photoinduced electron transfer
PET	Positron emission tomography
PHPMA	Poly(*N*-2-hydroxypropyl)methacrylamide)
PHEMA	Poly(2-hydroxyethyl methacrylate)
PI	Phosphatidylinositol
PI3K	Phosphoinositide 3-kinase
PMAETMA	Poly([2-(methacryloyloxy)ethyl]trimethyl-ammonium chloride)
PMCA	Plasma membrane calcium ATPase
POD	Peroxidase
PVA	Poly(vinyl alcohol)
QCM	Quartz crystal microbalance
QD	Quantum dot
PS	Phosphatidylserine
QY	Quantum yield
Rhod2	Rhodamine 2

RLU	Relative light units
rGO	Reduced graphene oxide
ROI	Regions of interest
Rorc	RAR-related orphan receptor C
RORγt	Retinoid acid-related orphan receptor gamma t
ROS	Reactive oxygen species
SC	Sodium cholate
SEM	Scanning electron microscopy
SERCA	Sarcoplasmic/endoplasmic reticulum calcium ATPase
SGLT	Sodium-glucose co-transporter
SIM	Structured illumination microscopy
SiR	Silicon rhodamine
siRNA	Small interfering RNA
SLC2A	Solute carrier family 2A
SNR	Signal-to-noise ratio
SRS	Stimulated Raman scattering
STDBA	Stilbene diboronic acid
STED	Stimulated emission depletion
STORM	Stochastic optical reconstruction microscopy
STRIDE	Spectral tracing of deuterium
SUR1	Sulfonylurea receptor
SWNT	Single-walled carbon nanotube
TAG	Triacylglycerol
T_1WI	T_1-weighted imaging
TAMRA	Tetramethylrhodamine
TCA	Tricarboxylic acid
TD-FLIM	Time-domain fluorescence lifetime imaging microscopy
TG	Triglycerides
TGF-β	Transforming growth factor β
Th17	T helper 17
THF	Tetrahydrofuran
TMB	3,3′,5,5′-tetramethylbenzidine
TMSPA	Trimethoxysilylpropyl methacrylate
TNR	Target-tissue-to-noise ratio
TPM	Two-photon microscopy
TPE	Tetraphenylethene
TPEF	Two-photon-excited fluorescence
TTF	Tetrathiafulvalene
TTP	Thymidine triphosphate
UDP	Uridine diphosphate
UTP	Uridine triphosphate
UV	Ultraviolet
UV-Vis	Ultraviolet-visible
VDCC	Voltage-dependent calcium channel
VIE	Vibration-induced emission
VLDL	Very low-density lipoprotein
WGA	Wheat germ agglutinin
XRD	X-ray diffraction
YFP	Yellow fluorescent protein

Data availability

No new data were created or analysed in this study.

Acknowledgements

H. W. wishes to thank the Jining Medical University and Shandong First Medical University. H. W. wishes to thank the Shandong Provincial Natural Science Foundation (ZR2023QB084) for support. W. H. Z. wishes to thank the Medical Sci-Tech Research Center of Ningxia Medical University and Shandong First Medical University. W. H. Z. wishes to thank the Natural Science Foundation of Ningxia Province, China (Grant No. 2023AAC05030) for support. K. W. wishes to thank the Shandong First Medical University and the University of Bath. K. W. wishes to thank the Shandong Provincial Natural Science Foundation (ZR2023QB181) for support. L. W. acknowledges support as a "Tang Scholar" (Nanjing University). S. E. L. thanks EPSRC for funding (EP/W036193/1). T. D. J. wishes to thank the University of Bath and the Open Research Fund of the School of Chemistry and Chemical Engineering, Henan Normal University (2020ZD01) for support.

References

1 M. S. Steiner, A. Duerkop and O. S. Wolfbeis, *Chem. Soc. Rev.*, 2011, **40**, 4805–4839.

2 H. Teymourian, A. Barfidokht and J. Wang, *Chem. Soc. Rev.*, 2020, **49**, 7671–7709.

3 M. G. Myers, A. H. Affinati, N. Richardson and M. W. Schwartz, *Nat. Metab.*, 2021, **3**, 737–750.

4 B. I. Reinfeld, M. Z. Madden, M. M. Wolf, A. Chytil, J. E. Bader, A. R. Patterson, A. Sugiura, A. S. Cohen, A. Ali, B. T. Do, A. Muir, C. A. Lewis, R. A. Hongo, K. L. Young, R. E. Brown, V. M. Todd, T. Huffstater, A. Abraham, R. T. O'Neil, M. H. Wilson, F. Xin, M. N. Tantawy, W. D. Merryman, R. W. Johnson, C. S. Williams, E. F. Mason, F. M. Mason, K. E. Beckermann, M. G. Vander Heiden, H. C. Manning, J. C. Rathmell and W. K. Rathmell, *Nature*, 2021, **593**, 282–288.

5 A. Rubio-Navarro, N. Gomez-Banoy, L. Stoll, F. Dündar, A. M. Mawla, L. Ma, E. Cortada, P. Zumbo, A. Li, M. Reiterer, N. Montoya-Oviedo, E. A. Homan, N. Imai, A. Gilani, C. Liu, A. Naji, B. Yang, A. C. N. Chong, D. E. Cohen, S. Chen, J. Cao, G. S. Pitt, M. O. Huising, D. Betel and J. C. Lo, *Nat. Cell Biol.*, 2023, **25**, 565–578.

6 M. J. Bollong, G. Lee, J. S. Coukos, H. Yun, C. Zambaldo, J. W. Chang, E. N. Chin, I. Ahmad, A. K. Chatterjee, L. L. Lairson, P. G. Schultz and R. E. Moellering, *Nature*, 2018, **562**, 600–604.

7 E. Georgiadou, E. Haythorne, M. T. Dickerson, L. Lopez-Noriega, T. J. Pullen, G. da Silva Xavier, S. P. X. Davis, A. Martinez-Sanchez, F. Semplici, R. Rizzuto, J. A. McGinty, P. M. French, M. C. Cane, D. A. Jacobson, I. Leclerc and G. A. Rutter, *Diabetologia*, 2020, **63**, 1368–1381.

8 D. Zhang, W. Jin, R. Wu, J. Li, S.-A. Park, E. Tu, P. Zanvit, J. Xu, O. Liu, A. Cain and W. Chen, *Immunity*, 2019, **51**, 671–681.

9 M. G. Vander Heiden, L. C. Cantley and C. B. Thompson, *Science*, 2009, **324**, 1029–1033.

10 T. Chen, Z. G. Xu, J. Luo, R. K. Manne, Z. Wang, C. C. Hsu, B. S. Pan, Z. Cai, P. J. Tsai, Y. S. Tsai, Z. Z. Chen, H. Y. Li and H. K. Lin, *Cell Metab.*, 2023, **35**, 1782–1798.

11 A. Cui, Y. Xue, W. Su, J. Lin, Y. Liu, G. Cai, Q. Wan, Y. Jiang, D. Ding, Z. Zheng, S. Wei, W. Li, J. Shen, J. Wen, M. Huang, J. Zhao, X. Zhang, Y. Zhao, H. Li, H. Ying, H. Zhang, Y. Bi, Y. Chen, A. Xu, Y. Xu and Y. Li, *Proc. Natl. Acad. Sci. U. S. A.*, 2024, **121**, e2318935121.

12 X. Sun and T. D. James, *Chem. Rev.*, 2015, **115**, 8001–8037.

13 V. B. Juska and M. E. Pemble, *Sensors*, 2020, **20**, 6013.

14 Y. Zou, Z. Chu, J. Guo, S. Liu, X. Ma and J. Guo, *Biosens. Bioelectron.*, 2023, **225**, 115103.

15 T. Ido, C. N. Wan, V. Casella, J. S. Fowler, A. P. Wolf, M. Reivich and D. E. Kuhl, *J. Labelled Compd. Radiopharm.*, 1978, **14**, 175–183.

16 F. Castell and G. J. R. Cook, *Br. J. Cancer*, 2008, **98**, 1597–1601.

17 H. Feng, X. Wang, J. Chen, J. Cui, T. Gao, Y. Gao and W. Zeng, *Contrast Media Mol. Imaging*, 2019, **2019**, 1–12.

18 D. A. Torigian, S. S. Huang, M. Houseni and A. Alavi, *CA. Cancer J. Clin.*, 2007, **57**, 206–224.

19 A. Shegani, S. Kealey, F. Luzi, F. Basagni, J. D. M. Machado, S. D. Ekici, A. Ferocino, A. D. Gee and S. Bongarzone, *Chem. Rev.*, 2022, **123**, 105–229.

20 E. Campbell, C. Jordan and R. Gilmour, *Chem. Soc. Rev.*, 2023, **52**, 3599–3626.

21 M. L. Bowen and C. Orvig, *Chem. Commun.*, 2008, 5077–5091, DOI: 10.1039/B809365B.

22 M. Conti and L. Eriksson, *EJNMMI Phys.*, 2016, **3**, 1–17.

23 H. Shimizu and B. Ishijima, *Psychiatry Clin. Neurosci.*, 1985, **39**, 251–256.

24 G. Blomqvist, S. Stone-Elander, C. Halldin, P. E. Roland, L. Widén, M. Lindqvist, C. G. Swahn, B. Långström and F. A. Wiesel, *J. Cereb. Blood Flow Metab.*, 1990, **10**, 467–483.

25 S. Purser, P. R. Moore, S. Swallow and V. Gouverneur, *Chem. Soc. Rev.*, 2008, **37**, 320–330.

26 D. O'Hagan, *Chem. Soc. Rev.*, 2008, **37**, 308–319.

27 N. A. Meanwell, *J. Med. Chem.*, 2018, **61**, 5822–5880.

28 A. Axer, R. P. Jumde, S. Adam, A. Faust, M. Schäfers, M. Fobker, J. Koehnke, A. K. H. Hirsch and R. Gilmour, *Chem. Sci.*, 2021, **12**, 1286–1294.

29 P. Bentler, K. Bergander, C. G. Daniliuc, C. Mück-Lichtenfeld, R. P. Jumde, A. K. H. Hirsch and R. Gilmour, *Angew. Chem., Int. Ed.*, 2019, **58**, 10990–10994.

30 M. Reivich, D. Kuhl, A. Wolf, J. Greenberg, M. Phelps, T. Ido, V. Casella, J. Fowler, E. Hoffman, A. Alavi, P. Som and L. Sokoloff, *Circ. Res.*, 1979, **44**, 127–137.

31 A. D. Van den Abbeele, *Oncologist*, 2008, **13**, 8–13.

32 O. Jacobson, D. O. Kiesewetter and X. Chen, *Bioconjug. Chem.*, 2014, **26**, 1–18.

33 K. J. Kearfott, D. R. Elmaleh, M. Goodman, J. A. Correia, N. M. Alpert, R. H. Ackerman, G. L. Brownell and W. H. Strauss, *Int. J. Nucl. Med. Biol.*, 1984, **11**, 15–22.

34 M. J. Adam, *J. Label. Compd. Radiopharm.*, 1999, **42**, 809–813.

35 A. Waki, Y. Fujibayashi, Y. Magata, A. Yokoyama, N. Sadato, T. Tsuchida, Y. Ishii and Y. Yonekura, *J. Nucl. Med.*, 1998, **39**, 245–250.

36 B. R. Landau, C. L. Spring-Robinson, R. F. Muzic, N. Rachdaoui, D. Rubin, M. S. Berridge, W. C. Schumann, V. Chandramouli, T. S. Kern and F. Ismail-Beigi, *Am. J. Physiol.: Endocrinol. Metab.*, 2007, **293**, E237–E245.

37 A. Diez-Sampedro, E. M. Wright and B. A. Hirayama, *J. Biol. Chem.*, 2001, **276**, 49188–49194.

38 M. Sala-Rabanal, B. A. Hirayama, C. Ghezzi, J. Liu, S. C. Huang, V. Kepe, H. Koepsell, A. Yu, D. R. Powell, B. Thorens, E. M. Wright and J. R. Barrio, *J. Physiol.*, 2016, **594**, 4425–4438.

39 T. Liu, J. Zhang, X. Wang, J. Yang, Z. Tang and J. Lu, *Curr. Med. Chem.*, 2014, **21**, 24–34.

40 N. R. Schechter, W. D. Erwin, D. J. Yang, E. E. Kim, R. F. Munden, K. Förster, L. C. Taing, J. D. Cox, H. A. Macapinlac and D. A. Podoloff, *Eur. J. Nucl. Med. Mol. Imaging*, 2009, **36**, 1583–1591.

41 Y. Wang, J. Zhu, X. Song, X. Wang, J. Yang and J. Zhang, *Bioorg. Med. Chem. Lett.*, 2014, **24**, 3882–3885.

42 R. Dapueto, R. Castelli, M. Fernández, J. A. Chabalgoity, M. Moreno, J. P. Gambini, P. Cabral and W. Porcal, *Bioorg. Med. Chem. Lett.*, 2011, **21**, 7102–7106.

43 R. Dapueto, R. B. Aguiar, M. Moreno, C. M. L. Machado, F. L. N. Marques, J. P. Gambini, R. Chammas, P. Cabral and W. Porcal, *Bioorg. Med. Chem. Lett.*, 2015, **25**, 4254–4259.

44 X. Zhang, Q. Ruan, Y. Jiang, Q. Gan and J. Zhang, *Transl. Oncol.*, 2021, **14**, 100966.

45 Q. Gan, X. Zhang, Q. Ruan, S. A. Fang and J. Zhang, *Mol. Pharm.*, 2021, **18**, 1356–1363.

46 L. Speizer, R. Haugland and H. Kutchai, *Biochim. Biophys. Acta, Biomembr.*, 1985, **815**, 75–84.

47 K. Yoshioka, H. Takahashi, T. Homma, M. Saito, K. B. Oh, Y. Nemoto and H. Matsuoka, *BBA, Biochim. Biophys. Acta, Gen. Subj.*, 1996, **1289**, 5–9.

48 Y. S. Tian, H. Y. Lee, C. S. Lim, J. Park, H. M. Kim, Y. N. Shin, E. S. Kim, H. J. Jeon, S. B. Park and B. R. Cho, *Angew. Chem., Int. Ed.*, 2009, **48**, 8027–8031.

49 M. Zhang, Z. Zhang, D. Blessington, H. Li, T. M. Busch, V. Madrak, J. Miles, B. Chance, J. D. Glickson and G. Zheng, *Bioconjug. Chem.*, 2003, **14**, 709–714.

50 Y. Ye, S. Bloch and S. Achilefu, *J. Am. Chem. Soc.*, 2004, **126**, 7740–7741.

51 Z. Cheng, J. Levi, Z. Xiong, O. Gheysens, S. Keren, X. Chen and S. S. Gambhir, *Bioconjug. Chem.*, 2006, **17**, 662–669.

52 J. Park, H. Y. Lee, M. H. Cho and S. B. Park, *Angew. Chem., Int. Ed.*, 2007, **46**, 2018–2022.

53 J. L. Kovar, W. Volcheck, E. Sevick-Muraca, M. A. Simpson and D. M. Olive, *Anal. Biochem.*, 2009, **384**, 254–262.

54 M. Vendrell, A. Samanta, S. W. Yun and Y. T. Chang, *Org. Biomol. Chem.*, 2011, **9**, 4760–4762.

55 T. Maric, G. Mikhaylov, P. Khodakivskyi, A. Bazhin, R. Sinisi, N. Bonhoure, A. Yevtodiyenko, A. Jones, V. Muhunthan, G. Abdelhady, D. Shackelford and E. Goun, *Nat. Meth.*, 2019, **16**, 526–532.

56 R. Huang, J. Vider, J. L. Kovar, D. M. Olive, I. K. Mellinghoff, P. Mayer-Kuckuk, M. F. Kircher and R. G. Blasberg, *Clin. Cancer Res.*, 2012, **18**, 5731–5740.

57 R. McMorrow, H. S. de Bruijn, I. Que, D. C. Stuurman, C. M. A. de Ridder, M. Doukas, D. J. Robinson, L. Mezzanotte and C. W. G. M. Lowik, *Mol. Imaging Biol.*, 2024, **26**, 616–627.

58 A. Nguyen, C. Bhandari, M. Keown, A. Malkoochi, M. Quaye, D. Mahmoud, N. Shah, D. Alzhanova, C. G. Cameron, J. Ferruzzi, S. A. McFarland, G. Shafirstein, R. Brekken and G. Obaid, *Mol. Pharm.*, 2024, **21**, 3296–3309.

59 A. Samanta, M. Vendrell, R. Das and Y. T. Chang, *Chem. Commun.*, 2010, **46**, 7406–7408.

60 M. W. Louie, H. W. Liu, M. H. C. Lam, Y. W. Lam and K. K. W. Lo, *Chem. – Eur. J.*, 2011, **17**, 8304–8308.

61 H. Y. Lee, J. J. Lee, J. Park and S. B. Park, *Chem. – Eur. J.*, 2011, **17**, 143–150.

62 J. Park, J. I. Um, A. Jo, J. Lee, D. W. Jung, D. R. Williams and S. B. Park, *Chem. Commun.*, 2014, **50**, 9251–9254.

63 S. Chen, Y. Fang, Q. Zhu, W. Zhang, X. Zhang and W. Lu, *RSC Adv.*, 2016, **6**, 81894–81901.

64 A. Jo, J. Sung, S. Lee, H. Nam, H. W. Lee, J. Park, H. M. Kim, E. Kim and S. B. Park, *Bioconjug. Chem.*, 2018, **29**, 3394–3401.

65 Y. Cheng, G. Shabir, X. Li, L. Fang, L. Xu, H. Zhang and E. Li, *Chem. Commun.*, 2020, **56**, 1070–1073.

66 G. W. Cline, B. M. Jucker, Z. Trajanoski, A. J. M. Rennings and G. I. Shulman, *Am. J. Physiol.: Endocrinol. Metab.*, 1998, **274**, E381–E389.

67 T. B. Rodrigues, E. M. Serrao, B. W. C. Kennedy, D.-E. Hu, M. I. Kettunen and K. M. Brindle, *Nat. Med.*, 2013, **20**, 93–97.

68 J. Li and J. X. Cheng, *Sci. Rep.*, 2014, **4**, 6807.

69 F. Hu, Z. Chen, L. Zhang, Y. Shen, L. Wei and W. Min, *Angew. Chem., Int. Ed.*, 2015, **54**, 9821–9825.

70 R. Long, L. Zhang, L. Shi, Y. Shen, F. Hu, C. Zeng and W. Min, *Chem. Commun.*, 2018, **54**, 152–155.

71 L. Zhang, L. Shi, Y. Shen, Y. Miao, M. Wei, N. Qian, Y. Liu and W. Min, *Nat. Biomed. Eng.*, 2019, **3**, 402–413.

72 Z. Liang, H. Pang, G. Zeng and T. Chen, *Anal. Chem.*, 2022, **94**, 8293–8301.

73 T. Abe, Y. Y. Lau and A. G. Ewing, *Anal. Chem.*, 1992, **64**, 2160–2163.

74 S. K. Jung, L. M. Kauri, W. J. Qian and R. T. Kennedy, *J. Biol. Chem.*, 2000, **275**, 6642–6650.

75 M. H. Asif, S. M. U. Ali, O. Nur, M. Willander, C. Brännmark, P. Strålfors, U. H. Englund, F. Elinder and B. Danielsson, *Biosens. Bioelectron.*, 2010, **25**, 2205–2211.

76 A. Fulati, S. M. U. Ali, M. H. Asif, N. U. H. Alvi, M. Willander, C. Brännmark, P. Strålfors, S. I. Börjesson, F. Elinder and B. Danielsson, *Sens. Actuators, B*, 2010, **150**, 673–680.

77 R. A. S. Nascimento, R. E. Özel, W. H. Mak, M. Mulato, B. Singaram and N. Pourmand, *Nano Lett.*, 2016, **16**, 1194–1200.

78 X. Wang, Y. Ma, M. Zhao, M. Zhou, Y. Xiao, Z. Sun and L. Tong, *J. Chromatogr. A*, 2016, **1469**, 128–134.

79 Q. L. Liao, H. Jiang, X. W. Zhang, Q. F. Qiu, Y. Tang, X. K. Yang, Y. L. Liu and W. H. Huang, *Nanoscale*, 2019, **11**, 10702–10708.

80 H. Xu, J. W. Aylott and R. Kopelman, *Analyst*, 2002, **127**, 1471–1477.

81 P. W. Barone, S. Baik, D. A. Heller and M. S. Strano, *Nat. Mater.*, 2004, **4**, 86–92.

82 L. Li, F. Gao, J. Ye, Z. Chen, Q. Li, W. Gao, L. Ji, R. Zhang and B. Tang, *Anal. Chem.*, 2013, **85**, 9721–9727.

83 R. Gill, L. Bahshi, R. Freeman and I. Willner, *Angew. Chem., Int. Ed.*, 2008, **47**, 1676–1679.

84 B. Liu, Z. Sun, P.-J. J. Huang and J. Liu, *J. Am. Chem. Soc.*, 2015, **137**, 1290–1295.

85 J. Li, Y. Li, S. A. Shahzad, J. Chen, Y. Chen, Y. Wang, M. Yang and C. Yu, *Chem. Commun.*, 2015, **51**, 6354–6356.

86 S. Jiang, Y. Zhang, Y. Yang, Y. Huang, G. Ma, Y. Luo, P. Huang and J. Lin, *ACS Appl. Mater. Interfaces*, 2019, **11**, 10554–10558.

87 T. Hu, K. Xu, S. Qiu, Y. Han, J. Chen, J. Xu, K. Chen, Z. Sun, H. Yi and Z. Ni, *J. Mater. Chem. B*, 2020, **8**, 7160–7165.

88 L. Guo, S. Chen, Y. L. Yu and J. H. Wang, *Anal. Chem.*, 2021, **93**, 16240–16247.

89 A. Liang, Y. Zhao, X. Huang and Z. Jiang, *Spectrochim. Acta, Part A*, 2022, **265**, 7160–7165.

90 X. Wang, Q. Li, Y. Guan and Y. Zhang, *Mater. Today Chem.*, 2016, **1–2**, 7–14.

91 J. Xu, P. Huang, Y. Qin, D. Jiang and H. Y. Chen, *Anal. Chem.*, 2016, **88**, 4609–4612.

92 J. Liu, C. Chen, H. Chen, C. Huang, Q. Ren, M. Sun, J. Tao, B. Lin and P. Zhao, *Anal. Chem.*, 2022, **94**, 16213–16221.

93 S. Liu, Y. Liu, Z. Zhang, X. Wang, Y. Yang, K. Sun, J. Yu, D. T. Chiu and C. Wu, *Anal. Chem.*, 2022, **94**, 14265–14272.

94 M. Fehr, S. Lalonde, I. Lager, M. W. Wolff and W. B. Frommer, *J. Biol. Chem.*, 2003, **278**, 19127–19133.

95 S. A. John, M. Ottolia, J. N. Weiss and B. Ribalet, *Pflüg. Arch. Eur. J. Phy.*, 2008, **456**, 307–322.

96 K. Deuschle, S. Okumoto, M. Fehr, L. L. Looger, L. Kozhukh and W. B. Frommer, *Protein Sci.*, 2009, **14**, 2304–2314.

97 H. Takanaga, B. Chaudhuri and W. B. Frommer, *Biochim. Biophys. Acta, Biomembr.*, 2008, **1778**, 1091–1099.

98 M. T. Kaminski, S. Lenzen and S. Baltrusch, *Biochim. Biophys. Acta, Mol. Cell Res.*, 2012, **1823**, 1697–1707.

99 I. Ruminot, J. Schmälzle, B. Leyton, L. F. Barros and J. W. Deitmer, *J. Cereb. Blood Flow Metab.*, 2017, **39**, 513–523.

100 N. M. C. Connolly, H. Dussmann, U. Anilkumar, H. J. Huber and J. H. M. Prehn, *J. Neurosci.*, 2014, **34**, 10192–10205.

101 V. Calbiague García, Y. Chen, B. Cádiz, L. Wang, F. Paquet-Durand and O. Schmachtenberg, *Exp. Eye Res.*, 2023, **226**, 109352.

102 A. Behjousiar, C. Kontoravdi and K. M. Polizzi, *PLoS One*, 2012, **7**, e34512.

103 K. Deuschle, B. Chaudhuri, S. Okumoto, I. Lager, S. Lalonde and W. B. Frommer, *Plant Cell*, 2006, **18**, 2314–2325.

104 K. Teasley Hamorsky, C. M. Ensor, Y. Wei and S. Daunert, *Angew. Chem., Int. Ed.*, 2008, **47**, 3718–3721.

105 H. Yoon, J. H. Ahn, P. W. Barone, K. Yum, R. Sharma, A. A. Boghossian, J. H. Han and M. S. Strano, *Angew. Chem., Int. Ed.*, 2011, **50**, 1828–1831.

106 J. V. Veetil, S. Jin and K. Ye, *J. Diabetes Sci. Technol.*, 2012, **6**, 1276–1285.

107 H. Hu, Y. Wei, D. Wang, N. Su, X. Chen, Y. Zhao, G. Liu and Y. Yang, *RSC Adv.*, 2018, **8**, 2485–2489.

108 M. Mita, M. Ito, K. Harada, I. Sugawara, H. Ueda, T. Tsuboi and T. Kitaguchi, *Anal. Chem.*, 2019, **91**, 4821–4830.

109 J. P. Keller, J. S. Marvin, H. Lacin, W. C. Lemon, J. Shea, S. Kim, R. T. Lee, M. Koyama, P. J. Keller and L. L. Looger, *Cell Rep.*, 2021, **35**, 109284.

110 M. Mita, I. Sugawara, K. Harada, M. Ito, M. Takizawa, K. Ishida, H. Ueda, T. Kitaguchi and T. Tsuboi, *Cell Chem. Biol.*, 2022, **29**, 98–108.

111 B. C. Ye, *Anal. Lett.*, 1998, **31**, 2349–2359.

112 R. Ballerstadt and J. S. Schultz, *Anal. Chem.*, 2000, **72**, 4185–4192.

113 L. J. McCartney, J. C. Pickup, O. J. Rolinski and D. J. S. Birch, *Anal. Biochem.*, 2001, **292**, 216–221.

114 R. Ballerstadt, A. Polak, A. Beuhler and J. Frye, *Biosens. Bioelectron.*, 2004, **19**, 905–914.

115 R. Ballerstadt, A. Kholodnykh, C. Evans, A. Boretsky, M. Motamedi, A. Gowda and R. McNichols, *Anal. Chem.*, 2007, **79**, 6965–6974.

116 S. Wang, T. Sherlock, B. Salazar, N. Sudheendran, R. K. Manapuram, K. Kourentzi, P. Ruchhoeft, R. C. Willson and K. V. Larin, *IEEE Sens. J.*, 2013, **13**, 4534–4541.

117 R. Dutt-Ballerstadt, C. Evans, A. P. Pillai and A. Gowda, *Biosens. Bioelectron.*, 2014, **61**, 280–284.

118 R. Ballerstadt, C. Evans, A. Gowda and R. McNichols, *J. Diabetes Sci. Technol.*, 2007, **1**, 384–393.

119 R. Dutt-Ballerstadt, C. Evans, A. P. Pillai, E. Orzeck, R. Drabek, A. Gowda and R. McNichols, *J. Diabetes Sci. Technol.*, 2012, **6**, 362–370.

120 B. Tang, L. Cao, K. Xu, L. Zhuo, J. Ge, Q. Li and L. Yu, *Chem. – Eur. J.*, 2008, **14**, 3637–3644.

121 D. Pallarola, N. Queralto, W. Knoll, M. Ceolin, O. Azzaroni and F. Battaglini, *Langmuir*, 2010, **26**, 13684–13696.

122 B. M. Cummins, J. Lim, E. E. Simanek, M. V. Pishko and G. L. Coté, *Biomed. Opt. Express*, 2011, **2**, 1243–1257.

123 D. Tang, Q. Li, J. Tang, B. Su and G. Chen, *Anal. Chim. Acta*, 2011, **686**, 144–149.

124 T. B. Hoang, B. T. Stokke, U. Hanke, E. A. Johannessen and A. Johannessen, *IEEE Sens. J.*, 2021, **21**, 4391–4404.

125 S. Hsieh, S. L. Hsieh, C. W. Hsieh, P. C. Lin and C. H. Wu, *J. Anal. Methods Chem.*, 2013, **2013**, 687265.

126 C. Boss, E. Meurville, J. M. Sallese and P. Ryser, *Biosens. Bioelectron.*, 2011, **30**, 223–228.

127 A. J. Müller, M. Knuth, K. S. Nikolaus and P. Herbrechtsmeier, *J. Diabetes Sci. Technol.*, 2012, **6**, 875–883.

128 Y. Song, H. Liu, H. Tan, F. Xu, J. Jia, L. Zhang, Z. Li and L. Wang, *Anal. Chem.*, 2014, **86**, 1980–1987.

129 C. A. Peng and S. Pachpinde, *Nanomater. Nanotechnol.*, 2014, **4**, 9.

130 K. L. Andrea, M. C. Brian, A. A. Alexander and L. C. Gerard, *Proc. SPIE*, 2015, **9332**, 933208.

131 Y. Fan, X. Tan, X. Liu, X. Ou, S. Chen and S. Wei, *Electrochim. Acta*, 2015, **180**, 471–478.

132 L. Chen, W. H. Tse, Y. Chen, M. W. McDonald, J. Melling and J. Zhang, *Biosens. Bioelectron.*, 2017, **91**, 393–399.

133 N. Krstić, J. Jüttner, L. Giegerich, M. Mayer, M. Knuth, A. Müller and C. Thielemann, *Ann. 3D Print. Med.*, 2023, **10**, 100111.

134 A. Pfützner, B. Tencer, B. Stamm, M. Mehta, P. Sharma, R. Gilyazev, H. Jensch, N. Thomé and M. Huth, *Sensors*, 2023, **23**, 4541.

135 Y. Aoyama, Y. Tanaka, H. Toi and H. Ogoshi, *J. Am. Chem. Soc.*, 1988, **110**, 634–635.

136 S. Anderson, U. Neidlein, V. Gramlich and F. Diederich, *Angew. Chem., Int. Ed. Engl.*, 1995, **34**, 1596–1600.

137 U. Neidlein and F. Diederich, *Chem. Commun.*, 1996, 1493–1494, DOI: 10.1039/CC9960001493.

138 A. S. Droz, U. Neidlein, S. Anderson, P. Seiler and F. Diederich, *Helv. Chim. Acta*, 2001, **84**, 2243–2289.

139 A. P. Davis and R. S. Wareham, *Angew. Chem., Int. Ed.*, 1998, **37**, 2270–2273.

140 E. Klein, M. P. Crump and A. P. Davis, *Angew. Chem., Int. Ed.*, 2005, **44**, 298–302.

141 N. P. Barwell, M. P. Crump and A. P. Davis, *Angew. Chem., Int. Ed.*, 2009, **48**, 7673–7676.

142 Y. Ferrand, E. Klein, N. P. Barwell, M. P. Crump, J. Jiménez-Barbero, C. Vicent, G. J. Boons, S. Ingale and A. P. Davis, *Angew. Chem., Int. Ed.*, 2009, **48**, 1775–1779.

143 G. Lecollinet, A. P. Dominey, T. Velasco and A. P. Davis, *Angew. Chem., Int. Ed.*, 2002, **41**, 4093–4096.

144 Y. Ferrand, M. P. Crump and A. P. Davis, *Science*, 2007, **318**, 619–622.

145 B. Sookcharoenpinyo, E. Klein, Y. Ferrand, D. B. Walker, P. R. Brotherhood, C. Ke, M. P. Crump and A. P. Davis, *Angew. Chem., Int. Ed.*, 2012, **51**, 4586–4590.

146 C. Ke, H. Destecroix, M. P. Crump and A. P. Davis, *Nat. Chem.*, 2012, **4**, 718–723.

147 P. K. Mandal, B. Kauffmann, H. Destecroix, Y. Ferrand, A. P. Davis and I. Huc, *Chem. Commun.*, 2016, **52**, 9355–9358.

148 H. Destecroix, C. M. Renney, T. J. Mooibroek, T. S. Carter, P. F. N. Stewart, M. P. Crump and A. P. Davis, *Angew. Chem., Int. Ed.*, 2015, **54**, 2057–2061.

149 T. J. Mooibroek, J. M. Casas-Solvas, R. L. Harniman, C. M. Renney, T. S. Carter, M. P. Crump and A. P. Davis, *Nat. Chem.*, 2015, **8**, 69–74.

150 P. Rios, T. S. Carter, T. J. Mooibroek, M. P. Crump, M. Lisbjerg, M. Pittelkow, N. T. Supekar, G. J. Boons and A. P. Davis, *Angew. Chem., Int. Ed.*, 2016, **55**, 3387–3392.

151 P. Ríos, T. J. Mooibroek, T. S. Carter, C. Williams, M. R. Wilson, M. P. Crump and A. P. Davis, *Chem. Sci.*, 2017, **8**, 4056–4061.

152 R. A. Tromans, T. S. Carter, L. Chabanne, M. P. Crump, H. Li, J. V. Matlock, M. G. Orchard and A. P. Davis, *Nat. Chem.*, 2018, **11**, 52–56.

153 T. Hoeg-Jensen, T. Kruse, C. L. Brand, J. Sturis, C. Fledelius, P. K. Nielsen, E. Nishimura, A. R. Madsen, L. Lykke, K. S. Halskov, S. Koščová, V. Kotek, A. P. Davis, R. A. Tromans, M. Tomsett, G. Peñuelas-Haro, D. J. Leonard, M. G. Orchard, A. Chapman, G. Invernizzi, E. Johansson, D. Granata, B. F. Hansen, T. A. Pedersen, J. Kildegaard, K. M. Pedersen, H. H. F. Refsgaard, L. Alifrangis, J. J. Fels,

A. V. Neutzsky-Wulff, P. Sauerberg and R. Slaaby, *Nature*, 2024, **634**, 944–951.

154 W. Liu, Y. Tan, L. O. Jones, B. Song, Q. H. Guo, L. Zhang, Y. Qiu, Y. Feng, X. Y. Chen, G. C. Schatz and J. F. Stoddart, *J. Am. Chem. Soc.*, 2021, **143**, 15688–15700.

155 C. Zhai, C. Xu, Y. Cui, L. Wojtas and W. Liu, *Chem. – Eur. J.*, 2023, **29**, e202300524.

156 C. Zhai, E. C. Zulueta, A. Mariscal, C. Xu, Y. Cui, X. Wang, H. Wu, C. Doan, L. Wojtas, H. Zhang, J. Cai, L. Ye, K. Wang and W. Liu, *Chem. Sci.*, 2024, **15**, 19588–19598.

157 W. L. A. Brooks, C. C. Deng and B. S. Sumerlin, *ACS Omega*, 2018, **3**, 17863–17870.

158 R. Nishiyabu, Y. Kubo, T. D. James and J. S. Fossey, *Chem. Commun.*, 2011, **47**, 1124–1150.

159 Y. Furikado, T. Nagahata, T. Okamoto, T. Sugaya, S. Iwatsuki, M. Inamo, H. D. Takagi, A. Odani and K. Ishihara, *Chem. – Eur. J.*, 2014, **20**, 13194–13202.

160 J. P. Lorand and J. O. Edwards, *J. Org. Chem.*, 1959, **24**, 769–774.

161 J. Yoon and A. W. Czarnik, *J. Am. Chem. Soc.*, 1992, **114**, 5874–5875.

162 T. D. James, K. R. A. S. Sandanayake and S. Shinkai, *J. Chem. Soc., Chem. Commun.*, 1994, 477–478, DOI: 10.1039/C39940000477.

163 T. D. James, K. R. A. S. Sandanayake and S. Shinkai, *Angew. Chem., Int. Ed. Engl.*, 1994, **33**, 2207–2209.

164 T. D. James, K. R. A. S. Sandanayake, R. Iguchi and S. Shinkai, *J. Am. Chem. Soc.*, 1995, **117**, 8982–8987.

165 J. Yoon and A. W. Czarnik, *Bioorg. Med. Chem.*, 1993, **1**, 267–271.

166 G. Wulff, *Pure Appl. Chem.*, 1982, **54**, 2093–2102.

167 G. Wulff, M. Lauer and H. Böhnke, *Angew. Chem., Int. Ed. Engl.*, 1984, **23**, 741–742.

168 R. R. Groleau, T. D. James and S. D. Bull, *Coord. Chem. Rev.*, 2021, **428**, 213599.

169 S. Franzen, W. Ni and B. Wang, *J. Phys. Chem. B*, 2003, **107**, 12942–12948.

170 W. Ni, G. Kaur, G. Springsteen, B. Wang and S. Franzen, *Bioorg. Chem.*, 2004, **32**, 571–581.

171 L. Zhu, S. H. Shabbir, M. Gray, V. M. Lynch, S. Sorey and E. V. Anslyn, *J. Am. Chem. Soc.*, 2006, **128**, 1222–1232.

172 B. M. Chapin, P. Metola, S. L. Vankayala, H. L. Woodcock, T. J. Mooibroek, V. M. Lynch, J. D. Larkin and E. V. Anslyn, *J. Am. Chem. Soc.*, 2017, **139**, 5568–5578.

173 X. Sun, T. D. James and E. V. Anslyn, *J. Am. Chem. Soc.*, 2018, **140**, 2348–2354.

174 X. Sun, B. M. Chapin, P. Metola, B. Collins, B. Wang, T. D. James and E. V. Anslyn, *Nat. Chem.*, 2019, **11**, 768–778.

175 H. Kijima, M. Takeuchi, A. Robertson, S. Shinkai, C. Cooper and T. D. James, *Chem. Commun.*, 1999, 2011–2012, DOI: 10.1039/A906825B.

176 C. J. Ward, P. Patel, P. R. Ashton and T. D. James, *Chem. Commun.*, 2000, 229–230, DOI: 10.1039/A909204H.

177 Z. Wang, D. Zhang and D. Zhu, *J. Org. Chem.*, 2005, **70**, 5729–5732.

178 W. Tan, Z. Wang, D. Zhang and D. Zhu, *Sensors*, 2006, **6**, 954–961.

179 S. Kabilan, J. Blyth, M. C. Lee, A. J. Marshall, A. Hussain, X. P. Yang and C. R. Lowe, *J. Mol. Recognit.*, 2004, **17**, 162–166.

180 A. Domschke, S. Kabilan, R. Anand, M. Caines, D. Fetter, P. Griffith, K. James, N. Karangu, D. Smith, M. Vargas, J. Zeng, A. Hussain, Y. Xiaoping, J. Blyth, A. Mueller, P. Herbrechtsmeier and C. R. Lowe, *Sensors*, 2004, **3**, 1320–1323.

181 X. Yang, X. Pan, J. Blyth and C. R. Lowe, *Biosens. Bioelectron.*, 2008, **23**, 899–905.

182 V. L. Alexeev, S. Das, D. N. Finegold and S. A. Asher, *Clin. Chem.*, 2004, **50**, 2353–2360.

183 R. Badugu, J. R. Lakowicz and C. D. Geddes, *Opt. Fiber. Sensor. Med. Appl. SPIE*, 2024, **5317**, 234–245.

184 V. Tharmaraj and K. Pitchumani, *RSC Adv.*, 2013, **3**, 11566–11570.

185 H. Bai, Q. Sun, H. Tian, J. Qian, L. Zhang and W. Zhang, *Chin. J. Chem.*, 2013, **31**, 1095–1101.

186 C. S. Lim, C. Chung, H. M. Kim, M. J. An, Y. S. Tian, H. J. Chun and B. R. Cho, *Chem. Commun.*, 2012, **48**, 2122–2124.

187 Y. J. Huang, W. J. Ouyang, X. Wu, Z. Li, J. S. Fossey, T. D. James and Y. B. Jiang, *J. Am. Chem. Soc.*, 2013, **135**, 1700–1703.

188 C. Wang, Y. Li and Y. Wei, *Sens. Actuators, B*, 2017, **247**, 595–601.

189 X. Zhang, C. Gao, S. Lü, H. Duan, N. Jing, D. Dong, C. Shi and M. Liu, *J. Mater. Chem. B*, 2014, **2**, 5452–5460.

190 T. Kajisa and T. Sakata, *Sci. Technol. Adv. Mater.*, 2017, **18**, 26–33.

191 A. K. Yetisen, N. Jiang, A. Fallahi, Y. Montelongo, G. U. Ruiz-Esparza, A. Tamayol, Y. S. Zhang, I. Mahmood, S. A. Yang, K. S. Kim, H. Butt, A. Khademhosseini and S. H. Yun, *Adv. Mater.*, 2017, **29**, 1606380.

192 W. Wu, T. Zhou, A. Berliner, P. Banerjee and S. Zhou, *Angew. Chem., Int. Ed.*, 2010, **49**, 6554–6558.

193 Z. B. Qu, X. Zhou, L. Gu, R. Lan, D. Sun, D. Yu and G. Shi, *Chem. Commun.*, 2013, **49**, 9830–9832.

194 T. Hao, X. Wei, Y. Nie, Y. Xu, K. Lu, Y. Yan and Z. Zhou, *Sens. Actuators, B*, 2016, **230**, 70–76.

195 K. Yum, J. H. Ahn, T. P. McNicholas, P. W. Barone, B. Mu, J. H. Kim, R. M. Jain and M. S. Strano, *ACS Nano*, 2012, **6**, 819–830.

196 J. Cai, W. Luo, J. Pan, G. Li, Y. Pu, L. Si, G. Shi, Y. Shao, H. Ma and J. Guan, *Adv. Sci.*, 2022, **9**, 2105239.

197 Q. Lu, Z. Wang, S. Bai, Y. Wang, C. Liao, Y. Sun, Y. Zhang, W. Li and Q. Mei, *J. Am. Chem. Soc.*, 2023, **145**, 5941–5951.

198 S. Kitaoka, M. Kojima, M. Koita, H. Koyama, C. Mori, M. Okabe, R. Ando, K. Kobayashi, R. Watanabe, Y. Takano, T. D. James and Y. Egawa, *Chem. Sci.*, 2025, **16**, 16645–16658.

199 J. K. Awino, R. W. Gunasekara and Y. Zhao, *J. Am. Chem. Soc.*, 2016, **138**, 9759–9762.

200 J. Qiao, H. Wu, H. Wei, L. Mao, T. Wang and L. Qi, *Anal. Chem.*, 2020, **92**, 4445–4450.

201 J. Axthelm, S. H. C. Askes, M. Elstner, U. R. G. H. Görls, P. Bellstedt and A. Schiller, *J. Am. Chem. Soc.*, 2017, **139**, 11413–11420.

202 M. Bielecki, H. Eggert and J. C. Norrild, *J. Chem. Soc., Perkin Trans. 2*, 1999, 449–456, DOI: 10.1039/A808896I.

203 H. Murakami, T. Nagasaki, I. Hamachi and S. Shinkai, *Tetrahedron Lett.*, 1993, **34**, 6273–6276.

204 T. D. James, K. R. A. Samankumara Sandanayake and S. Shinkai, *Nature*, 1995, **374**, 345–347.

205 P. Linnane, T. D. James, S. Imazu and S. Shinkai, *Tetrahedron Lett.*, 1995, **36**, 8833–8834.

206 T. D. James, H. Shinmori and S. Shinkai, *Chem. Commun.*, 1997, 71–72, DOI: 10.1039/A606552J.

207 H. Eggert, J. Frederiksen, C. Morin and J. C. Norrild, *J. Org. Chem.*, 1999, **64**, 3846–3852.

208 S. Arimori, L. I. Bosch, C. J. Ward and T. D. James, *Tetrahedron Lett.*, 2001, **42**, 4553–4555.

209 S. Arimori, L. I. Bosch, C. J. Ward and T. D. James, *Tetrahedron Lett.*, 2002, **43**, 911–913.

210 B. Appleton and T. D. Gibson, *Sens. Actuators, B*, 2000, **65**, 302–304.

211 S. Arimori, K. A. Frimat, T. D. James, M. L. Bell and C. S. Oh, *Chem. Commun.*, 2001, 1836–1837, DOI: 10.1039/b105994g.

212 S. Arimori, M. L. Bell, C. S. Oh, K. A. Frimat and T. D. James, *J. Chem. Soc., Perkin Trans. 1*, 2002, 803–808, DOI: 10.1039/b108998f.

213 M. D. Phillips and T. D. James, *J. Fluoresc.*, 2004, **14**, 549–559.

214 M. D. Phillips, T. M. Fyles, N. P. Barwell and T. D. James, *Chem. Commun.*, 2009, 6557–6559, DOI: 10.1039/B909230G.

215 W. Zhai, L. Male and J. S. Fossey, *Chem. Commun.*, 2017, **53**, 2218–2221.

216 W. Yang, H. He and D. G. Drueckhammer, *Angew. Chem., Int. Ed.*, 2001, **40**, 1714–1718.

217 G. Heinrichs, M. Schellenträger and S. Kubik, *Eur. J. Org. Chem.*, 2006, 4177–4186.

218 J. Zielonka, J. Joseph, A. Sikora, M. Hardy, O. Ouari, J. Vasquez-Vivar, G. Cheng, M. Lopez and B. Kalyanaraman, *Chem. Rev.*, 2017, **117**, 10043–10120.

219 J. T. Suri, D. B. Cordes, F. E. Cappuccio, R. A. Wessling and B. Singaram, *Langmuir*, 2003, **19**, 5145–5152.

220 S. Gamsey, A. Miller, M. M. Olmstead, C. M. Beavers, L. C. Hirayama, S. Pradhan, R. A. Wessling and B. Singaram, *J. Am. Chem. Soc.*, 2007, **129**, 1278–1286.

221 D. B. Cordes, S. Gamsey and B. Singaram, *Angew. Chem., Int. Ed.*, 2006, **45**, 3829–3832.

222 Y. H. Li, L. Zhang, J. Huang, R. P. Liang and J. D. Qiu, *Chem. Commun.*, 2013, **49**, 5180–5182.

223 Y. Liu, C. Deng, L. Tang, A. Qin, R. Hu, J. Z. Sun and B. Z. Tang, *J. Am. Chem. Soc.*, 2010, **133**, 660–663.

224 X. Wu, L. R. Lin, Y. J. Huang, Z. Li and Y. B. Jiang, *Chem. Commun.*, 2012, **48**, 4362–4364.

225 J. Axthelm, H. Görls, U. S. Schubert and A. Schiller, *J. Am. Chem. Soc.*, 2015, **137**, 15402–15405.

226 J. Ramos-Soriano, S. J. Benitez-Benitez, A. P. Davis and M. C. Galan, *Angew. Chem., Int. Ed.*, 2021, **60**, 16880–16884.

227 W. Zhai, X. Sun, T. D. James and J. S. Fossey, *Chem. – Asian J.*, 2015, **10**, 1836–1848.

228 K. Nan, Y. N. Jiang, M. Li and B. Wang, *Biosensors*, 2023, **13**, 618.

229 T. D. James and S. Shinkai, *J. Chem. Soc., Chem. Commun.*, 1995, 1483–1485, DOI: 10.1039/C39950001483.

230 J. Zhao, M. G. Davidson, M. F. Mahon, G. Kociok-Köhn and T. D. James, *J. Am. Chem. Soc.*, 2004, **126**, 16179–16186.

231 V. V. Karnati, X. Gao, S. Gao, W. Yang, W. Ni, S. Sankar and B. Wang, *Bioorg. Med. Chem. Lett.*, 2002, **12**, 3373–3377.

232 G. Kaur, H. Fang, X. Gao, H. Li and B. Wang, *Tetrahedron*, 2006, **62**, 2583–2589.

233 T. Kawanishi, M. A. Romey, P. C. Zhu, M. Z. Holody and S. Shinkai, *J. Fluoresc.*, 2004, **14**, 499–512.

234 H. Shibata, Y. J. Heo, T. Okitsu, Y. Matsunaga, T. Kawanishi and S. Takeuchi, *Proc. Natl. Acad. Sci. U. S. A.*, 2010, **107**, 17894–17898.

235 Y. J. Heo, H. Shibata, T. Okitsu, T. Kawanishi and S. Takeuchi, *Proc. Natl. Acad. Sci. U. S. A.*, 2011, **108**, 13399–13403.

236 M. Fukuhara, H. Takehara, K. Barthelmes, B. Kersch-Hunt, J. E. Gardiner, Y. Kanda, A. Matsumoto, T. D. James and T. Ichiki, *J. Mater. Chem. B*, 2025, **13**, 15273–15281.

237 L. Zhang, F. Su, S. Buizer, H. Lu, W. Gao, Y. Tian and D. Meldrum, *Biomaterials*, 2013, **34**, 9779–9788.

238 L. Zhang, F. Su, S. Buizer, X. Kong, F. Lee, K. Day, Y. Tian and D. R. Meldrum, *Chem. Commun.*, 2014, **50**, 6920–6922.

239 M. Deng, G. Song, K. Zhong, Z. Wang, X. Xia and Y. Tian, *Sens. Actuators, B*, 2022, **352**, 131067.

240 M. Mortellaro and A. DeHennis, *Biosens. Bioelectron.*, 2014, **61**, 227–231.

241 K. Cowart, *J. Diabetes Sci. Technol.*, 2019, **15**, 160–166.

242 J. I. Joseph, *J. Diabetes Sci. Technol.*, 2020, **15**, 167–173.

243 M. P. Christiansen, L. J. Klaff, R. Brazg, A. R. Chang, C. J. Levy, D. Lam, D. S. Denham, G. Atiee, B. W. Bode, S. J. Walters, L. Kelley and T. S. Bailey, *Diabetes Technol. Ther.*, 2018, **20**, 197–206.

244 A. Dehennis, M. A. Mortellaro and S. Ioacara, *J. Diabetes Sci. Technol.*, 2015, **9**, 951–956.

245 J. Kropff, P. Choudhary, S. Neupane, K. Barnard, S. C. Bain, C. Kapitza, T. Forst, M. Link, A. Dehennis and J. H. DeVries, *Diabetes Care*, 2016, **40**, 63–68.

246 S. K. Garg, D. Liljenquist, B. Bode, M. P. Christiansen, T. S. Bailey, R. L. Brazg, D. S. Denham, A. R. Chang, H. K. Akturk, A. Dehennis, K. S. Tweden and F. R. Kaufman, *Diabetes Technol. Ther.*, 2022, **24**, 84–92.

247 A. W. Czarnik and T. D. James, *ACS Sens.*, 2024, **9**, 6320–6326.

248 J. Tang, D. Ma, S. Pecic, C. Huang, J. Zheng, J. Li and R. Yang, *Anal. Chem.*, 2017, **89**, 8319–8327.

249 B. Wang, K. H. Chou, B. N. Queenan, S. Pennathur and G. C. Bazan, *Angew. Chem., Int. Ed.*, 2019, **58**, 10612–10615.

250 M. Deng, Y. Qiao, C. Liu, Z. Wang, J. Shi, T. Pan, Y. Mao, Z. Mei, F. Huang and Y. Tian, *Sens. Actuators, B*, 2019, **286**, 437–444.

251 K. Wang, R. Zhang, X. Yue, Z. Zhou, L. Bai, Y. Tong, B. Wang, D. Gu, S. Wang, Y. Qiao, Q. Liu, X. Xue, Y. Yin, R. Xi and M. Meng, *ACS Sens.*, 2021, **6**, 1543–1551.

252 K. Wang, R. Zhang, X. Zhao, Y. Ma, L. Ren, Y. Ren, G. Chen, D. Ye, J. Wu, X. Hu, Y. Guo, R. Xi, M. Meng, Q. Yao, P. Li, Q. Chen and T. D. James, *J. Am. Chem. Soc.*, 2023, **145**, 8408–8416.

253 E. L. Que, R. Bleher, F. E. Duncan, B. Y. Kong, S. C. Gleber, S. Vogt, S. Chen, S. A. Garwin, A. R. Bayer, V. P. Dravid,

T. K. Woodruff and T. V. O'Halloran, *Nat. Chem.*, 2014, **7**, 130–139.

254 E. Smedler and P. Uhlén, *Biochim. Biophys. Acta, Gen. Subj.*, 2014, **1840**, 964–969.

255 P. Uhlén and N. Fritz, *Biochem. Biophys. Res. Commun.*, 2010, **396**, 28–32.

256 J. Lechleiter, S. Girard, E. Peralta and D. Clapham, *Science*, 1991, **252**, 123–126.

257 L. S. Jouaville, F. Ichas, E. L. Holmuhamedov, P. Camacho and J. D. Lechleiter, *Nature*, 1995, **377**, 438–441.

258 N. Bazargani and D. Attwell, *Nat. Neurosci.*, 2016, **19**, 182–189.

259 Z. Shang, X. Yang, Q. Meng, S. Tian and Z. Zhang, *Smart Mol.*, 2023, **1**, e20220007.

260 D. Saimi and Z. Chen, *Smart Mol*, 2023, **1**, e20230002.

261 J. Yang, Z. Chen, M. Fang and Z. Li, *Smart Mol.*, 2024, **2**, e20240034.

262 Y. Wang, Y. Hu and D. Ye, *Angew. Chem., Int. Ed.*, 2022, **61**, e202209512.

263 G. D. Thiabaud, M. Schwalm, S. Sen, A. Barandov, J. Simon, P. Harvey, V. Spanoudaki, P. Müller, J. L. Sessler and A. Jasanoff, *ACS Sens.*, 2023, **8**, 3855–3861.

264 M. E. Graziotto, C. J. Kidman, L. D. Adair, S. A. James, H. H. Harris and E. J. New, *Chem. Soc. Rev.*, 2023, **52**, 8295–8318.

265 J. Zhang, X. Peng, Y. Wu, H. Ren, J. Sun, S. Tong, T. Liu, Y. Zhao, S. Wang, C. Tang, L. Chen and Z. Chen, *Angew. Chem., Int. Ed.*, 2021, **60**, 25846–25855.

266 H. Wang, H. Wang, T. Xiu, X. Zhang, Y. Tang, W. Zhang, W. Zhang, P. Li and B. Tang, *Angew. Chem., Int. Ed.*, 2025, **64**, e202506728.

267 P. H. Tong, T. Y. Wu, M. Li, H. B. Wang, F. Zheng, L. Xu and W. T. Dou, *Smart Mol.*, 2025, **3**, e20240059.

268 S. Wang, H. Song, C. Yin and F. Huo, *Coord. Chem. Rev.*, 2025, **543**, 216940.

269 H. Yang, X. Wu, X. Lv, F. Huo, K. Ma and C. Yin, *Chin. Chem. Lett.*, 2025, 112204, DOI: 10.1016/j.cclet.2025.112204.

270 X. Zhang, N. Zhou, F. Huo and C. Yin, *Chin. Chem. Lett.*, 2026, 112364, DOI: 10.1016/j.cclet.2026.112364.

271 W. Zong, R. Wu, M. Li, Y. Hu, Y. Li, J. Li, H. Rong, H. Wu, Y. Xu, Y. Lu, H. Jia, M. Fan, Z. Zhou, Y. Zhang, A. Wang, L. Chen and H. Cheng, *Nat. Meth.*, 2017, **14**, 713–719.

272 X. Kang, Z. Du, S. Yang, M. Liang, Q. Liu and J. Qi, *Smart Mol.*, 2024, **2**, e20240033.

273 Y. Zhang, X. Lv, Y. Wang, X. Chen, J. Zhang and D. Su, *Smart Mol.*, 2024, **2**, e20240031.

274 Y. Zhang, L. Bai, X. Wang, Y. Zhao, T. Zhang, L. Ye, X. Du, Z. Zhang, J. Du and K. Wang, *Nat. Meth.*, 2024, **22**, 177–186.